W7-AS Contributions to the 13th International Conference on Plasma Surface Interactions in San Diego/USA, May 18-22, 1998

W7-AS Contributions to the 25th EPS Conference on Controlled Fusion and Plasma Physics in Prague, June 29 to July 3, 1998

W7-AS Contributions to the 17th IAEA Fusion Energy Conference in Yokohama, Oct 19 – 24, 1998

IPP III/259

March 2000

PSI 1998

W7-AS Contributions to the 13th International Conference on Plasma Surface Interactions

(May 18-22, 1998, Bahia Hotel, San Diego, CA, USA)

CONTENTS

EPS 1998

W7-AS Contributions to the 25th EPS Conference on Controlled Fusion and Plasma Physics

(Prague, Czech Republic, June 29 to July 3, 1998)

CONTENTS

IAEA 1998

17th IAEA Fusion Energy Conference

(Yokohama, Japan Oct 19 – 24,1998)

CONTENTS

Turbulent SOL transport in stellarators and tokamaks

M. Endler

Max-Planck-Institut für Plasmaphysik, EURATOM Association, 85740 Garching, Germany

Abstract

Spatially highly resolved Langmuir probe measurements of ion saturation current and floating potential fluctuations in the SOL and edge of several tokamaks and stellarators have revealed the spatial structure of these fluctuations. The knowledge of the phase angle and coherency between the fluctuations of these quantities is important for a comparison with models and for the calculation of the induced radial transport.

The fluctuations occur as individual events of interchange character, causing burst-like E×B flows which are very localised in poloidal position and in time. The resulting particle transport can account for the confinement time inferred from particle balance considerations and from the observed gradients in the SOL.

The role of fluctuations of the electron temperature and of the magnetic field and our understanding of the instability mechanism acting in the plasma edge is summarised. A brief account is given on the changes of the fluctuations and the resulting transport when discharge parameters are varied.

1 Introduction

The interest in plasma turbulence within nuclear fusion research is based primarily on the fact that turbulent convection due to fluctuating E×B velocity is, at least in the edge and scrape-off layer (SOL) of all major fusion experiments on which this has been verified, a major contribution to the observed "anomalous" radial transport [1–5]. By investigating the fluctuations of various plasma quantities we hope to understand better the instability mechanisms underlying plasma turbulence and to get insight into how to modify the fluctuation-induced transport. In this paper, I shall summarise our knowledge of the basic properties of fluctuations in the SOL and the related radial transport. These basic properties have been found to be quite the same in devices as different in size and magnetic

configuration as tokamaks and stellarators, as JET and "table-top" tokamaks. I shall restrict myself on the "electrostatic" fluctuations of plasma density $\tilde{n}$, electron temperature $\tilde{T}_e$ and electric potential $\tilde{\Phi}_{pl}$, except for section 5 where the role of magnetic fluctuations and the meaning of the notion "electrostatic fluctuations" are discussed. Furthermore, I shall not consider fluctuations and transport associated with "Edge Localized Modes" (ELMs).

Many fluctuation measurements in the SOL rely on the high spatial and temporal resolution of Langmuir probes (see, e. g., [6–8]), which have the additional advantage that several fluctuating quantities like ion saturation current fluctuations $\tilde{I}_{sat}$ and floating potential fluctuations $\tilde{\Phi}_{fl}$ can be measured. Frequently, for lack of better knowledge, temperature fluctuations are neglected and I_{sat} fluctuations are taken to be $\propto \tilde{n}$, and $\tilde{\Phi}_{fl} \propto \tilde{\Phi}_{pl}$. However, recently $\tilde{n}$, $\tilde{T}_e$ and $\tilde{\Phi}_{pl}$ have been measured simultaneously with Langmuir probes on various devices with slightly different techniques, offering the chance to verify the validity of the conclusions drawn from $\tilde{I}_{sat}$ and $\tilde{\Phi}_{fl}$ measurements [9–13]. Further density fluctuation diagnostics such as the poloidally resolved measurement of the H_α or D_α light [14, 15, 5], collective scattering [16–18, 5], radially resolved measurement of the line radiation emitted by a fast lithium beam [19] and microwave reflectometry [20, 21], confirm the results obtained with Langmuir probes. Mirnov coils and miniaturised Rogowski coils have been used to detect fluctuations of the magnetic field and electric current.

Reviews on fluctuations and transport in toroidal magnetic confinement devices can be found in [22–24] and an overview on diagnostic methods for fluctuation investigations is given in [25].

In this paper, I first report on the basic properties of the electrostatic fluctuations in the SOL in section 2 and then establish their relation with radial transport in section 3. A very brief account on our theoretical understanding of the instability mechanism in section 4 will be followed by a discussion of the role of fluctuations of the magnetic field in section 5 and of the influence of plasma parameters on fluctuations and transport in section 6, before I draw conclusions in section 7.

2 Properties of electrostatic fluctuations in the SOL

Fluctuation measurements in the SOL with a single detector, e. g., one Langmuir probe, give a time signal which at first sight much resembles random noise. Most of the spectral power

is located at frequencies below 10–50 kHz, and the spectra are decaying towards higher frequencies. Measurements with poloidal resolution reveal structures propagating poloidally in the ion diamagnetic drift direction [14, 2, 5]. The direction of propagation is consistent with the idea that these structures are convected by the poloidal E×B drift due to the radial electric field in the SOL. The structures are randomly distributed in time and in poloidal direction, they grow and decay again. They have also been called "blobs" [2, 26] or "events" [27, 28]. The spatio-temporal structure of the fluctuations can be characterised by various data analysis techniques, e. g., by calculating the frequency-wavenumber spectra $S(\vec{k},\omega)$ (either "locally" using a two-point method [1, 29] or from the data of multi-tip arrays [30, 5]), the spatial-temporal correlation function [31, 5], or by biorthogonal decomposition [32]. The diagnostic channels were frequently arranged only in poloidal direction. From the correlation function, parameters like correlation time, poloidal correlation length and poloidal propagation velocity have been extracted to characterize changes in the fluctuations when discharge parameters are varied [5]. An algorithm to identify and parametrise the above mentioned fluctuation events has been conceived and used for advanced statistical analysis and conditional averaging of fluctuation data [28, 33]. The typical fluctuation parameters obtained are a correlation time (lifetime of the events, not autocorrelation time) of 10–50 μs, a poloidal correlation length of 1–4 cm and a poloidal propagation velocity of a few 100 m/s up to a few 1000 m/s, the lower values of the velocity being found chiefly on experiments with a toroidal magnetic field of 2–3 T such as ASDEX [5] or W7-AS at 2.5 T [27], the higher values on experiments with a toroidal magnetic field of 1–2 T such as Pretext [1], TEXT at 1 T [34] or W7-AS at 1.25 T [27].

In radial direction, correlation lengths of the fluctuations have been found to be typically by a factor of 2 smaller than poloidal correlation lengths [2, 29, 35–37]. Due to the poloidal propagation of the fluctuations, a simultaneous poloidal resolution is required to avoid the erroneous interpretation of the measurements: Structures which are oblique in the poloidal-radial plane, together with their poloidal velocity, will show a radial propagation if observed at a single poloidal position, as was recently pointed out by Bleuel et al. [38]. In those cases where fluctuations in the SOL were measured with simultaneous radial and poloidal resolution, very low radial (as compared to poloidal) propagation velocities of $\sim$ 100 m/s or below were found [2, 26, 37].

What has been reported up to now in this section on the spatial and temporal structure is true for the fluctuations of both I_{sat} and Φ_{fl}. The database of simultaneous $\tilde{n}$, $\tilde{T}_e$ and $\tilde{\Phi}_{pl}$ measurements is much smaller, and nothing at all is known about fluctuations of the ion temperature T_i. Density fluctuations behave quite similar to $\tilde{I}_{sat}$, whereas the poloidal correlation length of $\tilde{T}_e$ was found to be smaller [11]. It is, however, an ongoing effort to establish the same knowledge of the spatial structure of $\tilde{n}$, $\tilde{T}_e$ and $\tilde{\Phi}_{pl}$ as has been achieved for $\tilde{I}_{sat}$ and $\tilde{\Phi}_{fl}$.

The phase angle between the fluctuating quantities is relevant for the calculation of the induced radial transport (see section 3) and for the comparison with theory (see section 4). Experimentally, the phase angle between $\tilde{I}_{sat}$ and $\tilde{\Phi}_{fl}$ has been found to be in the range $\frac{1}{4}\pi$–$\frac{1}{2}\pi$ for the frequency range containing most of the power [24, 5]. Simultaneous measurements of $\tilde{n}$, $\tilde{T}_e$ and $\tilde{\Phi}_{fl}$ in the SOL with fast swept Langmuir probes gave phase angles close to 0 between $\tilde{n}$ and $\tilde{T}_e$ [39, 12, 13] and $\frac{1}{3}\pi$–$\frac{1}{2}\pi$ between $\tilde{\Phi}_{fl}$ and $\tilde{n}$ [12].

In the direction parallel to the magnetic field, very high correlations (frequently 80–90 %) over distances of 6–12 m were found on several devices, both for $\tilde{I}_{sat}$ [40, 41, 31, 37] and $\tilde{\Phi}_{fl}$ [42, 38, 43]. The plasma edge turbulence thus has a "two-dimensional" structure with filaments extending only few cm perpendicular to the magnetic field but many metres in parallel direction (this does not imply that the parallel dynamics may be neglected in models, see section 4). These filaments are directly visible on high speed movies and videos from ASDEX [44, 45], DITE [45], TFTR [46, 15] and COMPASS [47]. The parallel correlation measurements were performed with Langmuir probes at different toroidal and poloidal locations, positioned approximately on the same magnetic field line. The radial position of one of the probes and the safety factor were then varied until maximum correlation was achieved, which occured at time delay 0. To determine the magnitude of the parallel wavevector component $k_{\|}$, magnetic field line tracing codes were used to determine the angle between the magnetic field and the line connecting the two toroidally separated probes at maximum correlation. The accuracy of this comparison is limited by the precision to which the plasma current and the toroidal field coil currents are known. Both $k_{\|} = 0$ within the errors [42, 41, 31, 38] and small non-zero values of $k_{\|}$ [42, 40, 43] have been reported for the SOL. In all cases, $k_{\|}/k_{pol} < 10^{-2}$ was found, and this ratio was smaller when a larger separation between the probes was available.

In contrast, a clear time delay or phase shift could be detected downstream on the same magnetic field line when a driving signal was actively fed into a Langmuir probe, corresponding to a finite $k_{\|}$ of the excited wave [43, 48, 49]. These data are consistent with an Alfvén-type wave propagating along the magnetic flux tube.

3 Electrostatic fluctuations and transport

Particle and thermal transport perpendicular to the magnetic field results due to correlated fluctuations of the plasma drift velocity $\tilde{\vec{v}}_{\perp}$ and density $\tilde{n}$ and/or temperature $\tilde{T}_e$ or $\tilde{T}_i$. The radial transport due to fluctuations of the radial plasma velocity is

$$\bar{\Gamma}_r = \langle \tilde{n}\, \tilde{v}_r \rangle \tag{1}$$

for particles and

$$\bar{Q}_{rj} = \frac{3}{2} \langle \tilde{p}_j\, \tilde{v}_r \rangle \tag{2}$$

for heat (species j) [50]. Given the phase angles between the fluctuating quantities as reported in section 2, the dominant contributions to $\bar{\Gamma}_r$ and $\bar{Q}_{re}$ are due to fluctuations of the radial E×B velocity, caused by fluctuations of the poloidal electric field component E_θ. To measure the turbulent fluxes therefore requires a simultaneous recording of $\tilde{n}$, $\tilde{T}_j$ and $\tilde{E}_\theta$ (or $\nabla_\theta \tilde{\Phi}$) at the same location with sufficient temporal and spatial resolution to resolve the dominant components of the fluctuations in the frequency-wavevector spectra. Except for a few results with a heavy ion beam probe (HIBP) [51], this has so far only been achieved using Langmuir probes. In these measurements, $\tilde{E}_\theta$ is calculated from the difference in $\tilde{\Phi}$ as measured by two probe tips separated a few mm poloidally. The radial particle transport $\bar{\Gamma}_r$ was in most cases calculated from $\tilde{I}_{sat}$ and $\tilde{\Phi}_{fl}$, neglecting the influence of temperature fluctuations. As simultaneous Langmuir probe measurements of $\tilde{I}_{sat}$, $\tilde{T}_e$ and $\tilde{\Phi}_{fl}$ were performed [39, 12, 13], it became evident that $\tilde{T}_e$ and $\tilde{n}$ are nearly in phase for the dominant spectral range of fluctuations and that the relative fluctuation amplitude $\tilde{T}_e/\bar{T}_e$ often is smaller than $\tilde{n}/\bar{n}$. Therefore, $\tilde{n}$ is overestimated by calculating it from $\tilde{I}_{sat}$ with the neglect of $\tilde{T}$. A more severe error is introduced by the assumption $\tilde{\Phi}_{pl} \sim \tilde{\Phi}_{fl}$. However, due to the measured phase between $\tilde{n}$, $\tilde{T}_e$ and $\tilde{\Phi}_{fl}$, this error does not severely affect the radial transport, eq. (1) and (2), as was recently pointed out by Pfeiffer et al. [12].

The coherency between $\tilde{I}_{sat}$ and $\tilde{\Phi}_{fl}$ or $\tilde{n}$ and $\tilde{\Phi}_{pl}$ is usually found to be in the order of 0.5 for the frequency range with significant spectral power, and, together with the phase

angles between the fluctuating quantities reported in section 2, a net transport of particles and heat directed radially outwards results (see, e. g., [22, 24] and references therein). If $\Gamma_r(t) = \tilde{n}(t)\,\tilde{v}_r(t)$ is plotted versus time, its probability distribution function is found to be highly asymmetric, reflected by large values for the third and fourth central moments (skewness and flatness) [5, 52]. A large fraction of the tansport is due to several high amplitude "events" during comparatively short intervals of time [5]. Likewise in space, the statistical event analysis of the poloidally resolved $\tilde{I}_{sat}$ and $\tilde{\Phi}_{fl}$ measurements in the SOL of ASDEX revealed that the poloidal extent of the regions of high outwards transport is smaller than for the underlying $\tilde{I}_{sat}$ and $\tilde{\Phi}_{fl}$ signals and that the largest $\tilde{\Phi}_{fl}$ events do not necessarily contribute most to the transport [33].

The particle fluxes thus calculated from simultaneous $\tilde{I}_{sat}$ and $\tilde{\Phi}_{fl}$ measurements at the LCMS and in the SOL have been compared with the global particle balance [1, 3, 41, 53] and with the observed density profile in the SOL [2, 3] on various tokamaks. Although the turbulent particle flux measured locally at one position in the plasma edge had to be taken as valid for the whole surface area of the torus, an agreement within a factor of 2 usually was found (see also section 6).

To assess the fluctuation-induced heat flux, eq. (2), $\tilde{p} = k_B(\tilde{n}\bar{T} + \bar{n}\tilde{T} + \tilde{n}\tilde{T})$ is usually written as $\tilde{p} = k_B(\tilde{n}\bar{T} + \bar{n}\tilde{T})$, neglecting the term $\tilde{n}\tilde{T}$ as of higher order in the fluctuating quantities. Accordingly, $\bar{Q}_r$ is subdivided into a "convective" part $\frac{3}{2}k_B\bar{T}\langle\tilde{n}\,\tilde{v}_r\rangle = \frac{3}{2}k_B\bar{T}\bar{\Gamma}_r$ and a "conductive" part $\frac{3}{2}k_B\bar{n}\langle\tilde{T}\,\tilde{v}_r\rangle$. Since $\bar{T}_e$ can be estimated fairly well using Langmuir probes, the convective part of the turbulent electron heat flux can be calculated, once the turbulent particle flux $\bar{\Gamma}_r$ is known. In TEXT, the values thus obtained were too low by a factor of the order of 2 to account for the global energy balance unless unreasonably high contributions from the conductive part were assumed [54]. In contrast, Vayakis concluded that, within the uncertainties of his measurement and invoking a conductive part of the same order of magnitude as the measured convective one, on DITE the global energy balance could be accounted for by the observed electrostatic fluctuations [53]. In an experiment actually measuring electron temperature fluctuations in the Caltech tokamak, Liewer et al. concluded that the observed turbulent fluxes could account for the global energy confinement found in this device, too [55]. In recent simultaneous $\tilde{I}_{sat}$, $\tilde{T}_e$ and $\tilde{\Phi}_{fl}$ Langmuir probe measurements in the SOL of the W7-AS stellarator, the particle transport calculated

from $\tilde{I}_{sat}$ and $\tilde{\Phi}_{fl}$ neglecting $\tilde{T}_e$ was found to be by a factor of 1–2 larger than the value calculated from $\tilde{n}$ and $\tilde{\Phi}_{pl}$. Furthermore, the conducted heat flux was found to be 0.5–1 times the convected heat flux [12].

No measurements of ion temperature fluctuations are available so far. In the context of turbulent convection due to E×B drift [5] one would, however, expect ion thermal energy $\frac{3}{2}p_i$ to be transported radially in a similar manner and at a similar rate as particles and electron thermal energy.

4 Theoretical understanding

The class of instabilities much discussed to be responsible for the turbulence observed in the plasma edge are drift wave instabilities in a very general sense. In the most simple version of an electrostatic drift wave, as it can be found in textbooks (e. g., [56]), perturbations of plasma density and electric potential are considered in the presence of a density gradient ∇n_0 perpendicular to the magnetic field. With ∇n_0 in x direction, the magnetic field in z direction and the wavevector of the perturbation chiefly in y direction, E×B drift in x direction due to the potential perturbation occurs, and so do electric currents perpendicular to the magnetic field due to polarisation and diamagnetic drifts. These currents are not divergence-free (for the diamagnectic current this is true only in the presence of a magnetic field gradient) but must be balanced by currents parallel to the magnetic field. These are carried mainly by the electrons due to their higher mobility. In a geometry periodic in z direction, the wavevector of the perturbation must then have a non-zero z component. An analysis of this simple model shows that the electrons tend to establish a Boltzmann distribution

$$\tilde{n} = \frac{e\tilde{\Phi}}{k_B T_e}. \tag{3}$$

If they could move unimpeded parallel to the magnetic field, and if polarisation drift and finite Larmor radius effects are neglected, this Boltzmann relation would hold exactly, and density and potential perturbation were in phase. In this case, the drift wave would propagate in y direction but would not be unstable. Every mechanism restricting the motion of the electrons parallel to the magnetic field adds to the phase shift between $\tilde{n}$ and $\tilde{\Phi}$ and drives the drift wave more unstable. The first such mechanisms considered were plasma resistivity (collisional drift wave) and trapping of electrons (see, e. g., [57] and references

therein). For the typical plasma parameters in the edge of fusion experiments the phase shift in such a simple model is still quite small. However, the Boltzmann relation (3) was in general not found to be satisfied experimentally in the plasma edge, neither in amplitude nor in phase between $\tilde{n}$ and $\tilde{\Phi}$ (see, e. g., [24] and references therein). In more realistic drift wave models and numerical simulations larger deviations from the Boltzmann relation are reproduced (see, e. g., [58–60]).

In toroidal geometry, suitable periodic boundary conditions are required in the confinement region, linking the y and z components of the perturbation wavevectors [61]. In contrast, in the SOL by definition each magnetic field line is limited by a target plate. Here, the sheath conditions introduce a new mechanism to impede the electron currents in z direction [62–66, 5]. The sheath "resistivity" scales differently from the bulk plasma resistivity (Spitzer resistivity) and depends also on quantities like the secondary electron emission of the target plates or the average net current to the target plates for each magnetic flux tube [5, 67]. This instability can still be called drift instability in the sense that it is derived using the drift approximation for velocities perpendicular to the magnetic field (see, e. g., [56] or the derivation in [68]) and that particle and energy transport perpendicular to the magnetic field is dominantly due to E×B drift.

A second way in which the target plates and the SOL geometry can influence plasma turbulence is through the formation of a radial electric field: Each magnetic flux tube is charged with respect to the target plates to a potential following the sheath equations (see, e. g., [69]). In first approximation, this potential is proportional to the electron temperature, but it also depends on the electric current to the target plates and the secondary electron emission coefficient for each flux tube [5, 67]. The radial profile of the resulting radial electric field is therefore intimately related to parallel gradients or changes in the connection length to the target plates, in short, to the whole SOL physics including the position of recycling and impurity sources. An additional possibility of influencing the plasma potential is the biasing of parts of the target plates. Examples for the interplay between the SOL geometry, the radial electric field, the radial profiles of Φ_{fl} and I_{sat} and also the fluctuation parameters can be found in [70, 5]. As the radial electric field induces a poloidal E×B drift, the radial shear of this drift velocity depends on the detailed shape of the radial plasma potential profile. The influence of this velocity shear on plasma turbulence and the possible

connection with the L-H transition has been discussed extensively ([71, 72], and references in the latter). Due to the complex nature of the problem, involving plasma edge geometry, recycling and possibly impurity radiation, no comprehensive model has been presented as yet.

Meanwhile it has become possible to compare the influence of the various terms on the properties of the turbulence simulated in numerical codes. Although the basic dynamics for edge and SOL plasma turbulence appear to be unchanged from a rather simplified model, it seems to be necessary to include all of heat transport and temperature fluctuations, gradients and curvature of the magnetic field, electromagnetic induction, electron inertia, sheath boundary conditions and radial electric field to quantitatively reproduce the observed fluctuation characteristics and induced transport [59, 73].

5 The role of magnetic fluctuations

Fluctuations of the magnetic field need to be considered in plasma edge turbulence in two ways. The first question is whether they play a role for the dynamics of the turbulence, the second whether they must be taken into account for the turbulent radial transport. The magnetic field is assumed to be stationary in simple drift wave models. On the other hand, fluctuating electric currents parallel and perpendicular to the magnetic field do occur in all these models, so fluctuations of the magnetic field naturally exist. The order of magnitude of broadband magnetic fluctuations observed with Mirnov coils is indeed consistent with the values expected due to the measured density and potential fluctuations in the SOL [5, 74].

The first of the above questions then is whether these fluctuations of the magnetic field are strong enough to influence the turbulence dynamics. According to estimates and numerical simulations, this is the case for a plasma pressure as it can be found close to the LCMS even in the SOL [75, 59]. The resulting turbulence in the simulations is stronger when including the magnetic fluctuations, but the nature of the dominant influence mechanism is still subject of discussion [59, 76].

The second question addressed is whether the fluctuations of the radial component of the magnetic field are sufficient to contribute a significant amount to the radial particle or heat transport via "magnetic flutter" [77]. Although in some cases fluctuating $E \times B$ transport was found to be too small to completely account for the energy balance in the SOL [54], the

amplitude of magnetic fluctuations was always found to be far too small to contribute significantly to the transport, at least in the SOL of tokamaks and stellarators [55, 54, 78, 24]. This was verified by direct measurements of the radial electron heat transport due to correlated fluctuations of parallel electron heat flux and radial magnetic field by means of a fast pyrobolometer in the SOL of TEXT-U [79]. The result that radial transport even of electron heat due to magnetic fluctuations is negligible is reproduced by numerical drift wave simulations for typical plasma edge parameters [59].

If the broadband magnetic fluctuations observed in the plasma edge are due to the fluctuating parallel electric currents of drift wave turbulence, a correlation between the signals of Mirnov coils and those of close-by Langmuir probes is expected. In most devices in which such correlations have been investigated, they were found to exist [80, 81, 82]. In recent direct measurements of parallel current fluctuations on CASTOR by means of a miniaturised Rogowski coil inserted into the edge plasma, a significant correlation with a $\tilde{\Phi}_{fl}$ measurement at the same position was found [74].

6 Influence of the plasma parameters on the SOL fluctuations and on the induced transport

For the comparison of experimental observations with the predictions of plasma turbulence models, the change in fluctuation parameters and E×B transport for variations of the discharge parameters are of particular interest. On the other hand, a comparison between the observed E×B fluxes and global particle and energy confinement time is required to assess the relevance of the measured fluxes for various discharge conditions in addition to the order-of-magnitude agreement reported in section 3. Only few such parameter scans have been done so far. Rowan et al. measured the E×B particle transport across the LCMS derived from $\tilde{\Phi}_{fl}$ and $\tilde{I}_{sat}$ measurements and compared the particle confinement time calculated from these data with the particle confinement time calculated from H_α measurements of the plasma source. This comparison was done for scans of the plasma density, the toroidal magnetic field and the radial plasma position in TEXT [3]. Endler et al. calculated fluctuation parameters like lifetime, poloidal correlation length, poloidal wavelength and poloidal propagation velocity of the fluctuations from the data of an H_α optical imaging diagnostic for variations of plasma density, toroidal magnetic field, plasma

current and vertical plasma position in ASDEX and compared the results with a linear target plate instability model [70, 5]. Bleuel calculated fluctuation parameter and radial E×B particle transport profiles from $\tilde{\Phi}_{fl}$ and $\tilde{I}_{sat}$ measurements in the SOL and slightly inside the LCMS for variations of plasma density, ECR heating power, magnetic field and gas species (hydrogen or deuterium) in W7-AS and compard the scaling of the E×B flux with the energy confinement time [37].

For the SOL fluctuation parameters (0–2 cm outside the LCMS), the following behaviour has been observed: With increasing average plasma density, the lifetime and the poloidal and radial correlation lengths increase, and the poloidal velocity (in the ion diamagnetic drift direction) decreases [5, 37]. In ASDEX, density and separatrix temperature had an inverse scaling in ohmic discharges with constant plasma current and magnetic field [83], so the observed changes in the fluctuation parameters could be due to a decrease of the temperature rather than an increase of the density. In W7-AS, however, the fluctuation parameters in the SOL remained unchanged when the ECR heating power (and thus T_e in the SOL) was varied at constant density. It seems therefore to be the plasma density or a related parameter rather than the electron temperature which influences the fluctuation parameters in the SOL. The second discharge parameter strongly affecting the poloidal and radial correlation lengths and the poloidal velocity of the fluctuations is the magnetic field: At low magnetic field, the correlation lengths and the velocity are larger, whereas the lifetime is not significantly changed [5, 37]. The strong dependence of the poloidal propagation velocity of the fluctuations in the SOL on the magnitude of the magnetic field becomes also evident when comparing data from different machines (see section 2 and references given there). A strong variation of the fluctuation parameters with vertical plasma position was found on ASDEX. In such a scan, the SOL configuration changed from single null upper X-point through double null to single null lower X-point, and the changes, however not yet understood, emphasize the importance of the detailed SOL and target plate configuration on the quantitative behaviour of the fluctuations [70].

The E×B particle fluxes measured at the LCMS slightly decrease with increasing plasma density in W7-AS. Together with a steepening of the density profiles, a lower anomalous diffusion coefficient is calculated [37]. The same was found in TEXT, where the particle confinement time derived was in good agreement with the values and the scaling

obtained from H_α measurements [3]. In W7-AS, likewise, the increase of the energy confinement time with plasma density is in qualitative agreement with the decrease of the turbulent particle flux. The same agreement was found for the increase of particle flux and decrease of energy confinement time when the ECR heating power is increased [37] (assuming again that particle and heat transport are due to the same turbulent convection and hence scale in a similar way). Changes in the magnitude of the magnetic field do not strongly affect the turbulent particle flux both in TEXT and in W7-AS, in contrast to their influence on the size and poloidal propagation velocity of the fluctuation structures.

The question remaining unanswered is whether the SOL fluctuations determine the anomalous transport across the LCMS and thus the global confinement time or whether they just adapt to take over the fluxes passing the LCMS due to processes originating in the confinement region.

7 Conclusions

The observation of the SOL fluctuations in tokamaks and stellarators suggests that they are of drift-wave type in a very general sense, as detailed in section 4. In addition to the terms used in the early drift wave models, the magnetic geometry (gradients and curvature of the magnetic field), magnetic induction due to fluctuating parallel electric currents, temperature fluctuations, sheath boundary conditions and possibly further effects must be included to account for the observed turbulence quantitatively in a numerical simulation. The interplay between the radial pressure gradients serving as source of free energy for the turbulence, the resulting radial transport flattening the gradients, parallel average electric currents onto the target plates (which are, together with the radial electron temperature gradient, determining the radial electric field), the location of plasma recycling sources or gas puffing and the geometry of the SOL is rather involved and not yet understood in detail.

The radial $E\times B$ particle flux calculated from measured floating potential and ion saturation current fluctuations usually agrees well with the flux inferred from radial profiles and particle balance analysis. Magnetic fluctuations play no direct role ("magnetic flutter" transport) in the SOL of tokamaks and stellarators. The question whether the observed energy confinement and radial temperature profiles are also consistent with the turbulent $E\times B$ heat transport requires further investigation.

The qualitative understanding of the instability mechanism offers the chance to influence the turbulence in the SOL, e. g., by applying DC or AC voltages to target plate sections or probe tips inserted into the SOL [84, 85].

Our increased understanding of SOL turbulence has been much advanced by the high spatial and temporal resolution offered by Langmuir probes and by the fact that this diagnostic allows a simultaneous measurement of density and potential fluctuations. Unfortunately, in large fusion experiments probes are restricted to the very edge. We are still lacking a diagnostic measuring plasma potential or electric field fluctuations deeper in the confinement region with a resolution comparable to Langmuir probes (except for the HIBP, which suffers from beam intensity problems in large devices). This and the *quantitative* understanding and the modification of SOL turbulence and transport will be the next goals of fluctuation investigations in stellarators and tokamaks.

References

[1] S. J. Levinson et al., Nucl. Fusion **24**, 527 (1984).

[2] S. J. Zweben and R. W. Gould, Nucl. Fusion **25**, 171 (1985).

[3] W. L. Rowan et al., Nucl. Fusion **27**, 1105 (1987).

[4] A. Rudyj et al., 16th EPS Conference on Controlled Fusion and Plasma Physics (Venice), volume 13B, part I, 27 (1989).

[5] M. Endler et al., Nucl. Fusion **35**, 1307 (1995).

[6] F. F. Chen, Electric probes, in *Plasma Diagnostic Techniques*, edited by R. H. Huddlestone and S. L. Leonard, chapter 4, pages 113–200, Academic Press, New York, 1965.

[7] J. D. Swift and M. J. R. Schwar, *Electrical Probes for Plasma Diagnostics*, Iliffe Books LTD, 1970.

[8] D. M. Manos and G. M. McCracken, Probes for plasma edge diagnostics in magnetic confinement fusion devices, in *Physics of Plasma-Wall Interactions in Controlled Fusion*, edited by D. E. Post and R. Behrisch, volume 131 of *NATO ASI series, Series B, Physics*, pages 135–209, New York, 1986, Plenum Press.

[9] R. Balbín et al., Rev. Sci. Instrum. **63**, 4605 (1992).

[10] C. Hidalgo et al., Phys. Rev. Lett. **69**, 1205 (1992).

[11] L. Giannone et al., Phys. Plasmas **1**, 3614 (1994).

[12] U. Pfeiffer et al., Contrib. Plasma Phys. **38**, 134 (1998).

[13] M. A. Meier, G. A. Hallock, and R. D. Bengtson, Contrib. Plasma Phys. **38**, 98 (1998).

[14] S. J. Zweben, J. McChesney, and R. W. Gould, Nucl. Fusion **23**, 825 (1983).

[15] S. J. Zweben and S. S. Medley, Phys. Fluids B **1**, 2058 (1989).

[16] I. H. Hutchinson, *Principles of plasma diagnostics*, Cambridge University Press, Cambridge, New York, Port Chester, Melbourne, Sydney, 1987.

[17] E. Holzhauer, G. Dodel, and ASDEX Team, Rev. Sci. Instrum. **61**, 2817 (1990).

[18] P. Devynck et al., Plasma Phys. Controlled Fusion **35**, 63 (1993).

[19] S. Zoletnik et al., Determination of electron density fluctuation correlation functions via beam emission spectroscopy, accepted for publication in Plasma Phys. Controlled Fusion (1998).

[20] H. J. Hartfuß, T. Geist, and M. Hirsch, Plasma Phys. Controlled Fusion **39**, 1693 (1997).

[21] E. Holzhauer et al., Theoretical and experimental investigation of the phase-runaway in microwave reflectometry, submitted to Plasma Phys. Controlled Fusion (1998).

[22] P. C. Liewer, Nucl. Fusion **25**, 543 (1985).

[23] A. Wootton et al., Plasma Phys. Controlled Fusion **30**, 1479 (1988).

[24] A. J. Wootton et al., Phys. Fluids B **2**, 2879 (1990).

[25] N. Bretz, Rev. Sci. Instrum. **68**, 2927 (1997).

[26] S. Zweben, Phys. Fluids **28**, 974 (1985).

[27] M. Endler et al., Physica Scripta **51**, 610 (1995).

[28] G. Theimer et al., Individual event analysis: A new tool for the investiagtion of structures in turbulence, in *Transport, Chaos and Plasma Physics 2*, edited by S. Benkadda, F. Doveil, and Y. Elskens, volume 9 of *Advanced Series in Nonlinear Dynamics*, pages 89–92, World Scientific, Singapore, New Jersey, London, Hong Kong, 1996.

[29] C. Ritz et al., Nucl. Fusion **27**, 1125 (1987).

[30] H. Niedermeyer et al., 18th EPS Conference on Controlled Fusion and Plasma Physics (Berlin), volume 15C, part I, 301 (1991).

[31] A. Rudyj et al., 17th EPS Conference on Controlled Fusion and Plasma Heating (Amsterdam), volume 14B, part III, 1464 (1990).

[32] S. Benkadda et al., Phys. Rev. Lett. **73**, 3403 (1994).

[33] G. Theimer, *Charakterisierung transportrelevanter turbulenter elektrostatischer Fluktuationen in der Abschälschicht des Tokamaks ASDEX mittels Darstellung als Superposition von raum-zeitlich lokalisierten Ereignissen*, PhD thesis, Technische Universität München, 1997, IPP report III/223, Max-Planck-Institut für Plasmaphysik, Garching.

[34] C. Ritz et al., Phys. Fluids **27**, 2956 (1984).

[35] M. Krämer and A. Carlson, 16th EPS Conference on Controlled Fusion and Plasma Physics (Venice), volume 13B, part III, 923 (1989).

[36] G. Wang et al., Evidence for spatial intermittency in plasma turbulence of the KT-5C tokamak, submitted to Phys. Rev. Lett. (1997).

[37] J. Bleuel, *Elektrostatische Turbulenz am Plasmarand des Stellarators Wendelstein 7-AS*, PhD thesis, Technische Universität München, 1998, in preparation.

[38] J. Bleuel et al., 23rd EPS Conference on Controlled Fusion and Plasma Physics (Kiev), volume 20C, part II, 727 (1996).

[39] H. Y. W. Tsui et al., Rev. Sci. Instrum. **63**, 4608 (1992).

[40] C. P. Ritz et al., Rev. Sci. Instrum. **59**, 1739 (1988).

[41] A. Rudyj, *Untersuchung transportrelevanter Fluktuationen in der Randschicht von ASDEX*, PhD thesis, Technische Universität München, 1990, IPP report III/160, Max-Planck-Institut für Plasmaphysik, Garching.

[42] K. M. Young, *Fluctuations and particle loss in ohmic heated discharges in the model C stellarator*, PhD thesis, Princeton University, 1968.

[43] R. D. Bengtson, D. L. Winslow, and D. W. Ross, Contrib. Plasma Phys. **38**, 104 (1998).

[44] H. Niedermeyer, High speed movie of plasma edge fluctuations on ASDEX, personal communication, see also annual report of the Max-Planck-Institut für Plasmaphysik, Garching, 1981, p. 10.

[45] D. H. J. Goodall, J. Nucl. Mater. **111 & 112**, 11 (1982).

[46] S. Zweben et al., J. Nucl. Mater. **145–147**, 250 (1987).

[47] J. Dowling, High speed CCD movie of plasma edge fluctuations on COMPASS, personal communication, UKAEA, Abingdon, 1997.

[48] A. Geier and H. Niedermeyer, Contrib. Plasma Phys. **38**, 86 (1998).

[49] D. L. Winslow et al., Phys. Plasmas **5**, 752 (1998).

[50] D. W. Ross, Comments Plasma Phys. Controlled Fusion **12**, 155 (1989).

[51] G. Hallock, A. Wootton, and R. Hickok, Phys. Rev. Lett. **59**, 1301 (1987).

[52] J. Petržílka and J. Stöckel, Contrib. Plasma Phys. **38**, 74 (1998).

[53] G. Vayakis, *Anomalous Transport in the Tokamak Edge*, PhD thesis, University of Oxford, 1991, AEA Fusion Report 123.

[54] C. Ritz et al., J. Nucl. Mater. **145–147**, 241 (1987).

[55] P. C. Liewer et al., Phys. Fluids **29**, 309 (1986).

[56] F. F. Chen, *Introduction to Plasma Physics*, Plenum Press, New York, London, 1984.

[57] B. B. Kadomtsev and O. P. Pogutse: "Turbulence in Toroidal Systems" in *Reviews of Plasma Physics* **5** (1970), M. A. Leontovich, editor, pages 249–400.

[58] S.-T. Tsai, F. W. Perkins, and T. H. Stix, Phys. Fluids **13**, 2108 (1970).

[59] B. Scott, Plasma Phys. Controlled Fusion **39**, 1635 (1997).

[60] A. Zeiler, J. F. Drake, and D. Biskamp, Phys. Plasmas **4**, 991 (1997).

[61] R. L. Dewar and A. H. Glasser, Phys. Fluids **26**, 3038 (1983).

[62] F. F. Chen, Plasma Phys. **7**, 399 (1965).

[63] W. B. Kunkel and J. U. Guillory, Proc. 7th Int. Conf. on Phenomena in Ionized Gases (Belgrade), volume 2, 702 (1965).

[64] A. V. Nedospasov, Soviet Journal of Plasma Physics **15**, 659 (1989).

[65] X. Garbet et al., Nucl. Fusion **31**, 967 (1991).

[66] H. L. Berk, D. D. Ryutov, and Y. A. Tsidulko, Phys. Fluids B **3**, 1346 (1991).

[67] M. Endler et al., J. Nucl. Mater. **220–222**, 293 (1995).

[68] B. Scott, Plasma Phys. Controlled Fusion **39**, 471 (1997).

[69] P. C. Stangeby, The plasma sheath, in *Physics of Plasma-Wall Interactions in Controlled Fusion*, edited by D. E. Post and R. Behrisch, volume 131 of *NATO ASI series, Series B, Physics*, pages 41–97, New York, 1986, Plenum Press.

[70] M. Endler, *Experimentelle Untersuchung und Modellierung elektrostatischer Fluktuationen in den Abschälschichten des Tokamak ASDEX und des Stellarators Wendelstein 7-AS*, PhD thesis, Technische Universität München, 1994, IPP report III/197, Max-Planck-Institut für Plasmaphysik, Garching.

[71] H. Biglari, P. H. Diamond, and P. W. Terry, Phys. Fluids B **2**, 1 (1990).

[72] K. H. Burrell, Phys. Plasmas **4**, 1499 (1997).

[73] X. Q. Xu and R. H. Cohen, Contrib. Plasma Phys. **38**, 158 (1998).

[74] J. Stöckel et al., 24th EPS Conference on Controlled Fusion and Plasma Physics (Berchtesgaden), volume 21A, part II, 625 (1997).

[75] A. V. Chankin, Plasma Phys. Controlled Fusion **39**, 1059 (1997).

[76] B. N. Rogers and J. F. Drake, Phys. Rev. Lett. **79**, 229 (1997).

[77] J. D. Callen, Phys. Rev. Lett. **39**, 1540 (1977).

[78] C. Ritz et al., Phys. Rev. Lett. **62**, 1844 (1989).

[79] G. Fiksel et al., Plasma Phys. Controlled Fusion **38**, A213 (1996).

[80] K. W. Gentle et al., 14th EPS Conference on Controlled Fusion and Plasma Physics (Madrid), volume 11D, part I, 81 (1987).

[81] Y. J. Kim et al., Nucl. Fusion **29**, 99 (1989).

[82] G. Vayakis, Nucl. Fusion **33**, 547 (1993).

[83] K. McCormick et al., J. Nucl. Mater. **176 & 177**, 89 (1990).

[84] K. I. Thomassen, Nucl. Fusion **11**, 175 (1971).

[85] B. Richards et al., Phys. Plasmas **1**, 1606 (1994).

3D Fluid Modelling of the Edge Plasma by Means of a Monte Carlo Technique

Y. Feng, F. Sardei and J. Kisslinger

Max-Planck-Institut für Plasmaphysik, EURATOM Association, D-85748 Garching, Germany

Abstract

An extended version of the 3D Monte Carlo edge plasma transport code EMC3 including more complex physics is presented. The balance equations for mass, momentum and energies are formulated in a general conservation form suited for direct application of the Monte Carlo solving algorithm. The new extended version is applied to the planned W7-AS island divertor. First results of the investigations, which are focused on neutral pump-out efficiency, power load distribution on the plates and high recycling performance, are presented.

1. Introduction

In the last years, the urgent need of 3D transport models for understanding the divertor physics in a helical device such as W7-AS has become evident. A 3D Monte Carlo code (EMC3) [1], based on a simplified version of Braginskii´s fluid equations [2], was developed in the last years and used successfully to interpret high recycling experiments in W7-AS island configurations [1,3,4]. However, the simplifications of the physical model (single fluid plasma ($T_e = T_i$), neglect of heat convection and parametric treatment of parallel momentum losses by using experimental data) restricted the code applicability so far.

Recently, the EMC3 code has been extended substantially. The ion parallel momentum equation has been completed by including the cross-B viscous and convective transport of parallel momentum as well as the friction with neutrals provided by the neutral code EIRENE [5], which was coupled selfconsistently to EMC3. In addition, the convective energy fluxes have been introduced into the heat balance equations and the electron and the ion energy transports were treated separately, which allows application of the code to low density plasmas, for which the electron temperature may largely differ from the ion temperature. The balance equations for mass, momentum and energies, which can be written into a general form, are treated with the same Monte Carlo algorithm, which solves both the diffusive and convective terms. The Monte Carlo procedure allows high flexibility in the 3D grid

construction for both the plasma and plasma-facing components. An extension of the EMC3/EIRENE code to include impurity transport is under way.

Additionally, the code has been parallelized on the massive parallel computing system Cray-T3E (784 application processing elements at present), leading to a roughly linear, drastic speed-up of the computations.

2. The EMC3 code

The EMC3 code solves a set of Braginskii's fluid equations in a three-dimensional space with a Monte Carlo technique. One of the main reasons for applying a Monte Carlo method is its high flexibility in the construction of the computational mesh. The magnetic islands and the discontinuous divertor plates in W7-AS and W7-X introduce a complex three-dimensional edge structure. Owing to the shear of the diverted magnetic structures, the helical variation of the island shape and the strong anisotropy of the transports, the feasibility of a computational mesh acceptable for standard finite-difference methods is still an open question. The Monte Carlo method, on the other hand, allows high flexibility in construction and distribution of the computational mesh. Instead of solving a linear matrix for the unknown quantities at the grid points, the EMC3 code follows Monte Carlo particles, which undergo convective and diffusive processes in parallel and cross-field directions. If the magnetic field line vectors are everywhere defined, particles can be traced along and across the B-field lines through the edge plasma, independent on the mesh and coordinates selected. The computational cells are required just for scoring the Monte Carlo particles representing physical quantities such as mass, momentum and energy. Therefore, the grid can be locally adjusted according to the physical resolution.

2.1 Fluid model

We assume a simple neutral plasma consisting of electrons and a single ion species, i.e. $n = n_e = n_i$. The plasma transports are described by a simplifed time-independent version of Braginskii's fluid equations for particle, momentum and heat balance. In the absence of the electric field and plasma current, the equations for mass, momentum and energy read

$$\nabla_{\parallel} \cdot nV_{\parallel} + \nabla_{\perp} \cdot (-D\nabla_{\perp} n) = S_p \tag{2.1}$$

$$\nabla_{\parallel} \cdot (m_i n V_{\parallel} V_{\parallel} - \eta_{\parallel} \nabla_{\parallel} V_{\parallel}) + \nabla_{\perp} \cdot (-m_i V_{\parallel} D \nabla_{\perp} n - \eta_{\perp} \nabla_{\perp} V_{\parallel}) = -\nabla_{\parallel} p + S_m \tag{2.2}$$

$$\nabla_{\parallel}\cdot(-\kappa_i\nabla_{\parallel}T_i+\tfrac{5}{2}nT_iV_{\parallel})+\nabla_{\perp}\cdot(-\chi_i n\nabla_{\perp}T_i-\tfrac{5}{2}T_iD\nabla_{\perp}n)$$
$$=k(T_e-T_i)+S_{ei} \qquad (2.3)$$

$$\nabla_{\parallel}\cdot(-\kappa_e\nabla_{\parallel}T_e+\tfrac{5}{2}nT_eV_{\parallel})+\nabla_{\perp}\cdot(-\chi_e n\nabla_{\perp}T_e-\tfrac{5}{2}T_eD\nabla_{\perp}n)$$
$$=-k(T_e-T_i)+S_{ee} \qquad (2.4)$$

where $p = n(T_i+T_e)$ and $\eta_{\perp} = m_i nD$. The signs $\parallel$ and $\perp$ denote the components parallel and perpendicular to the magnetic field. The parallel transport coefficients $\eta_{\parallel}$, κ_i and κ_e are considered to be classical, while the cross-B transports are usually assumed to be anomalous with D, χ_i and χ_e being determined from experiments. S_p and S_m are the ionization source and momentum loss via charge exchange with neutrals. In the present version, S_{ee} and S_{ei} represent the energy loss or gain of electrons and ions due only to the hydrogen neutrals. All the volume sources due to neutrals are provided by the EIRENE code.

The transport Eqs. (2.1) through (2.4) obey a generalized conservation principle. Introducing the dependent variable f standing for density, parallel velocity and ion or electron temperature, we can rewrite Eqs. (2.1) through (2.4) into a common Fokker-Planck form [6]:

$$\nabla_{\parallel}\cdot[\alpha_{\parallel}f-\nabla_{\parallel}(\beta_{\parallel}f)]+\nabla_{\perp}\cdot[\alpha_{\perp}f-\nabla_{\perp}(\beta_{\perp}f)]=S \qquad (2.5)$$

where $\alpha_{\parallel}$, $\beta_{\parallel}$, $\alpha_{\perp}$, $\beta_{\perp}$ and S represent transport coefficients and source terms which are specific to a particular meaning of f (see Table 1).

Table 1
Meaning of the symbolic transport coefficients and sources associated with f

	mass	momentum	heat
f:	n	$V_{\parallel}$	$T_{e,i}$
$\alpha_{\parallel}$:	$V_{\parallel}$	$m_i nV_{\parallel}+\nabla_{\parallel}\eta_{\parallel}$	$\frac{5}{2}nV_{\parallel}+\nabla_{\parallel}\kappa_{e,i}$
$\beta_{\parallel}$:	0	$\eta_{\parallel}$	$\kappa_{e,i}$
$\alpha_{\perp}$:	0	0	$(\chi_{e,i}-\frac{5}{2}D)\nabla_{\perp}n$
$\beta_{\perp}$:	D	$m_i nD$	$n\chi_{e,i}$
S:	S_p	$-\nabla_{\parallel}p+S_m$	$\mp k(T_e-T_i)+S_{ee,i}$

In spite of the different structure of the boundary conditions for the mass, momentum and energy equations, the concept of the generalization of the fluid equations enables us to formulate a general numerical method, which can be used for determining the whole set of plasma parameters n, $V_{\parallel}$, T_i and T_e.

2.2 Monte Carlo method

Equation (2.5) describes the conservation of a physical quantity such as mass, momentum and energy during the convective and diffusive processes which can be simulated by following Monte Carlo particles. Particles are randomly generated according to a given source distribution and then followed in small time steps Δt. The corresponding random walk step, $\Delta \mathbf{r}$, is determined by:

$$\Delta \mathbf{r} = \sqrt{2\beta_{\parallel}\Delta t}\,\xi_{\parallel} + \alpha_{\parallel}\Delta t + \sqrt{4\beta_{\perp}\Delta t}\,\xi_{\perp} + \alpha_{\perp}\Delta t \qquad (2.6)$$

where $\xi_{\parallel}$ and $\xi_{\perp}$ are the 1D and 2D random unit vectors parallel and perpendicular to B, respectively. The first and the third terms on the r.h.s. of Eq. (2.6) represent diffusion, the others convection of Monte Carlo particles in the two specific directions. Particles are traced and scored in a given mesh. If a particle is lost to target plates or to other sinks, a new particle is started and the computation continues until the desired statistical accuracy is achieved. Finally, the distribution function f is given by:

$$f = Q_s \cdot \frac{\Delta t \cdot \Delta N_p}{N_p \cdot \Delta v} \qquad (2.7)$$

where N_p is the total number of the particles followed and ΔN_p is the number of particles scored in the volume element Δv. Q_s is the total source strength including the contributions of volume sources and surface sources specified on the boundary.

The time step Δt appearing in Eqs. (2.6) and (2.7) does, of course, not mean that the solution of the problem depends on the time step chosen in the computation. In fact, the quantity $(\Delta t \Delta N_p)/N_p$ is just the average time interval spent by the particles to travel through the volume element Δv. This quantity is completely determined by the transport coefficients, source distributions and boundary conditions. As long as the time step is kept sufficiently small, it has no effect on the final solution.

2.3 Computational mesh

An optimal choice of the computational mesh is essential to improve the computation performance. Two points have to be considered in the mesh construction. First, a mesh is needed to store the Monte Carlo particles representing physical quantities such as density, velocity and temperatures. The transport coefficients listed in Table 1 depend strongly on such quantities. Due to both the high non-linearity of the equations and the large difference

between the parallel and perpendicular transports, a nonuniform cell distribution is necessary to meet the physical requirements. Second, for tracing Monte Carlo particles the magnetic field lines need to be specified. The mesh should be able to accurately define them, in order to avoid a time-consuming integration procedure for the field lines of the individual particles. According to these considerations, we choose magnetic coordinates for particle tracing as they allow a simple representation of the B-field lines. However, due to the large number of the grid points needed to describe the complex magnetic surface geometry, storage problem will emerge if the plasma parameters are based on the same mesh. Therefore, in order to reduce the memory and to speed up the computations, two different meshes are defined, the basic geometric mesh for tracing particles and a coarser physical mesh for representing plasma parameters, which can be locally adjusted according to the required resolution.

Figure 1 illustrates the cell distributions of an ι=5/9 W7-AS configuration at a cross section of a lower divertor. The basic geometric mesh consists of about 200,000 grid points, covering a half period of the edge configuration, according to the stellarator symmetry in W7-AS. The grids on each cross section are adjusted as to meet both the geometrical and physical requirements. The toroidal geometric grids, on the other hand, are constructed uniformly and then reduced to give a nonuniform subset which represents the physical mesh satisfying the required resolution, for example, finer cells at the plates (right figure).

In order to speed up the computation, it is necessary to represent the target plates in the magnetic coordinates as well.

3. Applications

Calculations are based on the divertor configuration given in the previous section. Pure hydrogen plasma is assumed with a total power outflow of 400 kW through the separatrix. This power is kept constant for all calculations. The edge plasma density is varied by increasing the total particle outflow to the targets. The diffusion coefficients are kept spatially constant, however scaled with the average edge density roughly as $1/\langle n\rangle_{sol}$, with $\chi_e = \chi_i = 2D$. Radial decay lengths of 2 and 4 cm are set on the last radial surface for the density and temperatures. Momentum entering the plasma core is absorbed, which corresponds to a boundary condition of $\mathbf{V}_{\parallel} = 0$ at the innermost surface contacting the main plasma. Bohm's boundary conditions are assumed at the plates. All source terms due to neutrals are calculated by the EIRENE code.

3.1 Low and high recycling

Two density cases resulting from the given particle fluxes of 6.25×10^{21} and 2.5×10^{22}/s to the targets are compared in Fig. 2, which shows the temperature and density distributions on a cross section cutting the lower divertor plates. The diffusion coefficient D is taken to be 1 m^2/s for the lower density case and decreases to 0.25 m^2/s as the density increases. Despite the small pitch angle of the magnetic field lines inside the islands, the parallel heat conduction dominates the energy transport for electrons, which is indicated both by the energy flux diversion and the weak dependence of the electron upstream temperature on the density. The ion energy transport, on the other hand, is governed by the cross-B anomalous heat conduction due to the weak parallel conductivity, especially in the higher density case. The electron and ion downstream temperature, $T_{e,down}$ and $T_{i,down}$, decrease from 24 and 39 eV to 9 and 12 eV as the density increases, which are still high enough for ionization of neutrals. Thus, no significant momentum losses via charge exchange contribute to the momentum balance. A very important momentum loss mechanism instead is the cross-B momentum transport resulting from the enhanced anomalous cross-B diffusion of the ions. Because of the large ratio of the connection length to the island size, perpendicular particle diffusion dominates over parallel convection in a large island region away from the targets. Momentum loss occurs if the ions exchange their momentum through diffusion inside the islands. For the lower recycling case, neutrals penetrate deeply into the islands, causing a monotonous radial drop of the density profile. Density increases with increasing recycling flux, especially at the downstream position close to the targets. The increasing density shifts the ionization zone outwards and decreases the down-stream temperatures, leading to a density rise in front of the targets. Toroidally away from the targets, the density peak is smoothed by diffusion, resulting in a rather broad density profile in the island SOL between the targets.

3.2 Energy and particle exhaust

Control of the energy and particle exhaust is the basic task of the island divertor, where the energy flux density to the plates must be kept below a technical limit. For the planned W7-AS divertor, ten discontinuous divertor plates are installed up-down symmetrically on the elliptical cross sections with a toroidal extension of 18 degrees each. Each divertor plate cuts poloidally two islands so that the ten plates cover a total toroidal length comparable to the single null divertor in a tokamak of the same size. However, unlike in tokamaks, the complex magnetic island structure introduces a two-dimensional distribution of the power load on each target, which can only be studied by a 3D model, for example the EMC3 code.

Figure 3 shows the power load distribution on a target for the high density case, which does not differ significantly from the low density case because of the inverse dependence of

the cross-B transport coefficients on the density. A large portion (84%) of the heating power is convected to the plates while the rest is radiated by neutrals. Energy flows along island fans to the targets, resulting in poloidally peaked profiles of the power load with a maximum of 1.7 MW/m^2 at the position of the largest connection length. Toroidally at the plate centre two tiles are introduced for diagnostic purposes, which are retracted in order to avoid direct exposure to the plasma. This explains why the power load distribution in ϕ direction is strongly inhomogeneous. The plates are optimized to allow operations of W7-AS with different magnetic configurations covering a wide ι range. In practice, for a given configuration, the power load distribution can be smoothed by twisting the plates poloidally. This, however, would restrict the operating configuration range.

In order to reach a steady-state operation at the presence of NBI heating the injected particles must be pumped out in the divertor. Neutrals are compressed in divertor chambers in which titanium gettered plates are mounted for absorbing the incoming neutrals. Figure 4 shows the distributions of the ionization rate, atom and molecule densities for the high recycling case. Ions flowing onto the targets are partly reflected as atoms and the rest is absorbed and emitted as cold molecules. The neutrals can directly enter the divertor chamber or indirectly through charge exchange with ions inside the islands. Reflection between the walls in the divertor chamber leads to reduction of the atom fluxes in favor of cold molecules, resulting in much higher densities for molecules than for atoms.

For a given absorbing area of the titanium plates (about 1.8 m^2 in total), the pumping speed is determined by the sticking probability and the influx of the neutrals into the divertor chamber. The dependence of the pumping speed on the divertor gap is shown in Fig. 5(a), in which the sticking probability for hydrogen atoms, due to lack of a reliable knowledge, is varied from 2 to 10% while for molecules it is fixed to be 2%. For a vary narrow divertor gap (<2 cm), all the neutrals coming into the chamber are absorbed by the titanium plates, showing a roughly linear dependence of the influx on the width of the divertor gap. With increasing gap width, more and more neutrals will escape from the chamber without being absorbed, which moderates the increase of the pumping speed and may even lead to decrease in pumping speed if the gap becomes too wide. The optimal width is about 5 cm, slightly depending on the sticking probability. In this case, the pumping speed reaches a value of $4 \times 10^{20}/s$ if the same sticking probability of 2% is assumed for both atoms and molecules. This allows a NBI heating power of 2 MW for the neutral particle injectors on W7-AS. Higher heating power (3.5 MW available) will increase the plasma edge density.

If the sticking probabilities for atoms and molecules are comparably small, more molecules are pumped out than atoms, as shown in Fig. 5(b). The pumping speed for atoms will exceed that for molecules if the atoms have a sticking probability higher than 7%.

4. Conclusions

The physical model in the EMC3 code has been greatly improved. The anomalous cross-B momentum transport terms are introduced which are found to give dominant contributions to the momentum balance due to the small pitch angles of the magnetic field lines in the islands. Separation of the electron and ion energy transports and introduction of the corresponding convective energy fluxes considerably extend the application range. All the fluid equations obey a same conservation principle, and are therefore treated with the same Monte Carlo algorithm. Parallelization of the EMC3 code leads to a roughly linear speed-up of the computations.

Simulations show that the anomalous cross-B transports play an important role in the mass, momentum and ion energy balance. Increasing the plasma edge density shifts the ionization zone outwards, leading to a density rise in front of the targets. Toroidally away from the recycling zones, the anomalous diffusion smooths the density distribution, resulting in a rather broad density profile in the edge. Calculations show inhomogeneous distributions of the power load on the targets. In the absence of impurities, 84% of the 0.4 MW heating power entering the island SOL is convected to the divertor plates, with a maximal energy flux of 1.7 MW/m^2 localized at the position of the largest connection length. Neutrals are well confined in the divertor chamber with a 5 cm divertor gap being the optimal choice for pumping out the neutrals. For an average edge density of 4×10^{19} m^{-3}, a pumping speed of 4×10^{20} /s is achieved, which allows a steady-state operation with NBI heating up to 2 MW. Higher heating power will increase the plasma edge density.

5. References

[1] Y. Feng et al., J. Nucl. Mater. 241-243 (1997) 930-934.

[2] S. I. Braginskii, Reviews of Plasma Physics, Vol.1, ed. by M.A. Leontovich, Consultants Bureau, New York (1965) p.205.

[3] F. Sardei et al., J. Nucl. Mater. 241-243 (1997) 135-148.

[4] P. Grigull et al., J. Nucl. Mater. 241-243 (1997) 935-940.

[5] D. Reiter, Jülich Report 1947, Jülich (1984).

[6] N.G. Van Kampen, Stochastic Processes in Physics and Chemistry (North-Holland, Amsterdam, 1981).

Captions

Fig.1. 3D grid distributions for a 5/9 island divertor configuration.

Fig.2. 2D distributions of the electron and ion temperatures and the density at the cross section of a lower divertor target for the particles fluxes of (a) 6.25×10^{21} and (b) 2.5×10^{22} /s.

Fig.3. Power load distribution on a target for the high density case where R and ϕ indicate the radial and toroidal directions.

Fig.4. 2D distributions of the ionization rate and atom and molecule density at the cross section of a lower divertor chamber for the high density case.

Fig.5. Dependence of the pumping speed on the divertor gap width (a) and the ratio of the pumped atoms and molecules as a function of the atom sticking probability (b).

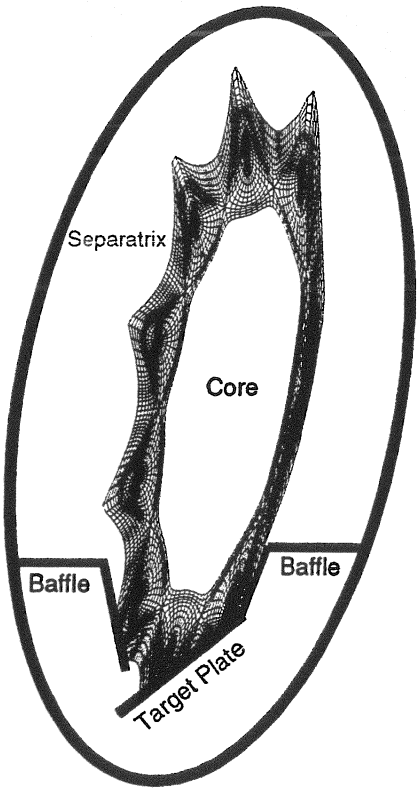
Separatrix
Core
Baffle
Baffle
Target Plate

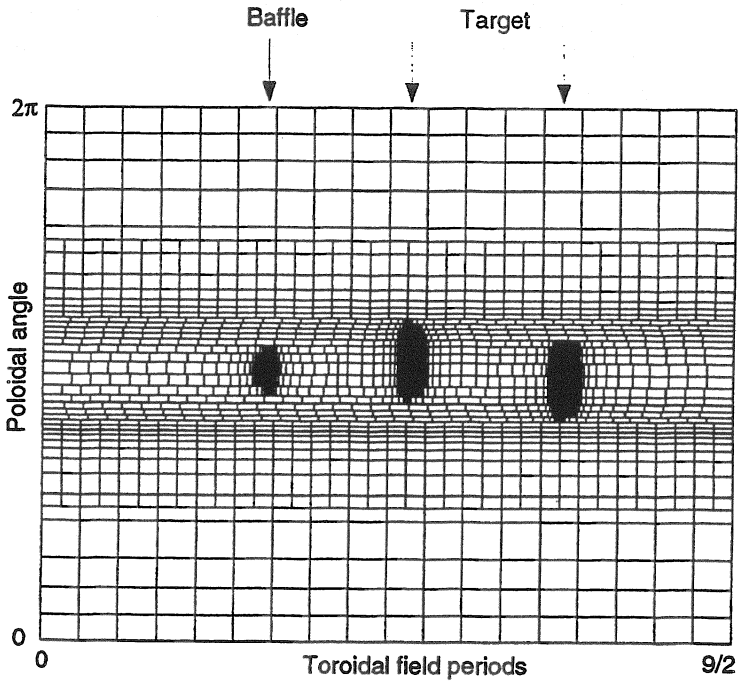
Baffle
Target
2π
0
Poloidal angle
0
Toroidal field periods
9/2

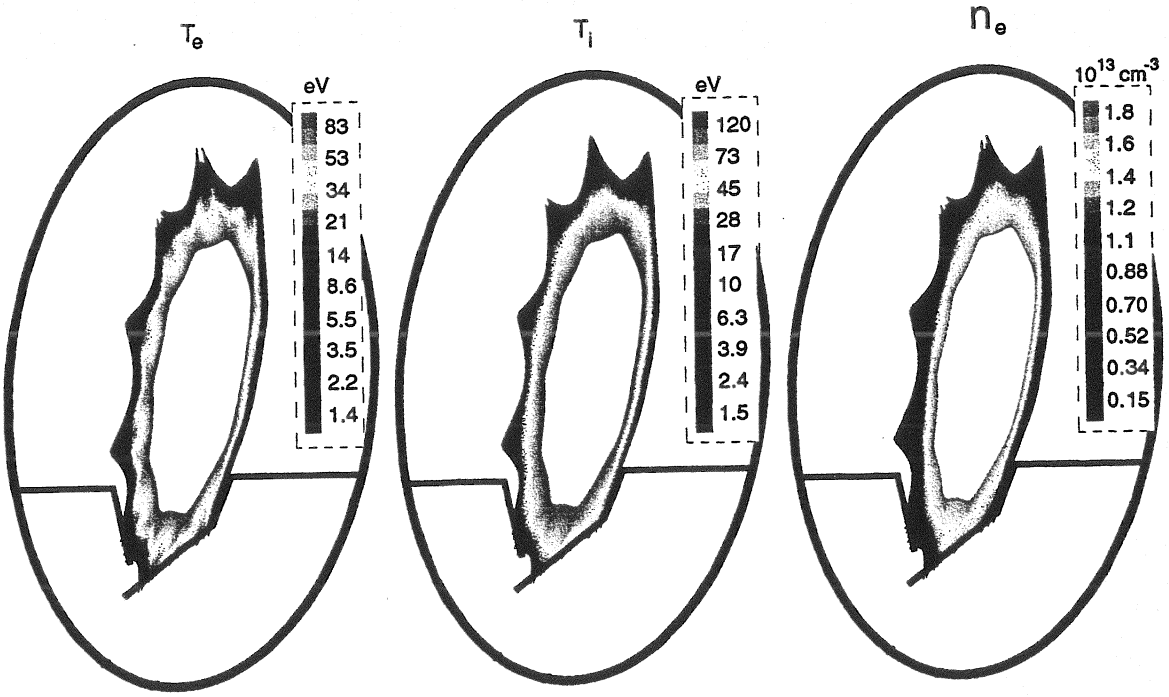
T_e
eV
83
53
34
21
14
8.6
5.5
3.5
2.2
1.4
T_i
eV
120
73
45
28
17
10
6.3
3.9
2.4
1.5
n_e
10^{13} cm^{-3}
1.8
1.6
1.4
1.2
1.1
0.88
0.70
0.52
0.34
0.15

(a)

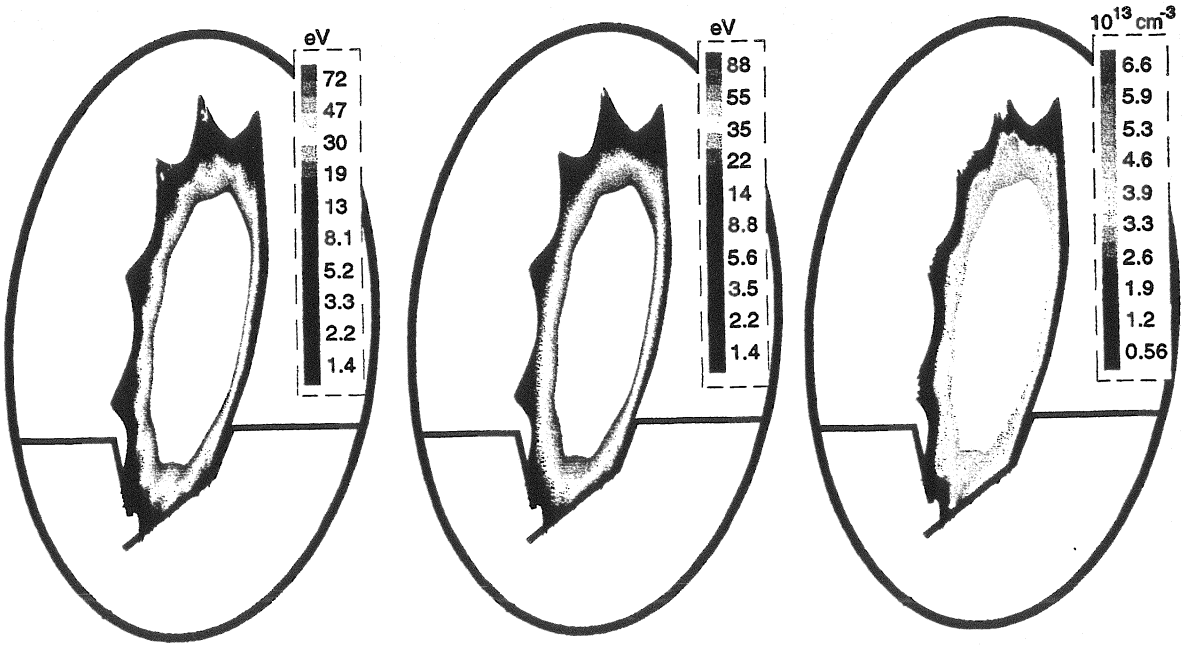
eV
72
47
30
19
13
8.1
5.2
3.3
2.2
1.4
eV
88
55
35
22
14
8.8
5.6
3.5
2.2
1.4
10^{13} cm^{-3}
6.6
5.9
5.3
4.6
3.9
3.3
2.6
1.9
1.2
0.56

(b)

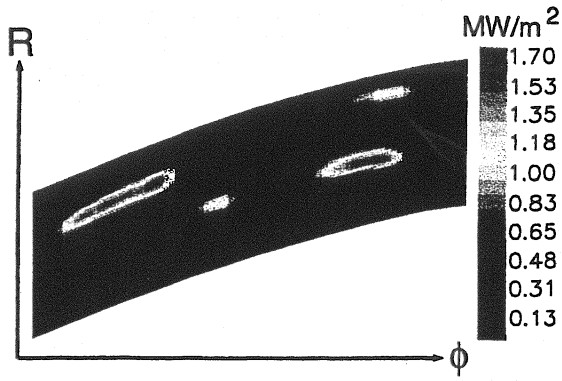
R
MW/m 2
1.70
1.53
1.35
1.18
1.00
0.83
0.65
0.48
0.31
0.13
ϕ

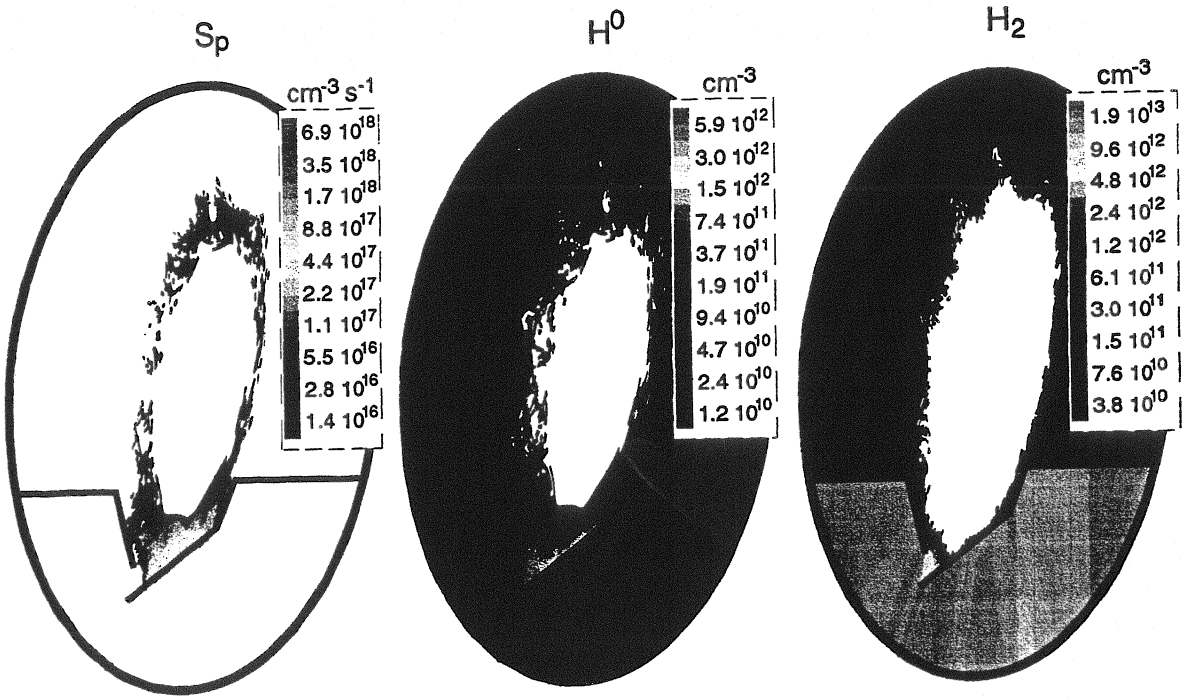
Sp
cm-3 s-1
6.9 10^18
3.5 10^18
1.7 10^18
8.8 10^17
4.4 10^17
2.2 10^17
1.1 10^17
5.5 10^16
2.8 10^16
1.4 10^16
H0
cm-3
5.9 10^12
3.0 10^12
1.5 10^12
7.4 10^11
3.7 10^11
1.9 10^11
9.4 10^10
4.7 10^10
2.4 10^10
1.2 10^10
H2
cm-3
1.9 10^13
9.6 10^12
4.8 10^12
2.4 10^12
1.2 10^12
6.1 10^11
3.0 10^11
1.5 10^11
7.6 10^10
3.8 10^10

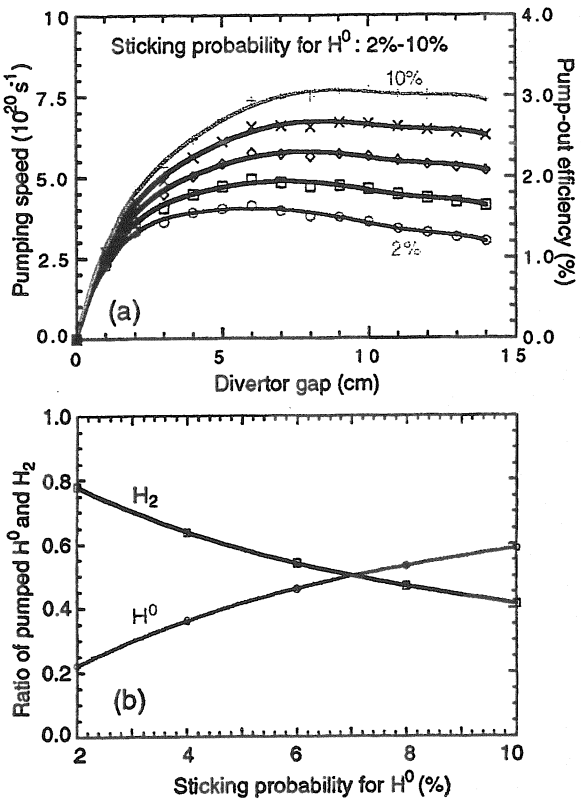
Sticking probability for H0 : 2%-10%
10%
2%
(a)
Pumping speed (10^20 s^-1)
Pump-out efficiency (%)
Divertor gap (cm)
H2
H0
(b)
Ratio of pumped H0 and H2
Sticking probability for H0 (%)

Edge Plasma Diagnostics on W7-AS and ASDEX Upgrade using fast Li Beams

S. Fiedler [a], R. Brandenburg [b], J. Baldzuhn [a], K. McCormick [a], F. Aumayr [b], J. Schweinzer [a], HP. Winter [b], W7-AS and ASDEX Upgrade team

[a] Max-Planck-Institut für Plasmaphysik, EURATOM Ass., D-85748 Garching, GERMANY

[b] Institut für Allgemeine Physik, TU-Wien, Ass. EURATOM-OEAW, A-1040 Wien, AUSTRIA

Abstract

Knowledge of the impurity concentration and temperature in the core plasma gradient region as well as the SOL is a vital element on the road to documenting and understanding the physics of L- and H-mode transport and the transport barrier itself. To this end, the Li-beam diagnostic capabilities on W7-AS and ASDEX Upgrade have been expanded to include the measurement of radial profiles of impurity ion density and temperature via charge-exchange-spectroscopy (Li-CXS).

After presenting the method of Li-CXS this paper describes the experimental setup on W7-AS as well as ASDEX Upgrade and presents first results on both experiments. Measurements of C^{6+} and Ne^{10+} spectral lines prove the viability of Li-CXS. In the plasma edge region of W7-AS ($r_{eff} > 8$ cm) a C^{6+} concentration of about 0.5% could be measured. Temperature values found for C^{6+} are similar to proton/deuteron temperatures.

The intensities of several LiI spectral lines (2p→2s, 3d→2p, 4s→2p, 4d→2p) have been measured and are used to critically check the underlying cross section database employed within the collisional-excitation Li-beam model, especially for collision processes involving higher Li-states ($n \geq 3$). It was found that the ratio of the spectral lines corresponding to 3d→2p and 2p→2s transitions is overestimated by the model. These deviations could be eliminated by using improved cross sections in the database.

1. Introduction

Li-beam diagnostics are a multi-purpose technique for investigating fusion edge plasmas. While the determination of electron densities by lithium impact excitation spectroscopy (Li-IXS) has already reached a satisfactory standard on both large fusion experiments at IPP Garching [1,2], neutral Li-beams can also be used to determine local concentrations as well as temperatures of impurity ions via charge exchange spectroscopy (Li-CXS) [3,4]. This method has been proposed by Winter [5] and was applied for the first time at the TEXTOR tokamak at KFA Jülich [6,7]. In order to achieve simultaneous Li-IXS and Li-CXS measurements, the setup for electron density measurements has been extended. First results prove the feasibility of Li-CXS with the improved Li-injector [1] in W7-AS plasmas.

2. Principles

From observation of the resonant line radiation profile of the injected Li-beam it is possible to deduce the electron density profile as well as the local Li(nl) state distribution along the injected Li-beam by modeling the Li-beam-plasma interaction. In addition to the impact excitation process the weakly bound outer electron of the Li-atom can also be captured by impurity ions. This charge - exchange process populates highly excited states of the impurity ions, giving subsequently rise to characteristic impurity line radiation. Observation of this line emission in conjunction with the calculated Li(nl) state distribution allows for evaluation of the impurity density profile along the injected Li-beam. In addition, the temperature profile of the impurity ions is determined from the spectral line shape.

3. Experimental setup on W7-AS

The existing Li-beam diagnostic layout [1] has been supplemented by a 14 channel observation system with a radial resolution of $\delta r \sim 6$ mm for a range of ~13 cm along the beam, corresponding to an effective plasma radius from 3 to 17 cm, cf. Fig. 1. Two glass lenses ($\Omega/4\pi \sim 2.9 \times 10^{-4}$ sr) image the light onto 14 bundles, each consisting of a 2x4 array of 400 μm quartz fibers. The bundles are coupled one by one to the entrance slit of a monochromator (ACTON, Czerny-Turner, f = 0.75 m) to permit spectral resolution for Li-CXS and LiI radiation. A two-dimensional detector (Proscan CCD camera, 512x512 pixels, each 19x19 μm^2) is directly connected to the monochromator exit. The spectral resolution can reach up to 0.018 nm/pixel, using a 1800 g/mm grating. An additional system of R928 or R3896 Hamamatsu photomultipliers in conjunction with interference filters (λ = 529.0 nm for C^{6+}, FWHM ~ 0.5 nm) can be coupled to the same light guides for simultaneous measurements at the 14 radial locations.

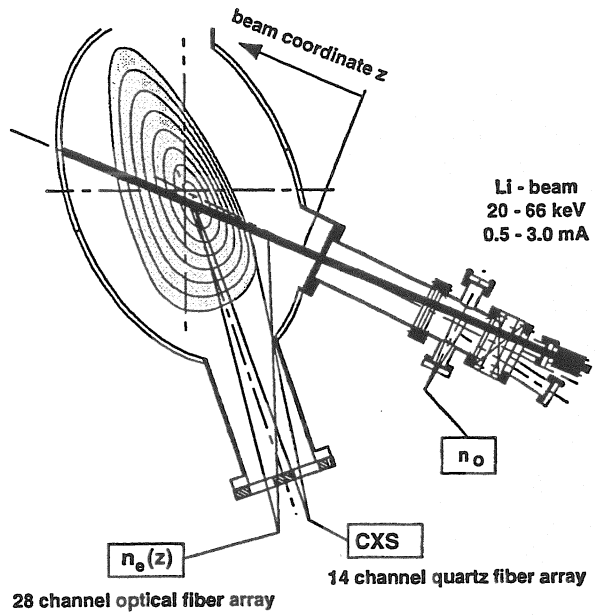

Fig. 1: Experimental set-up on the W7-AS stellarator. The observation geometry for Li-IXS (28 channels), Li-CXS (14 channels) and neutral density N_o is indicated.

The extraction geometry of the Li-beam injector was changed to increase the Li-beam current delivered by the gun [1]. These experiments were carried out at 50 keV injection energy with an equivalent neutral Li-beam current of 1.9 mA and a Li-beam diameter of $D_{FWHM} \leq 1$ cm.

4. Experimental setup on ASDEX Upgrade

On the ASDEX Upgrade tokamak the Lithium beam diagnostics has a new location 33 cm above midplane. It is equipped with a completely rebuilt 35 channel optics to measure electron density profiles, a 16 channel charge exchange optics and a 3 channel neutral density monitoring system (Fig. 2). At the new position of the ion gun, which is similar to the one on W7-AS, the magnetic field is weaker. There is also additional μ-metal shielding around the ion beam. Thus, we expect magnetic field effects on the lithium beam (E = 35 keV, I = 1.2 mA) to be reduced considerably.

4.1 Electron density measurement setup

In the former optical system each spatial channel consisted of three 400 μm fibers. The light collection/transmission efficiency varied drastically from fiber to fiber and the system was sensitive to the beam position [8]. To overcome these difficulties, a new head for the fiberguides was built with each spatial channel corresponding to a bundle of 35 quartz fibers (100/130 μm). The light from each bundle is coupled to a 48 m long, 600 μm monofiber (numerical aperture = 0.37) that carries the light to the detection units. About seven percent of the incoming light can be collected in this way. A new BK7 optical system -a wedge and two lenses- was built to gather light into 35 channels from about 16 cm along the beam path. The observation region can be radially shifted by a couple of centimeters, allowing it to be adjusted to different plasma scenarios. Each detection unit is equipped with an interference filter (T > 40%, FWHM ≤ 0.7 nm) followed by a photomultiplier.

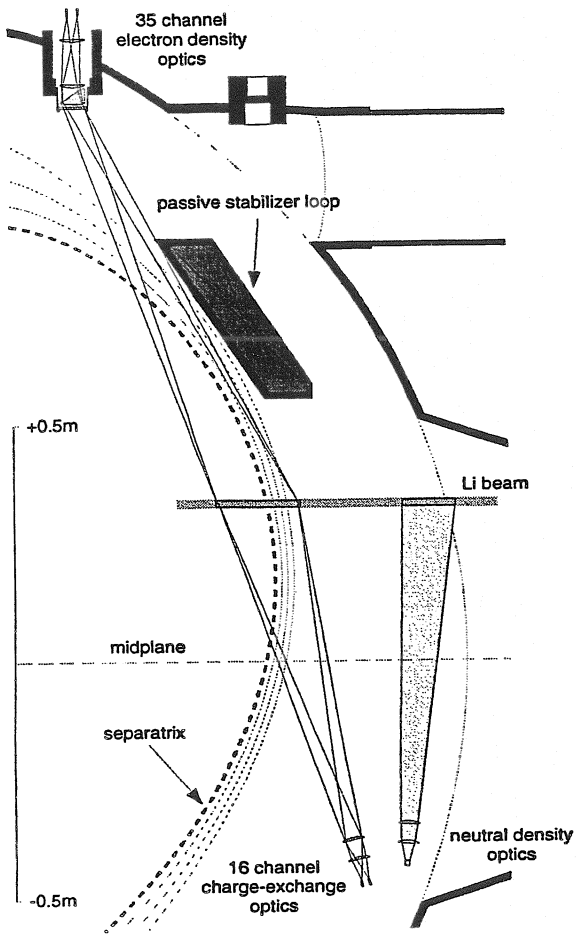

Fig. 2: Optical observation systems of extended lithium beam diagnostics on ASDEX Upgrade.

4.2 CXS measurement setup

Two quartz lenses ($\Omega/4\pi \sim 1.5\times10^{-3}$ sr) focus the light onto an array of 16 quartz fibers (400 μm) enabling the radial distribution of the emitted light in a 16 cm region around the separatrix to be measured with 1 cm spatial resolution. The fibers are coupled to the entrance slit of the same CXS spectroscopic system as described for W7-AS. Temporal resolution is limited by the

readout time of the CCD detector for 16 channels (13 ms).

4.3 Neutral density measurement setup

Two BK7 lenses ($\Omega/4\pi \sim 1.8\times10^{-3}$ sr) focus the light onto an array of 21 quartz fibers (400 μm) that are grouped into three bundles. The light is gathered from a region far from the separatrix where lithium excitation by collision with neutrals is the dominant process [2]. Each channel is equipped with an interference filter ($T > 40\%$, FWHM ≤ 0.7 nm) to select the Li(2p→2s) line.

5. Lithium beam composition

Since the cross sections for charge exchange processes from the Li donor atom into excited states of various plasma impurities depend strongly on the originating Li(nl) states, the composition of the Li-beam is of great importance for evaluating CXS data. We have therefore investigated several LiI spectral lines (2p→2s, 3d→2p, 4s→2p, 4d→2p) in W7-AS and ASDEX Upgrade discharges.

While the measurements of the most relevant line Li(2p→2s) at $\lambda = 670.8$ nm were performed to calibrate the CXS setup relative to the Li-IXS photomultiplier setup (see below), all other LiI lines were investigated to check the attenuation model of the Li-beam [9]. In a first approach on W7-AS, measured intensities of emission from higher levels were found to differ considerably (30-60%) from corresponding theoretical values. We observed no dependence on magnetic field strength and beam energy (20-66 keV). The plasma density had a strong influence on the conformity of experimental and theoretical values, with the deviation becoming larger at higher densities.

As the major reason for these disagreements, inadequate scaling relations for excitation and ionisation processes involving electrons and protons in the underlying database [10] were identified. These have now been measured and recalculated by more advanced means and have been found to be considerably lower than the (scaled) cross sections used so far (cf. Fig. 3).

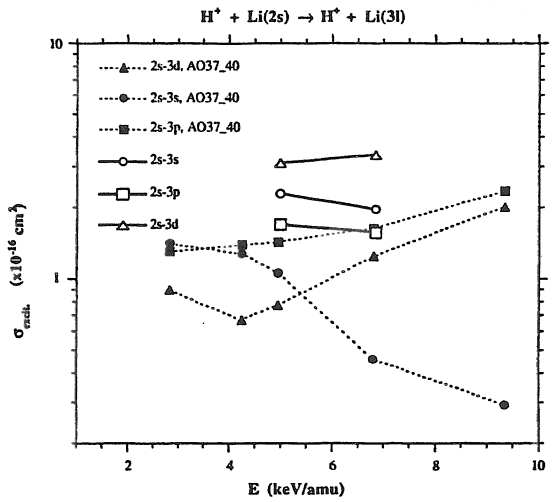

Fig. 3: Comparison of proton impact excitation cross sections from the current database [10] with recent atomic orbital - close coupling calculations (AO37_40). Calculated values are significantly lower than scaled values from the database.

When comparing experimental values of relative Li(nl) population numbers with results from the improved beam modelling, an excellent agreement can be stated (Fig. 4).

However, since the relative population of the Li(3d) state in the Li-beam is in the range of 1%, and populations of all other Li(nl) levels ($n > 2$) are even smaller, the influences of these new cross sections on electron density

calculations remain below 10% (cf. Fig. 5).

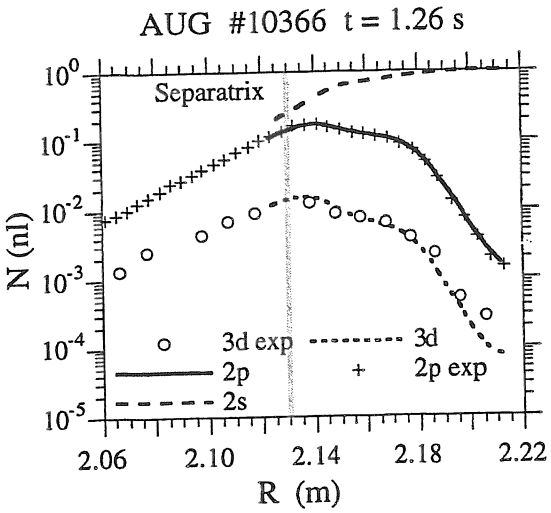

Fig. 4: Radial profiles of relative Li(nl) populations when the Li beam penetrates the plasma edge. Experimental results prove the reliability of the beam modelling when utilising the new cross sections.

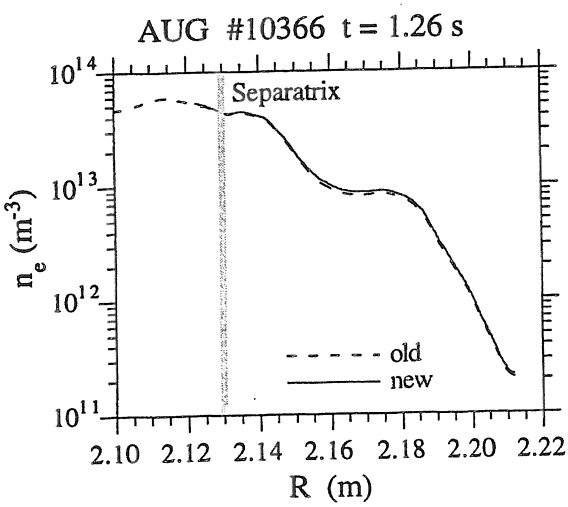

Fig. 5: Comparision of reconstructed electron density profile using 'new' and 'old' cross sections. The influences on the electron density calculations remain below 10%.

6. CXS investigations on W7-AS

6.1 Impurity density profiles

To determine the absolute concentration of C^{6+} impurity ions, both Li-beam diagnostic systems are necessary (IXS and CXS). While the IXS system (28 PM) records the Li(2p) light emission, the CXS system (CCD-camera) delivers the CVI line radiation at 529.0 nm. Since both systems use different observation optics, the detection efficiency has to be cross-calibrated. This is done by measuring the Li(2p) light with both systems, the IXS-PM- ($U_{2p}^{PM}(i)$) and the CXS-CCD-system ($U_{2p}^{CCD}(i)$), respectively in one calibration discharge.

$$U_{2p}^{PM}(i) = k_{671}^{PM}(i) \cdot n_{Li} \cdot A_{2p\to 2s} \cdot N(2p)$$
$$U_{2p}^{CCD}(i) = k_{671}^{CCD}(i) \cdot n_{Li} \cdot A_{2p\to 2s} \cdot N(2p) \qquad (1a/b)$$

k denotes the detection efficiency for the two systems at $\lambda = 671.0$ nm, i the corresponding radial channel, $A_{2p\to 2s}$ the transition probability, n_{Li} the particle density of the Li-beam and N(2p) the relative occupation number of the 2p-state. The CXS-signal ($U_{529}^{CCD}(i)$) can be expressed by

$$U_{529}^{CCD}(i) = k_{529}^{CCD}(i) \cdot v_{Li} \cdot n_{C^{6+}} \cdot n_{Li} \cdot \sum_{nl} \sigma_{529}(nl) \cdot N(nl) \qquad (2)$$

Calculating the ratio of equations (1b) and (2) for the discharges in question and using the ratio of equations (1a) and (1b) for the calibration discharge, the C^{6+} density can be expressed by

$$n_{C^{6+}}(z_{Li}(i)) = \frac{U_{529}^{CCD}(i)}{U_{2p}^{PM}(i)} \cdot \frac{k_{671}^{PM}(i)}{k_{671}^{CCD}(i)} \cdot \frac{k_{671}^{CCD}(i)}{k_{529}^{CCD}(i)} \cdot \frac{A_{2p\to 2s} \cdot N(2p)}{v_{Li} \cdot \sum_{nl} \sigma_{529}(nl) \cdot N(nl)} \qquad (3)$$

In equation (3) the first ratio describes the measured signals ratio (IXS and CXS systems), the second ratio is determined by the calibration procedure (see above) and the third ratio expresses the different detection

probabilities of the CCD camera at the two wavelengths. v_{Li} denotes the Li-beam particle velocity and $\sigma_{529}(nl)$ the cross section for electron capture from the Li(nl)-level, giving rise to line radiation at $\lambda = 529.0$ nm. The relative occupation numbers N(nl) of the Li-beam atoms are calculated in the reconstruction process for the electron density (Li-IXS, [9]). The described algorithm was applied in a series of equivalent discharges ($P_{ECRH} = 400$ kW, D_2, $\iota = 0.34$, $B_z = 20.0$ mT, up/down limiters attached, $\int n_e dl(HCN) = 2x10^{19}$ m^{-2}) to determine the C^{6+} impurity ion density for different radial positions [different z_{Li} in equation (3)]. The result is shown in Fig. 6. The C^{6+} impurity ion concentration increases from about 0.41% at $r_{eff} = 16.7$ cm to 0.63% at $r_{eff} = 8.3$ cm. In the gradient region of the profile good agreement is found with the result from the H-CXS diagnostics [11].

For a single light guide in the radial range of the maximum of the Li(2p) profile we also investigated the signal-to-background ratio for other impurity ions. While the ratio was about 0.25 for C^{6+} we found a ratio of 0.2 for C^{5+} and B^{5+} respectively, clearly demonstrating the applicability of Li-CXS also for these impurity ions. The exposure time of the CCD camera was about 5.7 ms with a readout time of 3 ms. Each 10 ms a CCD-picture was recorded. The Li-beam was chopped electronically with a beam on - and off time of 40 ms each. Thus 4 CCD-pictures could be used to determine Li-CXS and background signals. For the determination of impurity densities the Li-CXS signals were summed over the Li-beam on-time interval (40 ms). No impurity ion concentrations giving rise to CXS-line radiation in the UV-spectral range could be investigated, due to insufficient transmission of the observation optics (glass).

6.2 Simulation of the charge state distribution

The IONEQ code [12] was used to simulate the radial carbon charge state distribution for W7-AS plasmas. Within this simulation the charge state distribution is calculated according to the Corona equilibrium. In addition the impurity transport fluxes are modelled by assuming resonable values for a diffusion coefficient and a convection velocity. As input data the electron density profile from the Li beam and the temperature profile from the Thomson diagnostics was used. The neutral gas density was modelled by the EIRENE code and calibrated with the H_α and the neutral density measurement of the Li beam diagnostics [13].

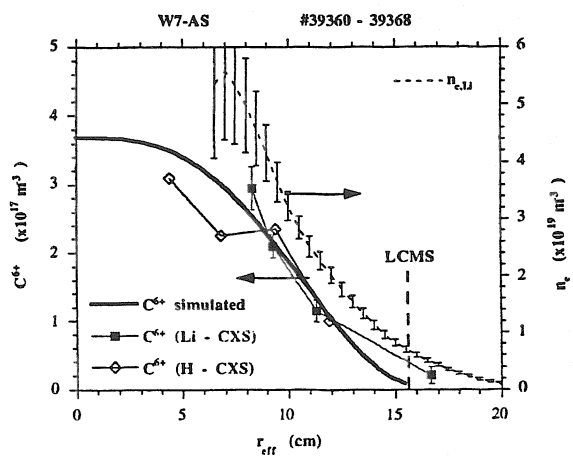

Fig. 6: Radial impurity density profile of C^{6+} and electron density profiles as a function of effective radius r_{eff} for discharges #39360 -39368. Thick line shows the result of a simulation with the IONEQ code. The last closed magnetic surface (LCMS) is indicated by a dotted line.

A good agreement was achieved with a diffusion coefficient of $D = 0.2\frac{m^2}{s}$

To account for the relatively high displacement of electron and C^{6+} density profiles a strong inward velocity of

$$v_{LCFS} = -4 \times \frac{D}{r_{LCFS}}\left[\frac{m}{s}\right]$$

with a radial dependency of

$$v(r) = v_{LCFS} \times \left(\frac{r_{eff}}{r_{LCFS}}\right)^2$$

had to be assumed and cannot be explained by uncertainties in the mapping process of local to magnetic coordinates, as the electron and impurity density profiles are measured at the same toroidal position. Only the electron temperature profile is subject to errors in the radial position of about 0.5 cm. By shifting the T_e profile 1 cm inwards and by the variation of the neutral density profile as well as the diffusion coefficient the influence of these parameters on the radial position of the simulated C^{6+} profile was found to be below a few millimetres (Fig. 6).

6.3 Impurity temperature profiles

Temperature values are obtained by fitting a Gaussian profile to the CCD-camera data. To reduce the scatter of the calculated spectral line widths, all CCD-pictures taken in the flat top phase of one discharge had to be summed up. This typically implies an integration time of about 300-400 ms. The time resolution will be improved by a better coupling of the light guide bundles to the spectrometer entrance slit, where now an important fraction of the light signal is being lost.

For the fitting procedure line broadening effects such as Zeeman splitting and l-level mixing are taken into account [7]. C^{6+} temperature values in the plasma edge obtained in the same series of discharges (see above) are shown in Fig. 7. For $r_{eff} < 12$ cm C^{6+} temperature values are similar to proton/deuteron temperatures measured via active neutral particle analysis [14].

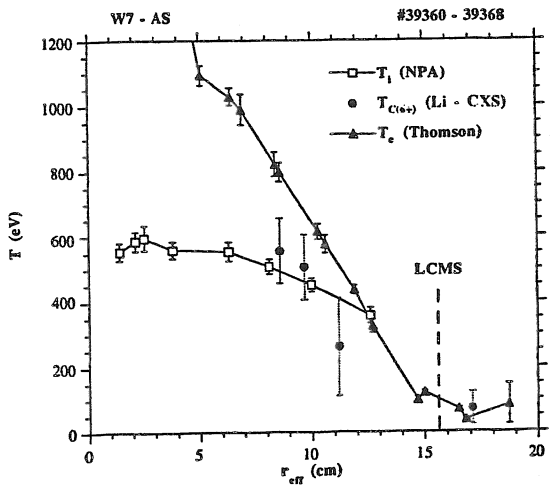

Fig. 7: Radial impurity temperature profiles of C^{6+}, electron temperature T_e and deuterium temperature T_{D+} measured by neutral particle analysis (NPA) [14].

7. CXS investigations on ASDEX Upgrade

Impurity density profiles

On ASDEX Upgrade we use the spectrometer and CCD camera for investigation of impurity ion spectral lines in the range from $250 < \lambda < 800$ nm. The complex temporal behaviour of the ASDEX Upgrade discharges poses severe difficulties for the Li-CXS method with the current setup. First results indicate the feasibility of Li-CXS for several impurities (Ne^{6+}, Ne^{10+}, O^+, He^+, B^{2+}). As an example Fig. 8 shows the profiles of electron and Ne^{10+} densities as a function of major radius R in a discharge (#10492, $\int n_e dl(DCN) = 8 \times 10^{19}\ m^{-2}$, $I_P = 1$ MA,

NI = 5.6MW) with a strong Ne gas puff.

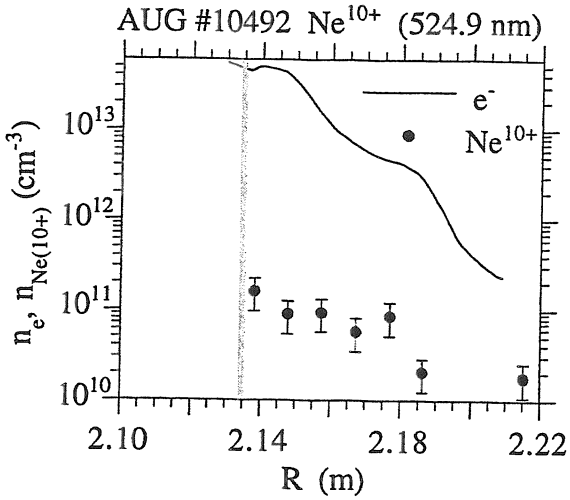

Fig. 8: Profiles of electron and Ne^{10+} densities in discharge #10492 as a function of major radius R. A strong Ne gas puff occured during this discharge. Signals have been averaged in the period $2.5 < t < 3$ s.

8. Conclusions

With the improved Li-injector now available we have demonstrated the applicability of Li-CXS, both for impurity density and impurity temperature measurements, on W7-AS. Concentrations found for C^{6+} ions are in the order of 0.5%. The radial profile in the gradient region coincides with values from the H^{o}-CXS-diagnostics. This profile could only be modelled by assuming a strong inwards velocity. Temperature values in the plasma edge can be considered to be equal to those for deuterium ions. Radial and temporal resolutions of 0.5 cm and 40 ms, respectively (400 ms for temperature measurements) could be achieved. By improving the detection efficiency mainly by using new fibers with smaller aperture and a new construction of the fibers-spectrometer coupling, the temporal resolution can probably be increased by more than a factor of 5. On the ASDEX Upgrade tokamak the applicability of Li-CXS could be demonstrated by measuring the radial profile of Ne^{10+} ions.

Acknowledgments

This work has been supported by Friedrich Schiedel-Stiftung für Energietechnik and by Kommission zur Koordination der Kernfusionsforschung at the Austrian Academy of Sciences.

References

[1] K. McCormick et al., Fusion Engineering and Design **34-35** (1997) 125
[2] S. Fiedler, IPP Report III/209 (1995)
[3] E. Wolfrum et al., Rev. Sci. Instrum. **64** (1993) 2285
[4] F. Aumayr et al., J. Nucl. Materials **196-198** (1992) 928
[5] H. Winter, Comments At. Mol. Phys. **12** (1982) 165
[6] R.P. Schorn et al., Appl. Phys. **B 52** (1991) 71
[7] R.P. Schorn et al., Nucl. Fusion **32** (1992) 351
[8] J. Schweinzer et al., 22th EPS Conf., Europhys. Conf. Abstr. **19C** III (1995) 253
[9] J. Schweinzer et al., Plasma Phys. Contr. Fusion **34** (1992) 1173
[10] D. Wutte et al., At. Nucl. Dat. Tables **65** (1997) 155
[11] J. Baldzuhn et al., Rev. Sci. Instrum. **68** (1997) 1020
[12] A. Weller, D. Pasini, A.W. Edwards, R.D. Gill and R. Granetz, JET-IR(87)10
[13] S. Fiedler et al., 23rd EPS Conf., Europhys. Conf. Abstr. **20C** Part III (1996) 1009
[14] M. Kick et al., 20th EPS Conf., Europhys. Conf. Abstr. **17C** Part I (1993) 357

Radiation measurements and modeling of the density limit on the W7-AS stellarator

L. Giannone, R. Burhenn, P. Grigull, U. Stroth, R. Brakel, R. Dux, A. Elsner, S. Fiedler, G. Kühner, F. Penningsfeld, G. Pereverzev, F. Wagner, A. Weller, C. Wendland, NBI Team and the W7-AS Team.

Max-Planck-Institut für Plasmaphysik,
EURATOM Association, D-85748 Garching, Germany

Abstract

Density limit discharges in the W7-AS stellarator with a strong density ramp were compared to a series of discharges with constant line integrated density approaching the maximum value achieved in the density ramp. The physics of the density limit in stellarators was demonstrated to be consistent with the predictions of the two point model, indicating that this model successfully describes the density limit process in both stellarators and tokamaks. The discharges with a strong density ramp were found to have broader density profiles than those discharges with constant line integrated density. The latter discharges had the electron density profile form found in the improved confinement H-NBI mode on W7-AS. Modeling of the radiation profile, to simultaneously match the measured bolometer and soft x-ray radial profiles of radiated power, implies that impurity density profiles were peaked and continuously increased during the discharge. The increase in radiated power decreased the net deposited power to the plasma and the diamagnetic energy fell. The aim of producing steady state discharges at the highest possible density is aided by the reduction of impurity sources by helium glow discharge cleaning.

1. Introduction

In W7-AS, a discharge with rising line integrated electron density reaches a maximum density, then the diamagnetic energy falls and the radiated power rises continuously until the discharge terminates. This maximum density defines the density limit in W7-AS. Discharges with a constant line integrated density (density plateau) were also studied. In discharges at successively higher density plateaus, the rate of diamagnetic energy decrease after the peak in diamagnetic energy was larger at higher densities. Decreasing net power to the plasma due to core radiation is believed to be responsible for the observed fall in diamagnetic energy.

The density profiles in discharges with a density ramp were markedly broader than those with a density plateau. These density plateau discharges are therefore closely related to the improved confinement scenario in W7-AS (H-NBI mode) but at densities in the vicinity of the density limit [1]. At sufficiently low densities, discharges of duration up to 1.8 s were possible. Such experiments in both tokamaks and stellarators are relevant to the future operation scenario of a reactor, as sustainable steady state high density discharges will be required for power handling and ignition [2].

Measurements of the time evolution of the density and temperature in front of the limiter were compared with predictions of simulations by the time dependent transport code ASTRA

[3] combined with a one dimensional scrape-off layer model of the plasma edge (the two point model) [4]. The addition of the impurity transport code STRAHL [5] allowed radiation profile measurements of the bolometer and soft x-ray cameras to be simulated. The increase in radiated power during density plateau discharges was due to a central peaking of the radiation power density. Such a peaking has been observed previously in the W-VIIA stellarator [6] and accounted for by neoclassical impurity transport of oxygen ions from the vessel walls and tungsten from the NI beams. In W7-AS, 3% shine through losses and 2% charge exchange losses were calculated. Impurity ions, produced by energetic ions impinging on the wall, could therefore have been a relevant factor in the observed discharge evolution.

2. Two point model

Simulations of the time evolution of the electron density and temperature measurements in front of the limiter were carried out with the time dependent transport code ASTRA. This code solves the particle balance, electron energy power balance and ion energy power balance equations as a function of time, allowing time dependent simulations to be carried out. The equations are one dimensional and averaged over closed magnetic flux surfaces. A module was added to ASTRA to describe the physics of the scrape off layer in terms of the two point model. The two point model is a one dimensional model based on electron heat conduction and pressure balance along the field line from the last closed flux surface to a limiter or divertor plate [4] and the predictions of this model have been shown to be consistent with observations in density limit experiments in limiter discharges in a tokamak [7]. A modified pressure balance equation along field lines to account for momentum loss effects due to ion-neutral friction is used [8] :

$$T_{es} = \left(T_{ed}^{7/2} + \frac{7}{4\kappa_o} q_{//s} L_c \right)^{2/7} \left(1 - \left(\frac{T_{ed}}{T_{es}} \right)^{7/2} \right)^{-2/7} \qquad (1)$$

$$2 n_{ed} T_{ed} = f_m n_{es} T_{es} \qquad (2)$$

where n_{es} and T_{es} are the density and temperature at the last closed flux surface, n_{ed} and T_{ed} are the density and temperature in front of the limiter, L_c is the connection length from the last closed flux surface to the limiter (typically 30 m - 100 m depending on the poloidal angle), κ_o is the factor in the electron thermal conductivity equation, f_m is the reduction factor in pressure along the field line and Δ_T is the temperature fall off length in the scrape off layer . The parallel heat flux to the limiter, $q_{//s}$, given by the perpendicular heat flux at the last closed flux surface, $q_\perp$, multiplied by the geometrical factor, L_c / Δ_E. The heat flux across a flux tube of length L_c is projected onto the limiter within an energy fall length $\Delta_E = 2/7\ \Delta_T$. This parallel

flux to the limiter is balanced by the sum of losses by ionization of neutrals, by impurity radiation and in the sheath in front of the limiter or divertor plate:

$$q_{//s} = 7L_c q_\perp / 2\Delta_T = n_D c_S \beta\xi + c_{rad} l \gamma_{imp} n_D^2 + \gamma n_D T_D c_S \qquad (3)$$

These equations can be solved for n_{ed}, T_{ed} and T_{es}, using n_{es} and $q_\perp$ as inputs.

3. Density ramps

The lithium beam diagnostic measures the time evolution of the radial profile of n_e, therefore providing the input value of n_{es}. The total radiated power is deduced from Abel inverted measurements of the line integrated power flux onto 4 μm gold foil absorbers of a 12 channel bolometer array and then $q_\perp$ is calculated from the deposited NBI power minus the total radiated power. The soft x-ray measurements are carried out with 2 cameras, each of 36 channels, of surface barrier diodes. The placement of a 12.5 μm beryllium foil in front of the entrance slit allows the filtering out of energy components below 1 keV.

A discharge at B = 2.5 T with 380 kW of neutral beam injection (NBI) heating and a density ramp that increased the central density from 5.5×10^{19} m^{-3} to 1.5×10^{20} m^{-3} in the time interval from 0.2 s to 0.6 s is shown in Fig. 1. The magnetic configuration, with an edge value of rotational transform, $\iota(a)$, of 0.34 is bounded by two tangential graphite limiters at the top and bottom of an elliptical cross section of magnetic flux surfaces. A comparison of the Langmuir probe measurements of n_{ed} and T_{ed} and the predictions of the modified two point model are also shown. The evolution of n_{ed} and T_{ed} are reasonably simulated with a continuously falling temperature and a density reaching a maximum at 0.5 s and a continuously falling temperature. In agreement with the usual description of the density limit in tokamaks, a critical edge density is reached at which the value of net power flux can no longer sustain power balance in front of the limiter and detachment from the limiter follows [9]. The physics of the density limit in stellarators can therefore be adequately described by the two point model indicating that this model describes the density limit process in both stellarators and tokamaks. After 0.56 s the radiated power is greater than the deposited power and the discharge rapidly collapses. However, no tearing mode instability is triggered in a stellarator in contrast to observations of a the density limit on a tokamak [10]. The difference in maximum value of density in front of the limiter predicted and observed, may be partially explained by the overestimation of the measured electron temperature suggested to occur in the presence of non-thermal electrons from the upstream plasma [9]. From the Langmuir probe measurements of ion saturation current, the calculated density is then underestimated.

Discharges with a Murakami parameter greater than the Greenwald limit were achieved transiently in W7-AS in this set of discharges. Similarly plasma parameters yielding values

above the Greenwald limit in tokamak density limit discharges have also been achieved transiently using pellet injection [11] or for a duration of 0.8 s with only a slow increase of radiated power [12]. Such global comparisons will be extended in the near future by measurements at the density limit of local electron density and temperature inside the last closed flux surface to compare to the edge operational diagram for tokamaks [13]. A sequence of energy detachment, an edge thermal instability, particle detachment and disruption at the density limit is observed below a critical edge temperature and above a critical edge density [14].

4. Density plateaus

Discharges at B = 2.5 T with 380 kW of NBI heating at successively higher line averaged densities starting from 5.5×10^{19} m^{-2} to 8.0×10^{19} m^{-2} or peak densities of 1.1 to 1.6×10^{20} m^{-3} showed that for each density plateau a peak in the diamagnetic energy was reached and that the level of radiated power rose during the discharge. Again the magnetic configuration was bounded by the two tangential limiters at the top and bottom of an elliptical cross section for discharges with $\iota(a)$ of 0.34. The limiter radius was at r = 16.2 cm. The diamagnetic energy decreased faster in those discharges at higher density. In Fig. 2, density plateau discharges before and after helium glow discharge cleaning at a density of 1.3×10^{20} m^{-3} display the extent to which wall conditioning can influence the time evolution. At a lower density the discharge takes longer to collapse because the radiated power does not increase to the same level so quickly. A simple explanation is that the impurity particle flux is drastically reduced. The particle flux to the limiter, as measured by the ion saturation current to a Langmuir probe embedded there, did not change after helium glow discharge cleaning. This indicates that the source of impurity ions at the surface have been modified by the discharge cleaning.

In addition to possible changes in the impurity flux, density and temperature profile changes or a change in particle or heat transport coefficients are also factors determining the evolution of the radiation profiles. At present, only the time evolution of the central electron temperature from Thomson scattering was available and the temperature profile from a single time point was scaled appropriately. Under these experimental limitations a detailed analysis is not possible. This analysis can be performed when the profiles of density and temperature from Thomson scattering every 50 ms are available in the near future. It will be then also possible to calculate the change in impurity flux at the boundary needed to adequately simulate the discharge prior to discharge cleaning.

The density profile evolution was measured by the lithium beam diagnostic. Even though the level of gas puffing is reduced after 0.5 s, the central density slowly increased and the density at r = 10 cm remained approximately constant, indciating a peaking of the density

profile during the discharge. The increasing central electron density and consequent plasma cooling is one factor involved in the observed deterioration in diamagnetic energy during the discharge.

5. Radiation profiles

The radial profiles of the diffusion coefficient, D, and inward pinch velocity, v, shown in Fig. 3 were calculated from measurements of the time evolution soft x-ray emission and Al impurity lines after aluminum impurity injection by laser blow-off [15]. The Al impurity lines were measured by a Jobin-Yvon spectrometer (Al XI) and a Bragg spectrometer (Al XII). The soft x-ray emission with and without impurity injection are subtracted to yield the net emission due to impurity injection. The electron density profiles of this discharge were within 10% of the density plateau discharge after helium glow discharge cleaning shown in Fig. 2. It should be noted that the following simulation of this density plateau discharge assumes that the measured diffusion coefficient and inward pinch velocity do not change significantly with density or density profile during the discharge.

Spectroscopic measurements of line radiation by the SPRED VUV spectrometer showed that the impurity elements carbon, chlorine and copper were dominant in the density limit discharges studied. Using the radial profiles of D and v derived from laser blow off experiments, together with the time evolution of the density and temperature profiles and an assumed constant impurity flux of each impurity at the boundary, simulations of the time evolution of bolometer and soft x-ray radiation profiles were carried out with the impurity transport code, STRAHL. This code calculates the impurity ion balance of a single impurity species according to the input parameters described and uses tabulated atomic rate coefficient data for ionization, radiative recombination, dielectronic recombination and charge exchange recombination to calculate the radiated power as a function of minor radius in the plasma. In Fig. 4, the measured and simulated radiation profiles for the bolometer and soft x-ray (12.5 μm beryllium foil filter) cameras for the density plateau discharge considered in Fig. 2 are compared. These simplified assumptions are sufficient to satisfactorily simulate the peaking of the measured bolometer and soft x-ray profiles. Maximum central relative impurity densities at the end of the discharge for carbon, chlorine and copper of 0.057, 0.004 and 0.0005 respectively, and therefore a Z_{eff} of 3.6, were estimated. The contribution to the radiated power density for the bolometer measurements in the center is in roughly equal proportions for each impurity element, while for the soft x-ray measurements they were 16%, 50% and 34% respectively. Because of the similar peaked power profiles from both chlorine and copper, a unique fit for the relative contributions of these elements to the two sets of measured data cannot be made. Simultaneous soft x-ray measurements of radiated power profiles at a number of beryllium filter thicknesses would increase the reliability of the

estimates of the relative proportions of each impurity element. Further experimental inputs, such as calibrated impurity line intensities from spectrometers or soft x-ray pulse height analysis measurements, would also increase the reliability of the estimates of Z_{eff}.

These simulations show that during the discharge the impurity density profiles with a central peak continuously increase, as the time constant for attaining equilibrium is much longer than the duration of the discharge. The consequent increase of the central radiated power and the decrease in net power to the plasma together with the slow central density rise, leads to a reduction of the central temperature which reinforces the increase in radiated power.

A comparison of the radiation profiles of a density plateau discharge at a line integrated density of 1.6×10^{20} m^{-3} and a ramped density limit discharge reaching the same line integrated density is shown in Fig. 5. At the time when the diamagnetic energy is falling in both discharges the radiation profiles are peaked, suggesting that in both cases core radiation is the ultimate limitation for reaching higher densities. A divertor is currently being installed for W7-AS and should significantly reduce the level of impurity particle influx and allow steady state discharges to be achieved. The identified impurities in particular can be strongly reduced by component baking or shielding to restrict particle flux onto exposed surfaces.

6. Conclusions

Modeling of density limit discharges with a modified two point model can reproduce the features of a falling temperature and rising density in front of the limiter plates. The plasma detaches when the net power flux at the plasma edge decreases so that power balance in front of the limiter plate can no longer be fulfilled. The plasma collapsed rapidly after the total radiated power was greater than the NBI input power. The simple one dimensional two point model therefore describes the physics of the density limit in stellarators and tokamaks.

The time dependent simulation of the bolometer measurements and soft x-ray radiation measurements with a beryllium foil filter using density and temperature profiles, ASTRA, STRAHL and simple assumptions about the impurity flux at the boundary were carried out. This has proved to be a valuable tool for the interpretation of density limit discharges in W7-AS. The integration of further experimental measurements, such as calibrated impurity line intensities from spectrometers, soft x-ray pulse height analysis and simultaneous soft x-ray radiation power densities at a number of filter thicknesses, should be a goal for increasing the reliability of the estimates of Z_{eff}.

It was demonstrated that in the density plateau discharges the centrally peaked radial profile of the radiation power density was due to peaked impurity density profiles with a time constant for attaining equilibrium longer than the duration of the discharge. Decreasing net power to the plasma due to increasing radiated power from the plasma core is shown to be responsible for the observed fall in diamagnetic energy. The decrease of diamagnetic energy

with time in density plateau discharges is influenced greatly by the vessel wall conditioning of helium glow discharges. Increased central temperatures and reduced total radiated power are then measured. The reduction of impurity fluxes to the discharge by the planned divertor for W7-AS will therefore be critical to achieving steady state operation at the highest possible density.

References

[1] U. Stroth et al., „High confinement NBI discharges in the W7-AS Stellarator", submitted to Plasma Phys. and Contr. Fusion., **40**, (1998).
[2] G. Janeschitz et al., Plasma Phys. and Contr. Fusion, **37**, (1995), 11A, A19.
[3] G. Pereverzev et. al, IPP Report 5/42, 1991.
[4] K. Borrass, Nucl. Fusion, **31**, (1991), 1035.
[5] K.Behringer, JET Report, JET-R(87)08, (1987).
[6] W-VIIA Team, NI Group, Nucl. Fusion, **25**, 1593, 1985.
[7] K. Borrass, Nucl. Fusion, **33**, (1993), 63.
[8] C.S. Pitcher and P.C. Stangeby, Plasma Phys. and Contr. Fusion, **39**, (1997), 779.
[9] P. Grigull et al., to be published in Proceedings of ITC-8 Conference, J. Plasma Fusion Research, 1998.
[10] W. Suttrop et al., Nucl. Fusion, **37**, (1997), 119.
[11] V. Mertens et al., Proc. 23rd EPS Conference on Contr. Fusion and Plasma Physics, (Kiev), (1996), Vol. I, 15.
[12] P.C. de Vries, J. Rapp, F.C. Schuller and M.Z. Tokar, Phys. Rev. Letters, **80**, (1998) 3519.
[13] W. Suttrop et al., Plasma Phys. and Contr. Fusion, **39**, (1997), 2051.
[14] V. Mertens et al., Nucl. Fusion, **37**, (1997), 1607.
[15] R. Burhenn et al., Proc. 24 th EPS Conference on Contr. Fusion and Plasma Physics, (Berchtesgaden), Vol. IV (1997), 1659.

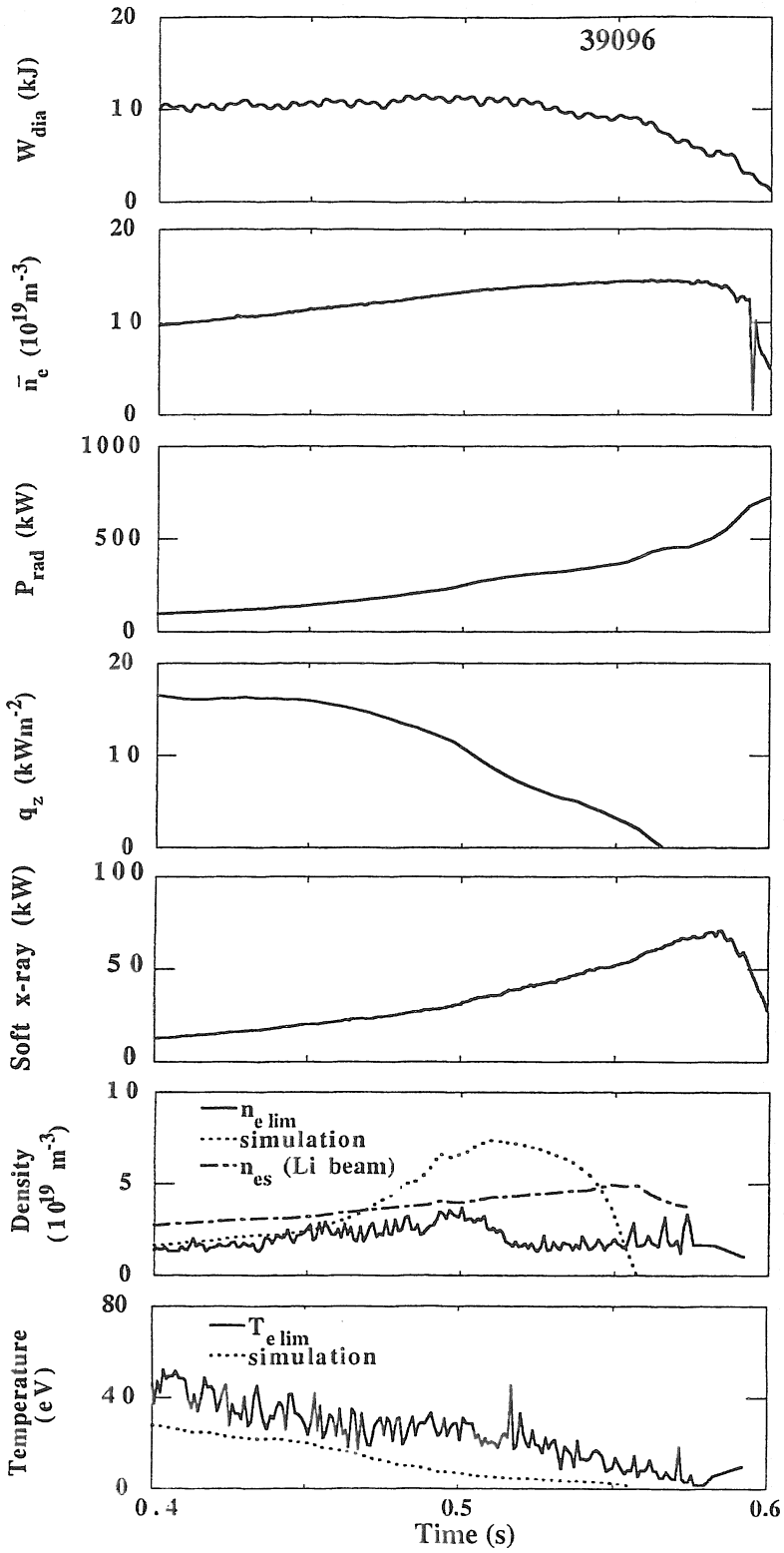

Fig. 1. Diamagnetic energy, line integrated density, radiated power and net heat flux at the plasma edge for a density limit discharge with a density maximum in front of the limiter at 0.5 s followed by detachment and a fall in the diamagnetic energy. After 0.56 s the radiated power is greater than the deposited power and the plasma collapses rapidly. The time evolution of the density and temperature in front of the limiter is compared to the calculated values from the modified two point model.

Radiation measurements and modeling of the density limit on the W7-AS stellarator

L. Giannone, R. Burhenn, P. Grigull, U. Stroth, R. Brakel, R. Dux, A. Elsner, S. Fiedler, G. Kühner, F. Penningsfeld, G. Pereverzev, F. Wagner, A. Weller, C. Wendland, NBI Team and the W7-AS Team.

Max-Planck-Institut für Plasmaphysik,
EURATOM Association, D-85748 Garching, Germany

Abstract

Density limit discharges in the W7-AS stellarator with a strong density ramp were compared to a series of discharges with constant line integrated density approaching the maximum value achieved in the density ramp. The physics of the density limit in stellarators was demonstrated to be consistent with the predictions of the two point model, indicating that this model successfully describes the density limit process in both stellarators and tokamaks. The discharges with a strong density ramp were found to have broader density profiles than those discharges with constant line integrated density. The latter discharges had the electron density profile form found in the improved confinement H-NBI mode on W7-AS. Modeling of the radiation profile, to simultaneously match the measured bolometer and soft x-ray radial profiles of radiated power, implies that impurity density profiles were peaked and continuously increased during the discharge. The increase in radiated power decreased the net deposited power to the plasma and the diamagnetic energy fell. The aim of producing steady state discharges at the highest possible density is aided by the reduction of impurity sources by helium glow discharge cleaning.

1. Introduction

In W7-AS, a discharge with rising line integrated electron density reaches a maximum density, then the diamagnetic energy falls and the radiated power rises continuously until the discharge terminates. This maximum density defines the density limit in W7-AS. Discharges with a constant line integrated density (density plateau) were also studied. In discharges at successively higher density plateaus, the rate of diamagnetic energy decrease after the peak in diamagnetic energy was larger at higher densities. Decreasing net power to the plasma due to core radiation is believed to be responsible for the observed fall in diamagnetic energy.

The density profiles in discharges with a density ramp were markedly broader than those with a density plateau. These density plateau discharges are therefore closely related to the improved confinement scenario in W7-AS (H-NBI mode) but at densities in the vicinity of the density limit [1]. At sufficiently low densities, discharges of duration up to 1.8 s were possible. Such experiments in both tokamaks and stellarators are relevant to the future operation scenario of a reactor, as sustainable steady state high density discharges will be required for power handling and ignition [2].

Measurements of the time evolution of the density and temperature in front of the limiter were compared with predictions of simulations by the time dependent transport code ASTRA

[3] combined with a one dimensional scrape-off layer model of the plasma edge (the two point model) [4]. The addition of the impurity transport code STRAHL [5] allowed radiation profile measurements of the bolometer and soft x-ray cameras to be simulated. The increase in radiated power during density plateau discharges was due to a central peaking of the radiation power density. Such a peaking has been observed previously in the W-VIIA stellarator [6] and accounted for by neoclassical impurity transport of oxygen ions from the vessel walls and tungsten from the NI beams. In W7-AS, 3% shine through losses and 2% charge exchange losses were calculated. Impurity ions, produced by energetic ions impinging on the wall, could therefore have been a relevant factor in the observed discharge evolution.

2. Two point model

Simulations of the time evolution of the electron density and temperature measurements in front of the limiter were carried out with the time dependent transport code ASTRA. This code solves the particle balance, electron energy power balance and ion energy power balance equations as a function of time, allowing time dependent simulations to be carried out. The equations are one dimensional and averaged over closed magnetic flux surfaces. A module was added to ASTRA to describe the physics of the scrape off layer in terms of the two point model. The two point model is a one dimensional model based on electron heat conduction and pressure balance along the field line from the last closed flux surface to a limiter or divertor plate [4] and the predictions of this model have been shown to be consistent with observations in density limit experiments in limiter discharges in a tokamak [7]. A modified pressure balance equation along field lines to account for momentum loss effects due to ion-neutral friction is used [8] :

$$T_{es} = \left(T_{ed}^{7/2} + \frac{7}{4\kappa_o} q_{//s} L_c \right)^{2/7} \left(1 - \left(\frac{T_{ed}}{T_{es}} \right)^{7/2} \right)^{-2/7} \qquad (1)$$

$$2 n_{ed} T_{ed} = f_m n_{es} T_{es} \qquad (2)$$

where n_{es} and T_{es} are the density and temperature at the last closed flux surface, n_{ed} and T_{ed} are the density and temperature in front of the limiter, L_c is the connection length from the last closed flux surface to the limiter (typically 30 m - 100 m depending on the poloidal angle), κ_o is the factor in the electron thermal conductivity equation, f_m is the reduction factor in pressure along the field line and Δ_T is the temperature fall off length in the scrape off layer . The parallel heat flux to the limiter, $q_{//s}$, given by the perpendicular heat flux at the last closed flux surface, $q_\perp$, multiplied by the geometrical factor, L_c / Δ_E. The heat flux across a flux tube of length L_c is projected onto the limiter within an energy fall length $\Delta_E = 2/7\ \Delta_T$. This parallel

flux to the limiter is balanced by the sum of losses by ionization of neutrals, by impurity radiation and in the sheath in front of the limiter or divertor plate:

$$q_{//s} = 7L_c q_\perp / 2\Delta_T = n_D c_S \beta \xi + c_{rad} l \gamma_{imp} n_D^2 + \gamma n_D T_D c_S \qquad (3)$$

These equations can be solved for n_{ed},T_{ed} and T_{es} , using n_{es} and $q_\perp$ as inputs.

3. Density ramps

The lithium beam diagnostic measures the time evolution of the radial profile of n_e, therefore providing the input value of n_{es}. The total radiated power is deduced from Abel inverted measurements of the line integrated power flux onto 4 μm gold foil absorbers of a 12 channel bolometer array and then $q_\perp$ is calculated from the deposited NBI power minus the total radiated power. The soft x-ray measurements are carried out with 2 cameras, each of 36 channels, of surface barrier diodes. The placement of a 12.5 μm beryllium foil in front of the entrance slit allows the filtering out of energy components below 1 keV.

A discharge at B = 2.5 T with 380 kW of neutral beam injection (NBI) heating and a density ramp that increased the central density from 5.5×10^{19} m^{-3} to 1.5×10^{20} m^{-3} in the time interval from 0.2 s to 0.6 s is shown in Fig. 1. The magnetic configuration, with an edge value of rotational transform, $\iota(a)$, of 0.34 is bounded by two tangential graphite limiters at the top and bottom of an elliptical cross section of magnetic flux surfaces. A comparison of the Langmuir probe measurements of n_{ed} and T_{ed} and the predictions of the modified two point model are also shown. The evolution of n_{ed} and T_{ed} are reasonably simulated with a continuously falling temperature and a density reaching a maximum at 0.5 s and a continuously falling temperature. In agreement with the usual description of the density limit in tokamaks, a critical edge density is reached at which the value of net power flux can no longer sustain power balance in front of the limiter and detachment from the limiter follows [9]. The physics of the density limit in stellarators can therefore be adequately described by the two point model indicating that this model describes the density limit process in both stellarators and tokamaks. After 0.56 s the radiated power is greater than the deposited power and the discharge rapidly collapses. However, no tearing mode instability is triggered in a stellarator in contrast to observations of a the density limit on a tokamak [10]. The difference in maximum value of density in front of the limiter predicted and observed, may be partially explained by the overestimation of the measured electron temperature suggested to occur in the presence of non-thermal electrons from the upstream plasma [9]. From the Langmuir probe measurements of ion saturation current, the calculated density is then underestimated.

Discharges with a Murakami parameter greater than the Greenwald limit were achieved transiently in W7-AS in this set of discharges. Similarly plasma parameters yielding values

above the Greenwald limit in tokamak density limit discharges have also been achieved transiently using pellet injection [11] or for a duration of 0.8 s with only a slow increase of radiated power [12]. Such global comparisons will be extended in the near future by measurements at the density limit of local electron density and temperature inside the last closed flux surface to compare to the edge operational diagram for tokamaks [13]. A sequence of energy detachment, an edge thermal instability, particle detachment and disruption at the density limit is observed below a critical edge temperature and above a critical edge density [14].

4. Density plateaus

Discharges at B = 2.5 T with 380 kW of NBI heating at successively higher line averaged densities starting from 5.5×10^{19} m^{-2} to 8.0×10^{19} m^{-2} or peak densities of 1.1 to 1.6×10^{20} m^{-3} showed that for each density plateau a peak in the diamagnetic energy was reached and that the level of radiated power rose during the discharge. Again the magnetic configuration was bounded by the two tangential limiters at the top and bottom of an elliptical cross section for discharges with $\iota(a)$ of 0.34. The limiter radius was at r = 16.2 cm. The diamagnetic energy decreased faster in those discharges at higher density. In Fig. 2, density plateau discharges before and after helium glow discharge cleaning at a density of 1.3×10^{20} m^{-3} display the extent to which wall conditioning can influence the time evolution. At a lower density the discharge takes longer to collapse because the radiated power does not increase to the same level so quickly. A simple explanation is that the impurity particle flux is drastically reduced. The particle flux to the limiter, as measured by the ion saturation current to a Langmuir probe embedded there, did not change after helium glow discharge cleaning. This indicates that the source of impurity ions at the surface have been modified by the discharge cleaning.

In addition to possible changes in the impurity flux, density and temperature profile changes or a change in particle or heat transport coefficients are also factors determining the evolution of the radiation profiles. At present, only the time evolution of the central electron temperature from Thomson scattering was available and the temperature profile from a single time point was scaled appropriately. Under these experimental limitations a detailed analysis is not possible. This analysis can be performed when the profiles of density and temperature from Thomson scattering every 50 ms are available in the near future. It will be then also possible to calculate the change in impurity flux at the boundary needed to adequately simulate the discharge prior to discharge cleaning.

The density profile evolution was measured by the lithium beam diagnostic. Even though the level of gas puffing is reduced after 0.5 s, the central density slowly increased and the density at r = 10 cm remained approximately constant, indciating a peaking of the density

profile during the discharge. The increasing central electron density and consequent plasma cooling is one factor involved in the observed deterioration in diamagnetic energy during the discharge.

5. Radiation profiles

The radial profiles of the diffusion coefficient, D, and inward pinch velocity, v, shown in Fig. 3 were calculated from measurements of the time evolution soft x-ray emission and Al impurity lines after aluminum impurity injection by laser blow-off [15]. The Al impurity lines were measured by a Jobin-Yvon spectrometer (Al XI) and a Bragg spectrometer (Al XII). The soft x-ray emission with and without impurity injection are subtracted to yield the net emission due to impurity injection. The electron density profiles of this discharge were within 10% of the density plateau discharge after helium glow discharge cleaning shown in Fig. 2. It should be noted that the following simulation of this density plateau discharge assumes that the measured diffusion coefficient and inward pinch velocity do not change significantly with density or density profile during the discharge.

Spectroscopic measurements of line radiation by the SPRED VUV spectrometer showed that the impurity elements carbon, chlorine and copper were dominant in the density limit discharges studied. Using the radial profiles of D and v derived from laser blow off experiments, together with the time evolution of the density and temperature profiles and an assumed constant impurity flux of each impurity at the boundary, simulations of the time evolution of bolometer and soft x-ray radiation profiles were carried out with the impurity transport code, STRAHL. This code calculates the impurity ion balance of a single impurity species according to the input parameters described and uses tabulated atomic rate coefficient data for ionization, radiative recombination, dielectronic recombination and charge exchange recombination to calculate the radiated power as a function of minor radius in the plasma. In Fig. 4, the measured and simulated radiation profiles for the bolometer and soft x-ray (12.5 μm beryllium foil filter) cameras for the density plateau discharge considered in Fig. 2 are compared. These simplified assumptions are sufficient to satisfactorily simulate the peaking of the measured bolometer and soft x-ray profiles. Maximum central relative impurity densities at the end of the discharge for carbon, chlorine and copper of 0.057, 0.004 and 0.0005 respectively, and therefore a Z_{eff} of 3.6, were estimated. The contribution to the radiated power density for the bolometer measurements in the center is in roughly equal proportions for each impurity element, while for the soft x-ray measurements they were 16%, 50% and 34% respectively. Because of the similar peaked power profiles from both chlorine and copper, a unique fit for the relative contributions of these elements to the two sets of measured data cannot be made. Simultaneous soft x-ray measurements of radiated power profiles at a number of beryllium filter thicknesses would increase the reliability of the

estimates of the relative proportions of each impurity element. Further experimental inputs, such as calibrated impurity line intensities from spectrometers or soft x-ray pulse height analysis measurements, would also increase the reliability of the estimates of Z_{eff}.

These simulations show that during the discharge the impurity density profiles with a central peak continuously increase, as the time constant for attaining equilibrium is much longer than the duration of the discharge. The consequent increase of the central radiated power and the decrease in net power to the plasma together with the slow central density rise, leads to a reduction of the central temperature which reinforces the increase in radiated power.

A comparison of the radiation profiles of a density plateau discharge at a line integrated density of 1.6×10^{20} m^{-3} and a ramped density limit discharge reaching the same line integrated density is shown in Fig. 5. At the time when the diamagnetic energy is falling in both discharges the radiation profiles are peaked, suggesting that in both cases core radiation is the ultimate limitation for reaching higher densities. A divertor is currently being installed for W7-AS and should significantly reduce the level of impurity particle influx and allow steady state discharges to be achieved. The identified impurities in particular can be strongly reduced by component baking or shielding to restrict particle flux onto exposed surfaces.

6. Conclusions

Modeling of density limit discharges with a modified two point model can reproduce the features of a falling temperature and rising density in front of the limiter plates. The plasma detaches when the net power flux at the plasma edge decreases so that power balance in front of the limiter plate can no longer be fulfilled. The plasma collapsed rapidly after the total radiated power was greater than the NBI input power. The simple one dimensional two point model therefore describes the physics of the density limit in stellarators and tokamaks.

The time dependent simulation of the bolometer measurements and soft x-ray radiation measurements with a beryllium foil filter using density and temperature profiles, ASTRA, STRAHL and simple assumptions about the impurity flux at the boundary were carried out. This has proved to be a valuable tool for the interpretation of density limit discharges in W7-AS. The integration of further experimental measurements, such as calibrated impurity line intensities from spectrometers, soft x-ray pulse height analysis and simultaneous soft x-ray radiation power densities at a number of filter thicknesses, should be a goal for increasing the reliability of the estimates of Z_{eff}.

It was demonstrated that in the density plateau discharges the centrally peaked radial profile of the radiation power density was due to peaked impurity density profiles with a time constant for attaining equilibrium longer than the duration of the discharge. Decreasing net power to the plasma due to increasing radiated power from the plasma core is shown to be responsible for the observed fall in diamagnetic energy. The decrease of diamagnetic energy

with time in density plateau discharges is influenced greatly by the vessel wall conditioning of helium glow discharges. Increased central temperatures and reduced total radiated power are then measured. The reduction of impurity fluxes to the discharge by the planned divertor for W7-AS will therefore be critical to achieving steady state operation at the highest possible density.

References

[1] U. Stroth et al., „High confinement NBI discharges in the W7-AS Stellarator", submitted to Plasma Phys. and Contr. Fusion., **40**, (1998).
[2] G. Janeschitz et al., Plasma Phys. and Contr. Fusion, **37**, (1995), 11A, A19.
[3] G. Pereverzev et. al, IPP Report 5/42, 1991.
[4] K. Borrass, Nucl. Fusion, **31**, (1991), 1035.
[5] K.Behringer, JET Report, JET-R(87)08, (1987).
[6] W-VIIA Team, NI Group, Nucl. Fusion, **25**, 1593, 1985.
[7] K. Borrass, Nucl. Fusion, **33**, (1993), 63.
[8] C.S. Pitcher and P.C. Stangeby, Plasma Phys. and Contr. Fusion, **39**, (1997), 779.
[9] P. Grigull et al., to be published in Proceedings of ITC-8 Conference, J. Plasma Fusion Research, 1998.
[10] W. Suttrop et al., Nucl. Fusion, **37**, (1997), 119.
[11] V. Mertens et al., Proc. 23rd EPS Conference on Contr. Fusion and Plasma Physics, (Kiev), (1996), Vol. I, 15.
[12] P.C. de Vries, J. Rapp, F.C. Schuller and M.Z. Tokar, Phys. Rev. Letters, **80**, (1998) 3519.
[13] W. Suttrop et al., Plasma Phys. and Contr. Fusion, **39**, (1997), 2051.
[14] V. Mertens et al., Nucl. Fusion, **37**, (1997), 1607.
[15] R. Burhenn et al., Proc. 24 th EPS Conference on Contr. Fusion and Plasma Physics, (Berchtesgaden), Vol. IV (1997), 1659.

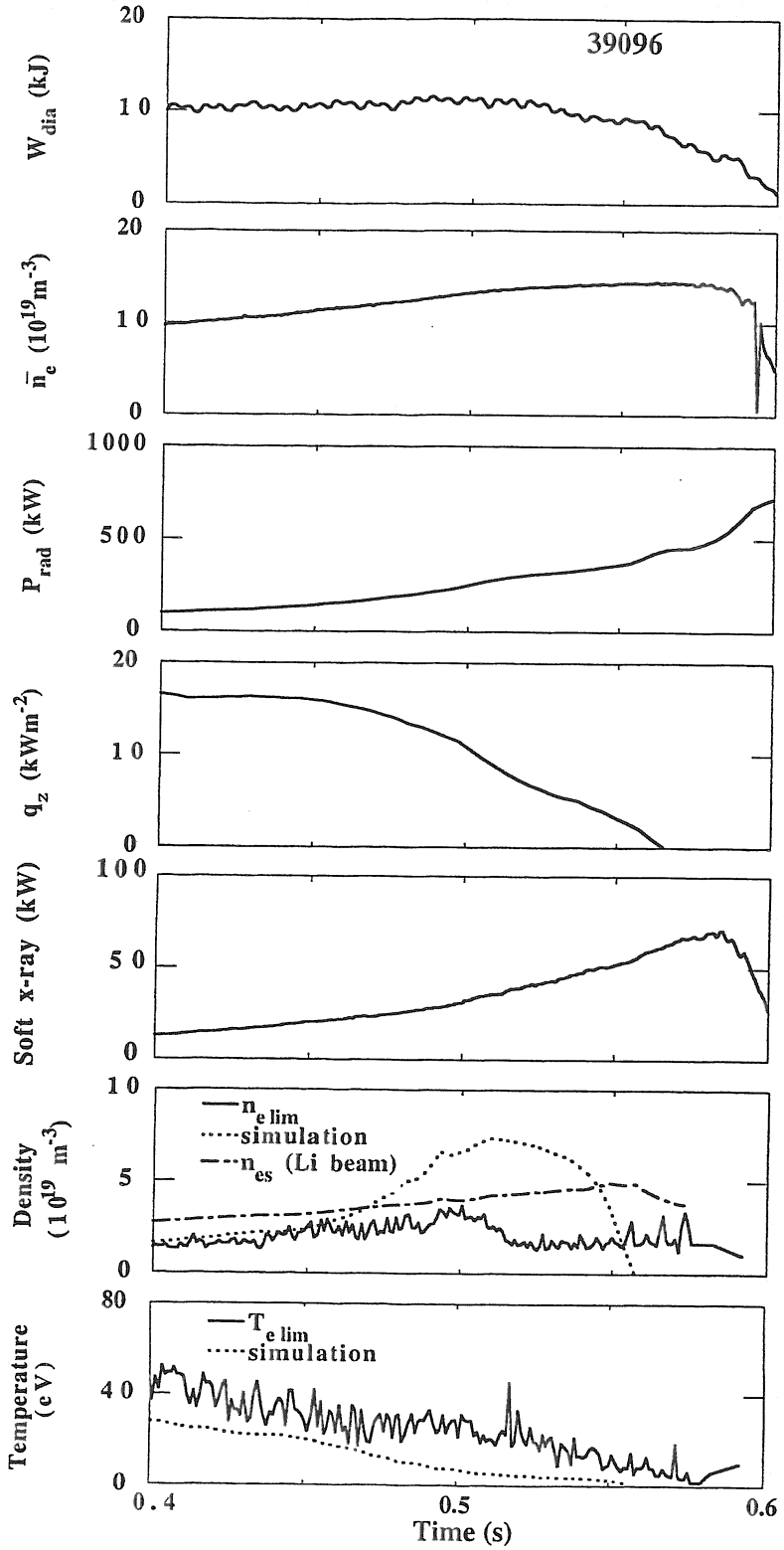

Fig. 1. Diamagnetic energy, line integrated density, radiated power and net heat flux at the plasma edge for a density limit discharge with a density maximum in front of the limiter at 0.5 s followed by detachment and a fall in the diamagnetic energy. After 0.56 s the radiated power is greater than the deposited power and the plasma collapses rapidly. The time evolution of the density and temperature in front of the limiter is compared to the calculated values from the modified two point model.

B2-EIRENE code modelling of an island divertor

G. Herre, P. Grigull, R. Schneider

Max-Planck-Institut für Plasmaphysik, EURATOM Ass., Boltzmannstrasse 2, D-85748 Garching, Germany

Abstract

The multifluid plasma scrape-off layer transport code B2 coupled to the EIRENE Monte Carlo neutral gas transport code was applyed to a proto-typical island divertor configuration in W7-AS. The approach predicts the accessibility of stable, layer-like energy detachment within a relatively broad density range. The island geometry with typically small field line pitch has the beneficial effects of efficient shielding of the main plasma against neutrals, and of strong momentum losses from the power carrying layer due to momentum radial transport. The latter reduces the peak power load and eases detachment. The power exhaust properties and the onset of detachment can be positively affected by the choice of the field line pitch which can be varied in W7-AS by superimposed control fields.

1. Introduction

In the context of the development and near future operation of large stellarators (e.g. LHD and W7-X), the search for adequate power and particle exhaust scenarios comparable to those in tokamak divertors has become mandatory. A favoured option generally compatible with stellarator-specific confinement concepts is the island divertor which utilizes macroscopic magnetic islands at the plasma boundary in combination with adequately arranged targets and baffles for plasma exhaust. The islands can be produced by intrinsic (e.g. W7-AS, W7-X) or relatively small additional perturbation fields. Nevertheless, the suitability of this concept has not yet been proven. The relevant data base is scarce and stems exclusively from few pre-investigations in CHS (local island divertor, LID) [1] and W7-AS (island configuration with inboard limiters) [2,3]. The present analysis applies the two-dimensional B2(Braams) edge plasma transport code [4] linked with the EIRENE neutral transport code [5,6] to a specific W7-AS island divertor configuration but allows, nevertheless, to exemplarily assess crucial elements of the concept. The study is part of an ongoing island divertor programme which comprises, besides this „proof of priciple", the further development of a more adequate 3D (Monte Carlo) edge transport code [3,7,8], the installation and study of a modular island divertor in W7-AS [3], and future investigations of an island divertor with flexible configuration in the W7-X device [9]. The paper continues previous studies [10] mainly by extending the parameter range to values relevant for detachment regimes. It addresses the questions whether in particular the extremely small field line pitch inside the islands and the neutral mean free path relative to the islands radial width allow to establish stable detachment at all in this approach, and to what degree island-specific 2D effects affect the scenarios. The aim is to give a status report.

The following chapter briefly describes the W7-AS magnetic field configuration and grids used for numerical computation; free parameters and boundary conditions are specified in Section 3. In Section 4, the results are presented and discussed. Section 5 gives a summary of the results and draws conclusions.

2. Magnetic field configuration and numerical grids

The W7-AS configuration (major radius $R = 2$ m, minor radius $a = 0.18$ m, five magnetic field periods, $B \leq 2.5$ T, rotational transform $\iota = 0.3 - 0.7$, low magnetic shear) is, at $\iota = n/m > 0.4$, bounded by a chain of macroscopic magnetic islands of the symmetry $5/m$. The radial position, size and internal rotational transform ι_i of the islands can be controlled by the externally adjustable edge rotational transform ι_a, a superimposed vertical field and/or, in the near future divertor phase, by additional control fields which may also compensate finite-β

effects. The planned island divertor is designed for configurations with $\iota_a \approx 5/9$ providing both, sufficient main plasma cross section and relatively large island dimensions (Fig. 1). For these reasons, this type was also chosen for the present analysis. In this case, the island cross sections shown in Fig. 1 belong to a unique island which closes after nine toroidal revolutions.

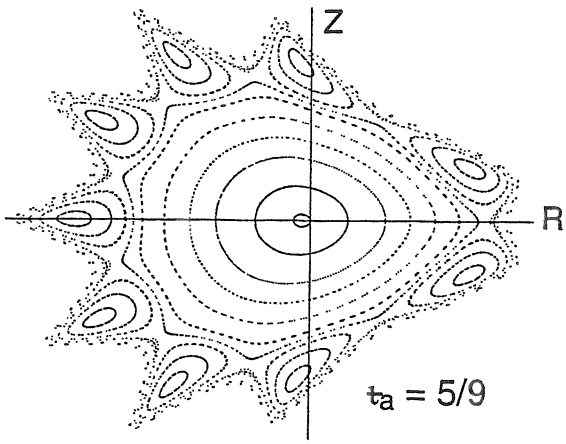

Fig. 1: Triangular cross section of the W7-AS magnetic field configuration with n/m = 5/9 boundary islands used for the B2-EIRENE code simulations. The cross sections change from triangular over elliptic to triangular with fivefold periodicity.

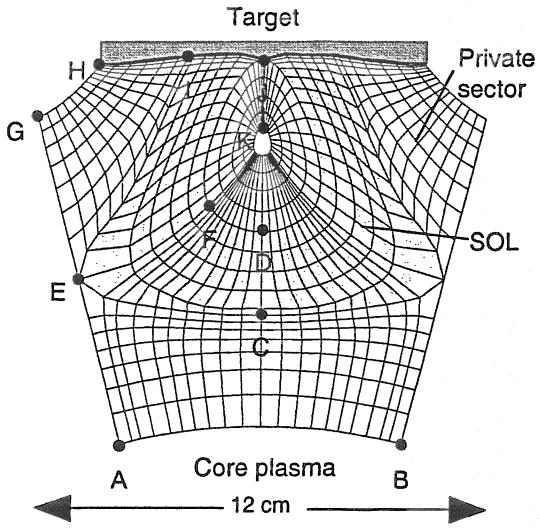

Fig. 2: Section of the EIRENE code numerical grid with points for text explanation. The grid is adapted to the helically averaged island structure.

As stellarators like W7-AS are strongly non-axisymmetric, the application of the two-dimensional B2 fluid approach requires helical averaging of the three-dimensional edge structure. For that purpose the B2 geometric coefficients were derived from a 3D grid (with closest approximation to orthogonality) by helically averaging distances and integrating up areas and volumes. Periodical boundary conditions at the connection to poloidally neighboured islands and inter-cell connections along the symmetry line outside the o-point (corresponding to line JK in Fig. 2) were treated by three topological cuts in the B2 grid. The EIRENE grid (Fig. 2) was generated by geometrically averaging the island structure along the helical coordinate. Computations were performed in the standard way: B2 results mapped onto the EIRENE grid provided the EIRENE input; the resulting neutral distribution mapped onto the B2 grid provided the next iteration B2 source terms etc.

3. Free parameters and boundary conditions

The B2 fluid approach solves the continuity, momentum and energy equations (details can be seen from Ref. [4]). Parallel transport is described by Navier-Stokes type equations; for the radial transport an a diffusive Ansatz is made. Particle radial diffusion coefficients were chosen according to the empirical W7-AS scaling $D_\perp = 2P_s^{0.85} n_{es}^{-1.1}$ (with P_s being the net power crossing the separatrix in MW and n_{es} the upstream separatrix density in 10^{19} m^{-3}) up to $n_{es} = 3\text{x}10^{19}$ m^{-3} [11]; above this density, $D_\perp$ was set to constant. Pinch velocities were assumed to be zero. The value of the electron anomalous heat diffusivity $\chi_{e\perp}$ was taken as three times $D_\perp$; the coefficient of anomalous cross field viscosity was set to $\eta_\perp = m_i n_e D_\perp$. At the inner grid boundary (line AB in Fig. 2), the total power outflux from the core P_c and the deuterium density were prescribed. Sheath boundary conditions [12] were used at the target plates. At the outside boundary of the private flux region (line GH), radial decay lengths (2 cm for densities and 3 cm for temperatures) have been fixed. Deuterium recycling coefficients were assumed to be $R = 1$ at the targets and $R = 0.98$ at the walls.

In oder to elucidate effects of the island geometry under less complex conditions, the upstream separatrix density n_{es} was scanned first for pure deuterium plasmas at varied field line pitch at the edge and relatively low power, P_c = 220 kW. The pitch variation approximately covers the experimentally accessible range in W7-AS and includes the standard pitch distribution (without additional correction fields, denoted as „medium pitch" in the following) and pitch values increased by a factor of four („high pitch") or decreased by a factor of two („low pitch"). At the standard distribution, the pitch poloidally averaged along the grid cells just inside the island separatrix (see Fig. 2) is $\sin\theta = 0.002$; the corresponding field line connection length from the upstream stagnation point to the target is $L_c = 98$ m. The effect of impurity radiation is then shown at medium pitch by an n_{es} scan at $P_c = 600$ kW with selfconsistent treatment of carbon as edge dominating, intrinsic impurity considering physical (TRIM code data [13]) and chemical sputtering from the carbon targets. The chemical sputtering efficiency was assumed to be 2% of the incoming particle flux.

4. Results and discussion

Pure deuterium plasmas. Figure 3 plots divertor plasma parameters versus the upstream separatrix density n_{es}. At medium field line pitch (solid lines), the course of the downstream parameters T_{ed}^{max} (maximum electron temperature), n_{ed}^{max} (maximum electron density) and Γ_{pt} (particle flux onto target) indicate the transition from a linear regime to divertor high recycling at $n_{es} \approx 10^{19}\,m^{-3}$ and the onset of slight (energy) detachment at $n_{es} \approx 2.5\times10^{19}$. Above $n_{es} = 2\times10^{20}\,m^{-3}$, volume recombination becomes strongly effective leading to complete detachment and unstationarity. The stable detachment scenarios show saturating n_{ed} and Γ_{pt} values, a divertor leakage for neutrals of about 1%, increasing divertor radiated power fractions f_r^{div} (Fig. 3c) and significant net momentum losses indicated by respective loss factors F_m (Fig. 3d, for definitions see below). With increasing upstream density, the ionization front is found to quickly move away from the target towards the x-points as it is more or less typical also for tokamak divertor geometries. As Fig. 4 shows, the island geometry with small field line pitch and the two „divertor tails" at close proximity (partially overlapping) involves, however, some characteristic features. Due to the specific 2D patterns in particular of energy and momentum flow, the downstream power carrying layer nearly homogeneously spreads over the scrape-off layer (SOL) between the two strike points as it is indicated by the parallel power flux $q_{\|d}$ profiles in Fig. 4b (peaking of the target thermal load q_t in the private sector (PS) is caused by increasing field line inclination in this range). The n_{ed} and in particular T_{ed} radial profiles are relatively flat over the whole n_{es} range (Fig. 4a) thus leading to a „layer" type detachment without strong profile changes.

This behaviour shall be illustrated by some details of the momentum balance. In analogy to simple two-point models [14], we define integral momentum loss factors for the SOL+PS region as

$$F_m^{tot} = \int_{SOL+PS} (S_{m\|} + \nabla_\perp \cdot \Gamma_{m\|}) dz d\psi \Big/ \int_{up} p_{up}^* d\psi \qquad (1)$$

with $S_{m\|}$, $\Gamma_{m\|}$, z and ψ being the volume source or sink of parallel momentum due to friction with neutrals (charge exchange, ionization), the radial flux of parallel momentum (convective + conductive), the coordinate parallel to B, and the magnetic flux, respectively. $p^*_{up} = n_{e,up}\, T_{e,up}\, (1+\gamma M^2)$ (with γ the adiabatic coefficient and M the Mach number) is the plasma pressure at the upstream position along line GEF in Fig. 2 (in analogy to a tokamak x-point divertor entrance). Loss factors F_m^{tr} considering only momentum transport were obtained by omitting $S_{m\|}$ in (1); the difference between both factors stands for the losses by friction with neutrals. Corresponding local loss factors f_m (along a flux tube) were obtained by substituting the integration over ψ by multiplication with the corresponding flux increment $\Delta\psi$. As Fig. 3d shows, there are big differences between integral and local loss factors. At detachment, the integral losses are dominated by friction with neutrals. The divergence term in Eq. (1) contributes about 20%-30% (mainly transported to the closed island range where it becomes balanced by parallel viscosity). It leads, however, to strong local losses along the flux tube

range with maximum upstream pressure (just inside the island separatrix) over the whole density range as it is indicated by the respective local loss factor f_m^{tr}, and to pressure increase in the PS. This momentum re-distribution superimposed to a nearly homogeneous concentration of momentum sinks by neutrals within the SOL range (see respective local pressure losses Δp^{tr} and Δp^{n} in Fig. 4c) strongly flattens the downstream pressure profiles and supports the formation of layer detachment.

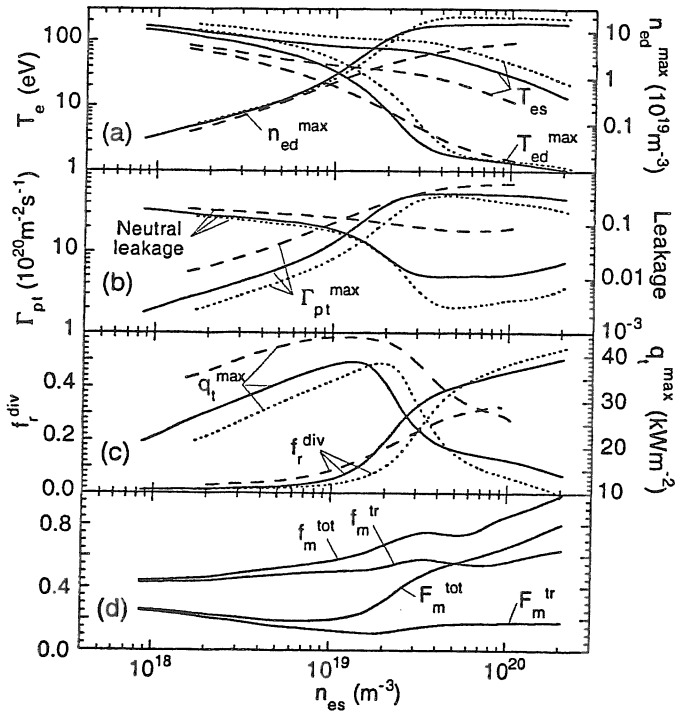

Fig. 3: Pure deuterium plasmas. Divertor plasma parameters versus the upstream density n_{es} (at point C in Fig. 2) at a power outflow from the core of P_c = 220 kW. Solid, dashed or dotted lines indicate medium, high or low field line pitch at the edge, respectively (see text). T_{es}, T_{ed}^{max}, n_{ed}^{max}, Γ_{pt}^{max}, q_t^{max} and f_r^{div} are the upstream and downstream electron temperatures, the peak downstream density, the maximum particle flux, the peak power load onto the target, and the divertor radiated power fraction, respectively. F_m and f_m are integral (SOL + private sector) and local (along the flux tube just inside the island separatrix) momentum loss factors, respectively. Upper indices indicate total losses (tot) and losses by momentum radial transport (tr, definitions see text).

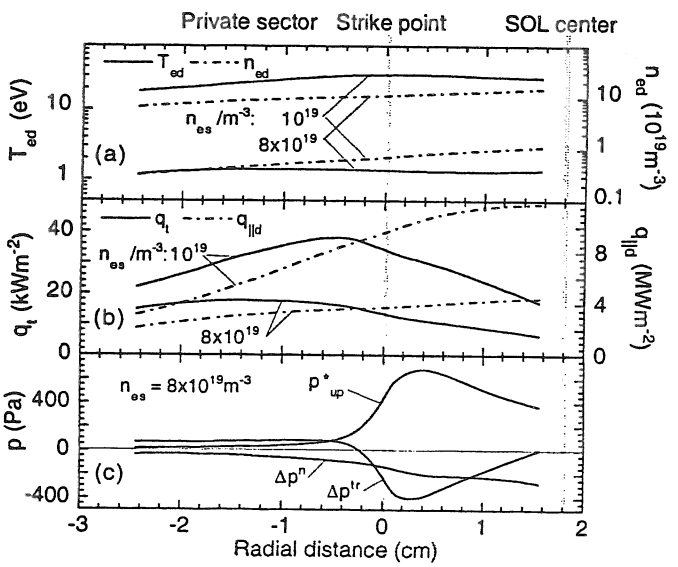

Fig. 4: Pure deuterium plasmas.
(a, b) Downstream parameter radial profiles (along line HJ in Fig. 2) for an attached and a detached scenario at medium field line pitch. $q_{\|d}$ is the downstream parallel power flux, other symbols as in Fig. 3.
(c) Upstream total plasma pressure p^*_{up} profile (along line GEF in Fig. 2) and pressure losses due to momentum transport (Δp^{tr}) and friction with neutrals (Δp^{n}) at detachment.

Modifying the field line pitch within the divertor region changes the field line connection lengths relative to the parallel gradient lengths, and by this the role of parallel transport relative to the cross field (radial) transport. At high pitch (dashed lines in Fig. 3), T_{es} is decreased by more than a factor of two. The intermediate high recycling scenario vanishes, the leakage for neutrals is about 10%, and detachment is less pronounced. From downstream parameter radial profiles (not shown) it is inferred, that the 2D smoothing effects mentioned are less efficient, but in the detached state the momentum sinks by neutrals are now peaked close to the strike line which finally leads to similarly flat $q_{\|d}$ profiles at highest density as with median pitch. The target peak load is, however, less reduced (Fig. 3c), and the density limit for stationary operation is decreased. Low pitch (dotted lines in Fig. 3) has the opposite effect. The onset of detachment is shifted to slightly higher density, the leakage for neutrals is favourably reduced

(about 0.3%), and the 2D features accentuated above become stronger developed but do not yet lead to qualitatively new scenarios. These results indicate that low pitch is basically preferable, but pitch variations within the accessible range may provide a „knob" to optimize scenarios with transport coefficients (not too strongly) deviating from the above assumptions.

Deuterium plasmas with carbon as intrinsic impurity. Applying the picture of coupled momentum and impurity radiation losses [14], one expects the same qualitative behaviour also for deuterium plasmas with carbon which is indeed reproduced by the results.

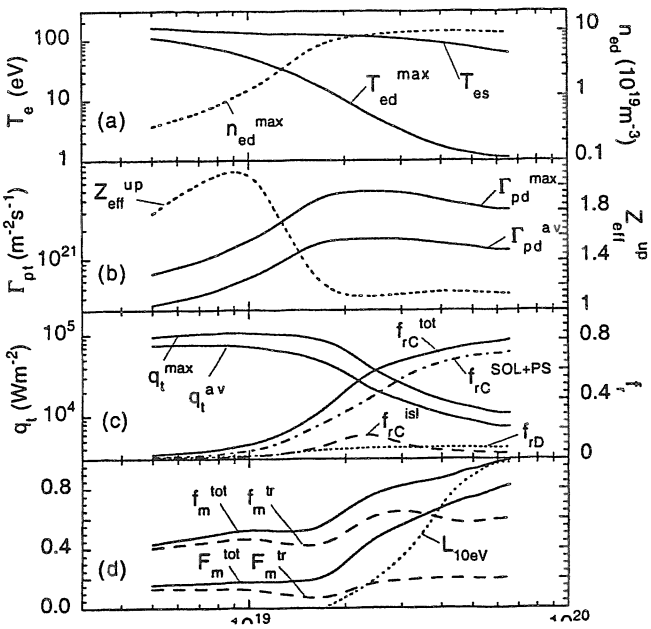

Fig. 5: Plasmas with carbon as intrinsic impurity. Divertor plasma parameters versus n_{es} at medium pitch and P_c = 600 kW. Lower indices in (c) denote the total line radiation from carbon (C) or deuterium (D); the upper index "isl" denotes the contribution from the closed island range. L_{10eV} (d) indicates the shift of the T_e

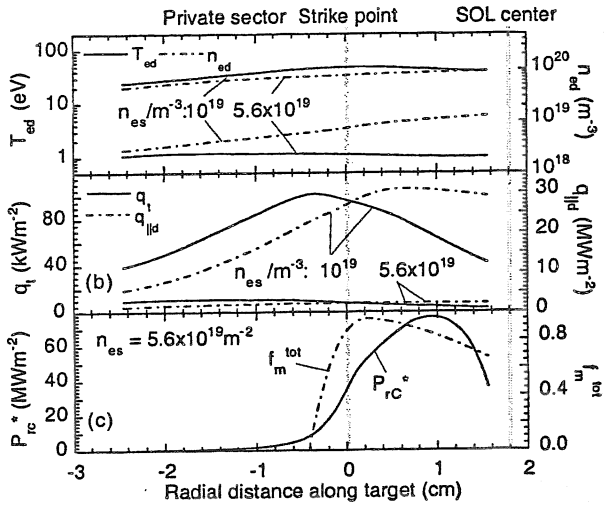

Fig. 6: Plasmas with carbon as intrinsic impurity. (a, b) Downstream parameter radial profiles for an attached and a detached scenario. Symbols as in Fig. 4. (c) Radial distribution of momentum losses f_m^{tot} (by momentum transport + friction with neutrals) and energy losses P_{rC} by carbon radiation (total emissivity integrated up along flux tubes).*

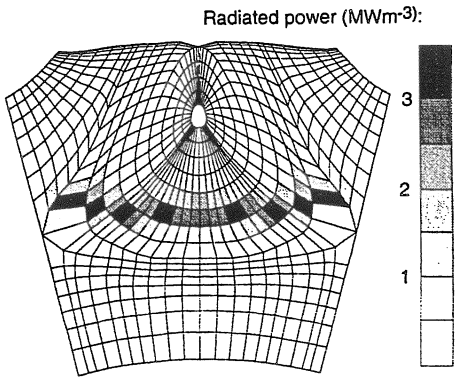

Fig.7: Distribution of the carbon line total emissivity for a detachment scenario at n_{es} = 5.6x10^{19} m^{-3}.

As Fig. 5 shows, stable detachment sets in at $n_{es} \approx 2\ 10^{19}\,m^{-3}$ and extends to 7 10^{19} m^{-3}. Similar to the pure deuterium case, it is partial in the sense that Γ_{pt} saturates but does not beak off (Fig. 5b). The divertor radiated power fraction f_{rC}^{div} due to carbon line radiation reaches up to 80%; the main part comes from the SOL region. Deuterium radiation contributes about 10% (Fig. 5c); energy losses due to charge exchange (not shown) are negligible. The ionization and radiation fronts are found to remain nearly parallel to the target indicating layer type detachment without strong profile changes also at these conditions. In analogy to the pure deuterium case, the development of the integral and local momentum loss factors in Fig. 5d as well as the downstream parameter radial profiles in Figs. 6a,b demonstrate again the strong effects of radial transport. The T_{ed} profiles are flat even before detachment, n_{ed} and $q_{\|d}$ are maximum within the SOL range between the two strike points. Momentum losses due to the superimposed effects of momentum radial transport and friction with neutrals as well as radiative losses concentrate at

this latter region (Figs. 6c, 7) thus leading to nearly homogeneous detachment over this radial range.

5. Summary and conclusions

The B2-EIRENE code package was applied to a proto-typical W7-AS island divertor configuration. The divertor operational regimes are found to pass through the same sequence of states from low recycling to detachment as in a tokamak x-point divertor, thus demonstrating the proof of principle for successful operation. The power exhaust properties and the onset of detachment can be positively influenced by the choice of the field line pitch at the edge which affects the efficiency of radial relative to parallel transport. Small pitch has the benefits of good shielding of the main plasma against neutrals and of strong momentum losses close to the island separatrix due to momentum radial transport which reduces the peak power load and supports detachment. Detachment is generally layer-like which may, similar to horizontal targets in tokamak divertors, implicate a somewhat reduced SOL- and therewith global density limit. Widening of the operational window should, however, be possible by optimizing the target geometry for preferential reflection of neutrals and restriction of detachment to the strike point vicinity (like e.g. in ASDEX Upgrade). Corresponding sensitivity studies are planned.

It is conjectured that basic elements of this picture are not strongly changed by 3D effects like varying flux tube cross sections and helically disconnected target plates. This is, however, speculative at present. More information is expected from the planned divertor experiment in W7-AS supported by a 3D (Monte Carlo) edge transport code which is under development [7,8].

References:

[1] A. Komori et al, J. Nucl. Mater. 241-243 (1997) 967
[2] P. Grigull et al., J. Nucl. Mater. 241-243 (1997) 935
[3] F. Sardei et al., J. Nucl. Mater. 241-243 (1997) 135
[4] B. J. Braams, A Multi Fluid Code for Simulation of the Edge Plasma in Tokamaks. Report No. (NET) EUR-FU/XII-80/87/68, Comm. of the EC, Brussels 1987
[5] D. Reiter, The EIRENE Code, Version Jan. 92, Users Manual, Report No. 2599, Institut für Plasmaphysik, Association EURATOM-KFA, 1992
[6] R. Schneider et al., J. Nucl. Mater. 196-198 (1992) 810
[7] Y. Feng et al., J. Nucl. Mater. 241-243 (1997) 930
[8] Y. Feng et al., this Conference
[9] H. Renner et al., J. Nucl. Mater. 241-243 (1997) 946
[10] G. Herre et al., J. Nucl. Mater. 241-243 (1997) 241
[11] P. Grigull et al., 10th Intern. Conf. on Stellarators, IAEA Technical Meeting, Madrid, Spain, 1995, Report EUR-CIEMAT, Vol. 30 (1995) p. 73
[12] K.-U. Riemann, J. Phys. D: Applied Physics 24 (1991) 493-518
[13] W. Eckstein, Report IPP 9/117, Garching, March 1998
[14] K. Borrass, D. Coster, R. Schneider, Controlled Fusion and Plasma Physics (Proc. 25th Eur. Conf., Berchtesgaden, 1997), Vol. 21A, Part IV, European Physical Society, Geneva (1997) 1461

Drift effects in W7-AS limiter and island divertor configurations

Y.Feng, **F.Sardei**, P.Grigull, G.Herre and W7-AS Team

Max-Planck-Institut für Plasmaphysik, EURATOM Ass.
D-85748 Garching, Germany

Abstract

Typical B-direction dependent asymmetries observed in the limiter and island SOL of W7-AS low-density ECRH discharges are shortly reviewed and explained in terms of classical drifts. While grad-B drifts are responsible for the up/down asymmetries of the limiter load, **ExB** drifts associated with temperature inhomogeneities in the plasma give rise to asymmetric plasma distributions in the limiter and island SOL. After a careful analysis of the transport implications of these drifts, simple 1D and 2D models have been defined, which reproduce consistently the experimental observations. The main results are confirmed by more rigorous treatment based on the 3D Monte Carlo transport code EMC3.

1. Introduction

For low density, low recycling ECRH discharges in W7-AS, B-direction dependent asymmetries of the plasma distribution in the SOL and of the power deposition and particle fluxes on the target plates have been observed for both limiter ($\iota < 0.4$) and island divertor ($\iota \geq 0.5$) configurations [1-3]. In both cases the asymmetries can be explained by classical drift effects.

In tokamaks, classical drifts have been shown to also affect the asymmetries of power and particle fluxes between the inner and outer divertor branches [4]. In particular, the ExB drift contributions to the cross-field particle transport can be of the same order of magnitude as that of the anomalous particle transport and of the poloidal component of the parallel transport, as estimated by Chankin for a typical tokamak scrape-off layer (SOL) [5]. Therefore, these terms have been included recently in several 2D edge transport codes in addition to the usual anomalous terms [6-8].

Classical particle drifts can be expressed either in guiding centre or fluid approximation [5,9]. In the fluid approximation, which is commonly used in the edge transport codes, the

classical cross-field particle flux density, which includes all relevant drifts, can be written in the form [10]

$$n\vec{V}_{\perp} = \frac{n}{B^2}\vec{E}\times\vec{B} + \nabla\times\left(-\frac{p_{i\perp}\vec{B}}{eB^2}\right) + \frac{p_{i\perp}\vec{B}}{eB^3}\vec{B}\cdot\nabla\times\frac{\vec{B}}{B}$$
$$+\frac{p_{i\perp}}{eB^3}\vec{B}\times\nabla B + \frac{p_{i\parallel} + mnV_{\parallel}^2}{eB^3}\vec{B}\times\left(\vec{B}\cdot\nabla\frac{\vec{B}}{B}\right) \qquad (1)$$

to first order in r_λ/L, with r_λ the Larmor radius and L the relevant gradient scale length. The first term on the r.h.s is the **ExB** drift, the second term is the magnetisation flux associated with Larmor rotation, the third term makes a small correction to the parallel guiding centre flux and is exactly compensated by the parallel component of the magnetisation flux. The last two terms describe the almost vertical drifts associated with the spatial variation of the magnetic field, namely the grad-B and curvature drifts. Being the curl of a vector, the magnetisation flux is divergence-free and thus drops out of particle transport equation. A similar expression can be written for the perpendicular momentum and energy fluxes. They also contain corresponding divergence-free magnetisation flux terms which drop out of the momentum and energy transport equations [10]. Thus the magnetisation fluxes do not lead to a redistribution of the plasma parameters nor to any asymmetry of particle and power deposition to the plates, as they do not carry fluxes to the material surfaces [11]. This is also supported by 2D particle kinetic simulations [12]. Therefore, the analysis can be restricted to the electric and vertical drifts. They mainly arise, respectively, from radial and poloidal temperature inhomogeneities and from the 1/R dependence of the main field.

2. Limiter configurations

2.1. Limiter SOL geometry

For W7-AS low ι (<0.4) configurations, smooth, resonant-free magnetic flux surfaces extend deeply into the SOL of two up/down symmetric rail limiters [Fig. 1(a)]. The two limiters are positioned up/down symmetrically at two neighbouring „elliptical" planes of symmetry and their aperture can be changed by shifting them vertically with respect to each other. For $\iota \approx 1/3$ and small limiter aperture, the SOL is governed by large flux bundles with connection lengths of 1, 2 and 3 toroidal transits [Fig. 1(b)]. They originate, in the first two cases, from the mapping of the limiters onto each other, in the third case from the mapping of

each limiter onto itself. The poloidal sequence of flux tubes with different connection lengths introduces a poloidal distribution of the plasma parameters in the SOL.

2.2. Up/down asymmetries

For low density, low recycling ECRH hydrogen plasma with small limiter aperture ($\langle n_e \rangle_{line} = 5\times10^{18}\ m^{-3}$, $Z_{lim} = 21.5$ cm), asymmetric and B-direction dependent power loads on the up/down limiters were typically found from calorimetric measurements. The observed ±20-30% up/down asymmetry is consistent with a parallel momentum imbalance driven by classical vertical particle drifts and can be estimated by a simple 1D parallel transport model. The ion vertical drift arising from the 1/R dependence of the toroidal field component is

$$n\vec{V}_d = \pm\frac{2p_i(1+M^2)}{eBR}\vec{z}^0 \qquad (2),$$

where M is the Mach number, $p_i = p_{i\perp} \approx p_{i\parallel}$ and ± indicates the B-field direction.

For the given plasma parameters, the parallel temperature drop in the SOL is negligible. Poloidal diffusion of particles and momentum is also negligible, owing to the large ratio of poloidal to radial scale lengths for a limiter SOL. Radial loss of parallel momentum by viscosity and radial diffusion is also ignored, as it gives no up/down contributions. Assuming, for simplicity, a circular cross section, the parallel particle and momentum transport equations for the SOL region read [3]

$$\frac{\Theta}{r_a}\frac{\partial}{\partial\theta}nV_{II} = S - \nabla_r \cdot n\vec{V}_d \qquad (3),$$

$$\frac{\Theta}{r_a}\frac{\partial}{\partial\theta}p(1+M^2) = -\nabla_r \cdot mnV_{II}\vec{V}_d \qquad (4),$$

with θ the poloidal direction, Θ the pitch of B, r_a the radius of the last closed magnetic surface, S the particle source in the SOL due to radial diffusion from the main plasma and $p = 2p_e = 2p_i$. The radial gradients are represented by the respective gradient lengths, namely $1/\lambda_p$ for eq. (3) and $1/\Delta_m$ for eq. (4). Considering the case of a vertical drift directed upwards, substituting eq. (2) into eqs. (3) and (4) and integrating from the midplane to the lower limiter, we get for the relative momentum loss of ions, δ, as defined by

$$\frac{2p_{t,lower}}{p_0} = \frac{1}{1+\delta} \qquad (5),$$

the relation

$$\delta = \frac{1.5}{2}\frac{mC}{eB_\iota \Delta_m}(\alpha + \frac{2T}{eB_\iota \lambda_p C}) \qquad (6),$$

where C is the sound speed and $\alpha = 0.82$ or 0.64 depending on whether the analysis refers to flux tubes mapping each limiter onto itself or mapping the two limiters onto each other. Assuming $\Delta_m = \lambda_p = 1$ cm, we get for the given plasma parameters $\delta = 0.29$ and 0.23 for the two flux tubes. This momentum loss for the ions flowing to the lower limiter is due to a vertical drift directed radially inwards, i.e. into the confined region. No loss occurs for the ions flowing to the upper limiter, as they drift radially outwards, i.e. into the open field line region contacting the limiters. That is, the pressure at the upper limiter is $p_{t,upper} = p_0/2$. Neglecting parallel temperature gradients in the SOL, we then get for the power asymmetry $P_{load,upper}/P_{load,lower} = p_{t,upper}/p_{t,lower} = 1+\delta$. This momentum imbalance is reversed if the B field is reversed.

2.3. Asymmetries of the radial density profiles

Additionally to the vertical drift discussed in the previous section, poloidal and radial **ExB** drifts arise in the limiter configuration shown in Fig. 1. The poloidal modulation of connection lengths shown in Fig. 1(b) implies a poloidal modulation of the radial decay lengths ($\lambda \propto L_c^{1/2}$) and hence of the radial plasma density and temperature profiles. Density profiles from low-density discharges, obtained from a Langmuir probe placed on the midplane at a triangular cross section [Fig. 1(b)], are shown in Fig. 2(a) for positive and negative B. In the absence of plasma, the probe intersects the boundary between flux tubes of longer and shorter connection lengths [Fig. 1(b)]. A poloidal **ExB** drift arising from the radial temperature gradients tends to shift this boundary in positive or negative poloidal direction. Depending on the sign of B, flux tubes of longer or shorter L_c, i.e. of broader or steeper density profiles, are then „seen" by the probe [Fig. 2(a)]. This effect has been reproduced by a 2D radial/poloidal model for particle and energy transport including the poloidal drift [3]:

$$\nabla_\perp(-D\nabla_\perp n + nV_{E_r xB}) = S - \frac{nC}{L_c} \qquad (7),$$

$$\nabla_\perp\{-(\chi_i + \chi_e)n\nabla_\perp T - 5TD\nabla_\perp n + 3nTV_{E_r xB}\} = -\frac{\gamma nTC}{L_c} \qquad (8),$$

where L_c is the 2D distribution of connection lengths, $T = T_i = T_e$, $\chi = \chi_i + \chi_e$ ($\chi_i = \chi_e = 3D$, $D = 1 m^2/s$).

At the poloidal probe position, the calculations reproduce the change in the slope, i.e. in the decay length of the density profiles in the region from r_{eff} = 14 to 17 cm, as measured by the probe [Fig. 2(b)]. Fig. 3 compares the density contours for positive and negative B calculated with this model in the relevant SOL region over the full poloidal angle. The plots clearly show the $\mathbf{E}_r$x**B** driven poloidal phase shift of the radial density profiles corresponding to the flux tubes with L_c = 1, 2 and 3 toroidal transits. Similar results have been obtained with more sophisticated 3D Monte Carlo transport simulations including the poloidal drift [1]. The profile variations in the outside SOL regions (r_{eff} > 17), however, cannot be explained by a poloidal **ExB** drift. Here, radial **ExB** drifts resulting from the poloidal temperature modulation must be taken into account [13]. They lead to radially inward or outward drift flows depending on the magnetic field direction. These drifts modify the shape of the density profiles consistently with the probe data [3].

3. Island divertor configurations

3.1. Island SOL geometry

At $\iota \geq 0.5$, the boundary of W7-AS is governed by intrinsic magnetic islands of considerable size, which define the topology of the island divertor [14]. The ι = 5/9 edge configuration, represented by a poloidal chain of 9 islands, has been chosen for standard divertor operation, as it offers the best compromise between large plasma and large island size and has the appropriate internal rotational transform. The present target arrangement consists of 10 inboard target plates placed symmetrically on both sides of the triangular cross section. Each plate intersects two islands at a variable radial position which can be changed by ι and a vertical magnetic field. In the cases analysed here, the islands are cut through the O-point (Fig. 4).

3.2. Poloidal asymmetries

The discharges investigated are at very low density, $\langle n_e \rangle_{line} < 10^{19}$ m^{-3}, and ECR heating power of about 200 kW. Fig. 4 compares the poloidal profiles of power deposition and particle outflux along the target plate from calorimetric and H_α measurements for positive and negative B. The profiles generally peak at the island (a), reflecting the larger connection length at this position. Here, the highest particle flux is found in the left SOL fan (contacting tile 1) of

the island for positive B, in the right one (tile 2) for negative B. A similar behaviour is observed for the power deposition.

A corresponding B-dependent asymmetry is found for the density contours of a 2D Langmuir probe array located at the inboard side of the triangular cross section [Fig. 5(a)]. The contour lines [Fig. 5(b)] reproduce correctly the poloidal structure of the vacuum island chain, but not its up/down symmetry [Fig. 5(a)]. After reversing the field direction, the observed asymmetry is reversed as well. This effect can be explained by a poloidal ExB drift inside the islands as follows. For the low density conditions of the analysed discharges, ionisation mainly occurs in the main plasma. The recycled particles diffuse outwards into the islands, where they experience a poloidal electric drift in addition to the parallel motion along the island fans . The drift originates from the radial electric field associated with the radial temperature drop from the separatrix to the O-point: $E = 3(T_{sep}-T_{Op})/er_{isl}$, r_{isl} being the average island radius at the separatrix. (The islands are intersected and electrically linked by the plates.) A particle accumulation results in the upper or lower island fans, depending on the field direction. From 3D transport simulations with the EMC3 code [15,16], the temperature difference between the island fan and the island core is estimated to be about 20 eV, which leads to a poloidal drift of about 1.5 km/s.

In the following we show that this poloidal drift governs the particle transport in the islands. First of all, the almost vertical grad–B and curvature drifts have no relevance for asymmetries inside the islands, owing to the helical path of the islands around the torus. Furthermore, for a low density plasma the estimated total particle flow per toroidal unit length due to the poloidal drift, $(\Gamma_\theta)_{tot} \approx 3T_{e,down}n_e/eB$ [4], dominates over the flow due to the radial drift, $(\Gamma_r)_{tot} \approx (T_{e,up}-T_{e,down})n_e/eB$, because of the small poloidal variation of the temperature, $T_{e,up} \approx 90$ eV and $T_{e,down} \approx 60$ eV [2]. These are temperatures at the upstream and target positions, as estimated from EMC3 code simulations and Langmuir probe array data (downstream value). The impact of both drifts on the particle transport is stronger than in tokamak divertors for the same plasma parameters and major radius, due to the larger toroidal length of the X-line (poloidal periodicity of N=9 for W7-AS compared to 1 for single-null tokamaks). As for the diffusive particle transport, the time scale for the particles to reach the targets by drift motion is $\tau_{drift} = d_{pol}/V_{E_rxB} = 4.7\times10^{-5}$ s, which is much shorter than that by cross-field diffusion $\tau_{diff} = (\Delta r)^2/(2D) = 8\times10^{-4}$ s, with $d_{pol} = 7$ cm, $\Delta r = 4$ cm and $D = 1$ m^2/s. Finally, the poloidal drift velocity is also substantially larger than the poloidal component of the parallel velocity, owing to the very small pitch of the magnetic field in the island reference frame ($\sin\theta_i \approx 0.001$). In fact, for a hydrogen sound speed consistent with

$T \equiv T_i = T_e = 60$ eV, we get $C_t \sin\theta_i = 100$ m/s, which is more than an order of magnitude smaller than the estimated drift velocity. For the same reason, the drift energy flux dominates over the parallel convection energy flux. Therefore, the particle and energy transports are decoupled from the parallel momentum transport.

Based on these considerations, a simple 1D poloidal fluid transport model for particles ($\mathbf{E}_r x\mathbf{B}$ drift) and heat ($\mathbf{E}_r x\mathbf{B}$ drift and parallel heat conduction) has been defined [2]:

$$\frac{d}{dy}(nV_{E_r xB}) = \{\ S_p;\quad 0;\quad -\frac{nC_t}{L_c} - D\frac{n}{\Delta_r \lambda_n}\ \} \qquad (9),$$

$$\frac{d}{dy}(-\Theta^2 \kappa T^{\frac{5}{2}} \frac{dT}{dy} + 3nTV_{E_r xB}) = (\ S_e;\quad 0;\quad -\frac{\gamma nTC_t}{L_c} - D\frac{5nT}{\Delta_r \lambda_n} - \chi\frac{nT}{\Delta_r \lambda_T}\ \} \qquad (10),$$

where the first terms on the r.h.s of the equations represent the particle and energy diffusion sources from the main plasma into the SOL, the second terms the negligible losses in the region from the X-point to the target boundary, and the third terms the losses to the plates and to the private region.

The resulting enhancement (for positive B) and reduction (for negative B) factor of the density over the region covering the poloidal depth of the plate region is about a factor of two, which is in good agreement with the asymmetry of the probe array data. For the temperature, on the other hand, the calculated asymmetry is less than 30%, which is also consistent with the probe array measurements and reflects the predominance of the parallel conduction over the drift-convection for the considered low-density plasma. The asymmetry of the calculated power fluxes between the upper and lower island fans of the lower island is about a factor of 2.4, which is stronger than the measured asymmetry of the power load on the plate at the corresponding strike points (about 50%, see Fig. 4). This discrepancy is due both to the poor calorimetric resolution of the relatively large tiles and to the missing power load hitting the plates from the private region, which has not been accounted for by the 1D model. The described asymmetry of the poloidal densities and its inversion with reversed B direction is confirmed quantitatively by the poloidal phase shift of the density distribution obtained from a more rigorous 3D simulation with the EMC3 code after including the estimated poloidal drift velocity [2]. The shift (shaded picture in Fig. 5(b)) is in excellent agreement with that of the density from the Langmuir probe array data (contour lines in Fig. 5(b)).

A problem in particle control may arise from discontinuous target plates in the presence of a strong poloidal particle drift. In fact, if the particle transport is dominated by the poloidal drift and if the toroidal extension of the plates is small, which is the case for the low-density discharges presented here, a significant fraction of the particle flux can drift poloidally outwards

in the toroidal regions between the plates. This may be crucial if these drifting particles diffuse into open field lines (like those in the private region or in open island structures). A careful optimisation of the plate design would be necessary if the problem persists for divertor-relevant high density conditions. On the other hand, higher densities imply lower downstream temperatures, which should reduce, according to simple estimates, the average radial electric field and thus the poloidal **ExB** drift in favour of the radial **ExB** drift. However, for large parallel temperature gradients and high recycling inside the islands, the electric field becomes fully 3D in the presence of discontinuous target plates. This makes its determination a non-trivial task both experimentally and numerically. Langmuir probe array data for high density conditions do not indicate sharply outlined poloidal asymmetries of the density contours nor simple reversal of the asymmetries with reversed field direction. Therefore, a definitive assessment of the classical drift effects on plasma transport for divertor-relevant conditions is not possible on the basis of the data available sofar.

4. Conclusions

Classical grad-B and **ExB** drifts have been shown to significantly perturb the symmetry of up/down limiter power loads and plasma density distributions in limiter and island divertor configurations for low density, high temperature ECRH discharges in W7-AS. For these plasma conditions, the poloidal **ExB** drift arising from radial temperature gradients inside the islands dominates not only over the radial **ExB** drift, but also over the poloidal component of the parallel motion, which no longer determines the particle transport. A parallel particle mapping onto the target plates becomes questionable in this case. The effects of the vertical and electric drifts on the plasma transport in both limiter and island configurations can be described with sufficient accuracy by relatively simple 1D and 2D models, and are confirmed by more rigorous 3D code simulations. For divertor-relevant high density conditions, lower target temperatures should reduce the magnitude of the poloidal electric drift, but parallel temperature gradients will lead to inhomogeneous poloidal and toroidal distribution of the radial electric field. A 3D resolving diagnostic of the plasma parameters will be needed for divertor-relevant plasma conditions to reliably estimate the impact of the electric drifts on the power exhaust and particle control in W7-AS and W7-X. A selfconsistent 3D treatment of the drifts will also be needed, which is beyond the present capability of the EMC3 code.

References

[1] Y. Feng et al., Proc. 22nd EPS Bournemouth, UK, Vol. 19C (1995) p. 325.

[2] Y. Feng et al., Plasma Phys. Control. Fusion 40 (1998) 371.

[3] Y. Feng et al., Contr. Plasma Phys. 38 (1998) 195.

[4] A. V. Chankin et al., Plasma Phys. Control. Fusion 36 (1994) 1853.

[5] A. V. Chankin, J. Nucl. Mater. 241-243 (1997) 199.

[6] T.D. Rognlien et al., J. Nucl. Mater. 196-198 (1992) 347.

[7] M.Baelmans et al., J. Nucl. Mater. 220-222 (1995) 982.

[8] G.J. Radford et al., Contr. Plasma Phys. 36 (1996) 187.

[9] S. I. Braginskii, Reviews of Plasma Physics, Vol. 1, ed. by M.A. Leontovich, Consultants Bureau, New York (1965) p.205.

[10] G.J. Radford et al., Contr. Plasma Phys. 36 (1996) 187.

[11] A. V. Chankin and P. C. Stangeby, Plasma Phys. Control. Fusion, 36 (1994) 1485.

[12] A. Bergmann and R. Chodura, Contr. Plasma Phys. 36 (1996) 220.

[13] F. Sardei et al., J. Nucl. Mater. 220-222 (1995) 736.

[14] F. Sardei et al., J. Nucl. Mater. 241-243 (1997) 135.

[15] Y. Feng et al., J. Nucl. Mater. 241-243 (1997) 930.

[16] Y. Feng et al., this conference

Figure captions

Fig. 1. (a) Two up/down symmetric rail limiters positioned at two neighbouring elliptical planes deeply cut the smooth flux surfaces of the $\iota \approx 1/3$ configuration.

(b) Connection length distribution in the limiter SOL at a triangular plane. A Langmuir probe is placed horizontally at the outboard side of the configuration.

Fig. 2. (a) Field reversal effects (shoulder) on the density profiles from Langmuir probe data.

(b) 2D simulation results. The shaded region is the radial transition zone between $L_c = 1$ and 3 toroidal transits.

Fig. 3. Radial/poloidal density contours in the SOL for ±B, showing poloidal modulations due to $L_c = 1,2,3$ toroidal transits.

Fig. 4. (Top): Calorimetric and H_α profiles along the target plate for two discharges with ±B.

(Bottom): Poloidal cross-section of the $\iota = 5/9$ configuration at the toroidal position of a target plate.

Fig. 5. (a) Moveable Langmuir probe array consisting of 16 probes placed on the inboard side of a triangular cross-section and shaped as to follow the magnetic edge structure.

(b) Density contour lines from the probe array compared to calculated distributions (shaded areas) from the EMC3 code for ±B.

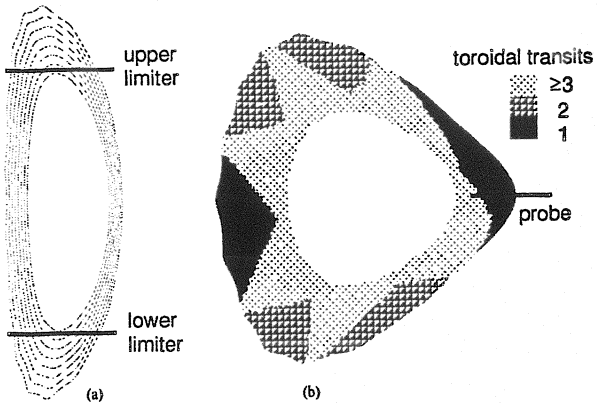
upper
limiter
lower
limiter
(a)
toroidal transits
≥3
2
1
probe
(b)

Fig. 1

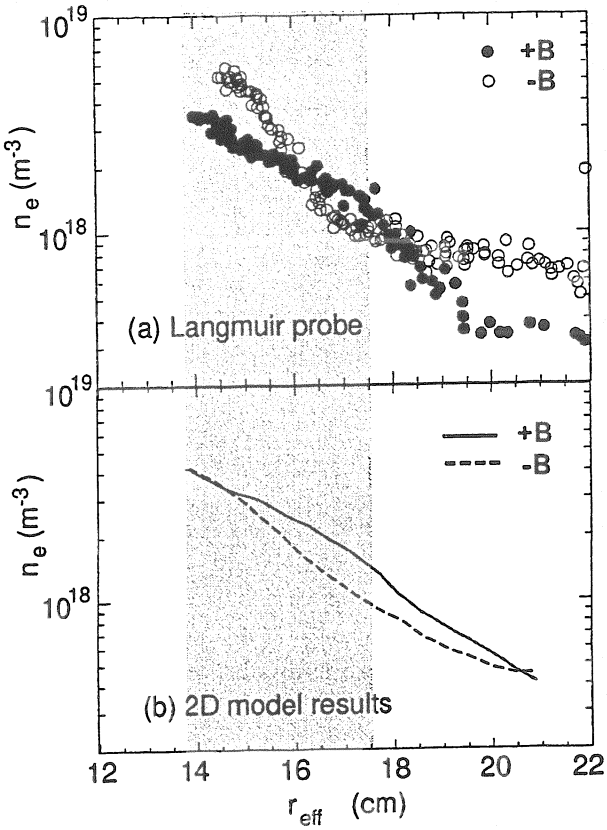
10^{19}
10^{18}
n_e (m^{-3})
+B
-B
(a) Langmuir probe
10^{19}
10^{18}
n_e (m^{-3})
+B
-B
(b) 2D model results
12
14
16
18
20
22
r_{eff} (cm)

Fig. 2

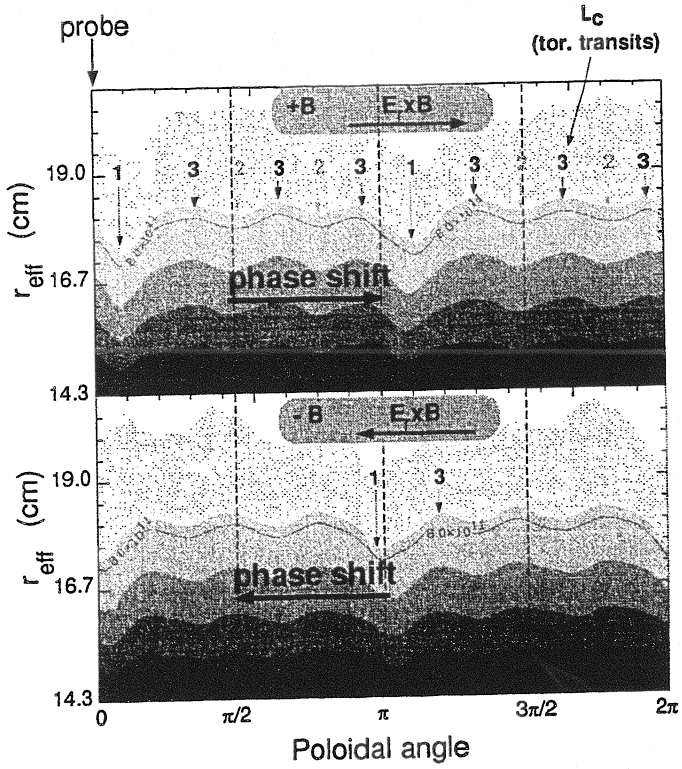
probe
L_c
(tor. transits)
+B
E x B
19.0
16.7
14.3
r_{eff} (cm)
1
3
2
phase shift
-B
E x B
19.0
16.7
14.3
r_{eff} (cm)
1
3
phase shift
0
π/2
π
3π/2
2π
Poloidal angle

Fig. 3

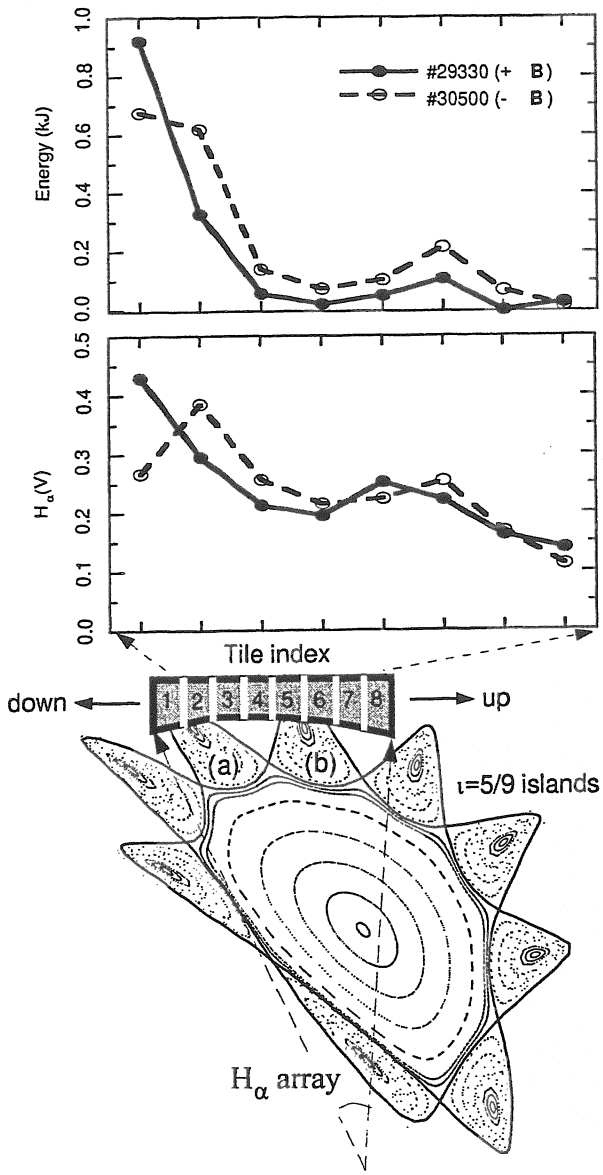
Energy (kJ)
1.0
0.8
0.6
0.4
0.2
0.0
#29330 (+ B)
#30500 (- B)
H_α(V)
0.5
0.4
0.3
0.2
0.1
0.0
Tile index
down
up
1
2
3
4
5
6
7
8
(a)
(b)
ι=5/9 islands
H_α array

Fig. 4

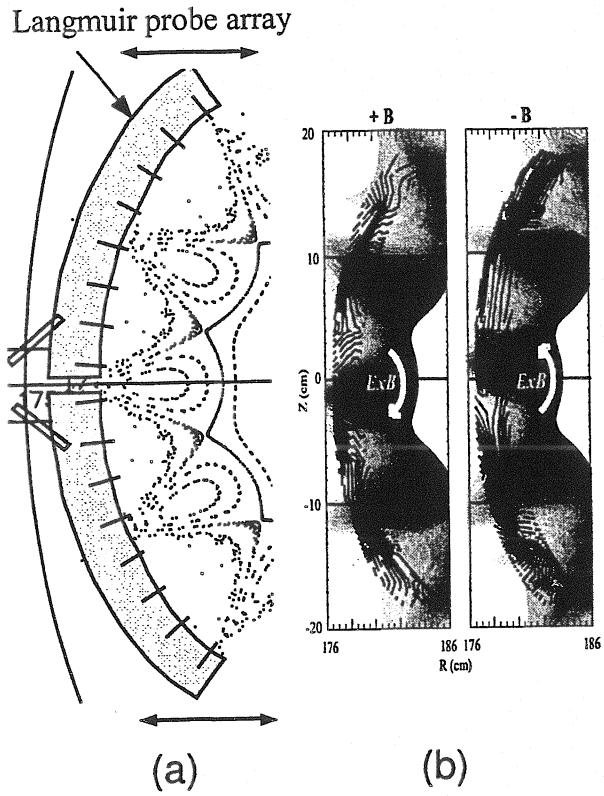
Langmuir probe array
+B
-B
20
10
0
-10
-20
Z (cm)
ExB
ExB
176
186
176
186
R (cm)
(a)
(b)

Fig. 5

EPS Proj

Spectroscopic measurement of the non-thermal electron-root feature in W7-AS

J. Baldzuhn, W7-AS Team
Max-Planck-Institut für Plasmaphysik, EURATOM-Association
85748 Garching, Germany

Introduction

In the advanced stellarator W7-AS [1], the radial electric field E_r [2] is measured by active charge exchange recombination spectroscopy (CXRS) [3] on He III: radial profiles of the poloidal and toroidal rotation velocity, the ion temperature and the helium density are determined after CX in a modulated diagnostic beam [4]. Then the radial force balance equation is solved with these measured data, providing radial profiles of E_r. In parallel, neoclassical DKES (Drift kinetic equation solver) transport code calculations [5] are performed, taking into account the W7-AS magnetic field geometry [6]. DKES provides, among other things, the neoclassical transport matrix as a function of the minor plasma radius, the collisionality and E_r. The ambipolarity condition of the particle fluxes is then solved to determine the neoclassical radial electric field. The measured and calculated E_r are compared [7]. In general, consistency is found.

The total number of possible solutions for the ambipolarity condition, the so-called roots, is always odd. At W7-AS, for most discharges the ion-root is predicted by DKES and measured by CXRS, showing strong negative E_r in the gradient region and small negative or slightly positive values near the plasma center. The strongly positive electron-root is predicted by DKES for the close vicinity to the magnetic axis. However, only in a few cases with particular discharge conditions those positive E_r could be observed experimentally. Most important, outward drifts of trapped suprathermal electrons are assumed to be decisive for the ambipolarity condition, rather than thermal electron fluxes [8].

The ECRH driven electron-root at 140 GHz

Strong positive E_r , as described before, are observed in W7-AS for 140 GHz ECRH second harmonic X-mode discharges at 2.5 T with perfectly located on-axis deposition. Up to + 600 V/cm are measured by CXRS close to the magnetic axis at minor radii $r < 5$ cm. An example for such a discharge with an ECRH power of 760 kW at low density is shown in figure 1 below. The high central electron temperatures T_e (upper left) result from the strong positive E_r (lower left) reducing the central electron heat diffusivity χ_e (lower right). This is confirmed by the steepened ∇T_e ($r \approx 3$ cm). The experimental heat balance analysis (dot-dashed) comes much closer to the neoclassical calculation for the ambipolar E_r (crosses) than to the calculation for $E_r = 0$ (points), supporting the existence of the strongly positive E_r. However,

the χ_e agreement near the plasma center is not very good, possibly indicating that the neoclassical DKES results are not valid for such strong E_r and high rotation velocities. For higher ECRH power (up to 1.25 MW), the electron-root is maintained even for higher electron densities $n_e(0)$ up to $\approx 7 \cdot 10^{19}$ m^{-3}. For low $n_e(0) \approx 2 \cdot 10^{19}$ m^{-3}, central $T_e(0)$ up to ≈ 6 keV are achieved.

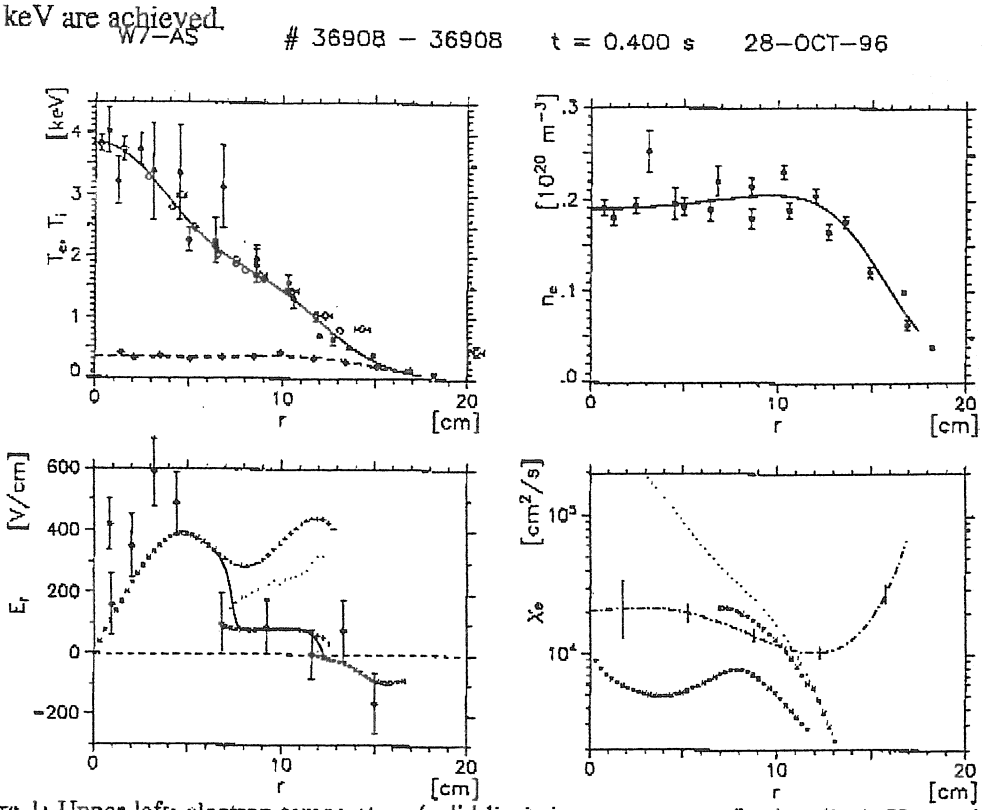

Figure 1: Upper left: electron temperature (solid line), ion temperature (broken line). Upper right: electron density. Lower left: radial electric field (dots: CXRS, crosses and points: neoclassical calculation). Lower right: electron heat balance (dot-dashed: experimental, crosses and points: neoclassical calculation).

For r > 6 cm, the neoclassical ion-root with small E_r is predicted by DKES (lower left, crosses) and measured by CXRS (lower left, dots). For r < 5 cm, CXRS measures positive E_r which is consistent to the neoclassical electron-root solution, calculated by DKES. From Monte-Carlo simulations [9], however, it is found that the radial electron fluxes being decisive for the ambipolarity condition in this case result from outward drifting suprathermal trapped electrons, created by the highly localized ECRH in the local magnetic field minimum in the ECRH launching plane. Hence the strongly positive E_r can be driven by that 'convective' contribution, rather than by thermal fluxes alone (as assumed by DKES). This is supported by the fact that the strongly positive E_r can be removed experimentally by removing this local magnetic field minimum, thus reducing the population of trapped suprathermal electrons (an effect which is not predicted by DKES). For this case the suprathermal tail is still predicted by the simulations, but with reduced radial fluxes. For slightly off-axis ECRH power deposition, electron cyclotron emission ECE measurements reveal rapid spontaneous transitions of the central T_e (on a timescale ≈ 300 µs), possibly indicating a bifurcation mechanism [11] (which can also not be explained by assuming thermal electron fluxes alone).

This behavior might be comparable to findings in the CHS heliotron [12]. Other experimental indications for the importance of the ECRH driven electron fluxes come from heating power scans, density scans and variations of the ECRH power deposition zone, revealing a threshold behavior for the appearance of the 140 GHZ electron-root. Finally, the ECE measurements reveal two different time scales for the T_e decay directly after switching the ECRH power off [8]: in radial regions with the strongly positive E_r a rapid decay (during less than 1 ms due to the instantaneously missing suprathermal fluxes, hence collapsing positive E_r accompanied by an instantaneously increasing χ_e) is followed by a slower decrease on a time scale comparable to the radial region outside the electron-root .

The thermally driven electron-root with 70 GHz?

Up to now, the thermal electron-root could not be realized free from any doubt experimentally. This is in contradiction to DKES calculations, which predict the appearance of the electron-root for low density ECRH discharges from the thermal fluxes only. To come closer to a situation where the thermal electron fluxes are more decisive for the ambipolarity condition, low density discharges with 70 GHz O-mode at 2.5 T with 370 kW are performed. They have reduced suprathermal electron fluxes roughly by a factor of two in comparison to 140 GHz [9] and, hence, higher significance of thermal fluxes.

High helium concentrations (about 30%) are maintained to provide a good signal-to-noise ratio for CXRS. During magnetic field scans the ECRH power deposition zone is shifted across the magnetic axis. The T_e profiles are monitored by ECE during these scans to control for the power deposition. For perfect on-axis deposition, the ∇T_e as well as $T_e(0)$ are maximum, providing the best chances for the formation of the electron-root. During these scans, T_i , E_r and the density of He III (in arb. units) are measured by CXRS. For the electron-root, increased $T_i(0)$ is expected because of the reduced χ_i as a consequence of the strong central E_r. It is still subject to investigations, why this effect cannot be observed for the 140 GHz electron-root. In parallel, the impurity density profiles are expected to become hollow as result of the outward convection due to their high Z (an effect which has already been demonstrated on He^{++} experimentally with the positive ion-root in W7-AS [10], for the 140 GHz electron-root as shown before, and which is also predicted by DKES calculations). As we perform CXRS on He III, we use that ion species to monitor the entire He III density profile. VUV measurements, radially resolved soft-X after ablation of Al and C, as well as bolometry are used additionally to detect the expected outward convection.

Figure 2 shows some results of the B scans. Perfect on-axis deposition is sustained for B ≈ 2.55 T, as supported by ECE. Maximum $T_e(0) \approx 3.5$ keV are obtained, slightly less than for the 140 GHz electron-root. A strong positive E_r (r = 1.6 cm) is observed by CXRS up to +550 V/cm at 2.55 T (middle), $E_r \approx 0$ V/cm is found for off-axis deposition. As expected, T_i (r = 1.6 cm) increases considerably (left) for on-axis, measured by CXRS as well as by CX

neutral particle energy analysis. The He III density profile (right) becomes clearly hollow for on-axis deposition (increased inv. peaking factor), an effect which disappears for off-axis. Unfortunately, these findings are restricted to an extremely narrow zone very close the the magnetic axis, within a minor radius r ≈ 1-3 cm. It is assumed that this is the reason why the VUV and soft-X measurements fail in supporting the outward convection for impurities. The spatial resolution for CXRS is restricted to about ± 1 cm. Also the radially resolved heat balance analysis, as performed for the 140 GHz electron-root, is impossible for this case because only one or two measurement points are within the interval with positive E_r. Increasing the heating power further to expand the radial zone is impossible because the 370 kW used for the scans are the maximum for the 70 GHZ gyrotrons available at W7-AS. Reducing the electron density further to enhance the observed effects is not possible because of the wall recycling fluxes, and because a minimum He density has to be maintained to allow for the CXRS measurements with a reasonable signal-to-noise ratio. The fast central T_e decay after switching the ECRH off and the spontaneous central T_e transitions for slight off-axis ECRH deposition, as described for the 140 GHz electron-root, are found for the 70 GHz discharges, too.

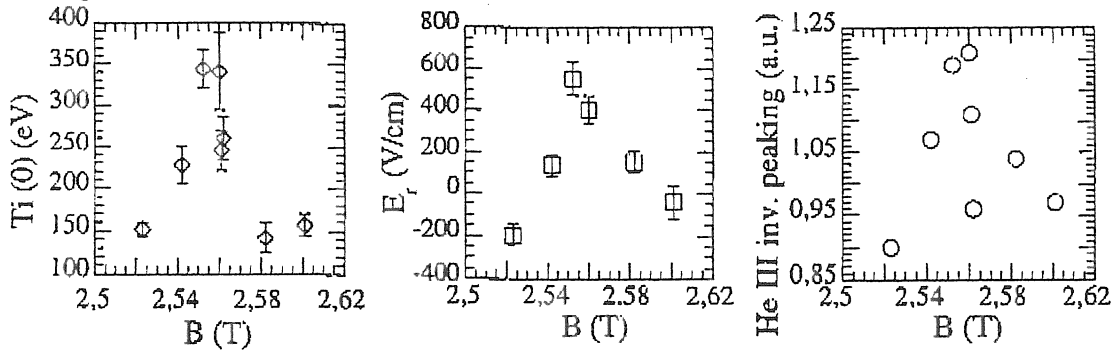

Fig. 2: Left: central ion temperature, middle: central radial electric field, right: inverse density profile peaking factor for He III. All versus the magnetic field strength measured at r= 1.6 cm.

References

[1] J. Sapper, H. Renner (1990) *Fusion Technol.* **17** , 62
[2] K. Itoh, S. Itoh (1996) *Plasma Phys. Control. Fusion* **38** , 1
[3] R.C. Isler (1994) *Plasma Phys. Control. Fusion* **36** , 171
[4] J. Baldzuhn, W. Ohlendorf (1997) *Rev. Sci. Instr.* **68** , 1020
[5] W.I. van Rij, S.P. Hirshman (1989) *Phys. Fluids B* **1** , 563
[6] H. Maassberg et al (1993) *Phys. Fluids B* **5** , 3627
[7] J. Baldzuhn, M. Kick, H. Maassberg, W7-AS Team (1998) *Plasma Phys. Control. Fusion* , accepted for publication
[8] H. Maassberg et al (1997) *Proc. 24th EPS Conf. Control. Fusion and Plasma Physics (Berchtesgaden)* vol. **21 A** , IV - 1605
[9] S. Murakami et al (1997) *Journal Plas. Fus. Res. Series* **1** ,*Proc. ITC-8 (Nagoya),* 122
[10] J. Baldzuhn et al (1997) *Proc. 24th EPS Conf. Control. Fusion and Plasma Physics (Berchtesgaden)* vol. **21 A** , IV - 1585
[11] M. Kick et al, invited topical paper, this conference
[12] A. Fujisawa et al (1997) *Phys. Rev. Lett.* **79** , 1054

Plasma edge turbulence: Comparison between theory and experiment

J. Bleuel, B. Scott, M. Endler, H. Niedermeyer, U. Pfeiffer, G. Theimer,
W7-AS Team
Max-Planck-Institut für Plasmaphysik, EURATOM Association, Garching, Germany

1. Introduction

The physics of plasma edge turbulence is very complex and all efforts towards a theoretical description rely on major simplifications. This implies the necessity to compare theoretical predictions and experimental observations in order to identify the most appropriate models.

While earlier investigations [1] focused mainly on the scaling behaviour of different fluctuation features like amplitudes and transport coefficients, the aim of this work is a detailed comparison of the structure, the statistical properties and the scales of these fluctuations in space and time. It is related to the investigation of electrostatic fluctuations by means of Langmuir-probe measurements in the SOL and the outer confinement zone of the Wendelstein 7-AS stellarator, which allowed a fully three-dimensional characterization of these fluctuations [2]. Within the last years, nonlinear simulation methods have been developed which can treat the saturated turbulent state represented by these fluctuations.

As no global simulation of a plasma discharge is feasible as yet, input parameters for these simulations must be taken from the experiments. These parameters are the local temperature and density, the temperature and density gradients and the radial fluxes of particles and energy.

By using spatially resolving Langmuir probe arrays for the simultaneous measurement of the fluctuating floating potential and ion saturation current in combination with a slowly swept Langmuir probe, all these input parameters could be directly measured or fairly well approximated.

2. The Model

The underlying model is a nonlinear electrostatic drift wave model, which describes the SOL plasma by taking the sheath dynamics at the target plates into account as parallel boundary conditions. By neglecting ion temperature effects and viscosity and assuming electrostatic fluctuations, a set of nonlinear equations can be derived, which describes the time evolution of the fluctuating quantities density, temperature and electrostatic potential on a twodimensional area perpendicular to the magnetic field. The model assumes zero parallel wavenumber. Two different numerical schemes have been applied to this set

of equations: The first one assumes the background gradients of density and temperature to be fixed in time (local model), while the second one allows for a self-consistent evolution of the plasma profiles together with the fluctuations (nonlocal model). The geometry of the machine is approximated by assuming the magnetic curvature to be constant along the magnetic field and that the connection length to the limiters is the same everywhere.

The experimental determination of the code's input parameters was realised by using a Langmuir probe array measuring both the fluctuating floating potential and ion saturation current simultaneously with high resolution in time and poloidal direction, and the average values of density and temperature by a slowly swept probe tip. The whole array was moved radially inwards during a stationary discharge phase in order to allow for a measurement of the plasma profiles. In case of the local model the determination of the local density and temperature and the gradients of density and temperature is sufficient, while for the nonlocal model the radial fluxes of particles and energy are needed instead of the gradients. The forementioned probe array allows the calculation of the radial particle flux from the simultaneous measurement of density and potential fluctuations if $E \times B$ drift is assumed as transport mechanism. For a direct calculation of the radial energy flux, temperature flucutation data would be necessary, which were not available for our investigations. However, it is known that temperature fluctuations are nearly in phase with the density fluctuations and that their relative amplitudes are also comparable [3]. Assuming temperature and density fluctuations to be in phase and of the same relative amplitude, one gets:

$$\mathbf{Q}_{rad} = 3kT\,\mathbf{\Gamma}_{rad} \quad , \tag{1}$$

if $\mathbf{\Gamma}_{rad}$ is the radial particle flux.

3. Results

At first glance, different fluctuation amplitudes in experiment and simulation results attract attention. In the local model, the amplitudes are by a factor of 3-5 larger than in the experiment. This occurs due to the assumption of fixed gradients of density and temperature made in this model. The nonlocal model gives much smaller amplitudes, by a factor of 2 smaller than in the experiment. This may be due to the assumption of a constant connection length to the target plates. In the experiment, the connection length varies with the radial position, resulting in steeper gradients of density and temperature than observed in the nonlocal simulations. Since the gradients are the major driving term, the lower fluctuation level is due to the simplification made by assuming a constant

connection length.

The structure of the fluctuations can be characterized by their correlation functions. Both the local and the nonlocal model can reproduce the poloidal structure of the fluctuations quite well (see Fig. 1). The poloidal velocity is made up of two parts: The fluctuations' poloidal velocity, which is in the electron drift direction, and the plasma rotation velocity due to radial electric fields, which is in the ion drift direction and typically overcompensates the fluctuations' propagation velocity. The local model neglects radial electric fields for numerical reasons and therefore its results can not be compared to the experimental results as far as poloidal velocities are concerned. The nonlocal model generates smaller radial electric fields than observed in the experiments because the temperature gradients generated in the simulations are smaller. Due to the sheath boundary condition at the target plates the radial electron temperature gradient largely determines the radial electric field in the SOL. If the different temperature gradients are taken into account, the poloidal velocity in experiment and nonlocal simulation is the same within the errors. Lifetime and poloidal size of the fluctuations show an agreement better than 30 %.

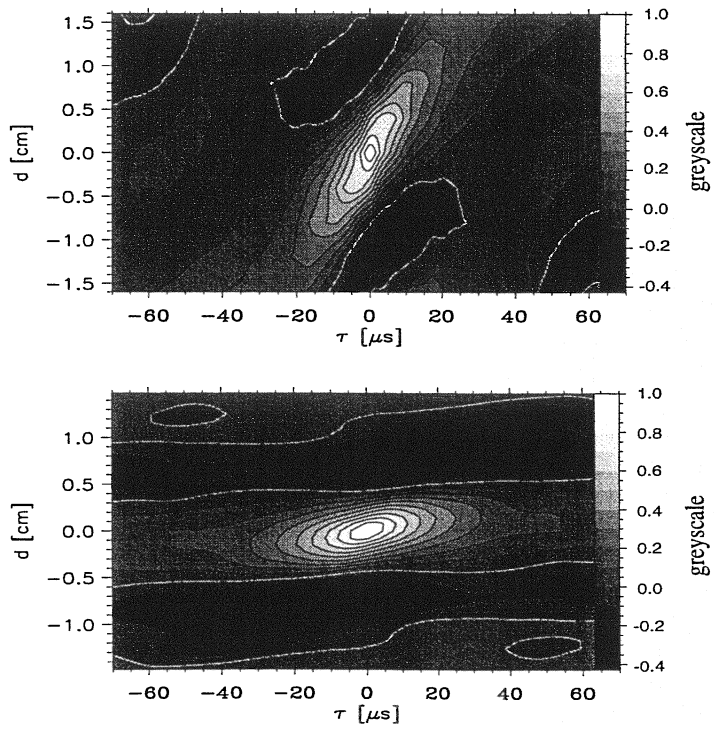

Figure 1: *Poloidal-temporal correlation function of floating potential fluctuations in the SOL of the Wendelstein 7-AS stellarator (top) and of simulated fluctuation data (nonlocal model, bottom).*

The two-dimensional structure of the fluctuations is qualitatively reproduced both by local and nonlocal models. In the radial direction, the neglect of magnetic shear is a critical issue. It may be the reason for the overestimation of the radial correlation length by a factor of two both in the local and the nonlocal model.
The floating potential fluctuations have a gaussian amplitude distribution function in all the experiments and numerical simulations. Despite of this, the ion saturation current distribution funtion observed depends on the radial density profile assumed. The assumption of constant gradients in the local model automatically leads to a gaussian distribution of the ion saturation current amplitudes. In the experiment and the nonlocal model the profiles are nearly exponential resulting in a non-gaussian distribution of ion saturation current amplitudes.
The simulated fluctuation spectra extend over a smaller frequency range than in the experiment. Investigations including ion temperature effects [4] showed much broader spectra, so that the neglect of them may be the reason for the difference observed here.

4. Conclusions

The results of nonlinear electrostatic drift wave simulations were compared to the observations of Langmuir probe arrays in the SOL of the Wendelstein 7-AS stellarator. While the basic structure of the fluctuations could be reproduced both by local and nonlocal models, only the nonlocal version of the code could reproduce the fluctuation amplitudes, the spectra (qualitatively) and the amplitude distribution functions correctly.
There are still differences between theory and experiment due to the simplifcations of these models: The radial scales are not described correctly since magnetic shear is not considered. There is also no radial propagation of fluctuations in the simulations while there is one in the experiments [2]. The width of the fluctuation spectrum is somewhat smaller in the simulations than in the experiments. This may be due to the neglect of ion temperature effects [4].

5. References

[1] P. C. Liewer, Nuclear Fusion 25 (5), p. 543, 1985
[2] J. Bleuel et. al., Proc. 24th EPS, volume 21A, part IV, p. 1613, Berchtesgaden 1997
[3] U. Pfeiffer et. al., Contrib. Plasma Phys. 38, p. 134, 1998
[4] B. D. Scott, Contrib. Plasma Phys. 38, p. 171, 1998

On the influence of rotational transform and magnetic shear on confinement in the W7-AS stellarator

R. Brakel, M. Anton, J. Chatenet, J. Geiger, T. Geist, H.-J. Hartfuß, M. Hirsch, G. Kühner, H. Maaßberg, U. Stroth, A. Weller, W7-AS Team, ECRH Group[1)]

Max-Planck-Institut für Plasmaphysik, EURATOM Association, Garching, Germany
[1)]*Institut für Plasmaforschung, Universität Stuttgart, Germany*

1. Introduction

Confinement in low shear stellarators is - at moderate β - known to be very sensitive to the boundary value ι_a of the rotational transform. Optimum confinement is established in narrow operation windows around low order major rationals ι_a =1/2, 1/3, etc. These regions are free from the otherwise densely spaced higher order rational ι-values [1]. In W7-AS, there is evidence that internal perturbations at such higher order rational flux surfaces cause confinement degradation by enhancing the anomalous electron energy transport. Their effect is reduced with increasing magnetic shear [2]. Although being very low in the vacuum field, magnetic shear is introduced at finite β by the intrinsic pressure driven (bootstrap, Pfirsch-Schlüter (PS)) and by externally (inductively, electron cyclotron resonance (ECR), neutral beam) driven currents.

Here, we compare experimental data from moderate density ECRH discharges in W7-AS with a simple transport model, which selfconsistently accounts for the mutual dependence of shear (from bootstrap and inductive current) and confinement by using an electron heat conductivity which depends on the magnetic shear and the location of rational ι-values.

2. The model

In the ECR heated discharges under consideration the electrons dominate the plasma confinement. The electron temperature profile $T_e(r)$ is calculated from a simplified power balance, which neglects convective and radiation losses as well as electron-ion coupling. Guided by experimental results [2], a dependence

$$\chi_e(r,\iota,\iota') = \chi_0(r) + \Sigma\, \chi_{nm}(\iota,\iota'),\ \ \chi_0 = \exp(\Sigma c_i (r/a)^i)\ \mathrm{m^2/s},\ \ \chi_{nm} = \alpha_{nm}\exp(\,-|\iota - n/m|/\delta\iota - \gamma|\iota'|$$

is assumed for the electron heat conductivity χ_e. χ_0 accounts for the transport at optimum confinement, the parameters c_i being adjusted to reproduce the experimental $T_e(r)$ in the absence of resonances. The neoclassical contribution to χ_e is included in χ_0. χ_{nm} describes an additional enhancement of χ_e near a rational value $\iota = n/m$ which is damped with increasing absolute value of the magnetic shear $\iota' = \mathrm{d}\iota/\mathrm{d}r$. a is the minor plasma radius; the parameters α_{nm}, $\delta\iota$, and γ have to be determined by comparison with experiments which vary $\iota(r)$.

The rotational transform profile $\iota(r)$ is calculated from the vacuum field and the toroidal bootstrap and inductive current densities, j_{OH} and j_{BS}. The PS current is neglected. For the bootstrap current density $j_{BS} = 0.7\, j_{BS}^{HH}$ is used, where j_{BS}^{HH} is the bootstrap current density in a circular tokamak [3]. The factor 0.7 adjusts the current to the value obtained with the DKES code [4] for optimum confinement (in the plateau regime a factor of 0.5 would be expected for a tokamak with the mean elongation of the W7-AS flux surfaces). The inductive current density profile is calculated from the tokamak neoclassical conductivity [3] and normalized such that bootstrap and inductive current balance to the given net plasma current I_p. Density and power deposition profiles, $n_e(r)$ and $P_{heat}(r)$, net plasma current and boundary value ι_a of the rotational transform are input to the model. For all conditions $Z_{eff} = 2$ and $T_e(a) = 100$ eV are used. $\iota(r)$ - and thus $\chi_{nm}(r)$ - and $T_e(r)$ are selfconsistently determined in an iteration procedure which starts with the optimum confinement profile for $T_e(r)$.

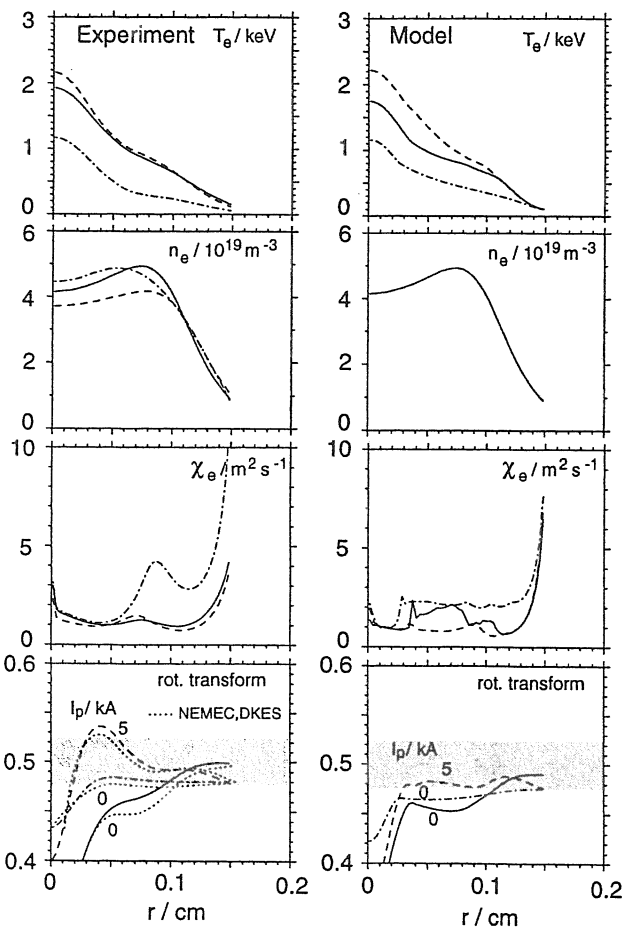

Fig. 1: Radial profiles of electron temperature, density and heat conductivity and profiles of the rotational transform for plasma currents of 0 and 5 kA and ι_a = 0.480 and 0.495. The shaded areas indicate the ι-range which is free from resonances with $m \leq 20$.
Left: experiment. Right: model.

3. Results

Experimentally, the dependence of confinement on the boundary value of the rotational transform and the net plasma current has been investigated in stationary discharges heated by 450 kW ECRH at central densities $n_e \approx 4 \times 10^{19}$ m^{-3} (B = 2.5 T, R = 2 m, a = 0.15 m, $\beta_0 \leq 0.6\%$, for details see [2]). In the model, rational values up to m = 20 and the following set of parameters have been used: $c_0 = -0.1$, $c_2 = -1.0$, $c_6 = 2.0$, $\delta\iota = 0.004$, $\gamma = 1.1$ m, and $\alpha_{nm} = 1.1\ g_{nm}^{-1}$ m^2/s. g_{nm} is the degeneracy of a n/m value, i.e. every rational number is counted only once.

Radial profiles are shown in Fig. 1 at selected values of ι_a and I_p which yield optimum and degraded confinement near ι_a = 1/2. At least at the outer radii, $r/a > 0.5$, the model reproduces the experimental profiles quite well. The T_e-profile flattens when $\iota(r)$ lies in the zone with densely spaced resonances, and becomes steep otherwise. A single density profile was used since the measured density profiles

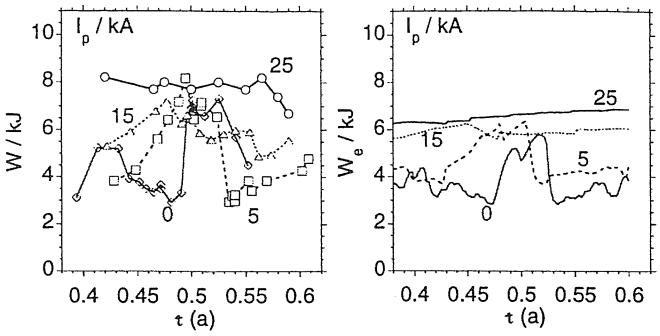

Fig. 2: Dependence of plasma energy (experiment, left) and electron kinetic energy (model, right) on the boundary value of the rotational transform for various plasma currents.

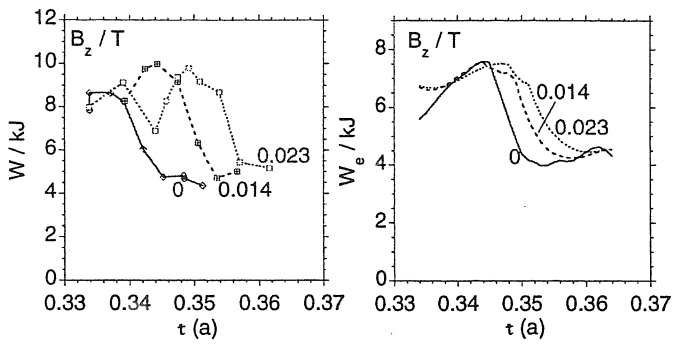

Fig. 3: Dependence of plasma energy (experiment, left) and electron kinetic energy (model, right) on the boundary value of the rotational transform for various values of the vertical magnetic field ($I_p = 0$).

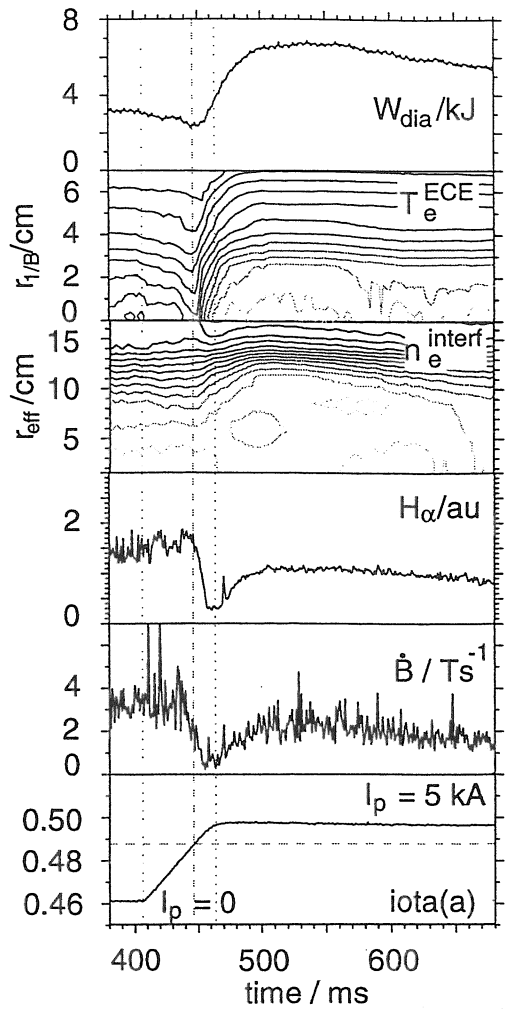

Fig. 4: Time traces of plasma energy, H_α light, magnetic fluctuations and boundary rotational transform, and time evolution of temperature (from ECE) and density (from interferometry) profiles during a transition from degraded to optimum confinement induced by a current ramp.

change only slightly (in the experiment the line averaged density was constant by feedback control). To calculate $\iota(r)$, the tokamak approximation has been used for j_{BS} and j_{OH} in both cases, experiment and model. ι-profiles calculated with j_{BS} and j_{OH} from the DKES code [4] and PS currents from the NEMEC code [5] are given for reference. The observed dependencies of global confinement are qualitatively reproduced for a wide range of ι_a and I_p by the model as well (Fig. 2).

The model can also account for details of confinement near $\iota_a = 1/3$ (Fig. 3, $a = 0.17$ m, $n_e \approx 8 \times 10^{19}$ m^{-3}). The shift of the optimum confinement zone to larger ι_a-values with a vertical magnetic field B_z arises at least partly from the positive shear which is introduced at the boundary by the vertical field. It has to be mentioned that these discharges have higher densities and some assumptions of the simple model may no longer be valid, e.g. the smallness of electron-ion coupling and PS currents.

Along with improved confinement, a reduction in the measured fluctuation level is observed when the rotational transform is moved into a resonance free region. Figure 4 shows a transition which is induced by a plasma current ramp from $I_p = 0$ to 5 kA. As soon as ι_a comes

into the resonance free region, confinement improves by a persistant steepening of the T_e-gradient, while the n_e-profile steepens transiently and then relaxes to its initial form. Comparing the stationary phases before and after the transition, the level of H_α light indicates improved particle confinement, which is compensated by a reduced gas puffing rate. The reduction of the fluctuation level is seen from the H_α light, microwave scattering and Mirnov probes. The frequency spectra of magnetic and density fluctuations narrow significantly (Fig. 5).

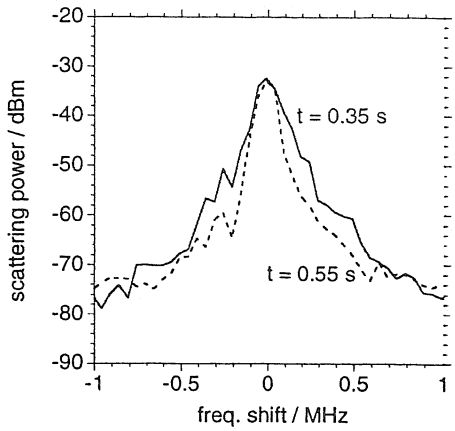

Fig. 5: Microwave scattering spectra before and after the transition for the dischargein Fig. 4.

Another way to obtain good confinement even in the presence of resonances is to provide sufficient magnetic shear in the boundary region, e.g. by an inductive current (see the 25 kA curve in Fig. 2, the bootstrap current is of the order 7 kA for optimum confinement). Although the temperature gradient strongly increases with shear [2], a clear correlation to the observed fluctuations has not yet been found.

4. Conclusions

In spite of its simplicity, the presented model reproduces the basic dependencies of confinement on rotational transform and plasma current induced shear in moderate β, ECR heated W7-AS plasmas. The qualitative agreement with experimental results over a wide range of parameters (ι_a, I_p, B_z) gives strong support to the hypothesis that electron energy transport is enhanced in the presence of higher order rational values $\iota = n/m$ with $m \leq 20$ of the rotational transform and that these perturbations are reduced by magnetic shear, independent of its sign. For optimum confinement such resonances have to be avoided at least in the boundary region, i.e. ι_a must be set to the resonance free regions near ι_a = 1/2, 1/3, etc, or shear must be sufficiently large, i.e. $\iota' \geq o(\gamma^{-1} \approx 1\ m^{-1})$, which is achieved with an inductive plasma current.

In the absence of high order resonances the measured fluctuation level reduces significantly. The mode structure of these fluctuations could not be identified and it is still unclear which kind of perturbations/instabilities enhance the electron transport.

References

[1] H. Wobig et al., *Plasma Phys. and Control. Nucl. Fusion Res (Proc. 11th Int. Conf. Kyoto, 1986)* Vol. 2 (IAEA: Vienna) 369 (1987)

[2] R. Brakel et al., *Plasma Phys. Control. Fusion* **39B** 273 (1997)

[3] F. L. Hinton and R. D. Hazeltine, Rev. Mod. Phys. **48** 239 (1976)

[4] W. I. van Rij and S. P. Hirshman, *Phys. Fluids B* **1** 563 (1989)

[5] S. P. Hirshman, W. I. van Rij and P. Merkel, *Comput. Phys. Commun.* **43** 143 (1986)

Impurity ions in ASDEX Upgrade and WENDELSTEIN 7-AS studied by lithium beam charge-exchange spectroscopy

R. Brandenburg[1], S. Fiedler[2], J. Schweinzer[2], G. Petravich[3], F. Aumayr[1], HP. Winter[1], W7AS- and ASDEX Upgrade teams[2]

[1] *Institut für Allgemeine Physik, TU Wien, Association EURATOM-OEAW, A-1040 Wien, Austria*
[2] *Max-Planck-Institut für Plasmaphysik, EURATOM-Association, D-85748 Garching, Germany*
[3] *KFKI-Research Institute, Dept. of Plasma Physics, H-1525 Budapest, Hungary*

1. Introduction

Impurity ion concentration and -temperature in the core plasma region as well as the scrape-off layer are essential for understanding the physics of L- and H-mode transport and the transport barrier itself. To gain access to these properties, the well established Li-beam diagnostic capabilities on both fusion experiments at IPP Garching (ASDEX Upgrade tokamak and WENDELSTEIN 7 AS stellarator) have been extended [1] and now include the measurement of radial profiles of impurity-ion density and -temperature by means of lithium beam charge-exchange spectroscopy (Li-CXS) [2,3,4,5].

2. Methodical principles

In competition with the impact excitation process, which serves for plasma electron density determination (Li-IXS), the weakly bound outer electron of the Li atom may also be captured by impurity ions. This charge-exchange process produces highly excited states of impurity ions and as a result characteristic impurity ion line radiation. Observation of such emitted spectral lines in conjunction with the modelled Li(*nl*) state distribution in the diagnostic beam allows for evaluation of the impurity density profile along the beam. In addition, temperature

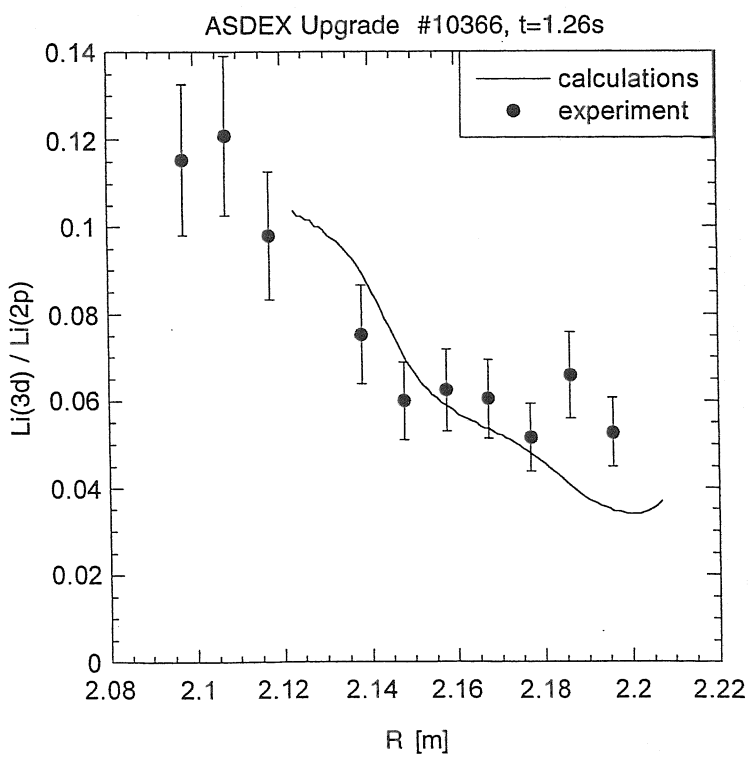

Fig. 1: Radial profile of Li(3d) and Li(2p) population ratio. Experimental results prove the reliability of the beam modelling.

profiles of impurity ions are derived from the respective spectral line shapes. Determination of absolute values from the diagnostic raw data requires a reliable database as well as a detailed modelling [6] of the diagnostic beam which has been checked recently [7] by observing the Li($3d \rightarrow 2p$) spectral line. Taking into account that the Li($3d$) level represents less than 1% of the beam atoms, excellent agreement between experimental results and theoretical values demonstrate a now satisfactory status of the beam modelling (fig. 1). Effective emission cross sections which describe charge exchange processes between Li atoms and impurity ions are calculated within the ADAS file system [8].

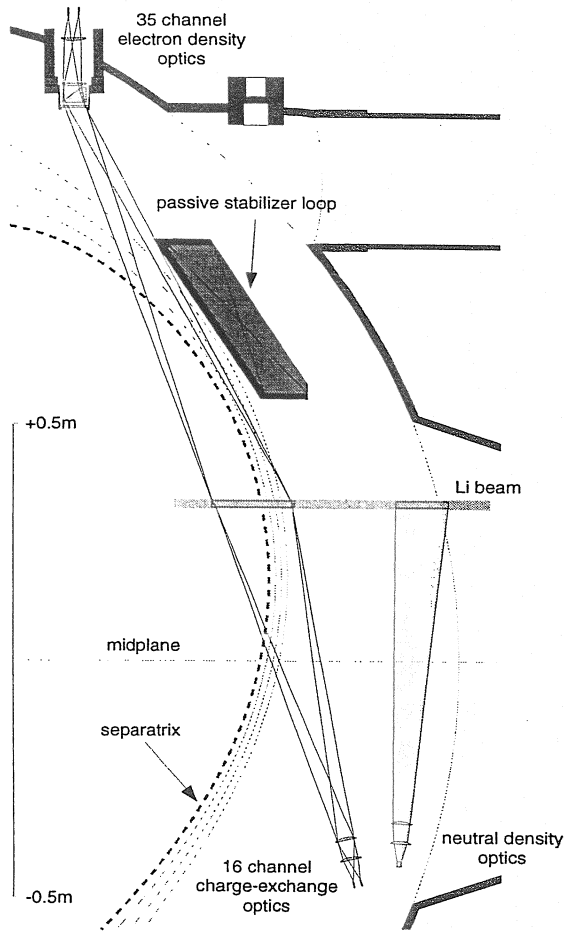

Fig. 2: Optical observation systems of extended lithium beam diagnostics on ASDEX Upgrade.

Evaluation of impurity density profiles

The current setups on both experiments have already been described extensively [1,9]. To determine the absolute concentration of impurity ions, both Li beam diagnostic methods are applied simultaneously [9]. While the photomultipliers of the IXS system record the Li($2p \rightarrow 2s$) light emission at λ = 670.8 nm, the CXS system (spectrometer + CCD camera) detects the impurity ion radiation. Since both systems use different observation optics (cf. fig. 2), the detection efficiency has to be cross-calibrated. This is done by measuring the Li($2p \rightarrow 2s$) radiation with both systems in one calibration discharge, as described in equs. 1a/1b.

$$U_{2p}^{IXS}(i) = k_{671}^{IXS}(i) \cdot n_{Li} \cdot A_{2p\rightarrow 2s} \cdot N(2p)$$
$$U_{2p}^{CCD}(i) = k_{671}^{CCD}(i) \cdot n_{Li} \cdot A_{2p\rightarrow 2s} \cdot N(2p) \qquad (1a/b)$$

k denotes the detection efficiency for the two systems at λ = 671.0 nm, i the corresponding radial channel, $A_{2p\rightarrow 2s}$ the transition probability, n_{Li} the particle density of the Li-beam and $N(2p)$ the relative occupation number of the Li($2p$)-state. The CXS-signal ($U_{imp}^{CCD}(i)$) can be expressed by

$$U_{imp}^{CCD}(i) = k_{imp}^{CCD}(i) \cdot v_{Li} \cdot n_{imp} \cdot n_{Li} \cdot \sum_{nl} \sigma_{em}(nl) \cdot N(nl) \qquad (2)$$

Calculating the ratio of equs. 1b and 2 for the discharges in question and using the ratio of equs.

1a and 1b for the calibration discharge, the impurity ion density can be expressed by

$$n_{imp}(z_{Li}(i)) = \frac{U_{imp}^{CCD}(i)}{U_{2p}^{IXS}(i)} \cdot \frac{k_{671}^{IXS}(i)}{k_{671}^{CCD}(i)} \cdot \frac{k_{671}^{CCD}(i)}{k_{imp}^{CCD}(i)} \cdot \frac{A_{2p\to 2s} \cdot N(2p)}{v_{Li} \cdot \sum_{nl} \sigma_{em}(nl) \cdot N(nl)} \qquad (3)$$

In equ. 3 the first ratio relates the measured signals of both systems, the second ratio is determined by the calibration procedure (see above) and the third ratio expresses the different detection probabilities of the CCD camera at the two wavelengths. v_{Li} denotes the Li-beam particle velocity and $\sigma_{em}(nl)$ the cross section for emission following electron capture from the Li(nl)-level. The relative occupation numbers $N(nl)$ of the Li-beam atoms are calculated in the reconstruction process for the electron density [6].

With the current setups, spatial resolution is $\Delta x = 0.5$ cm on W7AS and 1 cm on ASDEX Upgrade; temporal resolution is limited by the readout time of the CCD camera to 80 ms for 16 simultaneous measurements.

3. Results

CXS investigations on W7-AS

The described algorithm was applied in a series of equivalent discharges ($P_{ECRH} = 400$kW, D_2, $\iota = 0.34$, $B_z = 20.0$ mT, up/down limiters attached, $\int n_e dl(HCN) = 2 \cdot 10^{19}$ m^{-2}) to determine the C^{6+} impurity ion density for different radial positions (different z_{Li} in equ. 3). The result is shown in fig. 2. The C^{6+} impurity ion concentration increases from about 0.41% at $r_{eff} = 16.7$ cm to 0.63% at $r_{eff} = 8.3$ cm. In the gradient region of the profile good agreement is found with the result from the H-CXS diagnostics [10].

Simulation of charge state distributions

The IONEQ code [11] was used to simulate the radial carbon charge state distribution for W7-AS plasmas. Within this simulation the charge state distribution is calculated according to the Corona equilibrium. In addition the neoclassical impurity transport fluxes are modelled by assuming resonable values for a diffusion coefficient and a convection velocity. As input data the electron density profile from the Li beam and the temperature profile from the Thomson diagnostics was

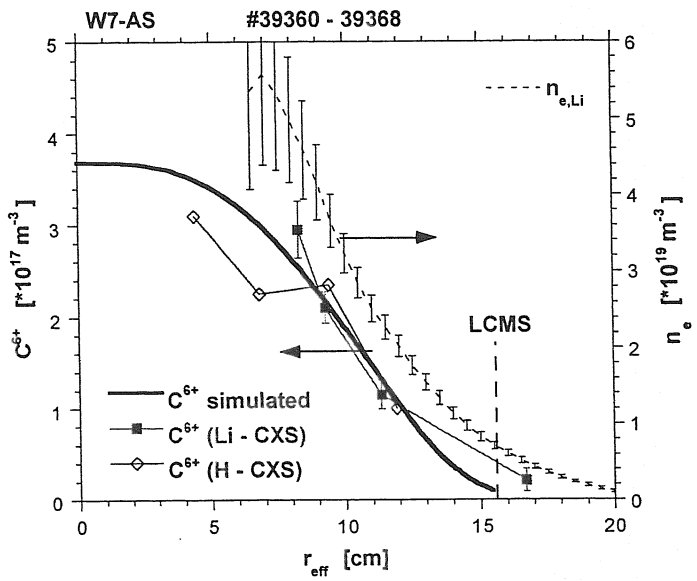

Fig. 3: Radial impurity density profile of C^{6+} and electron density profiles as a function of effective radius r_{eff} for discharges #39360 - 39368. The strong line shows the result of a simulation with the IONEQ code.

used. The neutral gas density was modelled by the EIRENE code and calibrated with the H_α and the neutral density measurement of the Li beam diagnostics [12]. Good agreement was achieved with a diffusion coefficent of $D = 0.2\ m^2s^{-1}$.

CXS investigations on ASDEX Upgrade

On ASDEX Upgrade we use the spectrometer and CCD camera for investigation of impurity ion spectral lines in the range from $250 < \lambda < 800$ nm. Although the complex temporal behaviour of the ASDEX Upgrade discharges poses severe difficulties for the Li-CXS method with the current setup, first results indicate the feasibility of Li-CXS for several impurities (He^+, Ne^{6+}, Ne^{10+}, O^{2+}, F^+, B^{2+}). Comparing radial resolution of data obtained with the Li beam and the hydrogen heating beam, respectively, we can clearly demonstrate the advantage of the Li-CXS method in the plasma edge (fig. 4).

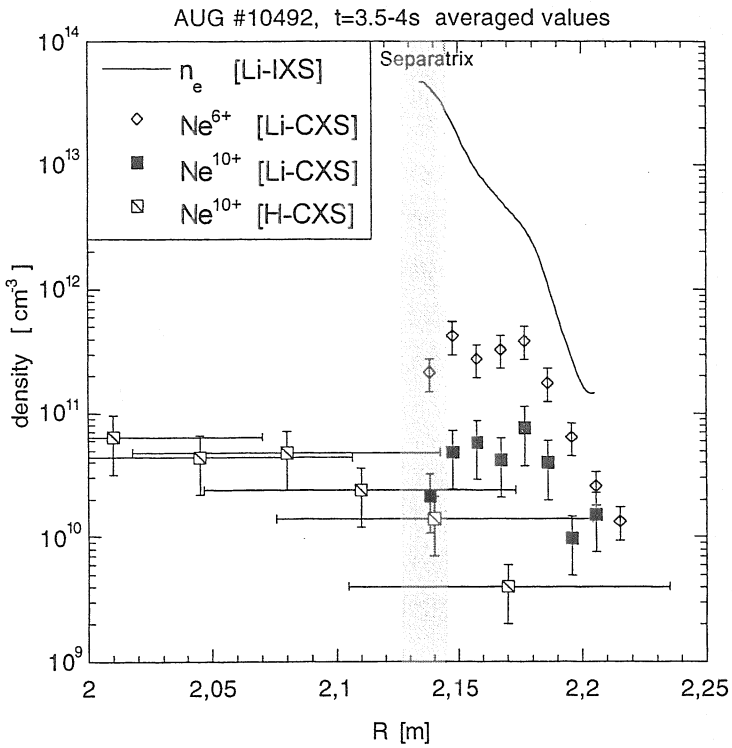

Fig. 4: Radial profiles of Ne^{6+}, Ne^{10+} and electron densities in a discharge with a strong Ne gas puff. Spatial resolution is much more accurate for Li-CXS data than for H-CXS data. Signals have been averaged in order to reduce scatter. Ne^{6+} data contain undetermined contributions from C^{6+} (both at $\lambda = 529$ nm) and appears systematically too high.

Acknowledgments

This work has been supported by Friedrich Schiedel-Stiftung für Energietechnik and by Kommission zur Koordination der Kernfusionsforschung at the Austrian Academy of Sciences.

References

[1] R. Brandenburg et al., 24th EPS Conf., Europhys.Conf.Abstr. **21A** Part I (1997) 477
[2] E. Wolfrum et al., Rev.Sci.Instrum. **64** (1993) 2285
[3] F. Aumayr et al., J.Nucl.Materials **196-198** (1992) 928
[4] R.P. Schorn et al., Nucl.Fusion **32** (1992) 351
[5] H. Winter, Comments At.Mol.Phys. **12** (1982) 165
[6] J. Schweinzer et al., Plasma Phys.Contr.Fusion **34** (1992) 1173
[7] R. Brandenburg et al., to be published
[8] http://patiala.phys.strath.ac.uk/adas/adas.html
[9] S. Fiedler et al., PSI conference 1998, to be published in Journal of Nuclear Materials
[10] J. Baldzuhn et al., Rev.Sci.Instrum. **68** (1997) 1020
[11] A. Weller, D. Pasini, A.W. Edwards, R.D. Gill and R. Granetz, JET-IR(87)10
[12] S. Fiedler et al., 23rd EPS Conf., Europhys.Conf.Abstr. **20C** Part III (1996) 1009

Observation of poloidal rotation by microwave reflectometry

C Christou, J Baldzuhn, M Hirsch and the W7AS team
Max-Planck-Institut für Plasmaphysik,
EURATOM Association, Boltzmannstr. 2, D-85748, Garching, Germany

Abstract

Density turbulence measurements are obtained by microwave reflectometry under various conditions and confinement regimes of W7AS. Properties of poloidal propagation of electron density fluctuations are investigated, and features observed in the microwave spectra are found to display different effects in the different confinement regimes studied. Use of the microwave reflectometer to measure poloidal propagation of electron density fluctuations is demonstrated.

Microwave Reflectometry

The W7AS microwave reflectometer [1,2] uses X-mode propagation and operates in the W band (75-110GHz). The instrument possesses two conical antennas oriented radially towards the centre of the torus axis and separated poloidally by 12° with their symmetry axis in the equatorial plane. The normal to the cutoff surface lies at a tilt angle of 2.6° to the probing direction resulting in an asymmetric fluctuation frequency spectrum. This diagnostic has been used to measure density profiles and to investigate fluctuation propagation by the phase runaway method [3]. There exist three possible components to the backscattered signal detected by the receiver antenna; (i) the coherently reflected signal with unshifted frequency, (ii) the symmetrically Doppler-broadened signal lying around the unshifted signal caused by radial movement of the cutoff layer, and (iii) the asymmetric frequency shifted sidebands caused by scattering from density fluctuations propagating in the poloidal direction across the field of view of the reflectometer.

Reflectometry and confinement

Differences in reflectometry spectra for different confinement regimes are illustrated in figures 1a-d, which show frequency-time plots obtained with two D_2 plasma shots heated by 400kW ECRH. The confinement time is different due to a small change in edge iota value. All other shot parameters are unchanged. The first example, with confinement time τ_e of 20ms and diamagnetic energy W_{dia} of 10kJ, shows a sideband feature clearly separated from the sharp central peak at the carrier frequency, in contrast to the second example (τ_e= 10ms, W_{dia} = 5kJ) where no such separation is observed. Additionally, analysis of the spectrum close to the carrier frequency shows that the central peak is broader and lower in the shot with the lower confinement time. A similar result occurs with NBI shots, where the peak at the carrier frequency is seen to become sharper with an increse in τ_e. Possible causes for the broadening of

the peak include the presence of the asymmetric feature at very small frequency shifts and the Doppler shift of the reflected signal caused by the radial movement of the cut-off layer

In order to quantify the sideband development, numerical routines have been developed to fit the signal with various curves. Usually, the backscattered frequency spectrum was fitted with a triple Gaussian curve. The degrees of freedom in these fits were the heights, widths and frequencies of the sidebands and of the peak near the carrier frequency. Good fits were obtained for time-frequency traces with pronounced sidebands. The fitting was not so succesful for shots in which no clear separation could be seen between sidebands and the peak near the carrier frequency. In the latter case the single apparent peak was found to be broader than the carrier peak observed in spectra with clearly defined sidebands, and this apparent single peak was found to reproducibly shift from the carrier frequency. It was therefore concluded that the single apparent peak contained both the peak at the carrier frequency and the sidebands.

Spectroscopic measurement of the radial electric field

The radial electric field E_r near the plasma edge is determined by spectroscopic measurement of the Doppler spectral line shift $\Delta\lambda$ in the B IV line at a wavelength of $\lambda_0 = 2822$ Å, due to the B IV poloidal rotation velocity [4]. Time traces of the wavelength shift $\Delta\lambda(t)$ are recorded at fixed minor radii between 13 cm (in the gradient region) and 19 cm (outside the plasma). The poloidal rotation velocity $V_\theta = c\,\Delta\lambda/\lambda_0$ is related to the B IV ion pressure gradient term $\partial p_I/\partial r$ and the $E\times B$ drift velocity corresponding to the simplified radial force balance equation:

$$V_\theta(r) = \frac{-1}{e Z_I B n_I(r)} \cdot \frac{\partial p_I(r)}{\partial r} + \frac{E_r(r)}{B}$$

Here, eZ_I is the ion charge, B is the magnetic field, and n_I the ion density. By determination of the ion pressure profile $p_I(r)$ the value of E_r at a particular minor radius is obtained [5]. For typical discharge conditions, V_θ is dominated by the $E\times B$ contribution (60% - 80%) in comparison to the $\partial p_I/\partial r$ contribution (20% - 40%). Therefore, the relative value of $V_\theta(r,t)$ and its temporal changes are a rough estimate for the temporal development of E_r during an individual shot. Those time traces are used to derive a qualitative comparison to the temporal frequency shift of the reflectrometry sideband. As E_r (and, thus $V_\theta(r,t)$) is a decisive factor for transport and confinement [6], that comparison reveals the significance of the reflectometry sideband feature in conjunction with the transport analysis in W7-AS.

For the evaluation of the electron poloidal rotation profile (which is given by the force balance equation above, correspondingly) the $E\times B$ contribution is taken into account as obtained by the procedure described above. The electron pressure gradient term is calculated from electron temperature and density data, delivered by Thomson scattering, electron cyclotron emission ECE, multichannel interferometry and Lithium-beam diagnostics.

Correlation of reflectometry and spectroscopy

Figure 2 is a contour plot of the spectral power measured for a 500kW NBI discharge in D_2. The confinement time, τ_e in this case was 20ms. The prominent feature in this signal is the

development of a strongly shifted sideband in the reflectometry spectrum. The poloidal rotation velocity for the same shot has been determined from the Doppler shift of the B IV emission line. and is shown in figure 3. Comparison of the two figures shows that the sideband shift increrases when the poloidal rotation increases and remains constant when the poloidal rotation value is constant. For shots with similar conditions but a lower confinement time, the measured poloidal rotation velocity is much lower, and also the fluctuation velocity is reduced to an extent that the shifted sidebands are indistinguishable from the peak at the carrier frequency.The velocity determined from Doppler shift measurements is the plasma poloidal drift velocity. whereas the reflectometer measures the propagation velocity of density fluctuations, which includes a poloidal rotation term and as well as the group velocity of the fluctuations in the plasma. Typical calculated values for poloidal propagation of density fluctuations are greater than a theoretically calculated electron poloidal drift velocity by a factor of 2-5 and are significantly greater than the ion poloidal rotation velocity. Uncertainty in the angle of incidence at the cut-off layer make absolute measurements difficult.

Confinement transitions

A time-frequency plot for a 1MW NBI-heated D_2 plasma is shown in figure 4. In this shot, confinement time has a higher valuein the time from 0.5 to 0.65s. During this phase τ_e is approximately 16ms and the poloidal rotation velocity is 4.0km/s, compared with τ_e of 13ms and $V_{poloidal}$ of 3.4km/s before and after this phase. The shift of the sideband measured by the reflectometer increases during the phase with better confinement, consistent with an increase in poloidal propagation velocity of density fluctuations. There is a clear reduction in the reflectometry signal at frequency values between the unshifted signal and the asymmetric sideband during the period of enhanced confinement. This may be due to the damping of density fluctuation activity in the 0 to 1MHz range during the higher confinement operation.

Conclusions

Microwave reflectometry is demonstrated to be a practicable tool for the analysis of poloidal propagation of density fluctuations, and backscattered spectra are seen to reflect confinement characteristics of the W7-AS plasma.

References

[1] H J Hartfuss et al (1994), *Rev Sci Instr* **65**, 2284, 1994

[2] M Hirsch et al (1996), *Rev Sci Instr* **67**, 1807, 1996

[3] H Holzhauer et al, private communication, 1998

[4] J. Baldzuhn, W. Ohlendorf, W7-AS Team (1997) *Rev. Sci. Instr.* **68** , 1020

[5] J. Baldzuhn et al (1998) *Plasma Phys. Control. Fusion* **40** , accepted for publ.

[6] K. Itoh, S.I. Itoh (1996) *Plasma Phys. Control. Fusion* **38** , 1

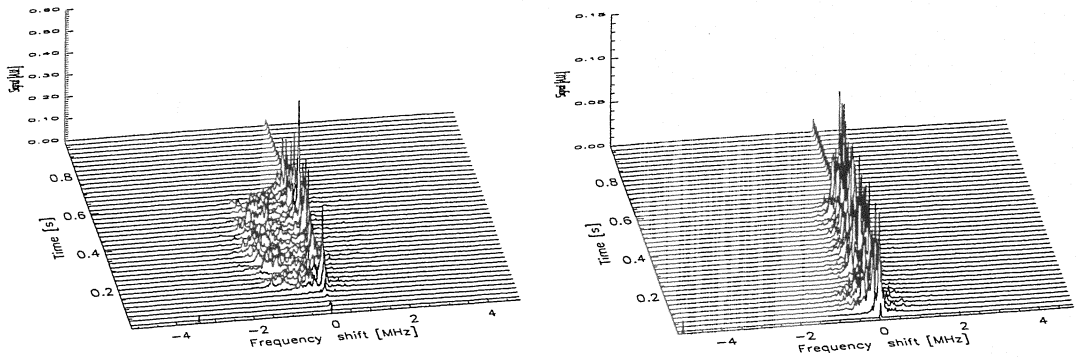

Figure1a&b: Reflectometer spectra from ECRH discharges. Left, τ_c=20ms: Right, τ_c=10ms

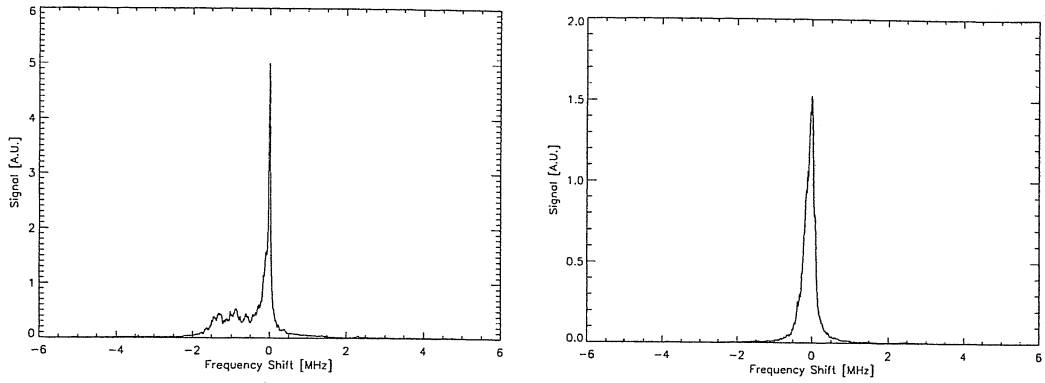

Figure 1c&d: Time-integrated sums of spectra shown in figures1a&b. Left, τ_c=20ms: Right, τ_c=10ms

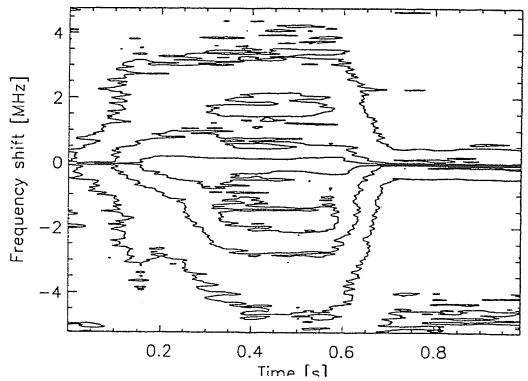

Figure 2:Time-frequency reflectometry spectrum

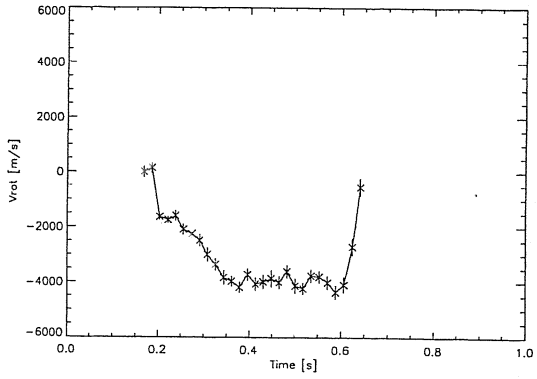

Figure 3: Ion poloidal rotation - same shot as fig2

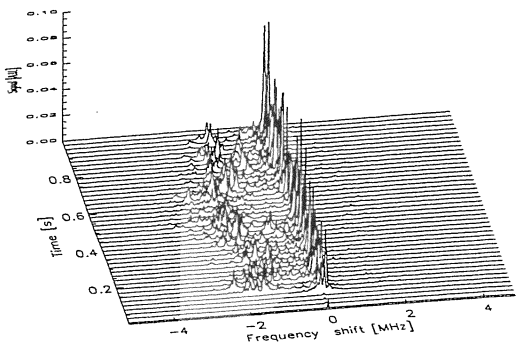

Figure 4:Time-frequency reflectometry spectrum

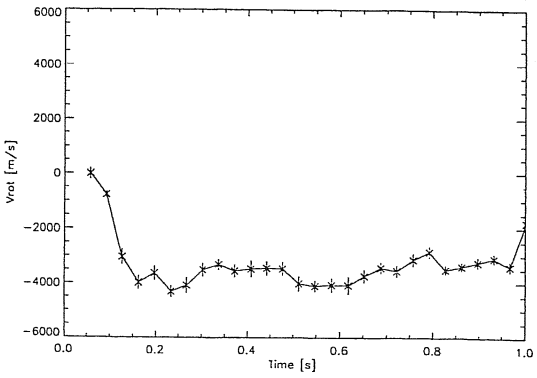

Figure 5: Ion poloidal rotation - same shot as fig 4

- τ_c increased from 0.5 to0.65s in figs 4 and 5

Polarimetric Line Density Measurements at W7-AS Using the Cotton-Mouton Effect

Ch. Fuchs and H. J. Hartfuss

Max-Planck-Institut für Plasmaphysik, EURATOM Ass., D-85748 Garching, Germany

A polarimeter based on the Cotton-Mouton effect has been developed and installed at the W7-AS stellarator. It is operated in the sub-millimeter wave region at frequencies between 500 *and* 650 *GHz. The change of the polarization state is calculated numerically using Segre's formalism and compared with measurements. The polarimeter demonstrated its capability to perform absolute, robust measurements of the line integrated electron density. An improved version for the future W7-X stellarator is briefly discussed.*

Introduction

Polarimetry makes use of the birefringence of a magnetized plasma. It can provide a robust measurement of the line integrated density, which is of special importance for long pulse operation as expected for future devices like the W7-X stellarator or for ITER. In this context a Cotton-Mouton polarimeter was proposed for ITER [1].

Both the Faraday and the Cotton-Mouton magneto-optic effects can be used for measurements of the line density. The Faraday effect is caused by circular birefringence which leads to a phase shift between the left- and the right-handed circularly polarized waves, resulting in a rotation of the plane of polarization; the magnetic field is parallel to the direction of propagation.

The Cotton-Mouton effect is observed if the magnetic field is perpendicular to the direction of propagation. The characteristic waves are linear polarized waves with the plane of polarization parallel and perpendicular to the magnetic field. The phase difference caused by linear birefringence leads to a change of the ellipticity. If the magnetic field $\vec{B}$ along the line of sight is known, the line density can be determined by a measurement of this phase difference.

Optimal conditions are provided by the Wendelstein stellarators which offer lines of sight where $|\vec{B}|$ is almost constant and the field component $B_{\|}$ in propagation direction of the wave is negligible. In this case the position of the plasma and the density profile need not be known and the Faraday effect is negligibly small.

Calculation of the changes in the polarization state

Owing to the small twist of the magnetic field, it is not possible to obtain pure o- and x-modes along the whole line of sight. In addition, a possible misalignment leads to $B_{\|} \neq 0$ which provokes an unwanted Faraday effect. A general formalism [2, 3] is used to describe the changes of the polarization state along the probing beam path. The polarization state is described by the three Stokes parameters s_1, s_2 and s_3, the components of the Stokes vector $\vec{s}$. The evolution along the line of sight (z-direction) is $d\,\vec{s}(z)/dz = \vec{\Omega}\,(z) \times \vec{s}\,(z)$. The vector $\vec{\Omega}(z)$ describes the plasma-wave interaction. The components Ω_1 and Ω_2 of the vector $\vec{\Omega}$ represent the Cotton-Mouton, while Ω_3 describes the Faraday effect. The quantity Ω_2 is non-zero due to the twist of the magnetic field. The beam path and an example of n_e, $\vec{B}$ and the components of $\vec{\Omega}$ along the chosen line of sight in W7-AS are shown in figures 1 and 2.

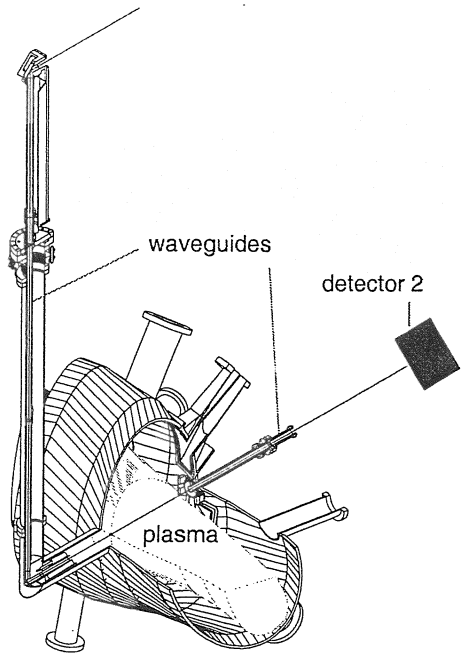

Fig. 1. Beam path at the W7-AS stellarator.

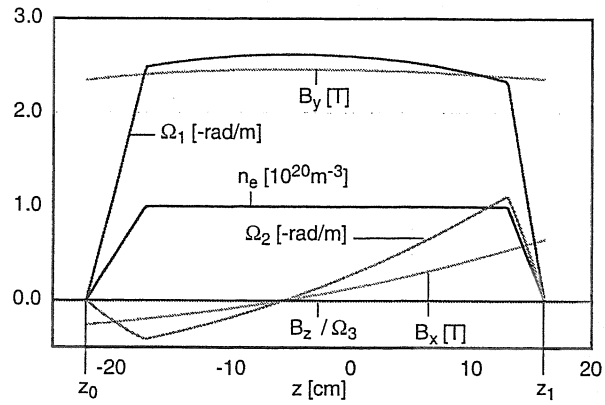

Fig. 2. Plasma parameters along the line of sight for a typical configuration of the magnetic field at W7-AS.

In the case of a dominating Cotton-Mouton effect and sufficiently small twist of the magnetic field ($\Omega_1 \gg \Omega_2$, Ω_3), the phase shift between the x- and the y-components of a launched wave with the direction of the magnetic field being mainly in y-direction is given by the quantity $W_1 = \int_{z_0}^{z_1} dz\, \Omega_1(z)$. For $\omega^2 \gg \omega_p^2$ and $\omega^2 \gg \omega_c^2$, where ω_p and ω_c are the plasma- and the electron cyclotron angular frequencies and $\omega = 2\pi f$ is the probing beam frequency, the approximation $\Omega_1 = (e^2/(2c\,m^2\,\omega^3)) \cdot \omega_p^2(B_x^2 - B_y^2)$ can be made. In this approximation, the quantity W_1 is exactly proportional to the electron line density $\rho_e = \int_{z_0}^{z_1} dz\, n_e(z)$. In the case of an almost constant magnetic field B, W_1 becomes independent on the shape of the density profile. An extensive discussion is given in [4].

Measurement of the Cotton Mouton effect

The quantity W_1 contains the line density ρ_e. Knowledge of the B-field allows the dependence of W_1 on ρ_e to be determined. To measure W_1, a modulation technique as proposed in [3] is used. The probing wave is composed of two orthogonal linear polarized waves. The phase between these waves is linearly shifted with a modulation frequency ω_m, leading to an elliptical modulation of the probing wave. The Stokes parameters before entering the plasma are $s_1(z_0) = 0$, $s_2(z_0) = \cos(\omega_m t)$ and $s_3(z_0) = \sin(\omega_m t)$, assuming identical intensity of the probing wave components.

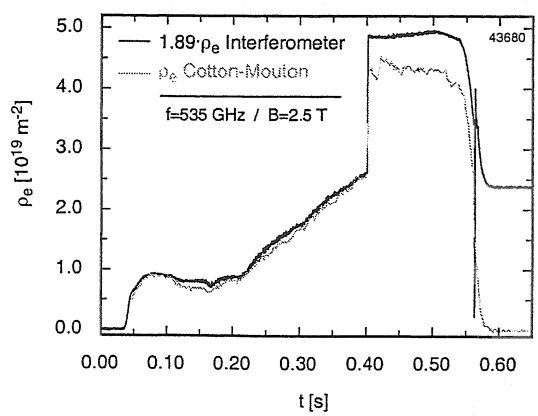

Fig. 5. Plasma discharge with pellet injection. The interferometer shows fringe jumps.

The Stokes parameter $s_2(z_1)$ after passing the plasma becomes $s_2(z_1) = \cos(\omega_m t + W_1)$ [4]. In this way, W_1 is just the phase difference between the Stokes parameters $s_2(z_0)$ and $s_2(z_1)$.

The given expression for Ω_1 is valid for high frequencies, but can lead to errors up to about 10 % for the set-up at W7-AS. Therefore more exact calculations using an expression for Ω_1 as given in [2] are conducted to obtain the line density ρ_e [4]. An example for a measurement of ρ_e is shown in figure 5. By performing systematic scans of the magnetic field at two different frequencies (535 and 627 GHz) and comparing the measured phase differences with calculated values, it could be verified that the Faraday effect, which depends on $w^{-2} \cdot B_{\|}$, is negligible. More results are discussed in [4].

Experimental set-up

The total experimental set-up is sketched in figure 3. A backwardwave oscillator (BWO) is used as a tunable radiation source in the frequency range 500–650 GHz. Oversized waveguides ($\phi = 24$ mm) are used throughout in the guided wave sections. The modulation of the wave ellipticity is accomplished in a way as described in [5]. A polarizing wire grid reflects the y-polarized component of the wave, whereas the x-component is guided to a delay line. After reflection at two mirrors which rotate the polarization plane by 90^0 this component is added to the reflected one. The phase difference of the two components depends on the wave frequency and the length of the delay line. A BWO-frequency modulation with $\omega_m/(2\pi) = 47$ kHz and $\Delta f = 300$ MHz then transforms to an ellipticity modulation of the probing wave. Detectors 1 (reference detector) and 2 (signal detector) with 45^0 analyzers deliver signals proportional to $s_2(z_0)$ and $s_2(z_1)$ respectively. Their phase difference is the quantity of interest which is evaluated digitally. Errors introduced by unwanted amplitude modulation of the BWO are eliminated by the interpretation code with data from a monitor detector at the BWO output.

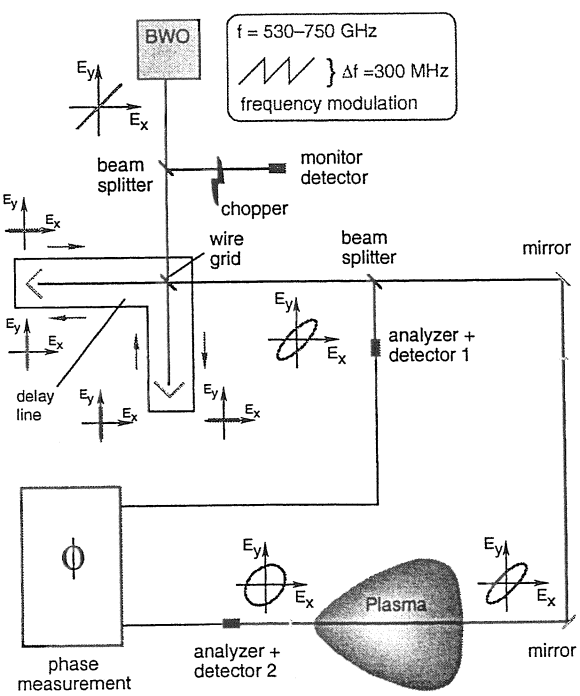

Fig. 3. Experimental set-up at the W7-AS stellarator.

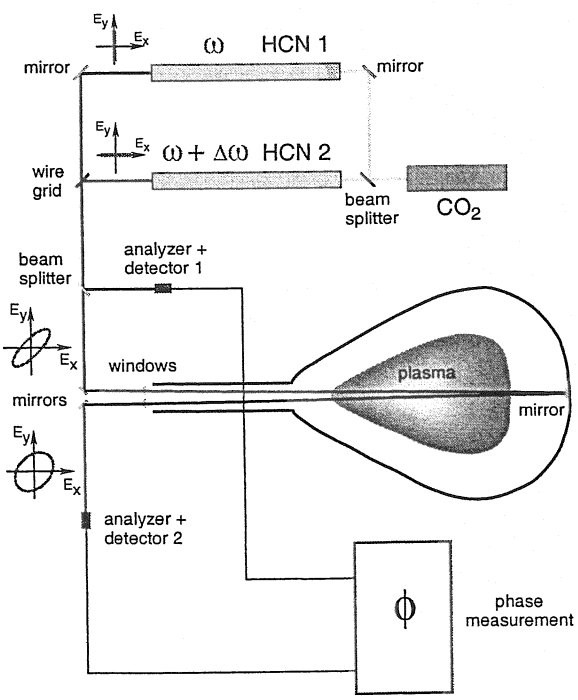

Fig. 4. Proposed experimental set-up for the W7-X stellarator.

Small changes of the polarization in the transmission line cause errors in the W_1 measure-

ment of about 1 %. Considering also misalignments in the probing beam path, numerical calculations result in maximum errors between −3 % and +2 % for the lowest B-field (1.25 T) where the effect is smallest. Another error results from different phase shifts for the x- and y-components in the transmission line in combination with BWO instabilities which lead to phase errors of about 1^0. Other errors include amplitude modulation caused by the frequency dependent vacuum window transmission, plasma diamagnetism and uncertainities in the probing beam frequency. Errors owing to refraction effects, which could lead to a path length difference for the x- and the y-polarized components of the probing beam, are negligible as proven by ray tracing calculations. The relative errors sum up to an error range of −5.5 % to 5.6 % for $B = 1.25$ T and −4.5 % to 5.1 % for $B = 2.5$ T in maximum, including maximum misalignment of the probing beam.

Proposal for an optimized set-up at W7-X

Based on the experience, an optimized set-up for W7-X is proposed. It is sketched in figure 4. Owing to the larger beam path in the plasma and the double-pass of the probing wave, the optimum frequency is about 900 GHz. In this case, the measured phase shift remains below 360^0 and the line density derived is unambiguously connected with the phase measurements. Therefore, HCN lasers with 890 GHz (preferably CO_2-pumped) are well suited as radiation sources. Two lasers with a small frequency offset ω_m of the order of 1 MHz deliver an elliptically modulated wave with a modulation frequency of ω_m by combining the orthogonal polarized beams. The two windows to the vacuum vessel are slightly tilted to avoid reflections. The transmission line should be fully quasi-optical to avoid polarization changes.
With an output power of the order of 10 mW, high signal-to-noise ratios can be reached. This enables a time resolution of about 1 μs and a phase resulution of 0.1^0 simultaneously. Systematic errors also could be in the region of 0.1^0. The corresponding density resolutions is about $n_e = 10^{17}\,\mathrm{m}^{-3}$ for $B = 2.5\ T$ and $n_e = 4 \cdot 10^{17}\,\mathrm{m}^{-3}$ for $B = 1.25\ T$.

Conclusion

The capability of the Cotton-Mouton effect for a robust measurement of the line integrated density at W7-AS has been demonstrated. This is of great importance for long pulse machines like the future W7-X. Both W7-X and W7-AS offer a favourable magnetic field topology for the method.
The main problem of the W7-AS set-up are the transmission properties of the oversized waveguides with respect to conservation of the polarization state; this is not discussed in this short contribution. Changes of the polarization state could be avoided in an advanced experimental set-up by using quasi-optical transmission techniques if space allows.

References

[1] P. Buratti, proposed and discussed at meetings with the European Home Team on microwave diagnostics for ITER (1995).

[2] S. E. Segre, Plasma Physics **20**, 295 (1978).

[3] S. E. Segre, Phys. Plasmas **2**, 2908 (1995).

[4] C. Fuchs and H. J. Hartfuss, Rev. Sci. Instrum., accepted for publication in 1998.

[5] V. F. Shevchenko, A. A. Petrov, V. G. Petrov, and Y. A. Chaplygin, Plasma Physics Reports **22**, 28 (1996).

Study of Alfvén Eigenmodes in Configurations of Different Shear at WENDELSTEIN 7-AS

C. Görner, A. Weller, M. Anton, J. Geiger, C. Nührenberg[1], F.-P. Penningsfeld, D. Spong[2], U. Stroth, W7AS-Team

Max-Planck-Institut für Plasmaphysik, EURATOM Association, D-85748 Garching

1. *Max-Planck-Institut für Plasmaphysik, EURATOM Association, Teilinstitut Greifswald, D-17489 Greifswald*
2. *Oak Ridge National Laboratory, Oak Ridge, Tennessee, USA*

I. Introduction

Alfvén eigenmodes are widely investigated in fusion experiments, since they are expected to be destabilized by energetic particles and eventually may cause losses of fast alpha particles in future fusion reactors. In current experiments, NBI-driven Alfvén eigenmodes are seen in stellarators and tokamaks but they differ by the way of mode formation. In the stellarator case with low shear the Global Alfvén Eigenmode (GAE) below the Alfvén continuum is expected, whereas in a tokamak-like case with high shear, Toroidal Alfvén Eigenmodes (TAE) are the dominant mode types.

Beside low shear, the advanced stellarator W7-AS is characterised by large aspect ratio (about 12) and a 3D-field geometry, which also influences the Alfvén spectra. The study of GAE modes in W7-AS can possibly be related to reversed shear scenarios in advanced tokamak experiments, where extended regions of low shear are present. On the other hand, by increasing the shear in W7-AS, the common physics of Alfvén eigenmodes in stellarators and tokamaks can be investigated in studying the transition from GAE to TAE modes depending on the profile of the rotational transform.

We compare experimental results with expectations based on the Alfvén continuum spectra, with numerical calculations using a gyrofluid model [1] and with a 3-dimensional MHD-code CAS3D [2].

In W7-AS, shear is modified with respect to the vacuum configuration by equilibrium currents (Pfirsch-Schlüter), bootstrap- and beam-driven Ohkawa-currents, which are usually compensated by an inductively driven current in order to achieve net-current-free operation. In the experiments described here, shear is changed by driving a plasma current of up to 12kA in both directions as shown for example in Fig. 1. Positive and negative shear can be generated, allowing to investigate a variety of different Alfvén continua including cases with GAE and TAE gaps.

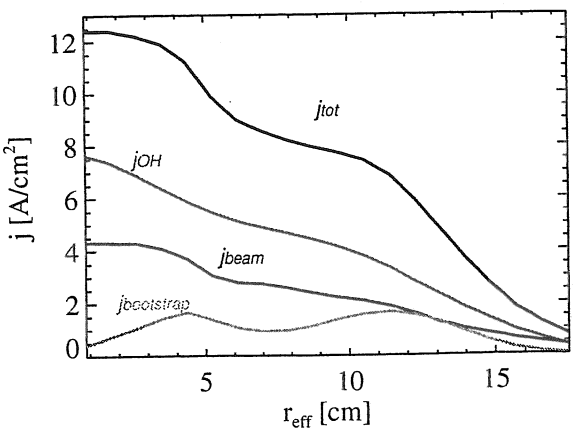

Figure. 1: Current densities in W7AS for shot #39042. Here, all currents are positive and a net total current is driven in order to increase the magnetic shear.

II. Experimental Plasma Set-up

Experiments are done with the standard magnetic field of $B = 2.5T$ and different values of the ohmic current to change strongly the shear of the magnetic configuration. In order to keep the edge value of the rotational transform ι_a constant, the vacuum iota ι_a^0 was adjusted depending on the ohmic current. See Fig. 2 for a sequence of ι-profiles with different magnetic shear but almost equal ι_a. Plasma heating is done purely with neutral beam injection (NBI), the ohmic power is negligible. Balanced injection is used in most cases to avoid effects from toroidal plasma rotation on mode frequencies and to minimize the beam-driven plasma currents. Usually a density ramp is performed to enable the study of mode frequencies that should scale like the Alfvén velocity $v_A = B/\sqrt{\mu_0 \rho}$ (ρ, mass density). The energy source for the excitation of Alfvén eigenmodes is provided by resonant fast particles from the NBI.

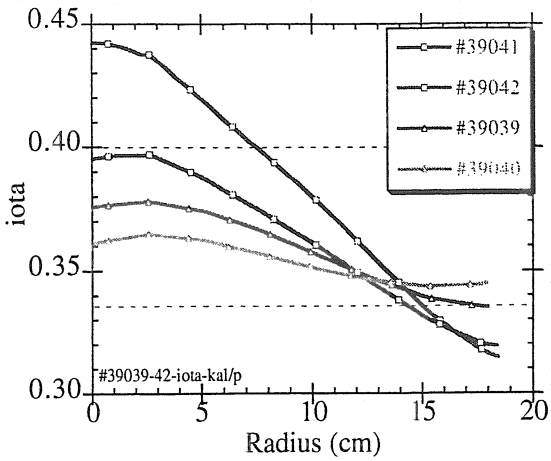

Figure 2: Magnetic shear-variation from ohmic current drive in W7AS. All profiles are sheared negative (positive shear in q in tokamaks).

III. MHD Diagnostics

An important tool to analyse the mode structures is a tomographic system for the soft-X radiation, composed of 10 cameras inside the vacuum vessel with a total number of 320 viewing chords [3]. The 2-D mode reconstructions can be done without assumptions about the magnetic topology. The spatial resolution is around 1 cm and tomographic reconstructions with experimental data showed the potential to identify structures up to poloidal mode numbers of $m = 9$ and a radial mode number $s = 1$. The sampling rate is up to 200 kHz, which is sufficient for analysing Alfvén-eigenmodes with typical frequencies of 30 kHz at W7-AS. Singular value decomposition (SVD) and filtering in the frequency domain on a rectangular grid radially limited by the borders of the soft-X profile, proved to be good tools for extracting the fluctuating part of the soft-X emission [3].

Since the soft-X emission is restricted to the hot plasma region (up to 70% of the plasma radius a for NBI discharges), the ECE diagnostic (100 kHz sampling), reflectometry (1 MHz) and magnetic pick-up coils (250 kHz) are used to check the tomographic reconstructions and to get further information about the mode structure near the plasma edge. The comparison of different diagnostics can be made in terms of the radial displacement of flux surfaces as deduced from the measurements.

IV. Transition from GAE to TAE modes with increasing magnetic shear

Alfvén eigenmodes like the GAE and TAE mode, which extend over a large part of the plasma cross-section are predicted to occur as weakly damped discrete solutions in the mag-

neto hydrodynamic (MHD) spectrum. They typically occur in frequency gaps of the continuous branch of solutions, the so called *Alfvén continuum*, consisting of a strongly damped class of radially localized eigenmodes. The frequencies of the Alfvén continua are given by the local dispersion relation $\omega^2 = (k_{\parallel} \cdot v_A)^2$, with $k_{\parallel} = (m\iota - n)/R$ the parallel wave number, n the toroidal mode number and R the major radius. The dependence on the ι-profile causes a characteristic difference in the gap structure of tokamaks and low shear stellarators. Two possible ways of gap formation are shown in Fig. 3. In the tokamak case with a strong shear a TAE mode contains a large number of poloidal harmonics, where the dominant poloidal mode number is inherited from the nearest Alfvén continuum at the same radius (see e.g. [4]).

In contrast, the low shear at W7-AS usually leads to a well defined (m, n)-structure of a GAE [5] (like in Fig. 3a). In discharges at $\iota_a \approx 0.35$, we increased the shear using ohmic currents such to create a TAE gap for $n = 2$, where only two adjacent poloidal mode numbers (m = 5 and 6) are involved over the whole plasma cross-section (discharge #39042 in Fig 2 and Fig. 3b). Experimentally, we in deed found the predicted TAE mode at a frequency of 63 kHz. This is a case, for which the full 2-D mode structure of a TAE mode could be obtained for the first time by soft-X tomography (Fig. 4a). Both components, the m = 5 in the inner region and the m = 6 in the outer region are seen in the tomograms in accordance with the expectations. The contributions of these two components to the mode eigenfunction have been derived quantitatively by poloidal Fourier analysis of the tomograms (see Fig. 4b). A comparison to theoretical expectation was done in 2 ways. First, numerical calculations of the linear growth rates with a gyrofluid code [1] taking into account the fast particle physics but using an axisymmetric approximation shows the destabilization of the mode. Secondly, to compare the mode structure calculations in the stable part of the MHD spectrum were performed using the CAS3D stability code which uses the proper 3-D equilibrium information, but neglects fast particles. Also there, TAE modes were found as discrete solutions with radially extended eigenfunctions. A comparison of the radial distribution of the leading Fourier harmonics (Fig.4 and 5) shows a slight disagreement in the radial position which may be due to uncertainties in the profiles entering the equilibrium and the CAS3D calculations. Good agreement

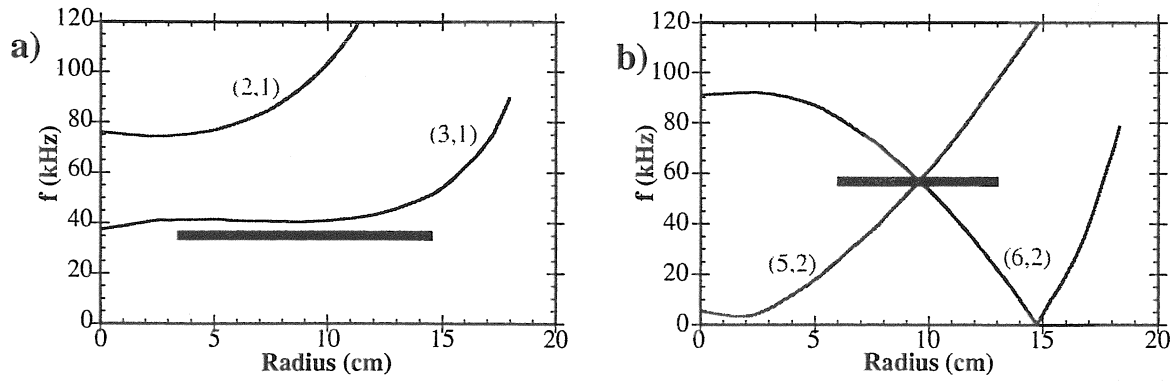

Figure 3: Alfvén continua for low (a) and increased magnetic shear (b).
a) GAE mode (plotted bar) in the gap below the (3,1)-continuum.
b) TAE gap mode in the gap induced by coupling of to two continua with $(\Delta m, \Delta n) = (1, 0)$.

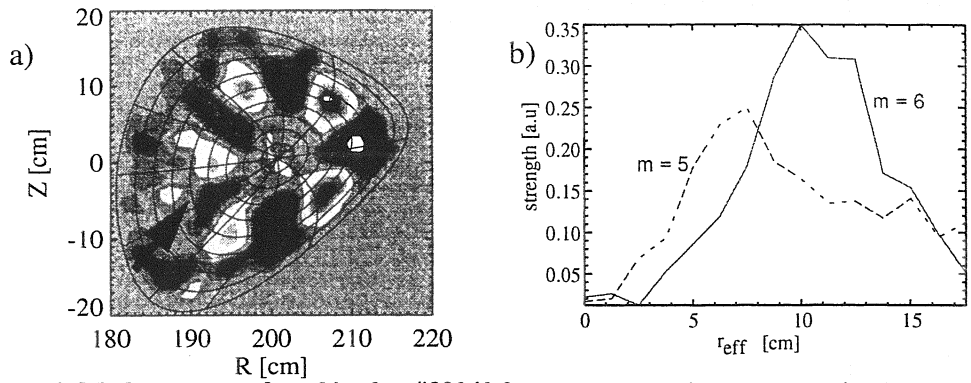

Figure 4: Mode structure found in shot #39042 from tomographic reconstruction.
a) Poloidal cross-section of the mode structure. The arrow marks the radial position, where the m = 5 structure changes to m = 6 (at r_{eff} = 9.5cm)
b) Radial distribution of Fourier-harmonics with m = 5 and 6 from tomographic reconstruction. The mode frequency in the laboratory frame is 47kHz.

was found for the frequencies, if the Doppler shift in the measured frequency due to poloidal plasma rotation (-15kHz) is accounted for.

Taking the shear value in the TAE-case as a reference, with increasing shear first the formation of a rational surface $\iota = 2/5 = 0.4$ is observed by the appearance of a pressure driven mode, which exists in the presence of the TAE mode. Further increase of shear leads to only weak mode-activity, that cannot be analysed anymore. With decreased shear (#39039 and #39040 in Fig. 2), GAE modes with $m = 3$ or $m = 5$ were found in accordance with the expectations together with additional mode activities. An attempt was made to excite TAE modes with different mode numbers by changing the edge rotational transform. First results indicate the presence of the TAE modes with the expected poloidal mode structure. These observations demonstrate the close relationships between the structure of global Alfvén eigenmodes in stellarators and tokamaks. More studies are needed to explain in particular the conditions for the destabilization of the different modes and their effect on the fast particle confinement.

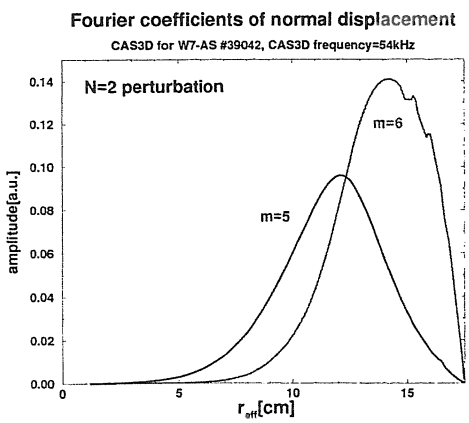

Figure 5: Mode structure found in shot #39042.
CAS3D-eigenvector for a n=2 perturbation with a frequency of 54kHz [6].

References

[1] D. A. Spong, B. A. Carriers, and C. L. Hedrick. *Pays. Plasmas*, **1** 1503, 1994.

[2] C. Nührenberg. *Phys. Plasmas*, **3** 2401, 1996.

[3] C. Görner, M. Anton, J. Geiger, W. von der Linden, A. Weller, S. Zoletnik, and W7AS-Team. In *24th EPS Conference on Controlled Fusion and Plasma Physics*, 1997.

[4] D. A. Spong. In *1996 International Sherwood Fusion Theory Conference*, Poster 3C11, Philadelphia, Pennsylvania, March 1996.

[5] A. Weller, D. A. Spong, R. Jaenicke, A. Lazaros, F. P. Penningsfeld, S. Sattler, W7-AS Team, and NBI-Group. *Physical Review Letters*, **72**(8) 1220, 1994.

[6] C. Nührenberg, J. Geiger, C. Görner, and A. Weller. In *Theory of Fusion Plasmas Varenna 1998*. to appear.

Parameter Dependencies of Temperature Fluctuations and their Correlation with Density Fluctuations in W7-AS

H.J. Hartfuß, M Haese and M. Hirsch
Max-Planck-Institut für Plasmaphysik, EURATOM Ass., 85748 Garching, Germany

Abstract *Electron temperature fluctuations down to a level of 0.1% can be measured with correlation radiometry of the electron cyclotron emission. The fluctuation spectra found can be characterized by two different components below and above about 10 kHz, propagating into different radial directions with strongly differing phase velocities. The high frequency component disappears under grad $T_e = 0$ conditions and is in-phase correlated with density fluctuations. The behaviour might qualitatively be understood in the frame of convective micro-turbulence. Parameter scans of density, temperature and the gradients of these quantities show that the "universal dependency" is on the local temperature: the temperature fluctuations normalized to the local temperature gradient decrease with increasing tem*perature.

Introduction

The radial electron heat transport is assumed to be driven in part by fluctuations of density, electric field, temperature and magnetic field. Temperature fluctuations at the plasma edge can be measured using probes. Correlation radiometry of the electron cyclotron emission (ECE) has made the measurement in the plasma core possible [1,2,3]. The sensitivity of a single ECE radiometer channel to temperature fluctuations is limited by the inherent thermal noise (wave noise) of the blackbody emission. The method developed at W7-AS [1,5] makes use of a pair of identical multichannel radiometers viewing the same plasma volume with two Gaussian beams symmetric to the horizontal midplane of W7-AS. Due to the observation along different lines of sight, the thermal noise decorrelates. The relative sensitivity to temperature fluctuations reached is about 0.1. The beam waist of a single sightline is about 2 cm. The resulting sensitivity to poloidal wavenumbers is limited to $k_\theta < 3.5\ cm^{-1}$. The radial resolution is typically 0.5 cm, the temporal resolution about 1 MHz. The resolutions are sufficient to study the fluctuations in more detail.

Parameter dependencies

The temperature fluctuation spectra consist of two components with different physical properties [4]. A strong component below about 10 kHz propagating inward and a broad component extending into the 100 kHz range propagating outward. The turbulent high frequency component is assumed to be the one which might be transport relevant. A quantitative analysis of transport is not possible due to the lack of information about the poloidal electric field fluctuations and their phase relation to the temperature fluctuations. However as a first attempt, parameter studies of the temperature fluctuation level have been carried out as the electron heat diffusivity shows characteristic dependencies. In a series of discharges the radial

fluctuation level, i.e. the square root of the relative spectral fluctuation power integrated over the frequency range 20-60 kHz, at 6 radial positions on the high field side of the temperature profile (see Fig. 1) has been investigated for dependencies on discharge parameters.

Broad flat temperature profiles can be conducted in W7-AS by using off-axis power deposition of the ECRH. In this case the temperature gradient vanishes in the radial observation region and fluctuations above 20 kHz disappear completely [4,6]. The low frequency component is unaffected by this measure.

The disappearance of the high frequency component would be expected if a turbulent mixing process is assumed which exchanges plasma volumes on the scale of a mixing length. In this case the turbulence, which itself might depend on local parameters, would only be observable by a temperature diagnostic through a finite temperature gradient. Density fluctuations in the observation region are not significantly affected by the flattening of the temperature profile. Assuming this process, for all parameter studies the local fluctuation level has therefore been divided by the local temperature gradient.

Because of the clear dependence of energy confinement time on heating power, the fluctuation level has been measured as a function of ECRH power in the range of 290 to 830 kW. As found already earlier [7], the fluctuation level decreases with increasing heating power. This result is in clear contradiction assuming a direct connection between transport and fluctuation level. From drift-wave calculations an increase of the normalized temperature fluctuations with the square root of T_e is expected [8]. The power scan results in a local temperature variation of 700 to 2000 eV. Again the experiments are in contradiction to the expectations. The fluctuations decraese with T_e^{α}, with $\alpha = -3/2$ as shown in Fig. 1.

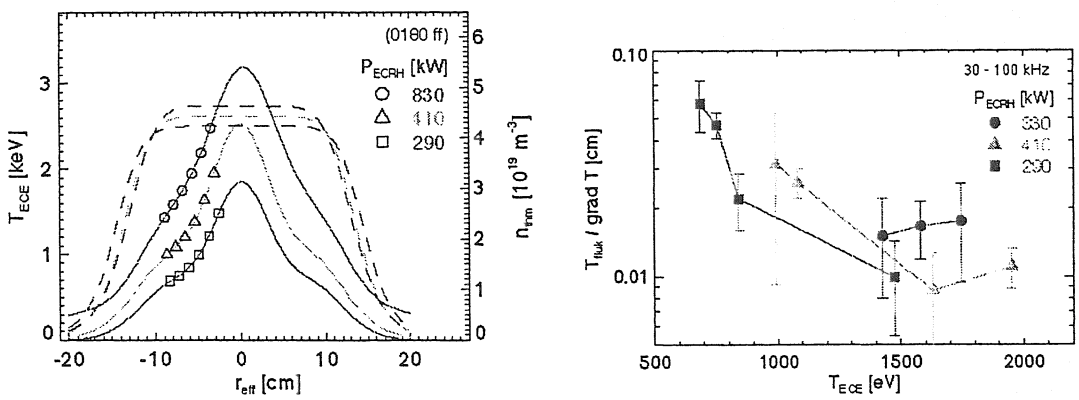

Fig 1: Temperature (solid lines) and density (dashed lines) profiles for 3 different ECRH heating powers. Temperature fluctuation measurements are conducted in the gradient region of the high field side as indicated in the temperature profiles (left figure). The rms-value of the high ferquency component of the fluctuations normalized to the local temperature gradient is decreasing with increasing local temperature.

Plasma turbulence depends on the electron density. With reflectometry measurements a decrease of the density fluctuations with increasing density is observed. A density scan in the frame of the temperature fluctuation studies has been conducted at constant heating power of 450 kW. The relative temperature fluctuation level decreases with increasing density. Because of constant heating power, besides the density profile, the temperature profile changes as well. Various

combinations of the local quantities temperature and density. i.e. pressure, pressure gradient and collision frequency were tested to look for dependencies of the local fluctuation level. No clear correlation could be found. As before, the only dependency found is the temperature dependency as given in Fig. 3 (left).
Higher densities lead to a stronger decrease of the fluctuation level with electron temperature.

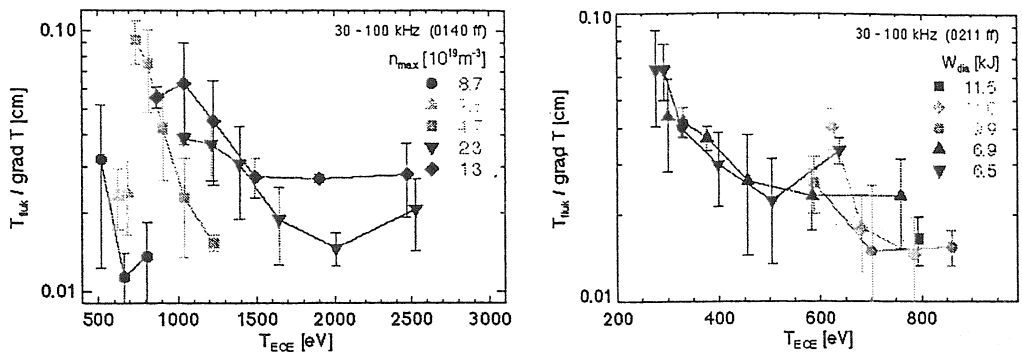

Fig. 2: The figures give the variation of the normalized temperature fluctuations as a function of the local electron temperature. Increasing the electron density from 1.3 to 8.7 $10^{19}m^{-3}$ increases the exponent of the T_e-dependence from -2 at low to -3.5 at high density (left figure).The right figure summarizes the results of a scan of the edge rotational transform between 0.34 and 0.365. Under constant heating conditions the temperature profile varies while the density profile is almost constant with a peak density of 8 10^{19} m^{-3}. The total stored energy varies from 6.5 to 11.5 kJ. The fluctuations can be described by a "universal" dependence like $T_e^{-1.2}$.

In W7-AS the confinement strongly depends on the edge value of the rotational transform. The total stored energy can vary by a factor of two and more under otherwise constant conditions of heating power and density. It is found that the lowest fluctuation level is found for plasmas with highest confinement. This might be a hint pointing to a connection between turbulence and transport. Unfortunately the profile of the rotational transform is not sufficiently known to plot the local fluctuation levels measured against local values of the rotational transform. The experiments are therefore interpreted as a variation of the local temperature under constant density conditions. As in the power scan, all measured fluctuation levels decrease with temperature in the same way as found in the power scan (Fig. 3 right).
The search for parameter dependencies is connnected with the question whether local or non-local parameters determine the turbulence and the confinement. This question cannot be answered finally. But it seems that the possibility to sort the measurements by temperature and temperature gradient, points to local plasma parameters. Summarizing all scans, it is supposed that the temperature fluctuations can possibly be described by a general law, which might besides the temperature and density profiles be determined also by their gradient lengths and other parameters characterizing the magnetic configuration and local shear etc.:

$$\tilde{T}_e = \nabla T_e \cdot \tilde{\Lambda}(T_e, n_e, L_T, L_n, \ldots), \quad \tilde{\Lambda} \propto 1/T_e^{\alpha}, \quad 1 \le \alpha \le 3.5$$

However, besides the dependencies described, no other ones have been found. The temperature dependency might be caused by increasing parallel heat exchange with increasing temperature.

Correlations with density fluctuations

In a combined experiment of correlation radiometry and reflectometry where both diagnostics share the same lines of sight, correlations between density fluctuations and temperature fluctuations have been found. The correlations are in-phase and are observed only for the high frequency turbulent component of the temperature fluctuations (Figs. 3) and are only found under conditions where both diagnostics view the same plasma volume, as has been verified on a shot-to-shot basis by shifting the reflectometry postion along the density gradient. The maximum coherenec found is about 0.3, probably due to the well known fact, that not all phase fluctuations seen by the reflectometer are caused by density fluctuations. The correlation rapidly deacrease with increasing distance between the observation volumes of reflectometry and ECE. The in-phase correlations of temperature and density fluctuations confirm the assumption of convective turbulence: inward convection increase both temperature and density and vice versa respectively [9].

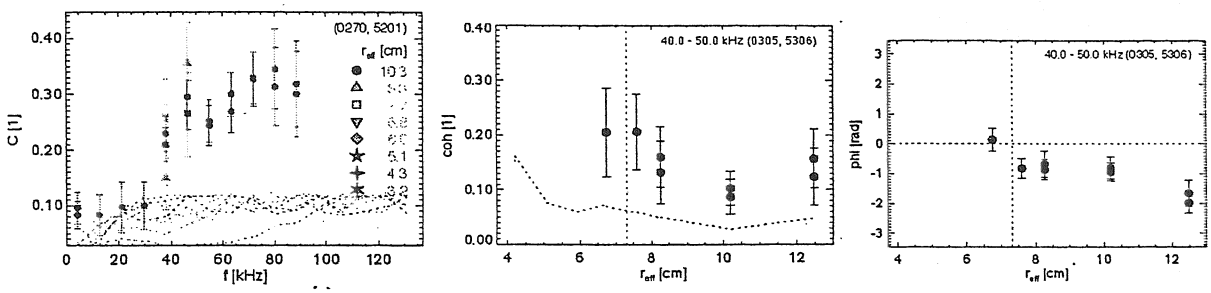

Fig. 3: Results as obtained with the combined reflectometer correlation radiometer experiment. Correlation between density and temperature fluctuations are found only for the high frequency component of the temperature fluctuations above about 30 kHz (left figure). The correlations are maximum if the radiometer and the reflectometer are viewing the same plasma volume and decrease rapidly with increasing distance (central figure). In the common volume the density and the temperature fluctuations are in phase. The phase change with distance reflects their radial propagation (right figure).

References

[1] S. Sattler and H.J. Hartfuss, Phys. Rev. Lett.**72**, 653 (1994)

[2] G. Cima et al., Phys. Plasmas **2**, 70 (1995)

[3] C. Watts et al. "Comparison of temperature measurements using different techniques" 10th Joint Workshop on ECE and ECRH ed. T. Donne and T. Verhoeven (Singapore: World Scientific, 1998) p. 147

[4] H.J. Hartfuss et al., Plasma Phys. Control. Fusion **38**, A227 (1996)

[5] S. Sattler and H.J. Hartfuss, Plasma Phys. Control. Fusion 35, 1285 (1993)

[6] M. Haese et al., "ECE Fluctuation Measurements on the W7-AS Stellarator" 10th Joint Workshop on ECE and ECRH ed. T. Donne and T. Verhoeven (Singapore: World Scientific, 1998) p. 131

[8] B. Scott, Phys. Fluids, B4, 2468 (1992)

[9] M. Haese et al., Rev. Sci. Instrum. accepted for publication (1998)

Second Harmonic Hydrogen Heating on the Stellarator W7-AS

D.A. Hartmann, G.Cattanei

Max-Planck-Institut für Plasmaphysik, EURATOM Association, D-85748 Garching

1. Introduction

Ion cyclotron resonance heating (ICRH) on the W7-AS stellarator has successfully been demonstrated for a hydrogen minority in a deuterium plasma [1]. This heating scheme, however, imposes severe restrictions on the torus wall condition since the heating efficiency drops drastically for hydrogen concentrations larger than 10%. Thus an alternative heating method is desirable. Second harmonic hydrogen heating is such a means. Using this heating scheme on W7-AS it was possible to sustain plasmas with ICRH alone and to heat NBI target plasmas. The heating efficiency was about 20% worse than that of hydrogen minority heating, but no significant impurity production was observed. Earier attempts to heat ECRH generated hydrogen plasmas were not successful; most likely because the RF power was not sufficiently high to generate a tail in the hydrogen distribution function.

2. ICRH only

Neutral beam (NBI) generated hydrogen start-up plasmas were successfully sustained solely with ICRH for up to 250 msec at the second hydrogen harmonic. About 1.1 MW of radio-frequency (RF) power were applied to one antenna. Pulse duration and maximum power were limited by arcs in the transmission lines. However, the approximate 500 kW power from the antenna, P_{RF}, (estimated from the change in antenna loading resistance with plasma) were sufficient to obtain plasmas with steady-state values of electron density, $n_e(0) = 5 \times 10^{19}\mathrm{m}^{-3}$, electron temperature, $T_e(0) = 300$ eV and hydrogen temperature $T_H(0) = 600$ eV. No increase in the bolometric signal was observed, thus there was no rise in impurity concentrations. The time dependence of the major plasma parameters of a typical shot is shown in Fig. 1. At higher densities steady-state could not be achieved with the maximum available power.

At sufficiently high RF power this heating method does require neither an initial seed nor a constant source of fast hydrogen. This is concluded from investigation of the time evolution of the central hydrogen energy distribution shown in Fig. 2. The distribution is measured with active charge exchange at an angle of 45° to the magnetic field lines. At t=200 msec when NBI is switched-off and ICRH is switched on, the plasma has not yet reached steady-state and the hydrogen energy distribution is determined by the slowing down spectrum of NBI. Within 25 msec the supra-thermal part of the distribution has vanished due to the very short equipartition time with the still cold electrons. During the following 50 msec the supra-thermal part slowly increases again following the rise in electron temperature. Eventually at t=275 msec and thereafter the distribution is

steady-state.

This "bootstrapping" of the hydrogen energy distribution is confirmed by measurements with a bandpass limited RF pickup probe. This probe is located toroidally opposite to the antenna. It is an indicator for the absorption of the launched RF-wave: high signal meaning poor absorption and vice verca. For second harmonic heating the absorption should increase with the fraction of tail particles. It is found that the probe signal is inversely correlated to the measured hydrogen flux at 2 keV.

The central hydrogen energy distribution agrees well with the steady-state solution of the quasilinear equation [2]. That solution is shown as a solid line in Fig. 2. The calculation is based on an RF-power density of 0.6 W/cm^3. This corresponds to a distribution of the 500 kW radiated power over a volume about half of the plasma volume of 1.6 m^3.

3. ICRH combined with NBI

ICRH at the second harmonic hydrogen frequency was applied to NBI target plasmas. With typical plasma parameters of $n_e(0) = 5 \times 10^{19} m^{-3}$, $T_e(0) \approx T_H(0) = 450$ eV and 400 kW NBI, both electron and ion temperature rose by about 200 eV when 500 kW of radiated RF power were applied for 300 msec. The hydrogen tail temperature rose from 7 keV to 9 keV with the In those experiments a small increase in bolometric signal of about 50 kW was observed and could predominantly be attributed to an increase in carbon radiation. The antenna was operated in 0 and in $\pi-$phasing. No substantial difference was found either in the antenna coupling resistance or in the bolometric signal.

By comparison of the increase in diamagnetic energy, W_{dia}, with established W7-AS confinement time scaling it was found that about 70% of the ICRH power radiated from the antenna were absorbed in the plasma. Fig. 3. shows the increase in diamagnetic energy as a function of radiated RF-power at different densities. The solid lines are calculated for the power dependence of the W7-AS confinement time scaling equating the absorbed RF power, P_{ICRH}, to 70% of the radiated RF power.

In a series of modulation experiments the RF power was square-wave modulated with frequencies between 2.5 and 200 Hz. A global confinement time model (dW/dt=-W/τ+αP_{RF}) was fitted to the measured amplitudes of Fourier components of the diamagnetic energy and to the phase shift between RF power and diamagnetic energy. α is the absorbed fraction of the radiated power and τ is the incremental confinement time. The experimental results are shown in Fig. 4. The solid lines are the fit to the data with α=0.5 and τ =12 msec. The discrepancy of the absorbed power from scaling and modulation measurements was also found for hydrogen in deuterium minority heating experiments. It is not yet understood.

The radial electric field in the outer region of the NBI plasma is negative with values up to -15 kV/m (measured passively on Bor). With ICRF it increases at fixed radial positions up to -23kV. DKES [3] calculations, however, show a weak dependence of

the radial electric field on the radial ion flux. Therefore it is not possible to decide if fast ion losses in the relatively large local mirror of W7-AS account for the missing RF power.

4. Discussion

Second harmonic hydrogen heating is a reliable means for heating of NBI plasmas and for sustaining plasmas at medium densities for the W7-AS stellarator. Earlier attempts to heat ECRH generated hydrogen plasmas were not successful. The available RF power at that time was only about 40% of the power of these recent experiments. This power was probably too low to generate and sustain a fast hydrogen tail. If so an increase in the heating efficiency at higher power could be expected especially in the successor experiment W7-X which should have better fast ion confinement.

5. Acknowledgements

We thank Dr. Brambilla for calculating the hydrogen energy distribution function, Dr. Baldzuhn for running DKES code, the ICRH group for the technical support with the RF systems, and the W7-AS team for providing the measured standard plasma parameters.

6. References

1. G. Cattanei et al., *23rd EPS conf. on Contr. Fusion and Plasma Physics, Kiev. 1996, pp. 499-502.*

2. M. Brambilla, *Kinetic Theory of Plasma Waves, Oxford, 1998.*

3. J. Baldzuhn, *private communications.*

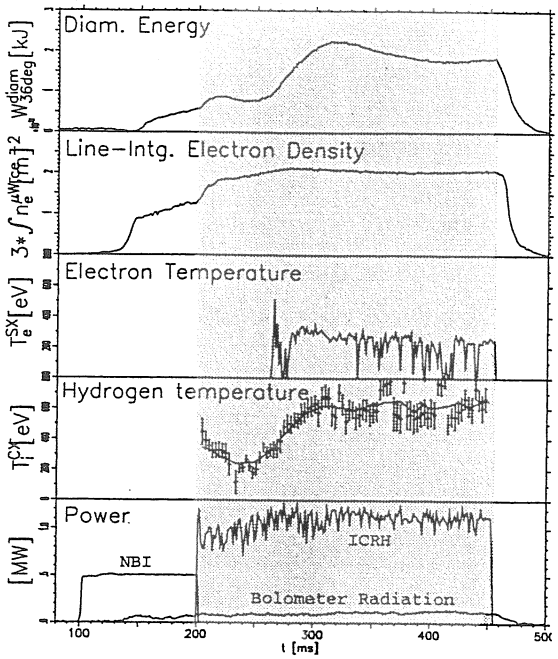

Figure 1: 2nd harmonic hydrogen plasma.

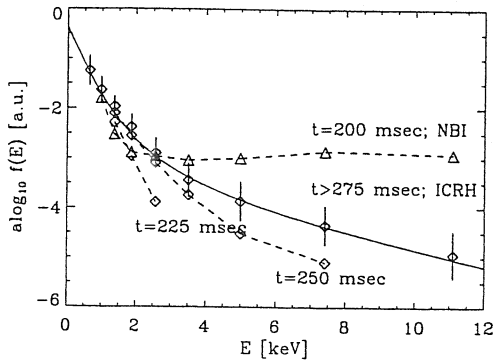

Figure 2: Hydrogen energy distribution function

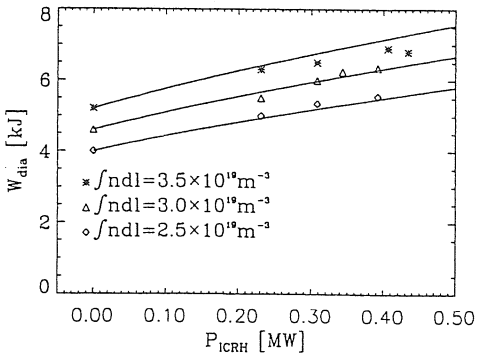

Figure 3: Diamagnetic energy for different power levels and densities.

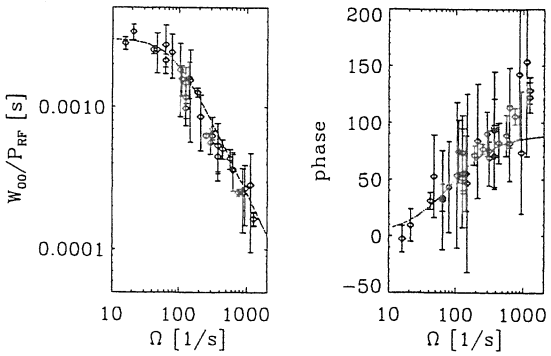

Figure 4: ICRH power modulation.

ELM-like Transport Events and their Impact on Confinement in W7-AS

M. Hirsch, M. Anton, J. Baldzuhn, J. H. Chatenet, C. Christou, M. Endler, J. Geiger, T. Geist, H.-J. Hartfuß, E. Holzhauer [1], G. Kühner, U. Stroth, S. Zoletnik [2]
and the W7-AS team

Max-Planck Institut für Plasmaphysik, EURATOM Ass., D-85748 Garching, FRG
[1] Institut für Plasmaforschung, Univ. Stuttgart, 70569 Stuttgart, FRG
[2] KFKI-RMKI, Budapest, Hungary

Introduction

In the stellarator W7-AS with plasma parameters close to the operational range of the quiescent H-mode, edge localized modes (ELMs) appear as bursts of turbulence associated with increased energy and particle flux across the last closed flux surface (LCFS) [1,2]. Confinement improves if the ELMs disappear and a quiescent H-phase is reached. In this phase the spectroscopically measured poloidal rotation increases together with the edge gradients for n_e, T_e and T_i.

Outside the parameter range of the quiescent H-regime for a great variety of plasma conditions relaxation phenomena are observed with characteristics similar to those of ELMs. We compare these ELM-like transport events with standard ELMs and study their qualitative dependence on the local plasma parameters and their possible influence on the quality of the confinement.

Characterization of ELM-like events

An example of ELM-like events in a discharge heated with 380 kW of NBI is shown in Fig. 1a. The magnetic configuration (edge rotational transform ι_a=0.350, plasma boundary defined by limiters) differs markedly from the operational range of the quiescent H-mode (ι_a=0.525±0.005, separatrix conditions). Neither an increase of heating power nor of density results in a quiescent H-mode. For comparison Fig. 1b shows typical ELM behaviour in a stationary ELMy H-mode at ι_a=0.523 with 400 kW of ECRH. The density is kept 10% below the threshold to a quiescent H-mode. A subsequent increase of the density induces the transition to the quiescent phase.

In both cases bursts of turbulence are correlated with a sudden loss of electron heat and an increase of H_α-emission. If intervals between this events are sufficiently long to be characterized (t > 200 μs) they appear like short H-phases, i.e. they show edge turbulence identical to the one in the quiescent H-mode [2]. Together with ELMs as well as together with the occurrence of ELM-like phenomena we observe periodic (10 - 30 kHz) but finite lifetime fluctuations (100 - 300 μs) with a poloidal mode number m = integer(ι_a^{-1}) in both density

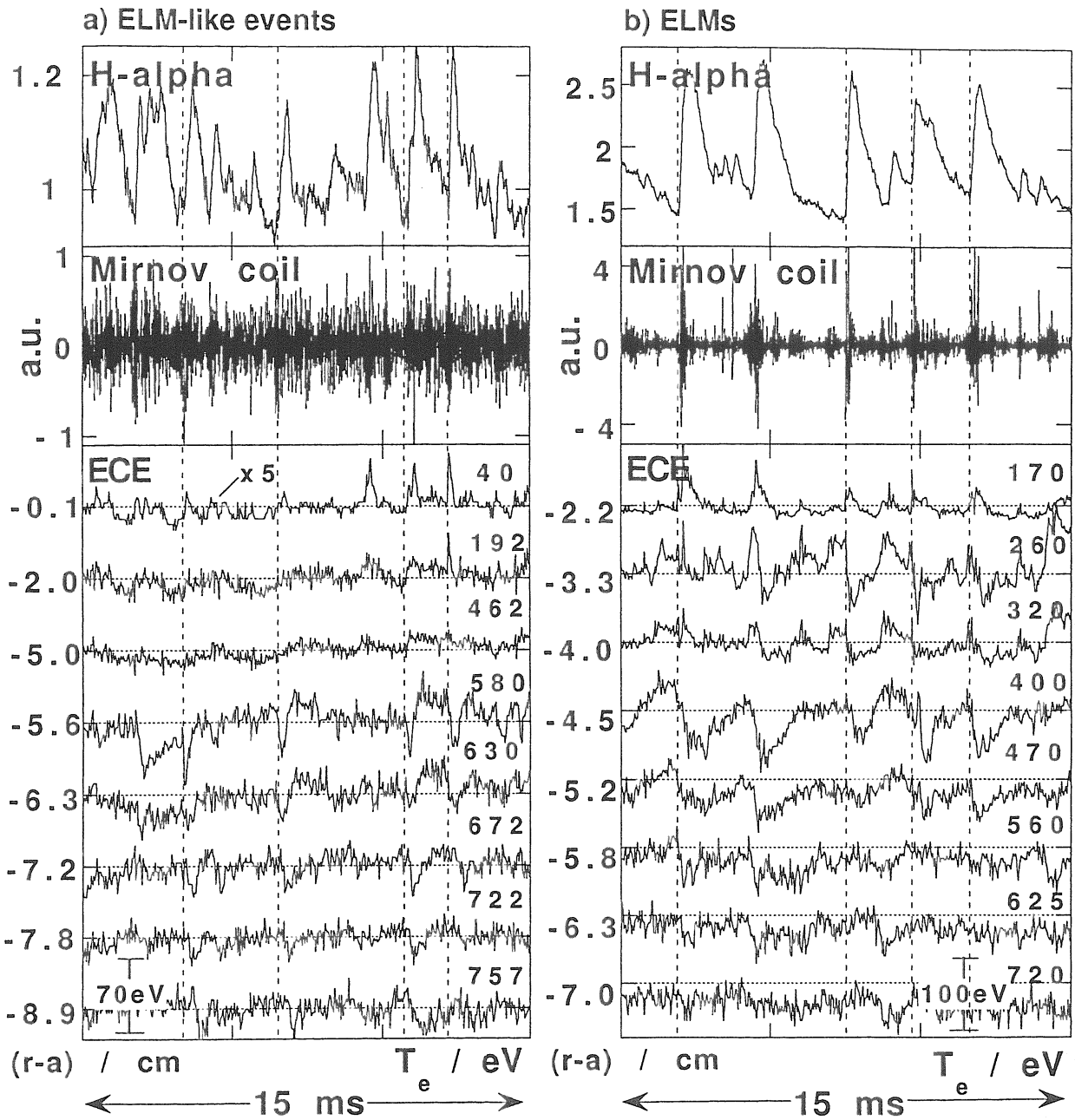

Fig. 1: Signals from Hα-emission, Mirnov coil (dominant coherent mode activity subtracted) and the outermost channels of the ECE radiometer measured a) during 15 ms of a stationary NBI-heated plasma (ι_a=0.350, limiter configuration) and b) during a stationary ELMy H-mode (ι_a=0.523, separatrix configuration). Some ELMs and ELM-like events are indicated by dashed lines.

and magnetic field [3,4]. This type of fluctuations is not seen during the quiescent H-mode. It is localized within the first few cm inside the LCFS and extends deeper into the plasma only if the pressure gradient is weak and confinement is poor. The temporal correlation of these instabilities with the short increase of transport related to each ELM or ELM-like event is a subject of further analysis. The magnetic precursor activity (f≈400kHz) which has been observed for ELMs [1] has not yet been investigated for ELM-like phenomena.

ELM-like phenomena and ELMs appear as transport events with increased electron heat and particle flux across the LCFS. The flattening of the edge density gradient is observed with

beam emission spectroscopy and reflectometry. The immediate loss of electron heat is characterized by a pivot point as shown by the ECE traces in Fig. 1. Whereas for ELMs this immediate energy loss affects less than the outermost 4 to 5 cm of the main plasma in case of the ELM-like events this region can extend up to 8 cm. In any cases, as a consequence of the fast edge cooling, a cold pulse propagates towards the plasma center on a diffusive time scale. This suggests that the inward propagating component of electron temperature fluctuations as measured at W7-AS [5] results from ELM-like events of differing size.

Dependence on plasma parameters

ELM-like phenomena are observed for a wide variety of discharge parameters (edge rotational transform, line averaged density) and different heating scenario with ECRH and NBI. Temperature and density profiles for the discharges used as an example in Fig. 1 are given in Fig. 2. At $\iota_a \approx 0.35$, with parameters clearly different from the quiescent H-mode operational range, the position of the pivot point of the ELM-like events varies within a few cm during the discharge and in general tends to be more than 3 cm inside the LCFS (3 to 5 cm inside LCFS for discharge in Figs. 1a and 2). The layer where the pivot point is observed is situated deeper inside the LCFS in configurations where the pressure gradient is shifted correspondingly. Single ELM-like events are more pronounced and more clearly separated from each other if pressure gradients are steep. If the pressure gradient is generally low events tend to merge in time and are less pronounced than in Fig. 1a.

This situation is clearly different for ELMs i.e. with operation parameters close to those of the quiescent H-mode operational window: Pronounced ELM-activity occurs with a pivot point that is mostly situated in a narrow layer approximately 3±0.5 cm inside the LCFS. However, no pronounced maximum of the pressure gradient exists at this position (Fig. 2). A steep pressure gradient develops right at this layer only after a quiescent phase is reached.

The dependence of ELM-like behaviour on the local temperature gradients has not yet been systematically analysed. In ELMy H-mode discharges the ELMs become more pronounced with increasing heating power and thus increasing temperature gradients. Below a

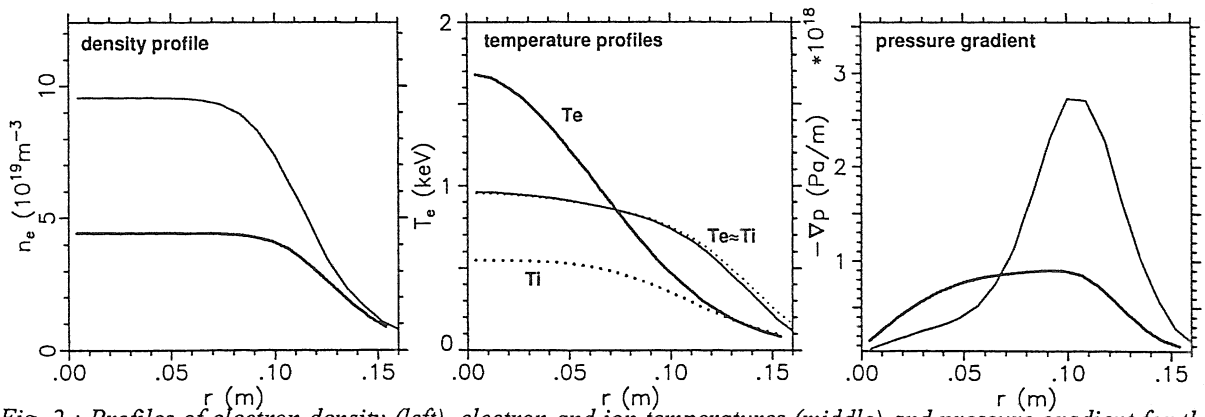

Fig. 2 : Profiles of electron density (left), electron and ion temperatures (middle) and pressure gradient for the discharges in Fig. 1. Thin lines correspond to the NBI heated discharge in 1a (#43715). For similar conditions optimum energy confinement in W7-AS is observed [6,7]. Thick lines correspond to the ELMy H-mode in Fig. 1b (#43536).

critical threshold power no ELMs are observed.

In order to identify the underlying instabilities, a stability analysis with respect to resistive and ideal interchange modes has been carried out for limiter dominated discharges ($\iota_a \approx 0.35$) which show ELM-like phenomena. In a radial range of the strong pressure gradients the NBI heated discharge in Figs. 1a and 2 is stable with respect to ideal interchange but marginally unstable with respect to the resistive interchange criteria. However, ELM-like phenomena are also observed in an ECR heated discharge with the same magnetic configuration which is expected to be linearly stable.

Impact on Confinement

In the ELMy H-mode at a heating power of 400 kW the typical energy loss per ELM is estimated from the profile changes to be <4% of the total stored energy at a typical ELM repetition frequency of about 1 kHz. As the energy confinement time is 25 ms a substantial fraction of the energy flux across the LCFS should be due to ELMs. Diamagnetic energy increases by up to 30% if an ELM free state is established. If ELM-like events disappear while other discharge parameters remain unchanged, an increase of the diamagnetic energy content of more than 20% has been observed. These observations indicate that a significant amount of energy flux is carried across the LCFS by ELMs or ELM-like events, respectively.

Conclusion

Both ELMs and ELM-like phenomena were found to be indistinguable with respect to their appearance as a burst in turbulence together with a transport event. For limiter dominated discharges at $\iota_a \approx 0.35$ the width and the localization of the layer where during an ELM-like event transport is transiently increased is correlated with width and maximum of the pressure gradient. However, for the ELMs observed close to the H-mode window the increase of transport occurs in a narrow layer where during the ELMy phase the pressure gradient shows no distinct maximum. Strong gradients occur only if ELMs disappear and a quiescent H-mode develops. Such the characteristics of both phenomena cannot be understood from the pressure gradient as the only driving force. In addition, also the stability of the transport barrier which is perturbed by the events will affect the behaviour of ELMs or ELM-like phenomena. These stabilizing elements are expected to be different for ELMs, i.e. under the separatrix conditions in the H-mode operational window and the configurations where ELM-like events occur.

References

[1] Hirsch M et al., Proc. 16th IAEA Conf. (Montreal) 2, 315 (1996)
[2] Hirsch M et al., Plasma Phys. Control. Fusion 40, 631 (1998)
[3] Zoletnik et al, this conference.
[4] Anton M et al, J. Plasma Fusion Res. SERIES 1, 259 (1998)
[5] Hartfuß H-J et al., Plasma. Phys. Control. Fusion 38, A227 (1996)
[6] Stroth U et al., Plasma Phys. Control. Fusion 40 (1998)
[7] Kick M et al., Proc. 16th IAEA Conf. 2, 27 (1996) and this conference

Electric Field and Transport in W7-AS

M. Kick, H. Maaßberg, M. Anton, J. Baldzuhn, M. Endler, C. Görner,
M. Hirsch, A. Weller, S. Zoletnik and the W7-AS Team

Max-Planck Institut für Plasmaphysik, EURATOM Association,
D-85748 Garching, Germany

Abstract:

At W7-AS, confinement properties are analysed and compared mainly with neoclassical predictions for quite different conditions. Low density ECRH discharges allow access to the very long mean free path regime for electrons (T_e up to 6 keV) whereas pure NBI and combined NBI/ECRH discharges at high density ($T_i \approx T_e \geq 1$ keV at $n_e \approx 10^{20}$ m^{-3}) lead to high performance (τ_E up to 50 ms). Depending on the achieved temperatures, the experimental transport analysis in the plasma core is consistent with the neoclassical predictions. The experimentally observed "electron root" feature with strong $E_r > 0$ is driven by the convective flux of ripple-trapped suprathermal electrons generated by the ECRH absorption. "Optimum" confinement is obtained in discharges with narrow density, but broad temperature profiles with steep gradients in the region of low densities and strong $E_r < 0$ close to the plasma edge. The large radial electric fields, both positive and negative, strongly reduce neoclassical transport. The achieved temperatures, however, are limited by the strong temperature dependence of the neoclassical transport.

1. Introduction

High temperatures are very important for the transport analysis in the stellarator long-mean-free-path (*lmfp*) regime. For these conditions, neoclassical theory predicts an unfavourable dependence of the transport coefficients on temperature. Thus, the transport

analysis in low-collisionality plasmas is suited best for the examination of the neoclassical predictions.

Within the traditional neoclassical theory, the radial electric field, E_r, plays an essential role in the confinement. A significantly improved confinement is predicted in the very *lmfp* regime with strongly positive E_r, the "electron root" [1] solution of the ambipolarity condition of the purely neoclassical particle fluxes. At W7-AS, this feature is predicted for the high power ECRH discharges with $T_e >> T_i$ and flat n_e and T_i profiles. Furthermore, multiple roots of the ambipolarity conditions may exist leading to a bifurcation problem which is quite similar to 1*st* order phase transitions in non-linear thermodynamics. For the highly peaked ECRH power deposition at W7-AS, however, suprathermal electrons being trapped in the toroidal mirror in the launching plane are responsible for an additional electron flux, Γ^{ECRH}, which may be comparable with the diffusive neoclassical ones and has to be included in the ambipolarity condition. The equivalent convective energy flux leads to a broadening of the "effective" deposition profile [2,3].

Close to the plasma edge at low temperatures, neoclassical theory fails. The confinement in this region is dominated by *"anomalous"* transport driven by fluctuations [4] as a *hypothesis*. Especially in W7-AS with the fairly low vacuum shear, the confinement properties depend sensitively both on the value of the rotational transform (rational values of ι can lead to confinement degradation) and on its shear, $\iota' = d\iota/dr$ [5,6]. For the "optimum" confinement discharges with narrow density and broad temperature profiles, fairly large negative E_r are measured [7-9] at outer radii which indicate very strong shear in the $E \times B$ poloidal plasma rotation close to the plasma edge. In the picture of fluctuation driven transport, both the magnetic shear ι', as well as the poloidal rotation shear, E_r', are expected [10] to decrease the radial correlation length of the fluctuations and, as a consequence, to reduce *anomalous* transport. However, the link between the spatial-temporal structure of the fluctuations and the driven transport is not clear yet.

2. ECRH-driven "electron root" feature

Strongly positive radial electric fields have been measured at W7-AS in low density discharges at high ECRH power levels. The electron temperature profiles are highly peaked (with $T_e(0)$ up to 6 keV) [11], whereas the ion temperature (only several 100 eV) and the density profiles are flat. The finding of the strongly positive E_r is related to an additional peaking of the central T_e profile indicating improved electron energy confinement. The corresponding experimental electron heat conductivity χ_e (from power balance) is much lower than the neoclassical one if E_r is not taken into account; see [9]. This feature is shown in Fig. 1 for a density scan with 1.2 MW ECRH power launched into the W7-AS "standard" configuration with a local minimum of the magnetic ripple leading to a significant fraction of trapped particles. Whereas T_e in the central "electron root" region decreases with increasing density, the T_e profile at intermediate radii is nearly independent on n_e. Thus, the $1/\nu$-scaling of the neoclassical electron transport in the outer "ion root" region with moderate E_r is directly confirmed.

For establishing the "electron root" feature, ECRH power and density thresholds have been found. These thresholds depend on the specific magnetic configuration, i.e. the fraction of trapped particles in the ECRH launching plane plays the dominant role. For example, the equivalent density scan with 1.2 MW in a "low mirror" configuration (i.e., much lower fraction of trapped particles in the ECRH launching plane) shows the "electron root" feature only at the lowest density of about $1.7 \cdot 10^{19}$ m^{-3}. For the W7-AS "standard" configuration (i.e., a significant fraction of trapped particles exists in the ECRH launching plane) the additional peaking of the central $T_e(r)$ together with strong $E_r > 0$ were found at the lowest densities of about $1.7 \cdot 10^{19}$ m^{-3} even at ECRH powers as low as about 400 kW.

The transient response of the central T_e when the ECRH power is reduced is shown by the ECE time traces in Fig. 2. At this density ($3.5 \cdot 10^{19}$ m^{-3}), the power

threshold for maintaining the "electron root" feature is between 400 kW and 800 kW. If the power is decreased below this threshold, the central peak of the T_e profile decays much faster than in the intermediate part of the profile which is determined by the "ion root" E_r. If the non-local (convective) radial flux, Γ_e^{ECRH}, of ripple-trapped suprathermal electrons contributes significantly to the ambipolarity condition, thus driving the "electron root" feature, the strongly positive E_r should decay on the ∇B-drift time scale (several 10 μs if the $\partial E_r/\partial t$ term is ignored). Then, the neoclassical heat diffusivity increases nearly instantaneously to the "ion root" level.

These conclusions are fully consistent with the fast transitions in the electrostatic potential profile measured with the heavy ion beam diagnostic at CHS; see [12]. In these experiments, both the density and the electron temperature, but also the ECRH power is much lower. Nevertheless, the observed spontaneous transitions in the radial electric field are very fast at CHS: the decay time of the strongly positive E_r is less than 100 μs. Also at W7-AS, spontaneous transitions in the "electron root" feature are indicated by the ECE data [11]. With slightly off-axis power deposition (close to the threshold in a B-scan) at low density and 1.2 MW power, the highly peaked T_e disappeared within 300 μs. In addition, to establish the "electron root" feature needs about three times longer which corresponds to the CHS findings in spontaneous transitions [12].

3. "Optimum" confinement with narrow density profiles

In high power purely NBI or combined NBI/ECR heated discharges, narrow density profiles in combination with steep temperature gradients and large $E_r < 0$ close to the plasma edge, where n_e becomes very small, are found. For this type of discharges, carried out at a rotational transform of $\iota \approx 1/3$ and shifted by a vertical field onto the inboard limiters, "optimum" confinement properties are found [7,8,13] with $T_e > T_i$ up to

1.5 keV and τ_E exceeding the ISS95 scaling [14] by at least a factor of 2. The experimental particle fluxes as well as the ion and electron energy fluxes are in good agreement with the neoclassical predictions up to 70% of the plasma radius. Furthermore, the predicted E_r obtained from the ambipolarity condition of the neoclassical fluxes is consistent with the experimental findings [9,15] even at the outer radii where the ambipolar neoclassical fluxes become very small. The measured steep outer temperature gradients (with $T_i \approx T_e$ within the experimental errors) allow for temperatures such high that neoclassical transport with its strongly rising temperature characteristic limits the bulk confinement. At the low outer densities, the strong steepening of the temperature profiles is consistent with a heat diffusivity χ only weakly dependent on density, i.e. χ is not proportional to 1/n, as found in [16]. For a fixed heating power the outer energy flux $Q \approx -n\chi T'$, allows for the high T' at low n.

Good wall conditioning and very low recycling are mandatory to obtain the narrow density profiles, see Fig. 3, and to provide global density control even for high NBI power levels (with a particle source strength of up to $2.5 \cdot 10^{20}$ /s) [7,8]. For NBI heated discharges under unfavourable recycling conditions, however, much broader density profiles and significantly lower temperatures were obtained; see Fig. 3 (dashed line). These different profiles have been obtained with different plasma limitation scenarios: (1) by symmetrically placed inboard limiters and (2) by movable limiters placed on top and bottom in the significantly elongated ("elliptical") planes. The two cases provide quite different recycling conditions. It is interesting to note that at the elliptical cross section the flux surface radial expansion is large so that the recycling fluxes for the top and bottom limiters are located at the very outside of the plasma. For the inboard limiters, however, flux expansion is much smaller, and, consequently, the neutrals can penetrate much deeper into the plasma thus leading to narrow density profiles ("density profile peaking") [17,18]. Moving the top and bottom limiters inward or applying a vertical magnetic field B_z allows to change from one limiter setting (inboard) to the other (top and bottom). In the latter case a broadening of the density profile relative to the

limiter position and a flattening of the temperature profile is observed. Eventually the density control gets lost if the contact to the inboard limiters disappears and the top and bottom limiters are the main limiting components. Once "optimum" confinement with narrow density profiles has been established it turns out to be very robust: even gas puffing, e.g., increases the central density, but does affect neither the density control nor the profile width.

Particle balance analyses clearly indicate [16,19,20] that the particle diffusivity at outer radii increases significantly with decreasing density. Then, for the narrow profiles with very low edge densities, the outer particle flux (being limited by particle sources at inner radii) determines the shape of the outer n_e profile. For the broad density profile, on the contrary, the flux increases with radius (the outer particle sources decay strongly with distance from the limiter). Thus the density profile roughly reflects the outer particle sources which, in turns, depend on the density profile. The particle fluxes at the plasma edge as found from the DEGAS and EIRENE code simulations [21,20] are by a factor of about 2 higher and decay much faster with distance from the limiter in the case of the broad density profiles compared to the narrow ones, see Fig. 4, right plot. Moreover, the outer (narrow) density profile is - within the experimental errors - independent of both the central density and the heating power. This result (see Fig. 3) supports the simple picture, that the shape of the density profile depends mainly on the recycling conditions, determined by limiter position and material composition. However, since the "optimum" confinement regime with narrow density profiles, establishes under NBI heating conditions central fuelling (by NBI) also contributes to the density profile peaking [13].

As a further aspect, the role of "edge physics" on the density control is briefly discussed. For the broad density profile of Fig. 3, no global density control was obtained and the central refuelling by NBI could not be balanced by the particle fluxes, i.e. the bulk density rises in time. In equivalent discharges with additional ECRH [16], global density control was obtained only for $P_{ECRH} \approx P_{NBI}$. As the ambipolar neoclassical particle fluxes are dominated by the electrons, the additional ECRH leads to an increased T_e which in

turn allows for higher particle fluxes. This picture might simply explain these early experimental findings ("ECRH density pump out").

For "optimum" confinement discharges with narrow density profiles, the temperature gradients at the outer radii are fairly steep (with $T_e \approx T_i$) and reflect the heating power; see Fig. 3. At about 2/3 of the plasma radius, the temperature flattens due to the strong temperature dependence of the neoclassical transport. Whereas the particle as well as the energy fluxes are in good agreement with the neoclassical predictions in this bulk part, the broad density discharge is different: the experimental heat fluxes from the energy balance are by a factor of about 2 larger than the neoclassical ones.

In order to separate the effect of a narrow density profile and the formation of the steep temperature gradients close to the plasma edge, an "H-mode" discharge under clear separatrix conditions (at $\iota = 0.52$) and with pure NBI heating was established. After the density-ramping phase (by applying a sufficient gas pulse), a "quiescent H-mode" phase with a broad density profile, but fairly low temperatures developed; see Fig. 5. Also for this case, the neoclassical prediction for the energy fluxes is too low compared with the power balance. In a further transition phase (between 0.32 s and 0.36 s), the density profile narrows and the regime of "optimum" confinement with narrow density profiles, as described above, develops with the identical features of the NBI discharges with contact to the inboard limiters at $\iota = 0.34$ (H-NBI regime reported in [13]; see also Fig. 3, dotted lines). A sequence of spontaneously evolving huge ELMs may lead to a strong particle pump out at the edge and allow for the transition to the state with the narrow density profile. This ELM activity in the transition phase is located very close to the separatrix (only found in the outer interferometry channel). Within this transition phase, despite of energy losses associated with the ELMs, a broad temperature profile with steep gradients at the outer radii establishes within about 20 ms which is comparable to the energy confinement time. After the strong ELM activity has disappeared, the central density continues to increase (loss of the density control with NBI fuelling leads to the cut-off in the ECE measurements of T_e), but also the profile further narrows. In this

"optimum" phase, the bulk energy transport is again in agreement with the neoclassical prediction.

In a quite different experimental scenario with an edge value of ι close to a critical one ($0.34 \leq \iota_a \leq 0.36$) [5,20] with a strong effect on the global confinement properties, the link between the density profile broadness and the steepening of the outer temperature profile is also observed. In these ECRH discharges (400 kW at $n_e \approx 6 \cdot 10^{19}$ m^{-3}) shifted onto the inboard limiters, the density is controlled by external gas puffing leading to higher edge particle fluxes compared to the NBI discharges without strong gas feed. Depending sensitively on the rotational transform at the edge, ι_a, a quite similar feature of narrow (broad) density profiles and steep (flat) edge temperature gradients develop [20]. EIRENE code simulations indicate an increased edge particle flux (by about 50%) for the broad density profile.

In summary, different experimental cases have been described with a close correlation between narrow density profiles with reduced particle edge fluxes and superior energy confinement with broad temperature profiles. The role of "edge physics" in terms of limiter versus separatrix, limiter location and conditioning but also ELM induced edge density pump out has been considered as well as central beam fuelling.

Generally, the narrow density profiles with fairly high temperature in the n_e-gradient region where neoclassical transport prevails, lead to rather high radial electric fields [8,9,13]. Only close to the plasma edge, the measured E_r are even stronger than the ambipolar neoclassical prediction. For these strongly negative E_r, however, the traditional neoclassical ordering fails [22]. On the other hand, additional convective contributions due to the low density and high temperature (direct losses of ripple-trapped ions) may also contribute to the ambipolarity condition (i.e., E_r becomes more negative). As an example, for the broad density profile shown in Fig. 3, the neoclassically predicted E_r is much less pronounced; see Fig. 4. For the "H-mode" phase and the "optimum" confinement with narrow density profiles in the separatrix discharge of Fig. 5, the neoclassically predicted and experimental E_r support this picture. However, the E_r are less negative and the

difference between both phases is less pronounced compared to the limiter examples of Fig. 4. For "optimum" confinement conditions the shear in the outer E_r, i.e. the velocity shear in the poloidal plasma rotation, is very large which might affect the *anomalous* transport.

4. Behaviour of Fluctuations

Density fluctuations in the plasma edge and their radial structure are measured by a Lithium beam (LiB) diagnostic with a radial resolution of 0.5 - 1 cm [23]. Their poloidal propagation properties are observed with a reflectometer using the Doppler shift of the reflected radiation measured under a finite poloidal tilt angle of the antenna [24]. The spatial structure of MHD modes is obtained from a 10-camera miniature soft X-ray system (MiniSox) [25]. A poloidal arrangement of 16 Mirnov coils allows the singular value decomposition (*SVD*) of the magnetic fluctuations and thus the reconstruction of the poloidal and temporal structure of different signal components [26]. A combined analysis of the signals from LiB and Mirnov coils reveals a significant correlation between several Lithium light channels inside the last closed magnetic surface *(LCMS)* and the Mirnov signals [27]. Thus, in most discharges (both ECR and NBI heated, exception: the quiescent "H-mode") a fluctuation feature with a rather broad frequency distribution around 10-30 kHz is observed. As the typical correlation time of this fluctuation is 50-100 μs, i.e. it contains a few oscillations only, it will be called *incoherent* in the following (it was called burst-like in [27]). The *SVD* shows a propagation of this feature in electron diamagnetic drift direction and an m = *integer* $(1/\iota_a)$ poloidal mode structure. Correspondingly, the poloidal "wavelength" of this *incoherent* feature is about 30-40 cm. With the parallel wavelength being very large ($k_{\parallel} \approx 0$) this implies, that this feature is "resonant" to the low order rational values of the ι profile. The radial extent should be dependent on the magnetic shear at the "resonant" surface as well as on the shear of the poloidal rotation, i.e. E_r'.

In addition, in NBI and combined NBI/ECR heated discharges, a dominant fluctuation component with a very narrow peak in the frequency spectrum at 25-40 kHz can show up, see Fig. 6, upper left plot. This *coherent* mode activity is identified as Global Alfvén Eigenmode (GAE) [28,29]. These modes are excited by resonant energetic ions from the mainly tangential NBI and propagate in the ion diamagnetic direction. Both, the frequency and the poloidal mode structure as derived from soft X-ray tomography agree with the predictions based an the Alfvén gap structure, and are very sensitive to the ι profile. It seems to be unlikely that these GAE modes significantly affect the confinement properties at W7-AS for the following reasons: The eigenfunction of the GAE modes peaks typically within 70% of the plasma radius [28] where neoclassical transport dominates for the "optimum" confinement. Furthermore, the Mirnov coil data indicate a fairly low amplitude: an upper limit at the "resonant" surface is estimated to be $\tilde{B}/B \leq 10^{-5}$. Compared to the *incoherent* feature, the correlation time of this GAE activity is rather large (0.5 ms to 2 ms).

For the NBI heated discharge of Fig. 6, the GAE mode activity strongly disturbs the interpretation of the LiB data. For fairly similar ECRH discharges (see also Sect. 3), however, this analysis is reliable since no GAE activity is driven. In general, high correlation with the Mirnov coil data is observed [27] indicating that the *incoherent* feature is localised close to the plasma edge. Although the density fluctuation amplitude is very similar inside the *LCMS* for "optimum" and "degraded" confinement, the radial correlation length is shorter for the "optimum" confinement conditions. At low densities where only a small radial electric field is expected, however, these *incoherent* fluctuations can even disappear without affecting the confinement [27].

When comparing the *coherent* and *incoherent* fluctuation components between conditions with "optimum" and "degraded" confinement (equivalent to the discharges discussed in Sect. 3), we note that at "optimum" confinement the average frequencies of both features are larger than at degraded confinement, whereas their correlation times are reduced, i.e. their frequency spectra broaden (see Fig. 6, left part).

The Doppler shift of the reflectometer signals reflected at density structures a few cm inside the *LCMS* increases strongly with the improvement of confinement. These observations can be explained by an increased poloidal propagation velocity of the density structures and/or a decrease of their poloidal wave vectors. Fig. 6 (right part) compares the radial profiles of E_r obtained from spectroscopy under "optimum" and "degraded" confinement conditions. As the poloidal propagation velocity of the perturbations and thus the measured frequency of fluctuations is affected by the poloidal $E \times B$ velocity, the strongly negative E_r could be an explanation for the higher frequencies observed with "optimum" confinement. In addition, the larger E_r is connected to a larger radial E_r shear. The corresponding shear in the poloidal $E \times B$ rotation can reduce both, the radial correlation length and the correlation time, thus reducing the radial extension of this *incoherent* feature.

As a reduced correlation time and radial extent of fluctuations is often thought to be associated with reduced anomalous transport, such a relation is conjectured here. It should be kept in mind, however, that a knowledge of the amplitude, correlation lengths and correlation time of density or magnetic fluctuations is not sufficient to determine the turbulent $E \times B$ transport. For an estimate of the fluctuation driven transport, information on electric potential or field fluctuations and their correlation and phase with the density fluctuations would be required in addition, information we are lacking for the confinement region. On the other hand, even if the two features discussed here were not directly responsible for the anomalous transport at the edge of W7-AS, those fluctuation components which are responsible, might well be subject to the same decorrelation mechanism due to the radial electric field shear as discussed above.

5. Conclusions

Neoclassical theory is confirmed by the experimental transport analysis in low-collisionality W7-AS plasmas, i.e., if the bulk plasma has sufficiently high temperatures.

This conclusion holds for the ion and electron heat conduction as well as for the particle transport. Also the predicted ambipolar electric field is consistent with experimental findings (except when the strongly positive "electron root" is predicted). Based on purely thermal neoclassical particle fluxes, the ambipolarity condition typically predicts these strongly positive E_r ("electron root") in low density ECRH plasmas which is not consistent with the experimental findings [30]. Only for special conditions, where a significant amount of the ECRH power is absorbed by ripple-trapped electrons, do the ECRH generated suprathermal electron fluxes lead to the strong $E_r > 0$. In this sense, an ECRH driven "electron root" feature was found at W7-AS (with T_e (0) up to 6 keV). However, the basic assumption of the conventional neoclassical theory (E_r small) is violated for ions (and impurities) by very large E_r. In the case of higher density, the radial electric fields are typically slightly negative allowing for the conventional neoclassical approach.

Global confinement properties are strongly dependent on the broadness of the density profiles and the recycling conditions. Only for narrow density profiles steep temperature gradients develop in the region of low densities leading to "optimum" energy confinement (maximum τ_E). Strongly negative E_r connected with strong $E \times B$ shear are measured at the outermost radii affecting the observed fluctuation features.

With respect to the next generation large stellarators with higher temperatures, neoclassical theory seems to be a reliable tool for the analysis of the main part of the plasma. The role of the radial electric field on reducing the neoclassical transport coefficients in the *lmfp* regime is experimentally confirmed both for the ions and for the electrons in further optimised stellarators. The edge region, i.e., the density gradient region, will be of similar size in larger devices and may play a minor role for the global confinement properties. However, two aspects need further clarification: the role of recycling and external pumping (walls, limiter and divertor) on the density profile control, and the fluctuation driven *anomalous* transport close to the plasma edge.

References

1 H. E. Mynick and W. N. G. Hitchon, Nucl. Fusion **23**, 1053 (1983)

2 M. Romé *et al.*, Plasma Phys. Control. Fusion **39**, 117, (1997),

3 S. Murakami *et al.*, J. Plasma Fusion Res. SERIES **1**, 122 (1998)

4 A. J. Wootton *et al.*, Phys. Fluids, **B2**, 2879 (1990)

5 R. Brakel *et al.*, *Proc. 25th EPS Conf. Contr. Fusion Plasma Physics,* Prague (1998)

6 R. Brakel *et al.*, Plasma Phys. Control. Fusion **39**, B283, (1997)

7 M. Kick, F. Wagner and the W7-AS Team, J. Plasma Fusion Res. SERIES **1**, 19 (1998)

8 M. Kick *et al.*, *16th International Conference Fusion Energy*, Montreal, 1996 (International Atomic Energy Agency, Vienna 1997), Fusion Energy 1996, Vol. 2, p. 27

9 J. Baldzuhn, *et al.*, Plasma Phys. Control. Fusion **40**, 117, (1997)

10 K. H. Burrell, Phys. Plasmas **4**, 1499 (1997)

11 H. Maaßberg *et al.*, submitted to Plasma Phys. Control. Fusion (1998)

12 A. Fujisawa *et al.*, J. Plasma Fusion Res. SERIES **1**, 84 (1998)

13 U. Stroth, *et al.*, Plasma Phys. Control. Fusion, **40**, 1551 (1998)

14 U. Stroth *et al.*, Nucl. Fusion **36**, 1063 (1996)

15 J. Baldzuhn *et al.*, J. Plasma Fusion Res. SERIES 1, 226 (1998)

16 H. Ringler *et al.*, Plasma Phys. Control. Fusion, **32**, 933, (1990)

17 F. X. Söldner *et al.*, Phys. Rev. Lett., **61**, 1105, (1988)

18 B. Unterberg *et al.*, Plasma Phys. Control. Fusion, **39**, B189 (1997)

19 R. Brakel *et al.*, *14th International Conference Plasma Physics Controlled Nuclear Fusion Research,* Würzburg, 1992 (International Atomic Energy Agency, Vienna 1993), Vol. 2, p. 501

20 O. Heinrich *et al.*, *Proc. 24th EPS Conf. Contr. Fusion Plasma Phys.*, Berchtesgaden, 1997, Vol. 21A IV, p. 1593

21 F. Sardei *et al.*, *Proc. 18th EPS Conf. Contr. Fusion Plasma Phys.*, Berlin, 1991, Vol. 15 C II, p. 193

22 H. Maaßberg *et al.*, J. Plasma Fusion Res. SERIES **1**, 103 (1998)

23 S. Zoletnik *et al.*, Plasma Phys. Control. Fusion, **40**, 1399 (1998)

24 E. Holzhauer, M. Hirsch *et al.*, submitted to Plasma Phys. Control. Fusion (1998)

25 C. Görner *et al.*, *Proc. 24th EPS Conf. Contr. Fusion Plasma Phys.*, Berchtesgaden, 1997, Vol. 21A IV, p. 1625

26 M. Anton *et al.*, *Proc. 24th EPS Conf. Contr. Fusion Plasma Phys.*, Berchtesgaden, 1997, Vol. 21A IV, p. 1645

27 S. Zoletnik *et al.*, *Proc. 25th EPS Conf. Contr. Fusion Plasma Phys.*, Prague, 1998

28 A. Weller *et al.*, J. Plasma Fusion Res. SERIES **1**, 263 (1998)

29 A. Weller *et al.*, Phys. Rev. Lett., **72**, 1220 (1994)

30 H. Maaßberg *et al.*, Phys. Fluids, **B5**, 3627 (1993)

Figure Captions

Fig. 1 Electron density and temperature profiles for density scan at P_{ECRH} = 1.2 MW (at 140 GHz X-mode launching) for the W7-AS "standard" configuration. Equal symbols and lines chosen for equal discharges.

Fig. 2 Time traces of the electron temperature measured by the ECE diagnostic (central ECE channels) for the discharge at $n_e \approx 3.5 \cdot 10^{19}$ m^{-3} in Fig. 1. The ECRH power is reduced from 1200 to 800 kW (left) and from 800 to 400 kW (right).

Fig. 3 Electron density and temperature profiles for "optimum" confinement conditions at different density and heating powers with pure NBI and combined NBI/ECRH (solid line: NBI, 1350 kW, combined with ECRH, 750 kW; dot-dashed line: NBI, 1300 kW, combined with ECRH, 350 kW; dotted line: 450 kW, pure NBI). A discharge with "degraded" confinement is given as reference (dashed line: 850 kW pure NBI).

Fig. 4 Left: The radial electric field profile from neoclassical prediction and from the poloidal rotation measurements for the "optimum" confinement discharge (solid line: neocl. predict., and full dots: measurement) and for the "degraded" confinement (dashed line: neocl. predict.) corresponding to discharges in Fig. 3 (also solid and dashed lines). Right: The corresponding "experimental" particle fluxes as derived from EIRENE code (dot-dashed line for the "optimum" confinement discharge) and DEGAS code (dotted line for the "degraded" confinement) calculations compared to the neoclassical predictions from DKES code (solid and dashed, respectively).

Fig. 5 Contour plots of density (left, from Li-beam) and of electron temperature (right, from ECE) vs. radius and time. The "quiescent H-mode", the transition and the "optimum" confinement phases are indicated.

Fig. 6 Left: Comparison of the spectra of *coherent* (upper left) and *incoherent* (lower left) $\partial \tilde{B} / \partial t$ singular value decomposition (SVD) components between a discharge with "optimum" confinement (full lines) and degraded (dotted lines) confinement. Right: The corresponding radial electric fields measured by spectroscopy for "optimum" confinement

(full symbols and line) and degraded (open symbols and dotted line) confinement, the radial position of the limiter is indicated within the spatial uncertainty.

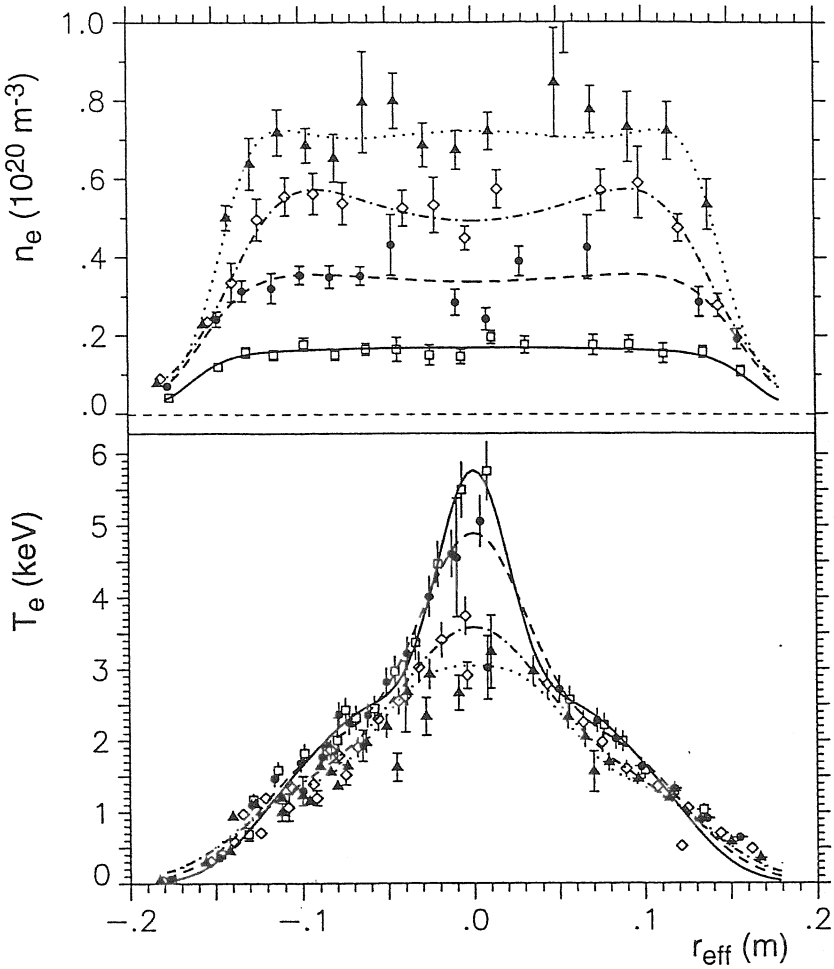

Fig. 1 Electron density and temperature profiles for density scan at P_{ECRH} = 1.2 MW (at 140 GHz X-mode launching) for the W7-AS "standard" configuration. Equal symbols and lines chosen for equal discharges

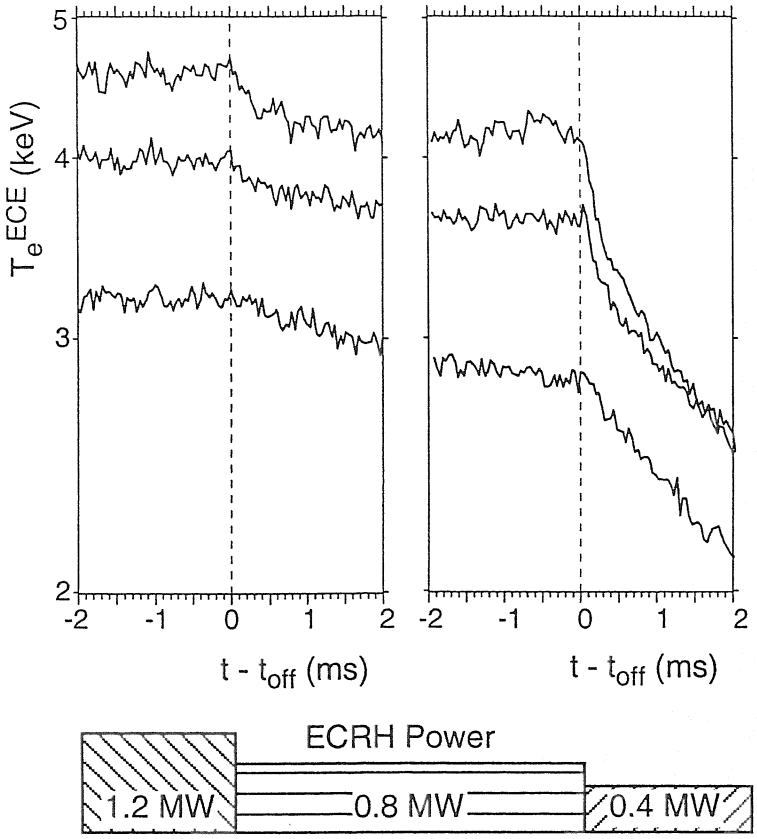

Fig. 2 Time traces of the electron temperature measured by the ECE diagnostic (upper 2 lines: central ECE channels ("electron root" feature), and lower lines: ECE channel at intermediate radius ("ion root"), respectively) for the discharge at $n_e \approx 3.5 \cdot 10^{19}$ m^{-3} in Fig. 1. The ECRH power is reduced from 1200 to 800 kW (left) and from 800 to 400 kW (right).

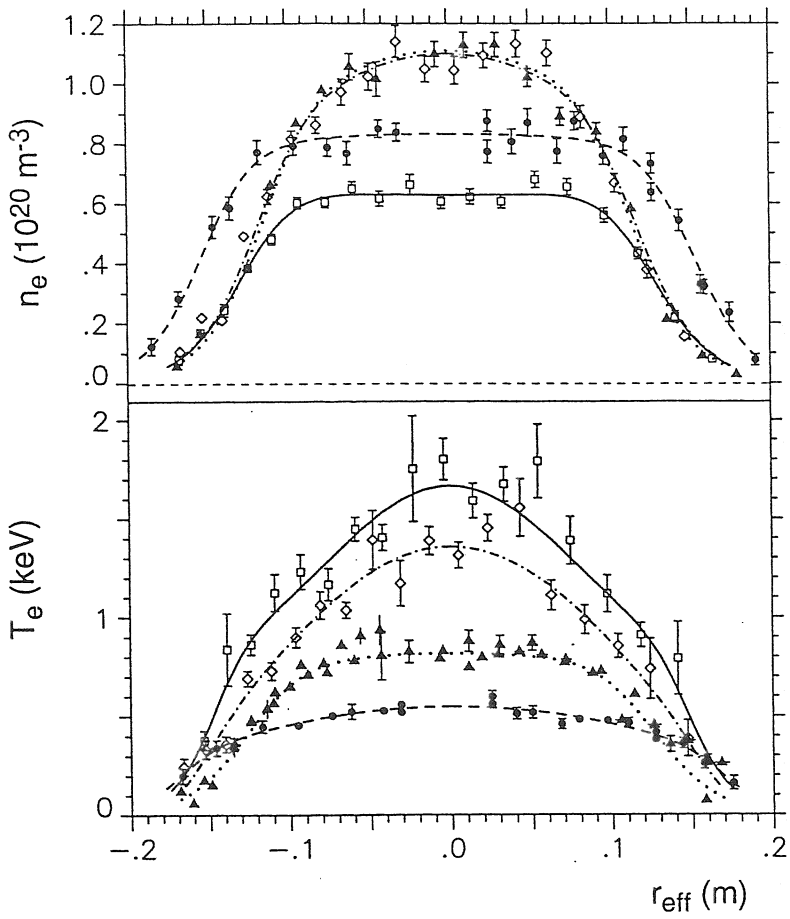

Fig. 3 Electron density and temperature profiles for "optimum" confinement conditions at different density and heating powers with pure NBI and combined NBI/ECRH (solid line: NBI, 1350 kW, combined with ECRH, 750 kW; dot-dashed line: NBI, 1300 kW, combined with ECRH, 350 kW; dotted line: 450 kW, pure NBI). A discharge with "degraded" confinement is given as reference (dashed line: 850 kW pure NBI).

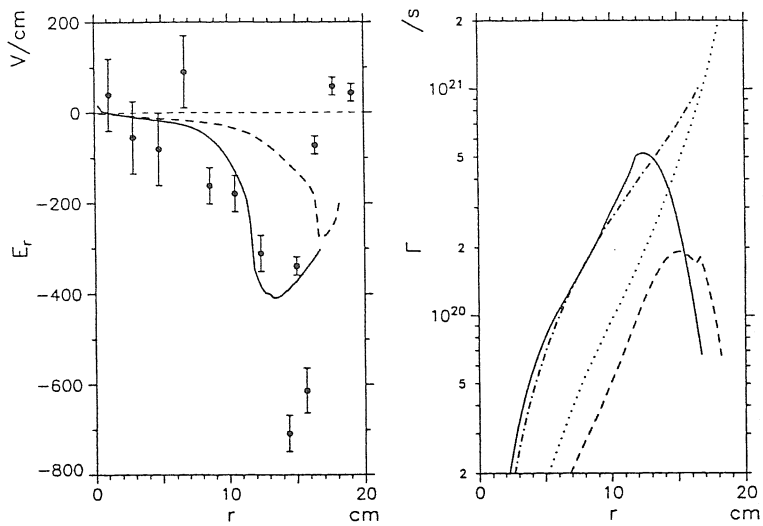

Fig. 4 Left: The radial electric field profile from neoclassical prediction and from the poloidal rotation measurements for the "optimum" confinement discharge (solid line: neocl. predict., and full dots: measurement) and for the "degraded" confinement (dashed line: neocl. predict.) corresponding to discharges in Fig. 3 (also solid and dashed lines). Right: The corresponding "experimental" particle fluxes as derived from EIRENE code (dot-dashed line for the "optimum" confinement discharge) and DEGAS code (dotted line for the "degraded" confinement) calculations compared to the neoclassical predictions from DKES code (solid and dashed, respectively).

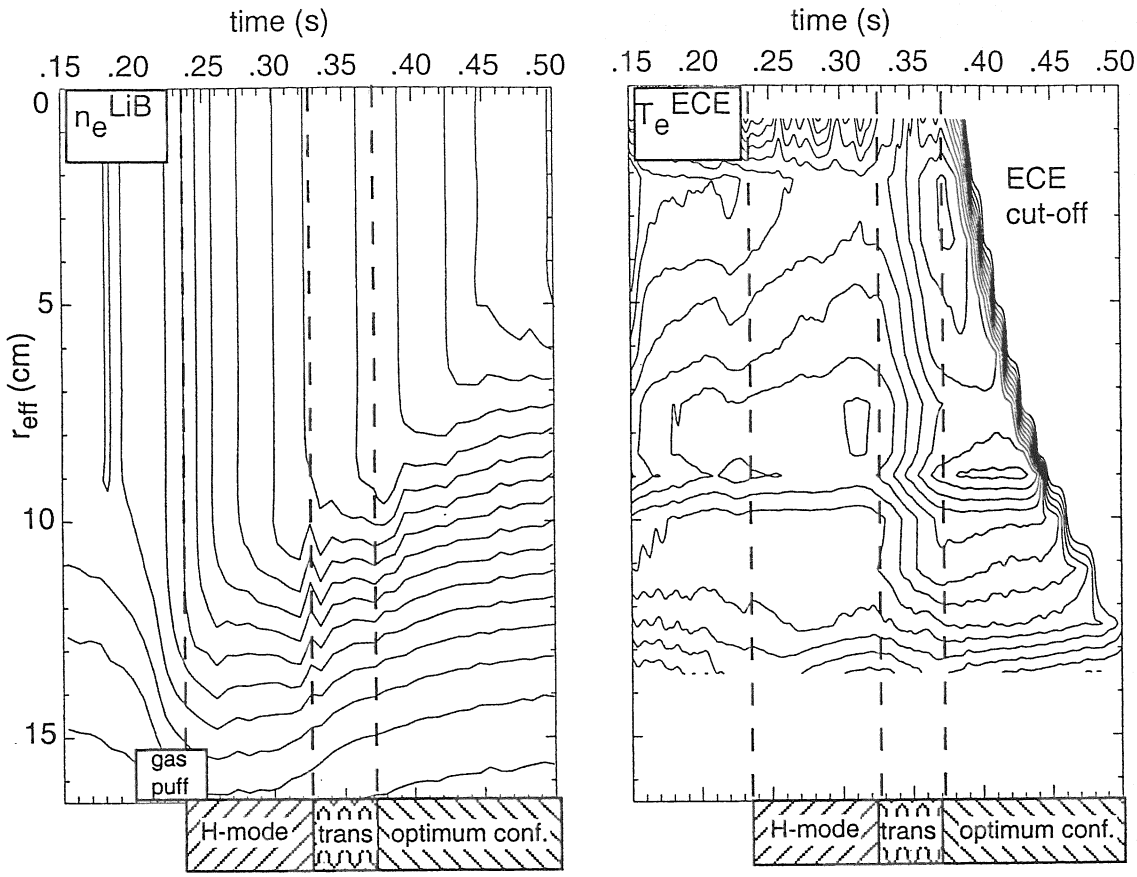

Fig. 5 Contour plots of density (left, from Li-beam) and of electron temperature (right, from ECE) vs. radius and time. The "quiescent H-mode", the transition and the "optimum" confinement phases are indicated.

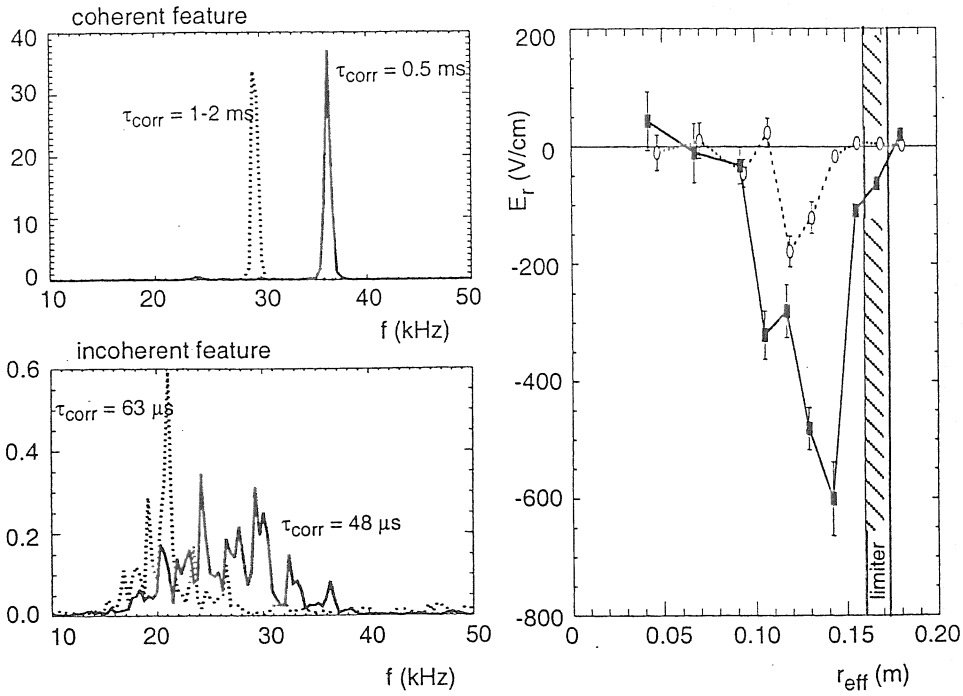

Fig. 6 Left: Comparison of the spectra of *coherent* (upper left) and *incoherent* (lower left) $\partial\tilde{B}/\partial t$ singular value decomposition (SVD) components between a discharge with "optimum" confinement (full lines) and degraded (dotted lines) confinement. Right: The corresponding radial electric fields measured by spectroscopy for "optimum" confinement (full symbols and line) and degraded (open symbols and dotted line) confinement, the radial position of the limiter is indicated within the spatial uncertainty.

Measurement of transient particle transport coefficients in W7-AS

J.P.T. Koponen, T. Geist, U. Stroth, O. Dumbrajs*, S. Fiedler, H.-J. Hartfuß, O. Heinrich and the W7-AS Team

Max-Planck-Institut für Plasmaphysik, EURATOM Association, Boltzmannstrasse 2, D-85748, Germany

**Department of Technical Physics and Mathematics, Helsinki University of Technology. FIN-02150, Espoo, Finland*

Introduction: The understanding of the particle transport in fusion devices is as important as the understanding of the energy transport. The particle transport is less studied than the energy transport due to larger experimental difficulties. In particular, perturbative particle transport experiments have the problem that both the production of density perturbations and accurate measurements of small perturbations in the plasma density are difficult to obtain.

The earlier experimental knowledge of the transport in the bulk plasma in the W7-AS stellarator has been based on transport studies made with equilibrium methods (particle balance) [1-3]. According to these studies the diffusion coefficient depends inversely on density and increases with heating power. The density dependence leads to an increase of the diffusivity in the plasma edge region. The particle balance method however does not separate between diffusive and convective fluxes.

A 10-channel microwave interferometer [4] was build at W7-AS for advanced time dependent particle transport investigations, which allow for a separation of diffusive and convective contributions to the particle transport. This paper reports on extensive transient particle transport studies carried out with the multichannel interferometer. The density perturbations were produced by modulating the gas feed to the plasma, as described in [5].

The method: Electron density perturbations were produced by modulating the particle source. The signal driving the gas valve was modulated sinusoidally which produced a harmonic perturbation propagating from the plasma edge to the center. Because the main particle source in W7-AS comes from the limiter, the perturbation of the source was small providing a density perturbation of 1-5 percent of the local density.

The 10-channel microwave interferometer measured the line integrals of the electron density. The electron density perturbation, i.e. the Fourier-coefficients of the density at the modulation frequency, are determined from the line integrals by inverting the real and the imaginary part separately with the inversion method described in [6].

In order to model the propagation of the density perturbation we solved the radial, Fourier-transformed particle transport equation [5]:

$$i\omega\tilde{n}(r) = \left(\frac{1}{r}\frac{\partial}{\partial r}r\right)\left(-D\frac{\partial}{\partial r}\tilde{n}(r) + V\tilde{n}(r)\right) + \tilde{P}(r). \tag{1}$$

Here r is the radius, ω is the gas puff modulation frequency, and thus the frequency of the harmonic perturbation propagating in the plasma. $\tilde{n}$ is the electron density perturbation, i.e., the Fourier-transform of the density at the gas puff modulation frequency ω. D is the diffusion coefficient and V is the convective velocity (if the sign is negative it is an inward directed pinch). $\tilde{P}$ is the modulated perturbative electron source simulated with the Monte-Carlo code EIRENE [7].
The measured complex perturbation profile is fitted with the simulated perturbation profiles solved from Eq. (1) by varying the transport coefficients D and V. The diffusion coefficient was a constant independent of the radius and the convective term was modeled with the expression $V = (a/(1 + exp(-(r + b)/c)) + d)(r/r_{boundary})$. To summarize, D had one parameter and V four: a, b, c, d. Increasing the amount of the parameters of D overparametrized the fitting problem. A fit example is illustrated in Fig. 1 and the resulting transport coefficients are sketched in Fig. 2. Note, that the inward convection occurs at the radial region where the amplitude grows in the direction of the propagation. This cannot be explained without an inward convective term.

Results: We carried out scans in the electron density (line averaged density $\bar{n} = 0.5...3\times 10^{19}$ m^{-3}, which equals to $1...6\times10^{19}$ m^{-3} peak density), ECH heating power $P_{ECH} = 180...470$ kW, and the magnetic field $B = 1.25$ T and $B = 2.5$ T. The rotational transform ι was always approximately 1/3 and the separatrix at 0.17 m. The regression analysis of the results from nearly 50 discharges gives a scaling for the transient particle diffusion coefficient of the form:

$$D = (0.84 \pm 0.05)n_e^{-1.18\pm0.13}T_e^{0.69\pm0.22}B^{-0.51\pm0.22}. \tag{2}$$

Here n_e is the central electron density in 10^{19} m^{-3}, T_e is the central electron temperature in keV and B is the toroidal magnetic field in T. The resulting dimension of D is m^2/s. The scaling is not valid in the region $r \geq 0.12$ m. The transport in the outer region is driven also by the convection and therefore the diffusion coefficient in that region is not well defined (we fitted constant D). Since only two interferometer channels go through the plasma center, the scaling might not be relevant at $r \leq 0.05$ m.
The earlier particle balance diffusion coefficient scalings in W7-AS are as follows. Ref. [1] reports power degradation of the diffusivity and that the doubling of the magnetic field makes D three times smaller. In [2] (an edge transport study) D scales like $1/(nB)$. The temperature dependence was only marginal. In [3] $D \sim 1/n^2$ or $D \sim 1/(nT_e)$ was not distinguishable. Our density dependence agrees with all these studies, but there

are differences in the temperature and magnetic field scalings. These differences can be commented in two ways. The particle balance studies are mainly valid in the outer region where our scaling is not valid. Furthermore, particle balance studies give in fact scalings of the total particle flux and not diffusion coefficient. Therefore the existence of a pinch at the boundary most likely causes this difference. Secondly, equilibrium and perturbation scalings may differ, if D depends e.g. on ∇n. Altough we did not see difference in our density scalings (see below).
In the inner plasma, the convective flux is negligible compared with the diffusive flux (in the example case Fig. 2, $r \leq 0.12$ m), only in the outer plasma $r \geq 0.12$ m the convection plays important role.
We did not find any clear dependence for the convective coefficient in the edge on plasma parameters. The magnitude of V at the outer region was typically -10 to -100 m/s. However, there is a relation between the radial point up to which the pinch is active (b in the model of the convection coefficient) and the radial point R_v where the density gradient region ends. This is illustrated in Fig. 3. The values for R_v were calculated from density profiles measured with Thomson scattering, thus independently of the multi-channel interferometer. The correlation found is a clear evidence that the density gradient in W7-AS is driven not only by the particle source but also by the inward convection. The inward convection might be driven by e.g. the turbulence in the outer plasma region.

Outward convection: Outward convection was detected with an ECH power $\geq$ 600 kW in shots with a hollow density profile. The analysis was not possible without a significant outward convective term in the inner plasma. With ECH of 1.3 MW, the density perturbation peaked at the plasma edge and could not propagate into the plasma. The opposite could be expected since the particle balance studies [1] with ECH power degradation predict a large diffusion coefficient D and hence a fast propagation to the center. With a large D, the data can be explained only if V is outward directed. A natural explanation for the outward convection is the neoclassical ∇T-term. Therefore we speculate, that the inward pinch might exist also in the inner plasma but is cancelled by the ∇T-driven outward transport for the smaller ECH powers.

Comparison with the equilibrium transport coefficients: The equilibrium transport coefficients can be calculated from the simulated equilibrium source profiles (EIRENE) and the measured electron density profiles. A comparison between the perturbative and equilibrium particle diffusion coefficient is illustrated in Fig 4. The ECH power was 470 kW, the magnetic field 2.5 T, $\iota \approx 1/3$, and $\bar{n}$=1,2 and 3 $\times 10^{19}$ m^{-3} (the middle density is shown). The coefficients agree within the error bars in the region not affected by the inward convection for all three densities.

References:
[1] F. Sardei et al, Proc. 17th EPS Conf., Amsterdam, Vol. 14B, Part II, 471, (1990).
[2] P. Grigull et al, J. Nucl. Mater., **196-198**, 101, (1992).
[3] O. Heinrich et al, 24th EPS Conf., Berchtesgaden, Vol. 21A, Part IV, 1593, (1997).
[4] T. Geist, E. Würsching, H.-J. Hartfuss, Rev. Sci. Instrum. **68**, 1162 (1997).
[5] K. W. Gentle, O. Gehre, K. Krieger, Nucl. Fusion, **32**, 217, (1992).
[6] J. P. T. Koponen, O. Dumbrajs, Rev. Sci. Instrum., **68**, 4038, (1997).
[7] D. Reiter, *report of KFA Jülich*, No. 2599, Institut für Plasmaphysik, (1992).

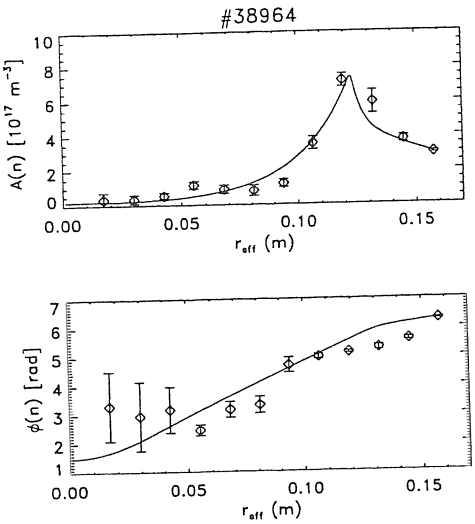

Fig. 1: *Amplitudes and phases and fits of density perturbations in #38964.*

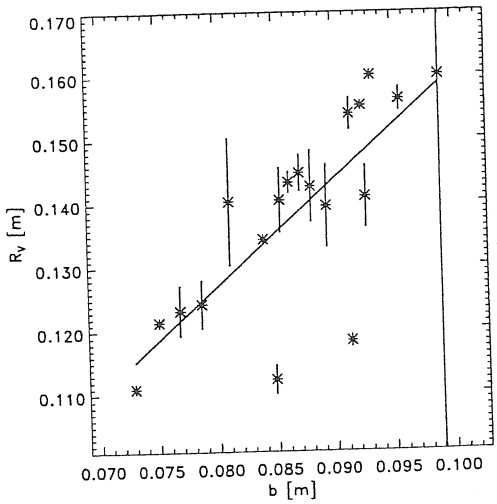

Fig. 3: *Radius R_v where the density gradient ends vs. radius up to which V is active.*

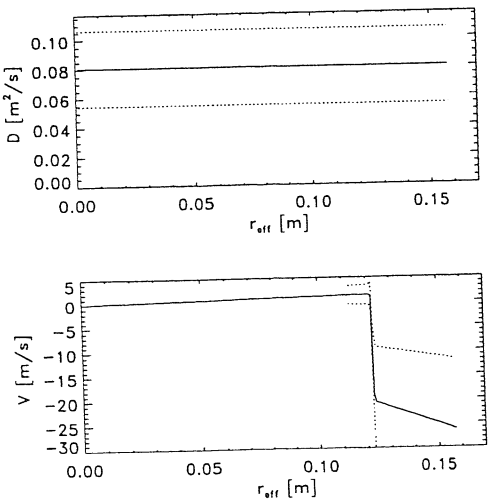

Fig. 2: *Diffusion coefficient and convection coefficient V resulting from the fit in Fig. 1. Dashed lines are error bars.*

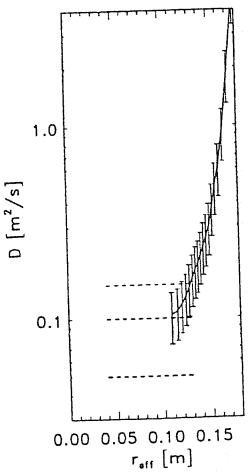

Fig. 4: *Comparison between the equilibrium (solid line) and perturbative diffusion coefficients (dashed lines), discharge 38964.*

EPS Prag

Topical lecture für Plasma Physics and controlled Fusion

Electron Bernstein Wave Heating and Emission via the OXB Process at W7-AS

H.P. Laqua, W7-AS Team
Max-Planck-Institut für Plasmaphysik, EURATOM Ass.
D-85748 Garching, FRG,
ECRH-Group
Institut für Plasmaforschung, Univ. Stuttgart, D-70569 Stuttgart, FRG

Abstract

The access to overdense plasmas ($n_e > n_{e,cutoff}$) for both, the electron Bernstein (EB) wave heating and the EB-wave diagnostic via the O-X-B mode conversion window was succesfully demonstrated at W7-AS. In the EB-wave heating experiments clear evidences for both mode conversion steps were detected and resonant absorption with a narrow profile was demonstrated. Also the inverse process, the EB-wave radiation of an overdense plasma was measured with an oblique viewing angle. The spectrum consists of a local cyclotron emission part and a nonlocal broadband high frequency part. Edge temperature perturbations excited by carbon injection were used to demonstrate the relation between frequency and position of emission.
Since for EB-waves no density limit exists, the operation window of the electron cyclotron heating and diagnostic could be extended to densities above the cutoff density.

Introduction

Electron cyclotron waves (EC-waves) are used in plasma physics for manifold purposes. Examples are EC-heating, EC-diagnostic, interferometry, polarimetry and reflectometry. All these applications have in common that they make use of electromagnetic waves and therefore are limited by the plasma cutoff density.
Besides the well known electromagnetic EC-waves, there also exist an electrostatic EC-wave, the electron Bernstein wave (EB-wave). For this wave no upper density limit exists, but propagation is only possible above a threshold density. Therefore EB-waves cannot be excited from the vacuum, but have to be generated via mode conversion from the electromagnetic waves. One possible way for this is the so called O-X-B process, which was proposed by J. Preinhaelter and V. Kopecký for electron cyclotron resonance heating [1] and which was recently demonstrated for fusion plasma heating in [2]. This process is a general physics phenomenon of EC-waves propagating in hot magnetised plasmas, such as ionosheric or fusion plasmas. Here O, X, and B represent the ordinary, extraordinary and the electron Bernstein modes. As shown in Fig. 1 the transverse refractive indices N_x of the O-wave and

X-wave along a wave trajectory in a density gradient are connected at the optimal launch angle φ without passing a region of evanescence ($N_x{}^2<0$) at the O-mode cutoff. Here in a first step an O-wave is converted into a slow X-wave. In a second mode conversion step an EB-wave is generated from the slow X-wave at the upper hybrid resonance (UHR), where the X-mode branch of the solution of the hot plasma dispersion relation is connected to the electron Bernstein branch. For EB-waves no density limit exists, they propagate towards the dense plasma center where they are absorbed by cyclotron damping. Both mode conversions are reversible, thus the B-X-O process can also take place. The mode conversion process requires an optimal parallel component $N_{\|}$ of the refractive index vector, or equivalently, an oblique launch angle φ for heating or a detection near an optimal angle φ for EB-wave emission (EBE). Further a plasma density above the O-wave cutoff and a frequency above the first cyclotron harmonic in the plasma. Since at the cyclotron resonance the plasma is optically thick for the EB-waves, it is a black body emitter for EB-waves the same as it is for electromagnetic EC-waves below the cutoff density. But in contrast to the electromagnetic waves for the EB-waves it is generally not possible to leave the plasma since they have a density threshold for propagation at the UHR, which totally encloses the inner part of the plasma. Indeed at the UHR they can be converted into slow X-waves but these are also not able to leave the plasma and are backconverted to EB-waves at their next contact with the UHR surface. The EB-wave radiation is trapped inside the plasma like in a hohlraum. Except for those EB-waves which were born with an optimal $N_{\|}$ (parallel to the magnetic field) for the B-X-O process or for those EB-waves which had achieved such an $N_{\|}$ component on their way in the plasma by scattering or magnetic configuration effects like the field line curvature. The optimal $N_{\|}$ or the optimal launch and viewing angle φ respectively are defined by the following relation [1]: $N^2_{\|,opt}=\cos^2(\varphi)=(Y/(Y+1))$ with $Y=\omega_{ce}/\omega$ (ω is the wave frequency, ω_{ce} is the electron cyclotron frequency). In a three dimensional plasma one has also to take into account the perpendicular (poloidal) refractive index $N_{\perp}$ or the poloidal angle θ, but in our experiments no variation of $N_{\perp}$ was performed. The shape of the angular window or the transmission function $T(N_{\perp},N_{\|})$ depends on the density scale length $L=n_e/(\partial n_e/\partial x)$ and is given by Mjølhus [3] with

$$T(N_{\perp},N_{\|})=$$
$$\exp\left\{-\pi k_0 L\sqrt{\frac{Y}{2}}\left[2(1+Y)\left(N_{\|,opt}-N_{\|}\right)^2+N_{\perp}^2\right]\right\},$$

where k_0 is the wave number. This angular dependence ($N_{\|}$- dependence) of the mode conversion was used in the experiments, among other criteria, to identify electron Bernstein wave heating and emission. Another criteria is the density threshold of the O-X-B and B-X-O processes respectively. It can only takes place

if the density is above the O-mode cutoff density of the emitted frequency. And finally for the heating experiments a special footprint for the X-B conversion exists, which is the parametric decay of a part of the launched waves due to the strong nonlinearity and the high power density at the upper hybrid resonance where the X-B mode conversion takes place.

Ray tracing

In model calculations with a ray tracing code for EB-waves the absorption, emission and propagation of EB-waves were simulated. We used the nonrelativistic hot dielectric tensor given by [4] and an isotropic electron temperature. Since the full stellarator field geometry was not implemented in this code, the magnetic field configuration at the EB-wave propagation volume was approximated by a toroidally symmetric field with $B(r_{eff}) = B_0 A / (A + r_{eff} / a)$ (A = 10.5, a = 0.1m) and no poloidal field was taken into account, which is sufficient to illustrate the basic features of the OXB-mode conversion and EB-wave propagation, but could not reproduce the experimental results completelly. Especially the measured Doppler shift of the EB-absorption and emission differs from the ray-tracing calculation by about 4 GHz. This may originate from the simplification made in describing stellarator configuration.

For these calculations density and temperature profiles similar to typical neutral beam sustained W7-AS plasmas were used. First we have similated the EB-heating. The ray trajectories in the equatorial plane are shown in Fig. 2 and Fig. 3. The beam is launched from the low field side and propagates through the cutoff, where it is converted into an X-mode. Then it moves back to the UHR-layer, where the X-B-conversion takes place. The EB-waves are absorbed near the cyclotron resonance. A small fraction of the beam power is lost at the UHR due to finite plasma conductivity. The power deposition zone for resonant heating strongly depends on the magnetic field and electron temperature as shown in Fig. 3. In the case of non resonant heating with no strong absorption in the plasma the launched EB-waves experience a cutoff layer ($N \rightarrow 0$) at the UHR surface, which in the nonresonant or higher harmonic ($\omega_{ce}/\omega < 1$) field totally encloses the inner plasma. The radiation is then trapped inside the plasma like in a hohlraum as it was already mentioned above. The power is then nonlocally dissipated by multiple pass absorption. In the resonant case due to the nonvanishing parallel component $N_{\parallel} \approx N_{z,opt}$ of the refractive index in the oblique launch the cyclotron absorption is strongly Doppler shifted.

In Fig. 4 the ray trajectories of the EBE are shown for different frequencies. Since all processes of mode conversion and cyclotron emission are reversible, for simplicity the simulation was started at the detector and the ray trajectories were

followed until 99% of the power was absorbed in the resonant case with cyclotron absorption inside the plasma. In the nonresonant case the calculation was stopped when the toroidal beam position exceeded the validity region of the approximated magnetic configuration (±3° toroidal angle from the launch position). The shaded area indicates the plasma volume where $1-1/e$ of the radiation is emitted and shows the localisation of resonant EB-emission. Each emitting volume is related with a frequency and the radiation intensity is expected to be at the thermal level as it is for electromagnetic EC-emission (ECE) below the cutoff density. The emitting frequency of EB-emission compared with perpendicular ECE is Doppler shifted due to the nonvanishing $N_{\|}$ component of the refractive index for the oblique angle of observation. In contrast to ECE, for nonresonant frequencies EBW radiation is not able to leave the plasma and is trapped inside the plasma like in a hohlraum (see 70 GHz beam in Fig. 4). The origin of this radiation is nonlocal and we expect a thermal emission intensity of the average plasma temperature.

EB-wave heating experiments

The experiments were performed at the W7-AS stellarator (major radius R=2.0m , minor radius a=0.18m) with two 70 GHz gyrotrons with 110 kW power each. A detailed description of W7-AS and its 70 GHz ECH system can be found in [5]. The central magnetic field was set between 1.25T and 2.0T and the edge rotational transform ι, taken from the magnetic reconstruction, near 0.35 according to the experimental requirements. The central density of the neutral beam injection (NBI) sustained target plasma was up to $1.6\ 10^{20}\ m^{-3}$, which is more than twice the 70 GHz O-mode cutoff density. Co- and counter NBI with 360 KW power each were used to compensate the momentum transfer to the plasma.

1. Variation of the launch angle.

The launch angle of the incident O-mode polarised wave was varied at fixed heating power (220 kW) at a nonresonant magnetic field. The increase of the total stored plasma energy (from the diamagnetic signal) depends strongly on the launch angle (see Fig. 5), which is typical for the O-X-conversion process, and fits well to the calculation. Here the power transmission function given by [3] was normalised to the maximum energy increase. The central density was $1.5\ 10^{20}\ m^{-3}$ and the central electron temperature was 500 eV. Heating at the plasma edge could be excluded since at the nonresonant magnetic field of 1.75T no electron cyclotron resonance existed inside the plasma. Due to technical limitation of the maximum launch angle, only the left part of the transmission function could be proved experimentally. The plasma energy content increased by about 1.5 kJ compared to a similar discharge with neutral beam injection (NBI) only. More than 70% of the heating power was found in

the plasma if the power scaling of the energy confinement ($P^{-0.6}$) was taken into account. Thus O-X-B-heating turned out to be efficient.

2. Density variation and parametric instability (PI).

In these experiments, it should be demonstrated, that a density threshold (O-cutoff) for the O-X-conversion exists and that the parametric decay process which is a footprint of the X-B conversion takes place. For this the plasma was build up by one 70 GHz gyrotron in X-polarisation in a resonant central magnetic field of 1.25T. Then the density was slowly ramped up to density above the O-cutoff. In parallel as shown in Fig. 6 a second 70 GHz beam O-mode polarised with the optimal launch angle and modulated with 20% amplitude was launched into the plasma. During the plasma build up thermal EC emission (ECE) was detected. As soon as the cutoff density is reached ECE vanished and O-X-B heating started, which caused an increase of the plasma energy and central soft-x emission shown in Fig. 6. Simultaneously the PI at the X-B-conversion process generated a decay spectrum, whose high frequency part could be measured with the ECE-detector. The modulation amplitude strongly exceeded that of the pump wave, what clearly demonstrated the nonlinear character (power threshold) of the PI. Fig. 7 shows the high frequency decay spectrum. Two red shifted and one blue shifted lines can be recognised. Their spectral distances to the 70 GHz pump wave, which was suppressed by a Notch filter, are multiples of the lower hybrid resonance (LHR) frequency (~900MHz). The spectrum of the LHR oscillation itself could be detected by a loop antenna. The LHR oscillation shows a high degree of correlation with the high frequency decay waves.

3. Resonant cyclotron absorption.

Here the central magnetic field was varied between 2.0T and 2.5T to show resonant absorption of the EB-waves. In the equatorial plane the magnetic field as a function of the effective radius r_{eff} is approximately given by the following relation: $B(r_{eff}) = B_0 A / (A + r_{eff} / a)$ with A= 10.5. The power deposition was estimated from the change of the temperature profile at the power switch-off. Since the density was far above the ECE cutoff, the temperature profiles were calculated from the soft-X emission and the Thomson scattering diagnostic. The central temperature was 500 eV. The X-ray emission was monitored by an array of 36 silicon detectors with a 25 μm beryllium filter. To obtain the radial X-ray emission profile the signals were inverted to the magnetic flux co-ordinates. The time resolution was 0.1 ms and the radial resolution was about 1 cm. In Fig. 9 the absorption profiles for different magnetic fields are shown. The absorption is strongly Doppler shifted due to the oblique launch and moves from the high field side at 2.0T through the center (2.2T) to the low field side at 2.3T with increasing magnetic field, which clearly

demonstrates the propagation and the local cyclotron absorption of the EBW's for the first time.

EB-emission experiments

The experiments were also performed at the W7-AS. Since the standard ECE-diagnostic at W7-AS uses fixed antennas with a viewing angle of 90° in respect to the magnetic field, the ECE radiometers were connected with an unused movable ECRH launch antenna. The W7-AS ECE-radiometer type is described in [6].

1. Calibration

The system was calibrated with thermal ECE (first harmonic O-mode at B_0=2.5 T) at a perpendicular (90°) viewing angle and at plasma densities below the O-mode cutoff. It was taken into account that for oblique observation the O-mode radiation is elliptically polarised, where as the receiving system is only sensitive to linear polarised radiation.

2. Density threshold.

The receiving mirror was turned to the optimum viewing angle of 47° with respect to the magnetic field and the plasma density was ramped up to above the cutoff density as shown in Fig.10. The plasma was sustained by two neutral beam injectors (NBI) with 360 kW power each. The central magnetic field was lowered to 2.1 T to compensate the Doppler shift of the EBE-spectrum. For comparison the plasma temperature measured with the soft-X filter method for the central line of sight is plotted at the top of Fig 9. Below, the low field side EBE radiation , the central EBE and the high field side EBE are shown. When the central density as measured with a microwave interferometer and by Thomson scattering reaches the cutoff density of the emitting frequency, the B-X-O window opens and EBE appears as shown in Fig. 9.

3. Angular window.

Scans of the viewing angle were performed for the first and second harmonic EBE as shown in Fig. 3 and the predicted angular windows at 47 ° for 2.1 T (69.14 GHz) and 55° for the second harmonic EBE at 1.25T could experimentally be reproduced. The radiation temperature was up to 70% of the temperature measured by soft-X emission and Thomson scattering. This might be due to reduced X-O conversion caused by density fluctuations at the cutoff surface as described in [2].

4. The EBE spectrum.

First, ECE and EBE spectra are compared. The central magnetic field was set at 2.4 T for which both spectra are in the spectral range of our detection system (61-78 GHz). In Fig. 11 both the thermal ECE-spectrum (first harmonic O-mode, $n_e<n_{e,cutoff}$, squares) received by the ECRH-antenna with 90° viewing angle and the EBE-spectrum at 47° (first harmonic, $n_e>n_{e,cutoff}$, circles) of an NBI sustained

plasma are shown. The ECE-spectrum reflects the plasma temperature profile. The EBE-spectrum is about 6 GHz Doppler shifted and shows the low field (frequency) side temperature gradient. The small pedestal at its low frequency part may originate from stray radiation emitted at the low density plasma edge. In order to record also the high frequency part of the spectrum, the magnetic field or the central EC-resonance frequency were reduced by 0.4 T corresponding to 11.2 GHz respectively. As shown in Fig. 12 instead of an high field side decay as is typical for ECE, the EBE-spectrum has a slowly decreasing broadband high frequency part. By a further shift of the EC resonance frequency we found, that the high frequency part is emitted up to about 1.7 times the EC-frequencies in the plasma. We think that this is the nonlocal "hohlraum" radiation as it has been already discussed in the previous section.

5. Cold pulses

These experiments were conducted to estabish the relation between the frequency of the thermal EBE and the radial position of the emission zone. Temperature perturbations at the plasma edge were set by carbon laser blow off. The amount of ablated carbon was matched to a value where we could find a sufficiently large temperature decrease in all EBE channels, but with a minimum disturbance of the plasma discharge, especially with no significant density increase. An example is shown in Fig. 9 where at 0.34 s the cold pulse was set. One could identify a steep temperature dip in the edge EBE channels (64.84 GHz, 72.26 GHz), a small dip in the channel central (69.14 GHz) and nearly no change in the average plasma density. In Fig. 13 the amplitude and the delay time in which the signal reaches 1/e of the amplitude of the cold pulse are plotted as a function of the emission frequency. Assuming that the cold pulse propagates from the outer radii towards the center, both the amplitude and the delay time indicate that for the thermal part of the spectrum there is a clear relation between the emitted frequency and the radial position of the emission. For the spectrum above 73 GHz no amplitude variation and no clear phase attachment could be found, which indicates the nonlocal character of the high frequency part of the EBE.

Summary and Conclusions

EC-heating of an overdense plasma with 70 GHz electron Bernstein waves was clearly demonstrated at W7-AS. The EB-waves were generated via mode conversion in the O-X-B process. Both, the angular dependence of the O-X-conversion and the parametric instability which is typical for X-B-conversion could be experimentally verified. The position of the narrow absorption profile, estimated from the soft-X emission, could be changed by a shift of the cyclotron resonance layer. Thus generation, propagation and local resonant cyclotron absorption of EB-waves was shown.

Also the inverse process, which is the EB-wave emission througth the OXB-mode conversion window from an overdense plasma was detected with an oblique observation angle. The emitted spectrum consists of two parts:
The thermal part reflects the local thermal emission of EB-waves and in principle a radial temperature can be reconstructed from this radiation. The high frequency part represents nonlocal "hohlraum" radiation since most of the EB-waves are trapped inside the plasma and only those rays which somehow obtain the optimal $N_{\|}$ and $N_{\perp}$ for the small angular window of the B-X-O process can leave the plasma.
Both the local and nonlocal character of the EBE spectrum was demonstrated by cold wave propagation with laser blow off.
Besides the anewed verification of the hot plasma wave theory and the insight into EB-wave physics in a fusion plasma, the OXB-process opens also a new operational window for EC-heating and EC-diagnostic beyond the cutoff for fusion as well as for ionospheric research.

References

[1] J.Preinhaelter and V.Kopecký , J. Plasma Phys. 10 ,1 (1973);
[2] H.P.Laqua et al., Phys. Ref. Let. 78, 18 (1997);
[3] E.Mjølhus, J. Plasma Phys. 31,7 (1984);
[4] T.H.Stix:"THEORY OF PLASMA WAVES"; McGraw-Hill, 1962
[5] H. Renner et al., Plasma Phys. Control. Fusion 31,10 (1989);
[6] H.J. Hartfuss et al., Plasma Phys. Control. Fusion 39, 1693 (1997)

Figures

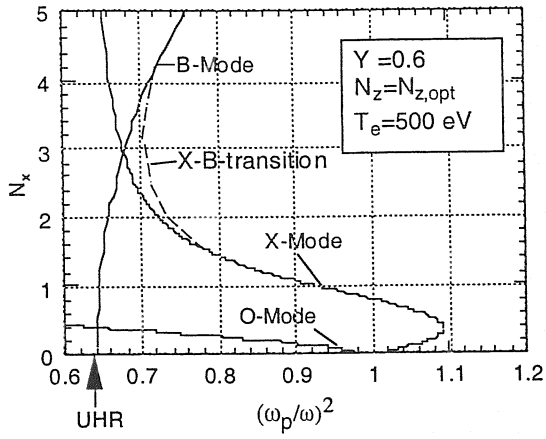

Fig. 1: Refractive index N_x versus ω_p^2/ω^2 for the O-X-B conversion process. The transition represents the connection of the X-mode and B-mode due to the hot dielectric tensor.

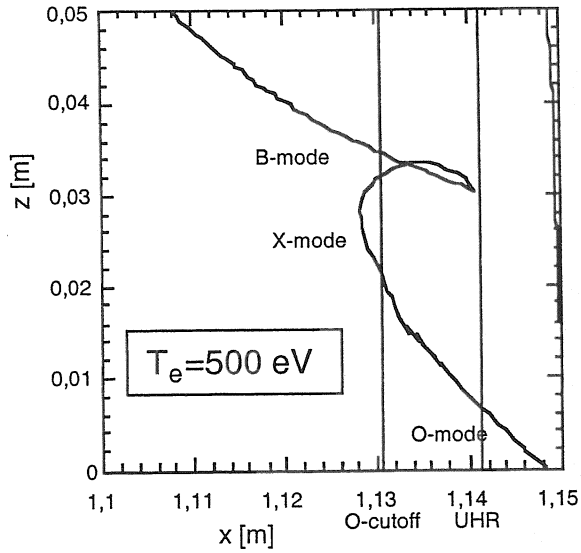

Fig. 2 Results of ray tracing calculations.

Ray trajectory in the density gradient region at the plasma edge for a magnetic field of 2.2 T.

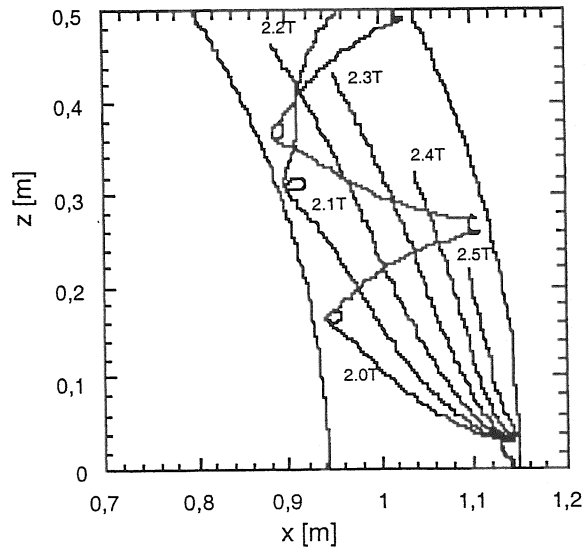

Fig.3 Results of ray tracing calcultions.
Ray trajectories of 70 GHz EB-waves in a plasma torus for different magnetic fields. The central density was 1.5 $10^{20}m^{-3}$ and the central temperature was 500 eV. In the resonant case the trajectory was calculated until 99% of the power was absorbed.

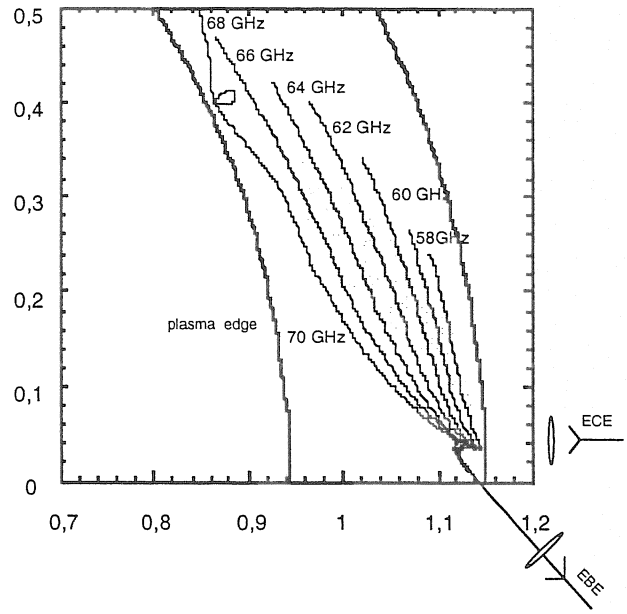

Fig. 4: Ray-tracing calculation of EBE at a central magnetic field of 2.1T , a central temperature of 600 eV and a central density of 0.9 10^{20} m^{-3}.

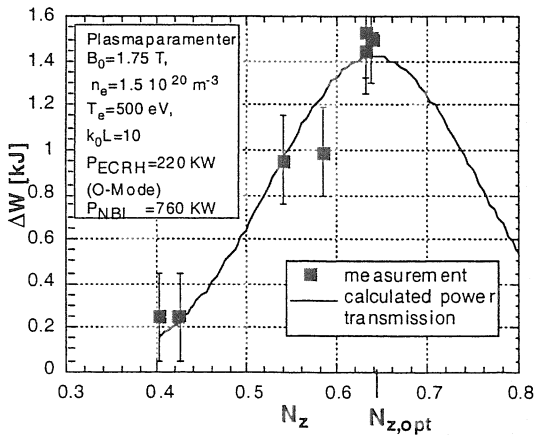

Fig.5: Increase of the plasma energy content by O-X-B-heating versus the longitudinal vacuum refractive index N_z of the incident O-wave. The solid line is the calculated transmission function multiplied by the maximum energy increase.

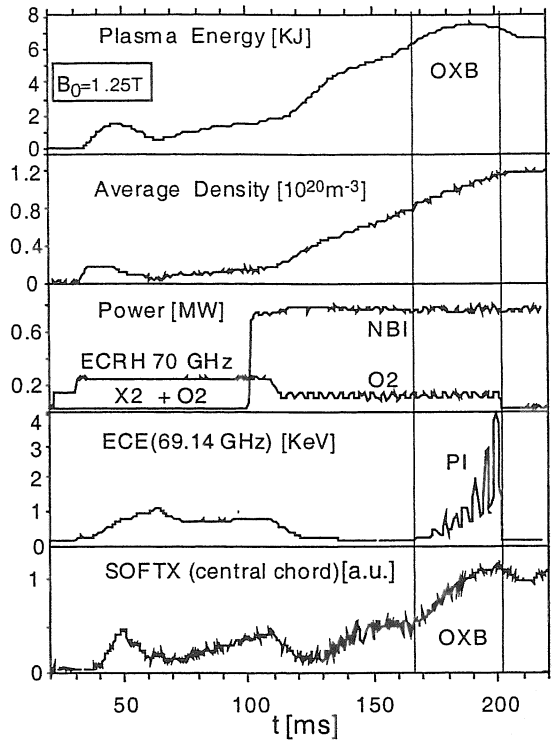

Fig. 6: Temporal development of some plasma parameter during a O-X-B heated discharge. From the top: plasma energy estimated from the diamagnetic signal, average density from the interferometric measurement, heating power, intensity of ECE and PI, central soft X signal. The markers show the O-X-B heating interval.

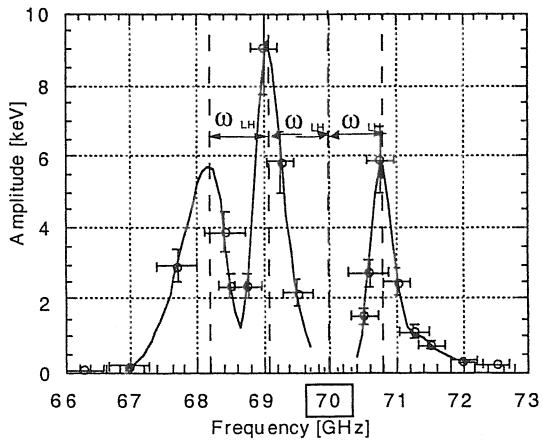

Fig. 7: High frequency spectrum of the parametric decay waves generated in the X-B-process. The incident wave frequency is 70 GHz and the LH frequency is about 900 MHz.

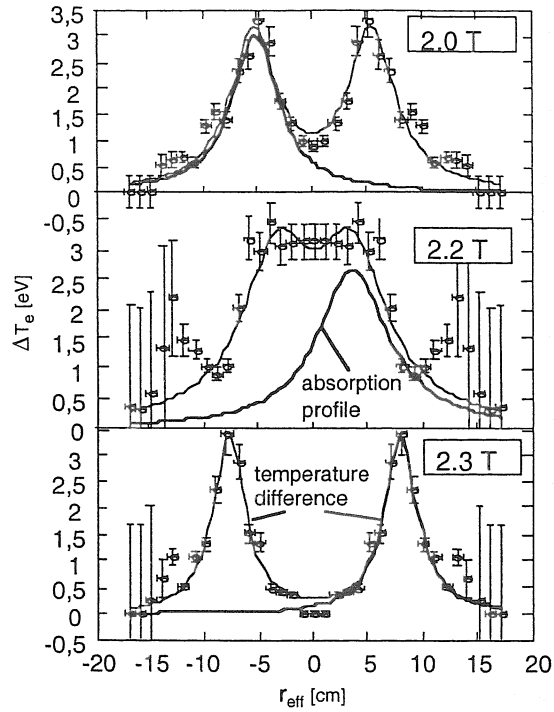

Fig.8 Changes of temperature 3ms after O-X-B heating switch-off and the related ECRH absorption profiles different central magnetic fields.

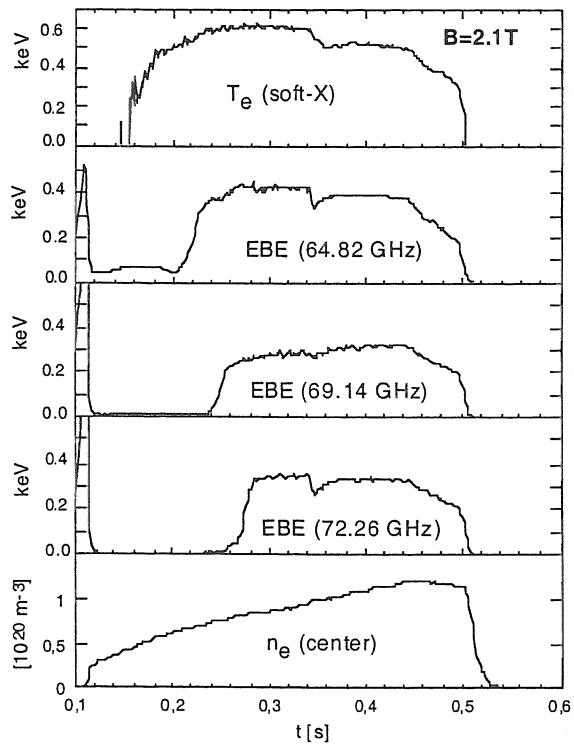

Fig. 9: Signals of an NBI sustained discharge with a density ramp. From the top: soft-X temperature, radiation temperature of the low field side edge EBE, central EBE and high field side edge EBE and central density. The temperature dip at 0.34 s is due to a perturbation induced by carbon laser blow off.

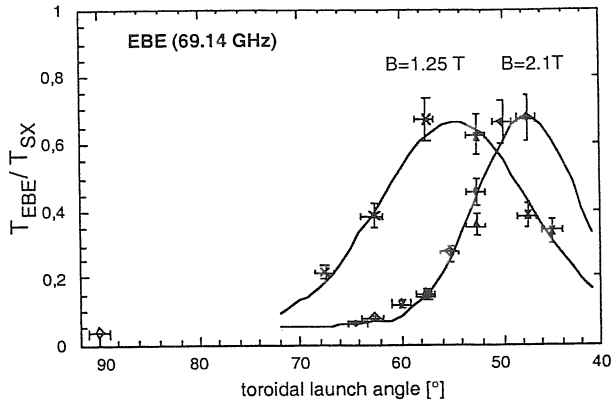

Fig. 10: Angular dependence of EBE for different central magnetic fields, for central density of 1 $10^{20}m^{-3}$ and temperature of 600 eV. The signal is normalised to the central soft-X temperature.

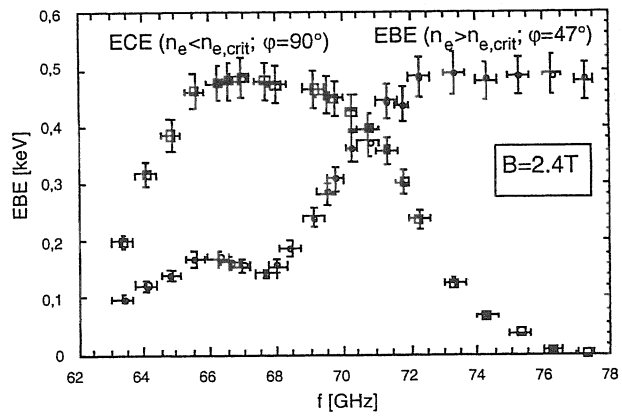

Fig. 11: Doppler-shifted EBE spectrum (circles) and ECE- spectrum (squares) for similar discharges but at different densities. In the EBE-discharge the central temperature was 700 eV.

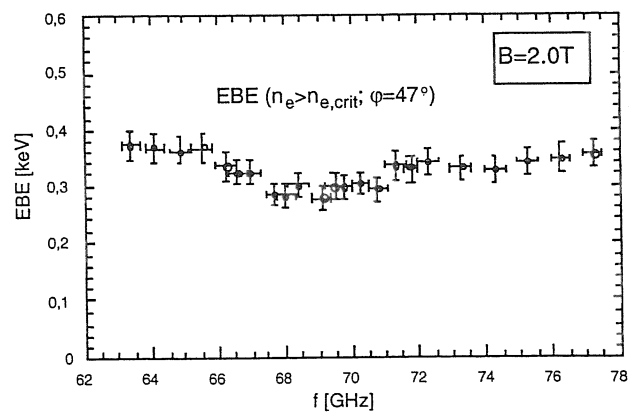

Fig. 12: High frequency part of the EBE spectrum. The central EC resonance frequency is shifted by about 11.2 GHz in respect to Fig. 4. Due to the confinement degradation with decreasing magnetic field the central temperature decreases to about 500 eV.

a)

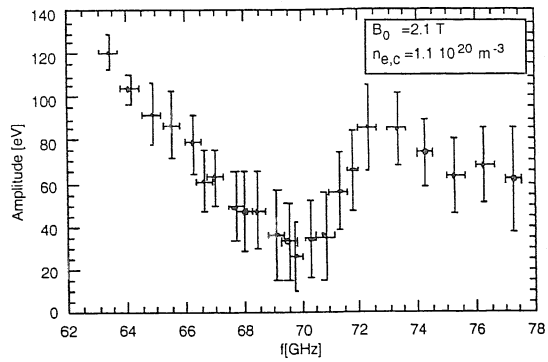

b)

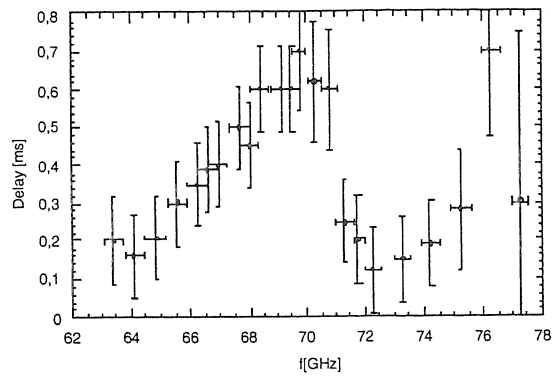

Fig. 13: a) Amplitude decay and b) delay time of the 1/e amplitude as a function of EBE frequency. Indicating the inward propagation of the temperature perturbation induced by carbon laser blow off at the plasma edge, thus demonstrating the localisation of the radiation origin.

Operational experience in W7-AS discharges with rotational transform from bootstrap current

F. Wagner, R. Jaenicke, M. Anton, L. Giannone, U. Stroth and W7-AS Teams
Max-Planck-Institut für Plasmaphysik, EURATOM-Association
85748 Garching, Germany

Introduction. The rotational transform in helical systems is usually produced by external coils - coils with lateral excursions in the case of W7-AS. In addition, a pressure driven bootstrap current, I_{BT}, develops in the plasma which increases the external rotational transform. With considerable bootstrap current the steady state characteristics of the helical system is still maintained, whereas the technical complexity of the non-planar coils could be reduced. On the other hand, the discharge development is more complex because the plasma current changes important quantities like the rotational transform, the magnetic shear and the shape of the flux surfaces which are linked to stability and confinement. This paper summarizes experimental results on the bootstrap current in W7-AS. Measured or calculated I_{BT} values are given for various discharge scenarios with respect to magnetic field, B, density, n, temperature, T, and heating power, P. Examples for the influence of larger bootstrap currents on confinement and plasma stability are shown. Usually the bootstrap currents in W7-AS are too small to drive substantial instabilities. Therefore also a discharge is presented where the current is further increased beyond the bootstrap current level by an additional loop voltage up to the limit where the plasma is strongly disturbed by MHD.

Bootstrap currents in W7-AS. The neoclassical bootstrap current is driven by finite plasma pressure and flows off axis in the pressure gradient region. In the plateau and long mean free path regime it is a complicated function of temperature, T, collisionallity, ν, and the magnetic field configuration. Therefore, calculations have to be performed with the DKES code [1] which takes into account the three dimensional shape of the flux surfaces. In W7-AS only the electron bootstrap current has to be considered. It can be measured in several ways. The simplest method is the stellarator operation proper, where the bootstrap current freely develops. However, within a discharge time of 1 to 2 s a stationary state is reached only in cases with low T_e and consequently small I_{BT} (Fig. 1). A stationary state is obtained much faster by preprogramming a net plasma current with the aid of the OH transformer. In net current free discharges, the compensating ohmic current component is opposite to I_{BT} and both currents have to be calculated. For finite net currents, the OH component is negligible if the loop voltage approa-ches 0. Generally reasonable agreement is found between calculated and measured bootstrap currents [2] especially when the uncertainty of Z_{eff} is taken into account. The current rise time is essentially given by the L/R time constant and can be modelled by time dependent codes like ASTRA.

Substantial bootstrap currents can be expected at high T_e. At low densities, where T_e stays

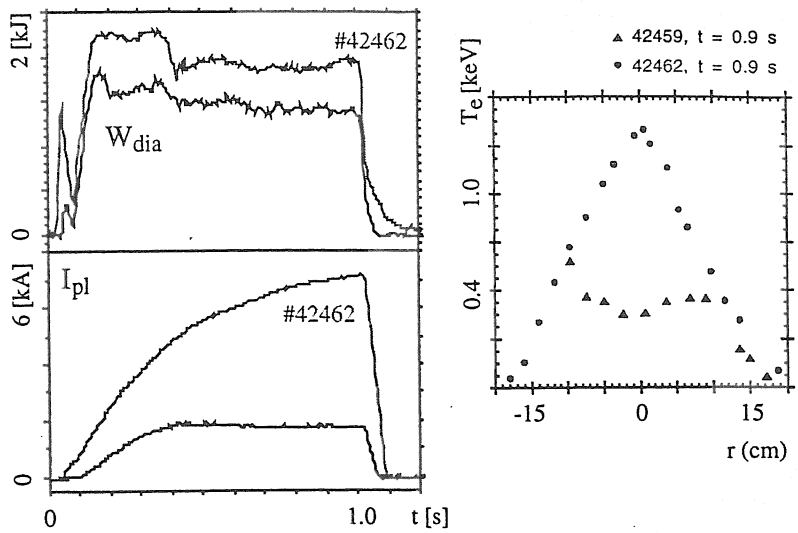

Fig.1. The two discharges shown differ by the toroidal field. In the case of on axis ECRH the electron temperature profile is peaked and a large bootstrap current develops. For B_0 increased by 5%, the ECRH is strongly off axis, the central electron temperature and the bootstrap current are significantly reduced (350 kw ECRH at 1.25T, $\langle ne \rangle = 1.5\ 10^{13} cm^{-3}$). The drop of W_{dia} at about 400ms is connected with the iota=1/3 surface close to the plasma boundary in agreement with changes in the MHD behaviour.

rather constant, I_{BT} increases with density and finally saturates (Fig. 2). At very high densities ($\langle n_e \rangle > 10^{14} cm^{-3}$, neutral beam (NBI) heated high β plasmas at 1.25T) I_{BT} is restricted to about 3 kA in W7-AS. The largest free-running I_{BT} of 8.5 kA has been measured with 800 kW ECRH at 2.5T ($\langle n_e \rangle \approx 3\ 10^{13} cm^{-3}$) and $T_e(0) \approx 3.5$ keV) where after 1.4s the current was still increasing. For 400 kW ECRH at 1.25 T bootstrap currents up to 10 kA can be extrapolated from discharges with zero loop voltage. A preliminary analysis indicates that even values of the order of $I_{BT} = 20$ kA can be expected for net current free discharges with 1.5 MW ECRH at 2.5T, rather low density ($\langle n_e \rangle \approx 2\ 10^{13} cm^{-3}$) and $T_e(0) \approx 5$ keV and also for discharges with combined ECRH and NBI (700 + 750 kW) and very good energy confinement (factor two above ISS95 scaling [3]) resulting in $T_e(0) \approx 1.7$ keV at $\langle n_e \rangle \approx 5\ 10^{13} cm^{-3}$. In this case also the influence of negative radial electric fields on the particle orbits (which increase the electron and decrease the ion bootstrap component) seems to be important [4].

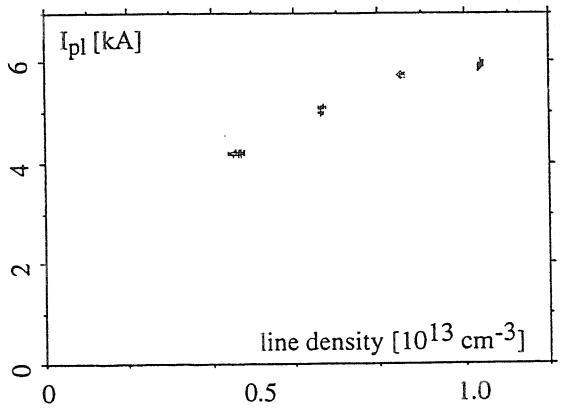

Fig.2. Density dependence of the non-stationary bootstrap current at t = 1s for 350 kW ECRH at 1.25T. The maximium density is about $\langle ne \rangle = 1.5\ 10^{13} cm^{-3}$.

Increase of rotational transform. As mentioned above, the largest free-running bootstrap current was found at 2.5T. Although I_{BT} scales with 1/B, almost the same value of $I_{BT} = 8.3$ kA was achieved at 1.25T with only 350 kW ECRH at t=1s. This occurs because the confine-

ment in W7- AS improves almost linearly with B and thus higher electron temperatures are achieved at higher magnetic fields. Because of $\Delta\iota \propto I_{pl}/B$, the largest increase of the rotational transform was therefore achieved at the lower field with a $\Delta\iota \approx 0.10$ for a plasma radius $a \approx 16$ cm and a major radius of 2 m.

Influence on confinement. The influence of a free running bootstrap currents on confinement follows roughly the results which were obtained for net current free discharges and which are only partly understood [5]. For small to medium currents, just the change of the boundary transform ι (a) and of the shear have to be taken into account. Similar to the current ramp-up phase in tokamaks a modulation of the energy content W_{dia} is observed which is probably related to field line resonances close to the plasma boundary (Fig. 1). In cases with a pronounced dependence of W_{dia} on ι (a), the discharge can follow that dependence with increasing current. A discharge with optimum confinement [6] is compared in Fig. 3 with a discharge with free I_{BT} but lower external rotational transform. The rising current contributes at first to the rotational transform missing for optimum confinement and the energy content W_{dia} reaches values comparable to the net current free discharge. Later on, the plasma confinement deteriorates with increasing current in this case. In discharges with large ohmic currents, such a deterioration is usually not observed [5]. For discharges with large shear (substantial internal currents at low density, high β or large net currents) no significant dependence of the confinement on ι (a) or the bootstrap current is observed or has to be expected.

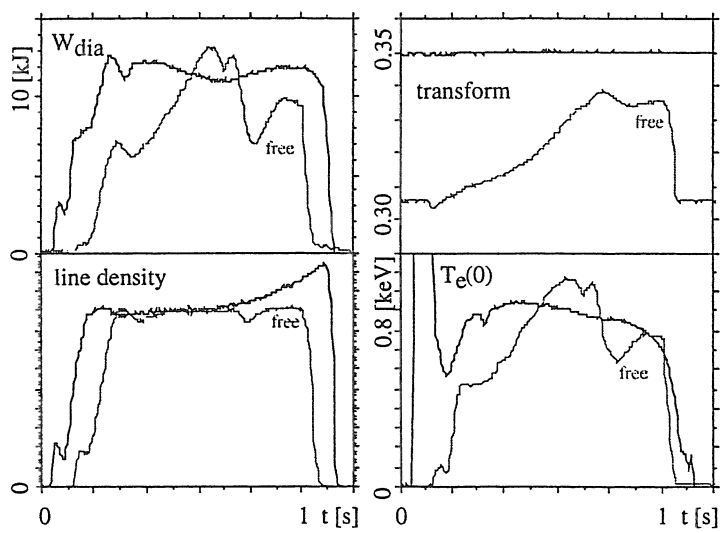

Fig.3. A net current free discharge with optimum confinement (2.5T, P_{NBI} = 350 kW, <ne> ≈ 1.0 $10^{14}cm^{-3}$) is compared with a similar discharge with free running bootstrap current starting at lower external rotational transform at the plasma boundary.

Development of Instabilities. Within the limitation of the pulse length to 1 to 2 s, bootstrap currents remain too small to drive significant instabilities. An example where fluctuations driven by I_{BT} alone were clearly visible is presented in Ref. [7]. They could at least partly identified as m=2 tearing modes. To demonstrate the stability behaviour of stellarators with non negligable external rotational transform [8] at still larger currents the bootstrap current can be further increased by applying an external loop voltage. A result is shown in Fig.4 (see also [7]).

Similar to tokamaks large amplitude m=2 tearing modes develop when ι (a) approches 1/2 and the ι =1/2 (or q=2) is close to the plasma boundary and T_e drops considerably. However, due to the improved positional stability by the external poloidal field no disruption occurs. The density and the plasma current stay almost constant and the discharge terminates only when the OH transformer can no longer supply the necessary large loop voltage.

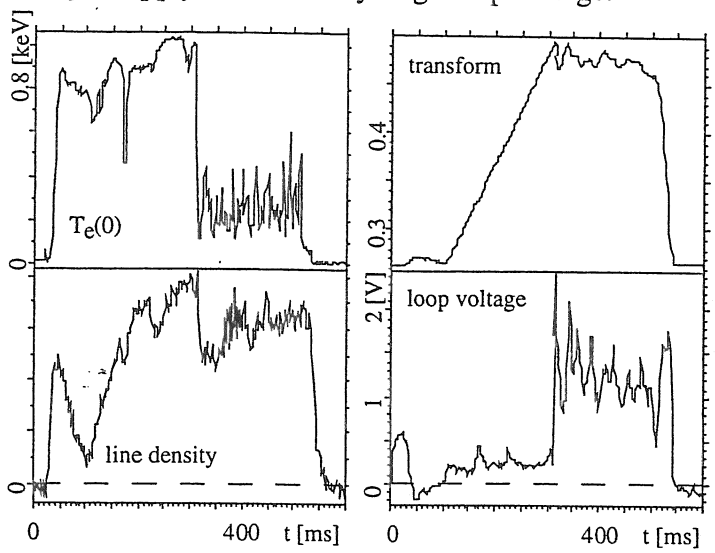

Fig.4. A low density discharge (1.25T, P_{ECRH} = 350 kW, <ne> = 1.0 $10^{13}cm^{-3}$) where the bootstrap current has been increased by applying an external loop voltage. At about 300ms the rotational transform at the plasma boundary approaches 1/2 and large amplitude m=2 tearing modes develop. which cool down the central electron temperature to about 300eV.

Conclusions. In W7-AS bootstrap currents up to 10 kA have been measured and currents up to 20 kA are estimated for net current free discharges at 2.5T. To obtain large bootstrap currents high electron temperatures are mandatory and this can be achieved in W7-AS only by ECRH. Depending on the electron temperature and the aspect ratio, pulse lengths of several seconds are necessary to reach a stationary maximum current. The largest increase of the external rotational transform, $\Delta\iota \approx 0.10$, was found at a reduced toroidal field of 1.25 T. In cases where the plasma confinement depends on ι (a) and on the magnetic shear, the confinement follows on the whole the modifications introduced by the bootstrap current. Plasma stability is no serious problem in stellarators with sufficient external rotational transform even at very large plasma currents. Nevertheless major resonances like ι =1/2 close to the plasma boundary should be avoided since in these cases current driven instabilities deteriorate the plasma confinement considerably.

References

[1] V. Erckmann et al, Plasma Phys. Control. Fusion **34**, 1917 (1992)
[2] H. Maassberg et al, Phys. Fluids **B5**, 3728 (1993)
[3] U. Stroth et al, Nucl. Fus. **36**, 1063 (1996)
[4] H. Maassberg, private communication (1998)
[5] R. Brakel et al, "On the influence of rotational transform and .. ", these proceedings
[6] U. Stroth et al, Plasma Phys. Control. Fusion **40**, 1 (1998)
[7] R. Jaenicke et al, Proc. 21th EPS Conf. Control. Fusion and Plasma Physics (Montpellier), vol. **18B**, I - 396 (1994)
[8] R. Jaenicke and WVII-A Team, Nucl. Fus. **28**, 1737 (1988)

Local and Global Transport in Perturbative Experiments in the Stellarator W7-AS

H. Walter, U. Stroth, J. Bleuel, R. Burhenn, T. Geist, L. Giannone, H. Hartfuß, J.P.T. Koponen, L. Ledl, G. Pereverzev and the W7-AS Team

Max-Planck-Institut für Plasmaphysik, EURATOM-IPP Association, Boltzmannstraße 2, 85748 Garching, Germany

Introduction

One of the most interesting questions about confinement raised in recent years is whether electron heat transport is governed by local processes only or also by non-local or global ones. The most sensitive methods to investigate the electron thermal diffusivity χ_e are perturbative experiments like power modulation or impurity injection to the plasma edge. In the first case, a heat pulse in the electron temperature travels from the core to the edge while in the second case, a cold pulse travels from the edge to the core. This paper reports on recent results from W7-AS obtained from heat-pulse experiments, which were carried out in plasmas in a large heating power range and cold-pulse experiments on discharges at very different plasma parameters.

Cold-pulse experiments

Systematic cold-pulse experiments were carried out in electron cyclotron resonance heated (ECH) discharges at line averaged densities from 0.7 to 7×10^{19} m^{-3} and a magnetic field strength of $B = 2.5\,T$. The heating power was 0.5 MW.

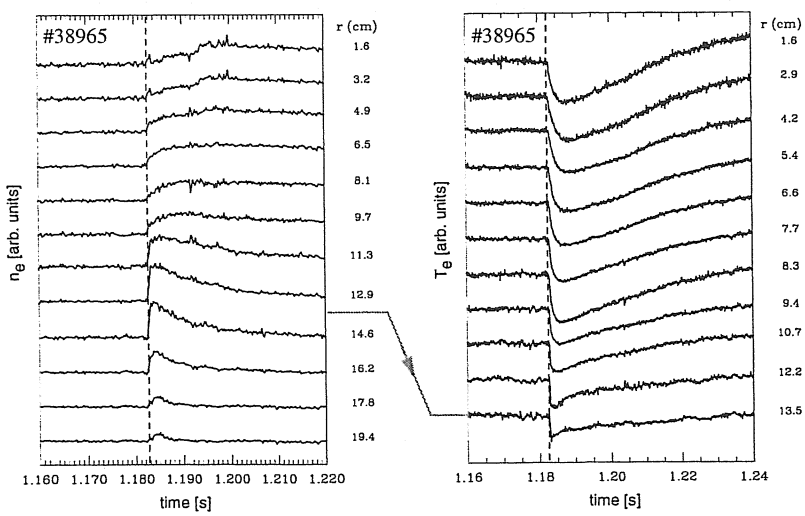

Fig. 1: Electron density and temperature evolution at different radii of a cold-pulse induced by carbon injection (dashed line).

In Fig. 1, the electron density and temperature evolution of a relatively large cold pulse are depicted. The density is measured by a 10-chord microwave interferometer. The line-averaged density prior to the injection is $3\times10^{19}\,m^{-3}$. From the measured density rise, the number of electrons injected into the plasma edge

is estimated to be $\lesssim 1\times10^{19}$. This has to be compared with a total number of 3×10^{19} plasma electrons. From the sharp increase in the density as shown in Fig. 1 it can be deduced that the electron source is located between $r = 10$ and 15 cm. In this region, the carbon clusters are completely ablated and the atoms ionized within 1 ms. The biggest density perturbation is $\Delta n \approx 1.5\times10^{19}\,\mathrm{m}^{-3}$. The fast density rise at the edge is followed by a slower density increase during 10 ms in the plasma center. In W7-AS, strong cold-pulses could only be generated if the amount of electrons introduced led to a maximum local density increase of $(\Delta n/n)_{max} \gtrsim 80\,\%$.

The temporal electron temperature evolution during the cold pulse is measured by an ECE radiometer. The temperature reacts to the density inverse. A sharp temperature drop in the outermost channels reflects the fast density increase in the particle source region. The temperature perturbation propagates to the plasma center. A central temperature increase, as reported e.g. from the TEXT tokamak [1], was never observed in W7-AS.

The cold-pulses were analyzed with the ASTRA time-dependent transport code [2]. The electron heat transport equation is solved including electron-ion coupling. A constant separatrix temperature is assumed as the boundary condition. The radiation losses are taken from bolometer measurements. The temporal evolution of the density profile is prescribed in the calculation according to the inverted line integrated measurements.

The results from two simulations with different models are shown in Fig. 2. The model where χ_e was set to the diffusivity profile χ_e^{pb} obtained from a power balance analysis from before the Carbon injection reproduces the fast temperature drop in the outermost channels (upper figure). This is due to an almost adiabatic temperature response to the density increase. For the dynamics of the edge temperature drop, radiation and ionization losses are of minor importance. This simple model fails to reproduce the temperature evolution at inner radii in detail.

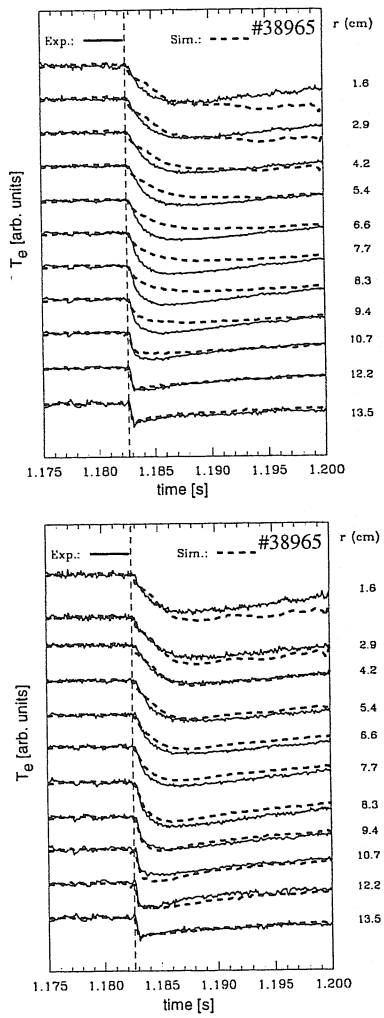

Fig. 2: Comparison of the simulated and measured electron temperature evolution for a large cold-pulse using two different models as described in the text.

The agreement in the core between simulation and experiment depends sensitively on how well the outer channels are reproduced. In the lower part of Fig. 2, a simulation is shown where the diffusivity was artificially enhanced by a factor of 2.7 for 1 ms immediately after the injection time. This increase was limited to $r > 10$ cm. The resulting additional reduction

in the simulated temperature at $r = 10.7\,\mathrm{cm}$ is small but sufficient to obtain the shown improvement of the fit of the inner channels. Furthermore, a weak local dependence ($\chi_e \sim \nabla T^{0.4}, \chi_e \sim T^{0.4}$ and $\chi_e \sim n^{-0.4}$ gives similar results) of the diffusivity was assumed to account for the long term evolution of the temperature. However, for the evolution in the first 2 ms this dependence is only of minor importance.

Although an explicit time dependence of the diffusivity is introduced for the plasma edge, this cannot be considered as a non-local effect. During the short time the diffusivity was enhanced, the electron distribution function was perturbed by a large fraction of cold electrons (the local density is doubled). This could very well lead to an enhancement of the local turbulence level. Hence there exists no evidence for non-local transport in cold-pulse experiments in W7-AS. This also holds for those experiments carried out so far on neutral-beam-heated discharges.

Heat Pulses Experiments

In early power modulation experiments in W7-AS, the heat-pulse propagation could be modeled using a χ_e as obtained from power balance analysis [3, 4]. This result could be interpreted in terms of a non-local transport model [5]. However, more recent experiments were consistent with $\chi_e \approx 2\chi_e^{pb}$ and therefore with a local ∇T dependence [6]. In order to clarify this contradiction, modulation experiments were carried out in a large power range, which was not accessible previously. The rotational transform was carefully chosen in order to assure optimum confinement conditions. The heating power was varied from 0.2 to 1.4 MW and modulated at 92 Hz for 800 ms. The density was $\bar{n}_e = 2 \times 10^{19}\ \mathrm{m}^{-3}$ and the field 2.5 T. The data obtained are of excellent quality.

In Fig. 3, the heat-pulse diffusivities χ_e^{hp} as obtained from bessel fits to phases and amplitudes of first and second harmonic perturbations are compared with the power balance values. The data confirm a ratio of χ_e^{hp}/χ_e^{pb} of about 2. Only at high power densities, the old result is recovered.

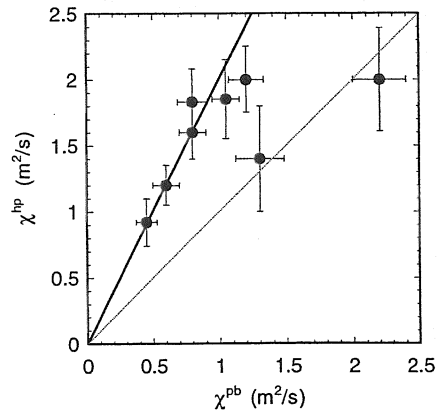

Fig. 3: Heat diffusivities from power balance and heat pulse analyses.

In order to test the parameter dependence of χ_e in detail, amplitudes and phases were simulated with the ASTRA code using the following models: (a) $\chi_e = \chi_e^{pb}$, (b) $\chi_e \sim T_e$, (c) $\chi_e \sim \nabla T_e$ and (d) $\chi_e \sim P^{0.5}$. In Fig. 4 calculated and measured amplitudes and phases are compared for two examples, $P = 0.43$ and 0.95 MW. In all cases, the central measured amplitudes are consistent with the ECH modulation amplitude and so, in contrast in to earlier experiments, no missing power was observed. At low heating power the models (a) - (c) fit the amplitude profile, and (c) and (d) fit the phase profiles. For all experiments with an ECH power $\lesssim 0.8$ MW

the model linear in ∇T reproduces the measurements. For high power, the Shafranov shift modulation leads to asymmetric amplitude and phase profiles. With a simple radial shift, simultaneous symmetrization of both profiles is not possible. In Fig. 4 the symmetrization was done for the phase profile. The amplitudes on the high and low field side differ as shown in the Fig. 4. The phases are reproduced rather well by (a) and (b). (c) fails completely and (d) deviate at larger radii and also cannot account for amplitudes.

These results confirm the results from Ref. [6] which were deduced from data with lower quantity. The question is, how to reconcile those results with the previous ones. One possible explanation could be that in the plasma a transition occurs from a local to a global model if e.g. the temperature gradient, which is related to the power per particle, exceeds a critical value. In the power scan, at $P > 0.8$ MW or $P/n > 2\times10^{-14}$ Wm^3 the old result of $\chi_e^{hp}/\chi_e^{pb} \approx 1$ is recovered. The early experiments were done in this range, although at $B = 1.25$ T. In order to investigate this hypothesis, the available data from a power scan at lower density and from the temperature decay phase after power switch-off have to be analyzed.

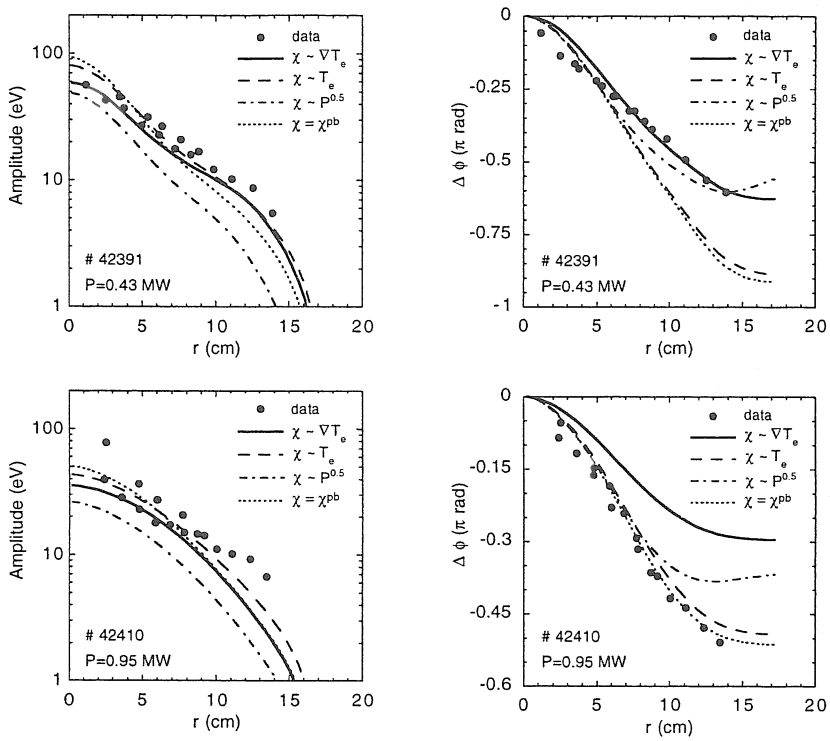

Fig. 4: Comparison between measured and simulated amplitude and phase profiles. ECH power is depicted in the center.

References

[1] K. W. Gentle *et al.*, Phys. Fluids **2**, 2292 (1995).

[2] G. Pereverzev *et al.*, IPP report 5/42, Max-Planck-Institut für Plasmaphysik, Garching, F.R.G. (unpublished).

[3] L. Giannone *et al.*, Nucl. Fusion **32**, 1985 (1992).

[4] H. J. Hartfuß *et al.*, Plasma Phys. Controlled Fusion **36**, B17 (1994).

[5] U. Stroth, L. Giannone, and H. J. Hartfuß, Plasma Phys. Controlled Fusion **38**, 1087 (1996).

[6] M. Peters, Ph.D. thesis, Technische Universiteit Eindhoven, 1995.

Properties of density and magnetic field fluctuations in the SOL and the edge regions of the W7-AS stellarator

S. Zoletnik[1,2], M. Anton[1], J. Bleuel[1], M. Endler[1], S. Fiedler[1], M. Hirsch[1], K. McCormick[1], J. Schweinzer[1] and W7-AS Team[1]

1) *Max-Planck Institut für Plasmaphysik, Association Euratom, Boltzmannstr. 2, Garching bei München, D-85748*

2) *KFKI Research Institute for Particle and Nuclear Physics, P.O.B. 49, H–1525 Budapest, Hungary*

Edge and Scrape Off Layer (SOL) electron density fluctuations in the W7-AS stellarator are investigated by Beam Emission Spectroscopy (BES) technique using the 48 keV Li-beam diagnostic[1]. This method enables a non-disturbing, spatially and temporally resolved measurement of correlation functions (and this way fluctuation amplitudes as well) across the SOL and the outer 20-30% of the confinement region. To complement the poloidally localized but radially resolved BES measurement, magnetic field fluctuations were recorded and correlated with Li-light fluctuations using poloidal arrays of Mirnov coils mounted on the vessel wall at three toroidal positions.

Experiment and data evaluation. The Li(2p) line radiation induced by collisions of plasma particles with the neutral Li-beam atoms is observed at 28 positions along the beam using a set of photomultipliers. The detection system has a bandwidth of 1 MHz. Although the photon noise on the photomultiplier signals does not decrease below 10% at the above bandwidth even at the maximum of the light profile, correlation functions

$$C^S(Z_1, Z_2, \tau) = \frac{1}{T}\int_0^T \tilde{S}(Z_1, t)\tilde{S}(Z_2, t+\tau)dt \tag{1}$$

can be determined with good accuracy if the integration time T is set longer than about 10 ms. Here $\tilde{S}(Z,t)$ denotes the fluctuating part of the light emission detected at point Z along the beam as a function of time.

Using an appropriate model of the atomic processes taking place in the beam[2] the light emission for any density profile can be calculated. If the beam is only weakly attenuated or the electron density fluctuation amplitude is small ($\leq 10\%$) then the connection between the beam light fluctuations and the electron density fluctuations can be approximated linearly but non-locally:

$$\tilde{S}(Z,t) \approx \int_0^Z \tilde{n}_e(Z',t)h(Z,Z')dZ'. \tag{2}$$

Weak attenuation holds for the SOL, while the condition of low fluctuation level is satisfied for the confinement region. Therefore the above linearization is a good approximation everywhere along the Li-beam for nearly all discharge conditions. By substituting the linear approximation of $\tilde{S}(Z,t)$ into equation (1) one arrives at a linear mapping from the correlation functions of the electron density fluctuations to the correlation functions of beam light fluctuations. By inverting this mapping as it is described in detail in [3] one can calculate the correlation functions of electron density fluctuations. Normalization of the correlation functions is done by using the fluctuation powers obtained from $C(Z,Z,0)$.

The time resolution of the correlation functions can be as good as $1\mu s$ but in order to reduce statistical noise it is typically set to about $5\mu s$. Spatial resolution is limited both by the intrinsic time constants of the atomic physics processes in conjunction with the Li-beam velocity and by the diameter of the beam to about 1 cm.

Magnetic field fluctuations are measured by sampling the signals of Mirnov coils with 3-5 μs time resolution. By applying the SVD technique to a poloidally distributed set of Mirnov coils at one toroidal position the dominant spatial and temporal structures are determined[4]. Additionally, the correlation between Mirnov coil signals and Li-beam light signals is calculated. Although this correlation can be different from the correlation between electron density fluctuations and magnetic field fluctuations, it can deliver valuable information as at least for low electron density discharges the beam light fluctuations correlation functions resemble the correlation functions of electron density fluctuations.

Results. After analyzing several hundred plasma discharges under various conditions ($t_a = 0.25 \ldots 0.55$, $n_e(0)=1 \times 10^{19} \ldots 8 \times 10^{19} m^{-3}$, ECRH, NBI, ICRH and combined heating scenarios) it was found that the observed fluctuation phenomena can be divided into four categories:

1. **Turbulent fluctuations in the SOL** with relative amplitudes between 10-40%. correlation times between 20-50 μs (decreasing towards the LCFS) and radial correlation lengths typically 1-2 cm. These fluctuations are present in all discharges and not sensitive to magnetic configuration changes. A typical space-time correlation function is shown on Fig. 1/a. The characteristics of these fluctuations are in good agreement with Langmuir probe measurements[5]. No correlation with magnetic fluctuations was observed.

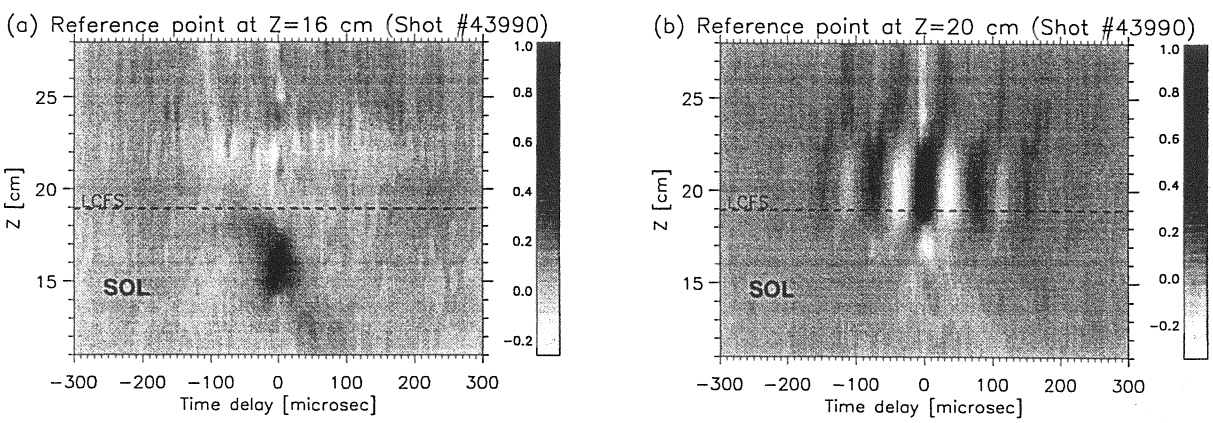

Fig. 1. Normalized Space-time correlation of electron density fluctuations relative to (a) a point in the SOL, (b) relative to a point 1 cm inside the LCFS. Horizontal axis plots time lag, vertical axis is coordinate along the Li-beam.

2. **Burst-like fluctuations** in the edge plasma. A few cm inside the LCFS one often observes temporally periodic but finite lifetime phenomena (Fig. 1/b). These are not correlated with fluctuations in the SOL, but well correlated with magnetic fluctuations as shown on Fig. 2. (Correlation $0.2 \ldots 0.7$ is observed, depending on plasma conditions.) The number of periods in the burst can vary from a single peak to about 5-6. The frequency of the burst is in the range of 10-30 kHz. The radial correlation length, number of peaks, frequency and phase structure along the beam sensitively depend on t, electron density and other plasma parameters, although all

burst properties are reproducible from shot to shot. Under certain conditions) these fluctuations are absent. SVD analysis of magnetic fluctuations[4] revealed, that the poloidal structure of the associated magnetic fluctuations can be best described by an $m = \mathbf{int}(1/\iota_a)$ mode perturbation with a correlation time of $100\mu s$ or less, where ι_a is the edge rotational transform and **int** means integer part.

3. **Relaxational phenomena.** Under certain plasma conditions fluctuations with 200-500μs correlation time appear both in the SOL and the edge plasma. They are most characteristic in a small ι window around $\iota_a = 0.523$ where they are the result of sudden flattenings followed by a gradual relaxation of the density profile around the LCFS. This behaviour is reflected by a radial anticorrelation between positions inside and outside the LCFS. The amplitude and extension depends strongly on plasma conditions. For a detailed discussion of such phenomena see [6].

4. **Mode activity.** In NBI heated discharges periodic fluctuations are observed in the edge plasma. They show periodic autocorrelations for several hundred microseconds and good correlation with magnetic fluctuations. They most probably correspond to GAE modes.

Discussion. As it is well known edge plasma phenomena can largely affect plasma confinement, therefore in this section we intend to discuss the relevance of the above phenomena to plasma confinement. Mode activity is not discussed as it appears or disappears without having any effect on the confinement. Relaxational phenomena as seen by the Li-beam diagnostic are merely a response of the density profile to some instability, therefore they are also neglected.

The first question one has to answer is whether SOL turbulence and burst-like fluctuations are merely the two facets of the same instability or they are different, i.e., does the characteristic of the turbulence change at the LCFS or not? Several arguments are found that there is a change at the LCFS:

- For the burst-like fluctuations strong correlation with magnetic fluctuations is observed as it is shown on Fig. 2. On the other hand any attempt to find correlation between magnetic fluctuations and Li-beam light fluctuations in the SOL was unsuccessful. Similar results were published from TEXT[8], where a correlation between Langmuir probe ion saturation current and magnetic field fluctuations was observed only if the probe was inserted inside the LCFS.

- As characteristics of SOL turbulence measured with the Li-beam diagnostic agree with Langmuir probe measurements, we have good reason to think the two diagnostics measure the same phenomenon. From the Langmuir probe measurements[7] it is known, that SOL turbulence in W7-AS has a typical poloidal wavelength of 5 cm. On the other hand, the poloidal wavelength of the burst-like fluctuations from the low-m structure of the correlated magnetic-field fluctuations is found to be several ten centimeters, nearly an order of magnitude longer than for the SOL turbulence. If additionally to the low-m structure the perturbations would have a local 5 cm poloidal wavelength structure as well, the Li-beam would additionally detect bursts with a frequency of 100-300kHz. This is well within the frequency response of the diagnostic, but was never seen.

- While the SOL turbulence can be seen in all discharges, in some cases the burst-like fluctuations disappear. In these cases the SOL turbulence remains unchanged and similar fluctuations are not detected inside the LCFS.

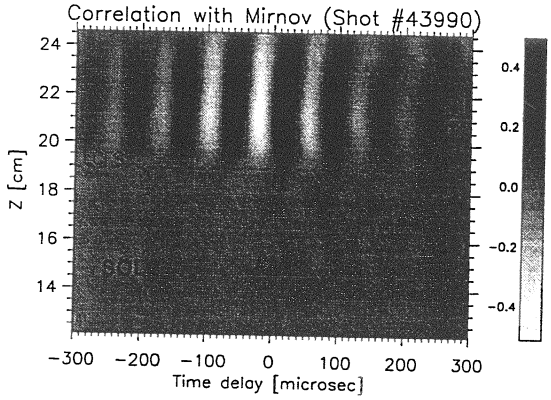

Fig. 2. Normalized correlation of Mirnov coil signal with all Li-beam light signals. The horizontal axis gives time lag, the vertical distance along the beam.

The above argumentation supports the former finding from ATF[9] that turbulence mechanisms are different on the two sides of the LCFS. However, as both the resolution of the Li-beam diagnostic and the accuracy of the LCFS position determination is around 1 cm, it cannot be ruled out that within one centimeter around the LCFS the same type of turbulence is present.

The importance of SOL turbulence for plasma confinement has already been discussed in the literature. The relevance of the burst-like fluctuations is not yet clear. It was found that at high electron density discharges ($n_e(0) \approx 8 \times 10^{19} m^{-3}$) around $\iota_a = 0.35$ the energy confinement time depends sensitively on edge ι, and the radial correlation length of the burst-like fluctuations increases with decreasing confinement time. However, at low electron density ($n_e(0) \approx 1 \times 10^{19} m^{-3}$) the burst-like fluctuations completely disappear for a certain magnetic configuration without any change in confinement time. In this case the confinement time is insensitive to ι_a. These observations indicate, that at low electron density the burst-like fluctuations are not important for confinement, but at high densities they might play a role in confinement.

Theoretical calculations to understand SOL turbulence on the basis of drift wave turbulence are presented in another paper [10]. In these calculations the crossing of the LCFS does not make enough difference to understand the observation that turbulence characteristics change at the LCFS. However, the present version of the simulation might be invalid under the plasma conditions found a few centimeters inside the confinement zone. Thus a direct comparison with theoretical calculations is not available for the whole observation volume at present.

References

[1] K. McCormick *et al. Fusion Engineering and Design* **34-35** 125 (1996)
[2] J. Schweinzer *et al. Plasma Physics and Contr. Fus.* **34** 1173 (1992)
[3] S. Zoletnik *et al. accepted for publication in Plasma Phys. Control. Fusion* **40** (1998)
[4] M. Anton *et al. J. Plasma Fusion Res.*, **SERIES**, **1** 259 (1998)
[5] M. Endler, *et al Nuclear Fusion* **35** 1307 (1995)
[6] M. Hirsch, *this conference*
[7] M. Endler, *et al. Physica Scripta* **51** 610 (1995)
[8] Y.J. Kim, *et al., Nuclear Fusion* **29** 99 (1989)
[9] C. Hidalgo, *et al. Nuclear Fusion* **31** 1471 (1991)
[10] J. Bleuel, *et al. this conference*

--Prof. Wagner--

INTERNATIONAL ATOMIC ENERGY AGENCY

17th IAEA Fusion Energy Conference
Yokohama, Japan, 19 - 24 October 1998

IAEA-FI-CN-69/CDP/05

ECRH AND ECCD EXPERIMENTS IN AN EXTENDED POWER RANGE AT THE W7-AS STELLARATOR

V. ERCKMANN, U. GASPARINO, H.P. LAQUA, H. MAASSBERG, W7-AS Team
Max-Planck-Institut für Plasmaphysik, EURATOM Association,
85748 Garching, Germany

ECRH Group
Institut für Plasmaforschung, Universität Stuttgart, Germany

K.S. KASILOV, N. MARUSHCHENKO
Institute of Plasma Physics, NSC-KhPTI, 310108 Kharkov, Ukraine

V. IRKHIN, S. MALYGIN
GYCOM, Nizhny Novgorod, Russia

ECRH AND ECCD EXPERIMENTS IN AN EXTENDED POWER RANGE AT THE W7-AS STELLARATOR

V. ERCKMANN, U. GASPARINO, H.P. LAQUA, H. MAASSBERG, W7-AS Team
Max-Planck-Institut für Plasmaphysik, EURATOM Association,
85748 Garching, Germany

ECRH Group
Institut für Plasmaforschung, Universität Stuttgart, Germany

K.S. KASILOV, N. MARUSHCHENKO
Institute of Plasma Physics, NSC-KhPTI, 310108 Kharkov, Ukraine

V. IRKHIN, S. MALYGIN
GYCOM, Nizhny Novgorod, Russia

Abstract

An overview on physics studies on Electron Cyclotron Resonance Heating (ECRH) and ECCurrent Drive (ECCD) in an extended parameter range at W7-AS is presented. Experiments were performed with an upgraded ECRH power of up to 1.3 MW at 140 GHz. Electron temperatures of up to 5.7 keV were measured, which can only be explained by the beneficial effect of positive radial electric fields ('electron root'). The experiments confirm, that the electric field is generated by ECRH driven particle losses in the specific stellarator magnetic field. ECCD experiments were performed at high input power (1.3 MW) resulting in EC-driven currents of up to 20 kA. The direction of the EC-driven current was varied in co- and counter-direction with respect to the bootstrap current in discharges with zero net-current. Three current contributions, i.e. the EC-driven current, the bootstrap current and the inductively driven current are calculated independently and modify the internal profile of the rotational transform significantly. A comparison with quasi-linear theory shows significant deviation in the co-current drive case, which may be attributed to strong MHD activity and/or violation of the quasilinear assumptions due to the high power density.

1. INTRODUCTION

Investigations on ECRH and ECCD at W7-AS [1] were continued with an upgraded ECRH heating power of up to 1.3 MW at 140 GHz, which corresponds to a resonant magnetic field of 2.5 T at 2nd harmonic X-mode (X2). The heating experiments cover the full accessible density range up to the cut-off density of 1.25×10^{20} m^{-3}, whereas we have restricted the ECCD experiments to densities around 0.25×10^{20} m^{-3}. The microwaves are absorbed in a narrow region around the resonant magnetic field and thus the power density increases up to 50 MW/ m^{-3} in a flux surface average, which is far beyond the limits, were linear theory holds and nonlinear phenomena are expected to occur. At high power density, the electron distribution function flattens at the resonance and the absorption is shifted towards higher energies thus generating a suprathermal tail [1,2]. This quasilinear effect increases the ECCD-efficiency with respect to linear theory. Nonlinear wave-particle interaction, which is maximum for ripple trapped electrons with small parallel velocities is, however, expected to reduce the ECCD efficiency. Furthermore, a strong deformation of the electron distribution function may be unstable thus affecting the driven current.

2. CENTRAL CONFINEMENT WITH STRONG ECRH

Experiments with strong X2-mode heating were performed in a wide density range at constant input power of 1.3 MW in low field side launch in the equatorial plane. Radial profiles of T_e and n_e are shown in Fig. 1. The central electron temperatures range from 5.7 keV at 1.7×10^{20} m^{-3} to 3 keV at 7.5×10^{20} m^{-3}. A pronounced steepening of the temperature gradients is

seen in the centre of the plasma at densities below 4×10^{20} m^{-3}. The stationary transport analysis of these discharges results in a central ($r/a < 0.3$) electron heat diffusivity, which is well below the neoclassical heat diffusivity, once electric fields are neglected. Strong positive radial electric fields up to 50 kV/m were measured in the plasma centre, which lead to good agreement with neoclassical theory including electric fields ('electron root solution'). It is worth noting, that the ions are energetically decoupled from the electrons under these conditions and the energy balance is dominated by the electrons.

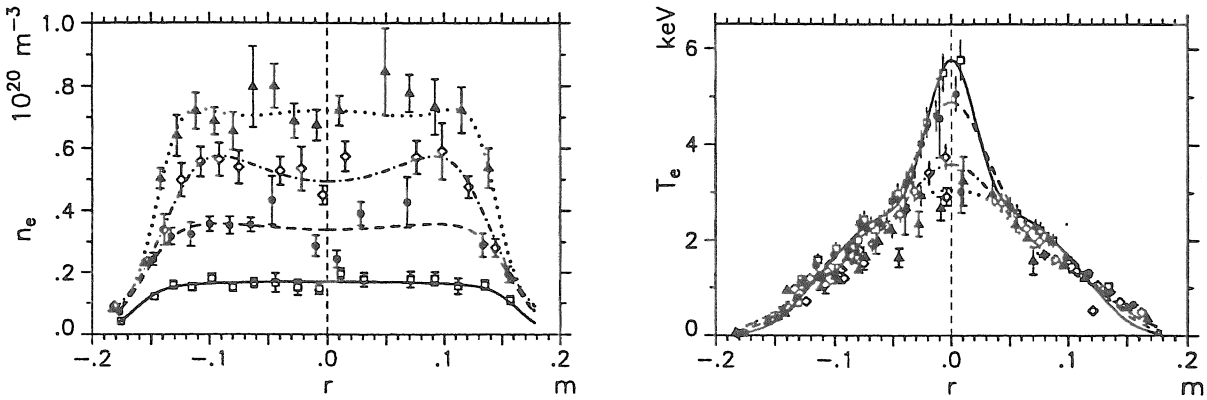

Fig. 1. Radial profiles of the electron density (left) and temperature (right) with 1.2 MW ECRH.

The appearance of the electric fields - and the corresponding steep temperature gradients- shows a threshold behaviour at a density around 0.2 - 0.4 $\times 10^{20}$ m^{-3}, a similar behaviour was measured during a power scan from 0.2 MW to 1.3 MW input power at constant density of 0.2×10^{20} m^{-3}, where the steepening occurred between 0.2 and 0.4 MW. The discharge could be placed at the threshold by careful adjustment of the heating power density while tuning the deposition region. The central electron temperature then is jumping iteratively between two states of low (say 4 keV) and high (5 keV) temperature during one discharge with some hysteresis between rise and fall-time constants. The experiments are explained by a substantial loss of fast trapped particles driven by ECRH itself, which in turn generates a positive electric field with its beneficial effect on the bulk electrons [3,4]. This picture is consistent with the results of switching experiments, where the central confinement is lost on a fast timescale (< 0.3 ms), whereas the remaining profile relaxes on the diffusion timescale. Also these switching experiments display a threshold nature while switching from 1.2 to 0.8 to 0.4 MW.

3. ELECTRON CYCLOTRON CURRENT DRIVE

A toroidal launch angle scan was performed at 1.2 MW launched power and a density of 2.5×10^{19} m^{-3} with inductive compensation of the EC driven current to maintain net current free conditions with $I_{ind} + I_{boot} + I_{ECCD} = 0$ (I_{ind} is the inductive component, I_{boot} and I_{ECCD} are the bootstrap and the EC-driven components, respectively). The microwaves were injected from low-field-side in X2 mode polarization, the polarization was adjusted according to the given launch angle from linear to elliptical polarization to provide optimum coupling of the microwaves. During the scan the toroidal magnetic field was adjusted to keep the Doppler shifted deposition profile close to the plasma axis ($\Delta B/B \cong 10\%$ for $|\varphi_{inj}| = 30^o$). Under these conditions, ray-tracing calculations predict a peaked deposition profile with flux surface averaged power densities of up to 50 MW/m^3. The required inductive loop voltage for current compensation is shown in Fig. 2 (left) as a function of the launch angle φ_{inj} ($\varphi_{inj} = 0^o$ corresponds to perpendicular injection, $I_{ECCD} = 0$). For a quantitative comparison of the measured data with theory we assume a linear superposition of the three current contributions, which is justified, because the suprathermal electrons generated by ECRH have only a negligible effect on the electric conductivity as confirmed by Fokker-Planck calculations [5]. The bootstrap current is calculated by the DKES code taking into account the ambipolar radial electric field, and the inductive current is calculated assuming neoclassical resistivity (effective charge $Z_{eff} = 3$-6), the calculations are performed for each individual discharge using the measured profiles of n_e and T_e. Then the EC driven current from the current balance $I_{ECCD} = -I_{ind} - I_{boot}$ is plotted in Fig. 2 and compared

with the linear theoretical ECCD current, I_{inj}. The maximum linear ECCD-efficiency from ray-tracing (based on the adjoint approach with trapped particles [6] included), $\eta_{ECCD} \cong 20$ A/kW corresponds to a normalized efficiency $\gamma_{ECRH} = n_e I_{ECCD} R / P_{ECRH} \cong 0.01 \times 10^{20}$ A/Wm^2.

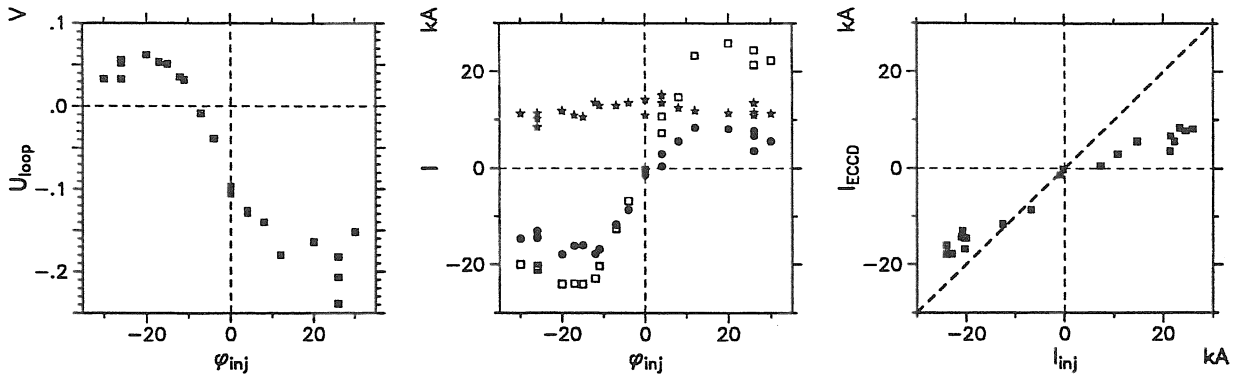

Fig. 2. Left: Loop voltage vs. toroidal angle of injection in net current free discharges, $U_{loop} = -(I_{boot} + I_{ECCD}) / R$. Perpendicular injection corresponds to $\varphi_{inj} = 0^o$. Centre: Theoretical (open squares) and data from current balance of the EC-driven current (dots) together with the bootstrap current (stars) as a function of the launch angle. Right: EC-driven current from current balance versus linear prediction.

As seen from Fig. 2 (right), where the 'experimental' I_{ECCD} is plotted versus theory, good agreement with linear theory is observed even at these extremely high power densities except for launch angles in co-direction. This may be a hint for a degradation of the CD-efficiency at high power density. The calculations of both the inductive and the bootstrap current are very conservative and are expected to be more reliable than the linear ECCD calculations, where the assumptions of the linear approach are likely to be violated. Non-linear effects in the wave-particle interaction in an inhomogeneous magnetic field are important especially at moderate launch angles. Thus the quasi-linear theory, which holds in a homogenous magnetic field must be reformulated. In addition the wave absorption increases the perpendicular energy and pushes electrons into the loss cone. In the bounce-averaged Fokker-Planck calculation the strong heating as formulated by the traditional quasi-linear diffusion term is balanced by the energy loss of mainly suprathermal ripple-trapped electrons. The radial ∇B-drift of suprathermal ripple-trapped electrons broadens the power deposition profile [3] but has no influence on the ECCD profile. In the electron distribution function, however, positive gradients with respect to $v_{||}$ close to the loss-cone boundary are found, which represent free energy and may drive the distribution function unstable. The fast growth rate of such kinetic instabilities affects the distribution function and can reduce the CD-efficiency, which would again require a reformulation of Fokker-Planck modelling.

In discharges with strong co-CD, MHD-activity is observed, which is absent in the counter-CD cases. This is explained by the strong change of the radial profile of the rotational transform while scanning from co- to counter-CD, because the different current contributions flow at different radial positions. The bootstrap current is localized in the pressure gradient region whereas the inductive current follows the plasma conductivity profile and the EC-driven current is localized around the resonance. Figure 3 shows radial profiles of n_e and T_e together with the rotational transform for co- and counter CD.

For co-CD the temperature profiles remain peaked and the ι –profile crosses the $\iota = 1/3$ and $\iota = 1/2$ surfaces with strong shear. The observed MHD-modes are the corresponding m=3 and m=2 modes, which may influence the current distribution. The modes are located around the rational ι values as measured by ECE, soft-X and Mirnov diagnostics. In the opposite case of counter-CD the $\iota = 0$ surface appears in the plasma centre and the temperature profile is flat within this surface indicating bad or no confinement within this surface. In consequence the EC-driven current within the $\iota = 0$ surface may be distributed over a wider volume than calculated by ray tracing, leading to a reduced power density, a lower deviation from a Maxwellian distribution function and thus to a better agreement with linear CD-theory.

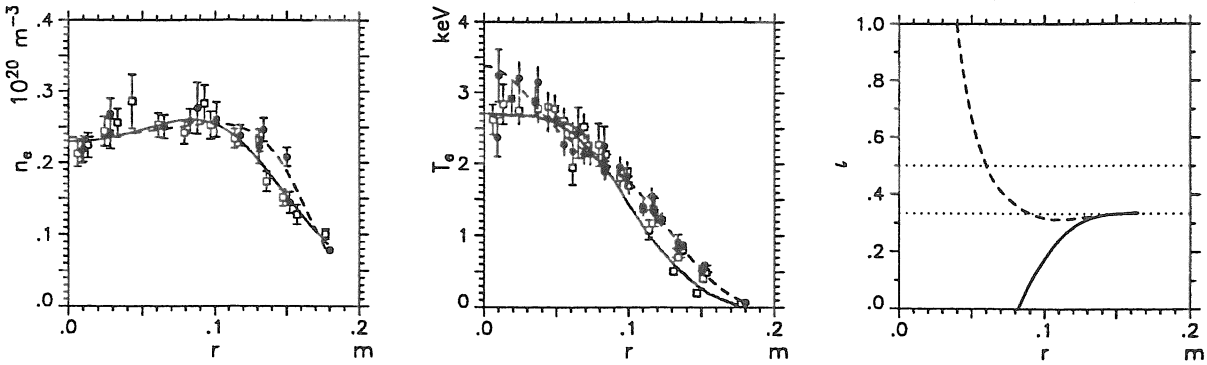

Fig. 3. Radial profiles of the electron density n_e (left), electron temperature T_e (centre) and rotational transform ι (right) for co- (dashed line) and counter-CD (solid line) at zero net-current, φ_{inj} = + and - 12°, respectively.

4. CONCLUSIONS

Experiments on ECRH and ECCD were performed at W7-AS with enhanced heating power, which is well beyond the previous frame of investigations. New physics arrives in the experiments and drives theory into the interpretation of strong kinetic effects. The central confinement of ECR-heated discharges is strongly influenced by ECRH specific features. Positive radial electric fields driven by fast electron losses in the plasma centre ('electron root') provide significantly enhanced electron confinement resulting in peak temperatures of 5.7 keV.

Net current free discharges with up to 20 kA of highly localized EC-driven currents in co- and counter-direction to the bootstrap current were investigated and compared with linear predictions. The experiments indicate under some conditions a deviation from linear ECCD theory, which asks for advanced kinetic modelling.

The radial profile of the rotatational transform was tailored by strong ECCD in a wide range from tokamak-like profiles, which exhibit rational resonances of ι with related MHD-activity, to inverse profiles, where ι = 0 with bad or no confinement appears in the inner plasma region.

REFERENCES

[1] ERCKMANN, V. and GASPARINO, U., Electron Cyclotron Resonance Heating and Current Drive in toroidal Fusion Plasmas, Plasma Phys. Control. Fusion 36 (1994) p. 1869.

[2] ROMÉ, M., ERCKMANN, V., GASPARINO, U., HARTFUSS, H.J., KÜHNER, G., MAASSBERG, H., MARUSHCHENKO, N., Kinetic modelling of the ECRH power deposition in W7-AS, Plasma Phys. Control. Fusion 39 (1997) 117-158.

[3] MURAKAMI, S., GASPARINO, U., IDEI, H., KUBO, S., MAASSBERG, H., MARUSHCHENKO, N., NAKAJIMA, N., ROMÉ, M., OKAMOTO, M., 5D Simulation study of suprathermal electron transport in non-axissysmmetric plasmas, Paper IAEA-CN-69/TH2/1 (R) THP1/1, this conference.

[4] MAASSBERG, H., BEIDLER, C.D., DYABILIN, K.S., GASPARINO, U., MURAKAMI, S., W7-AS TEAM, The neoclassical 'electron root' feature in the W7-AS stellarator, submitted for publication to: Plasma Phys. Control. Fusion.

[5] MARUSHCHENKO, N., GASPARINO, U., MAASSBERG, H., ROMÉ, M., Bounce averaged Fokker-Planck code for the description of ECRH in a periodic magnetic field, Comput. Phys. Comm. 103, (1997) 145-156.

[6] ROMÉ, M., ERCKMANN, V., GASPARINO, U., and KARULIN, N., Electron cyclotron resonance heating and current drive in the W7-X stellarator, Plasma Phys. Control. Fusion 40 (1998) 511-530.

INTERNATIONAL ATOMIC ENERGY AGENCY

17th IAEA Fusion Energy Conference
Yokohama, Japan, 19 - 24 October 1998

IAEA-FI-CN-69OV2/4

OVERVIEW ON W7-AS RESULTS WITH RELEVANCE FOR WENDELSTEIN 7-X AND THE LOW-SHEAR STELLARATOR LINE

WAGNER, F., ANTON, M., BALDZUHN, J., BLEUEL, J., BRAKEL, R., BURHENN, R., CATTANEI, G., ENDLER, M., ERCKMANN, V., FENG, Y., FIEDLER, S., GEIGER, J., GEIST, T., GRIGULL, P., HARTFUSS, H.-J., HARTMANN, D., HERRE, G., HIRSCH, M., HOLZHAUER, E., JÄNICKE, R., KICK, M., KISSLINGER, J., KOPONEN, J., KÜHNER, G., LAQUA, H.P., MAASSBERG, H., SARDEI, F., STROTH, U., WELLER, A., ZOLETNIK, S., CHATENET, J.H., DORST, D., ELSNER, A., GIANNONE, L., GÖRNER, C., HACKER, H., KARGER, F., KNAUER, J., KÖNIG, R., LAQUA, H., MCCORMICK, K., NIEDERMEYER, NÜHRENBERG, C., OTT, W., PENNINGSFELD, F.-P., SALAT, A., SCHNEIDER, F., THEIMER, G., WALTER, H., WENDLAND, C., WERNER, A., WÜRSCHING, E., ZEILER, P.

Max-Planck-Institut für Plasmaphysik, EURATOM Association, Garching, Germany

IAEA-FI-CN-69/OV2/4

OVERVIEW ON W7-AS RESULTS WITH RELEVANCE FOR WENDELSTEIN 7-X AND THE LOW-SHEAR STELLARATOR LINE

WAGNER, F., ANTON, M., BALDZUHN, J., BLEUEL, J., BRAKEL, R., BURHENN, R., CATTANEI, G., ENDLER, M., ERCKMANN, V., FENG, Y., FIEDLER, S., GEIGER, J., GEIST, T., GRIGULL, P., HARTFUSS, H.-J., HARTMANN, D., HERRE, G., HIRSCH, M., HOLZHAUER, E., JÄNICKE, R., KICK, M., KISSLINGER, J., KOPONEN, J., KÜHNER, G., LAQUA, H.P., MAASSBERG, H., SARDEI, F., STROTH, U., WELLER, A., ZOLETNIK, S., CHATENET, J.H., DORST, D., ELSNER, A., GIANNONE, L., GÖRNER, C., HACKER, H., KARGER, F., KNAUER, J., KÖNIG, R., LAQUA, H., MCCORMICK, K., NIEDERMEYER, NÜHRENBERG, C., OTT, W., PENNINGSFELD, F.-P., SALAT, A., SCHNEIDER, F., THEIMER, G., WALTER, H., WENDLAND, C., WERNER, A., WÜRSCHING, E., ZEILER, P.

Max-Planck-Institut für Plasmaphysik, EURATOM Association, Garching, Germany

Abstract

The Wendelstein stellarator programme of Garching has developed low shear stellarators with successively optimised designs to remove the intrinsic deficiencies of this 3D concept. W7-X, presently under construction, is in internal terminology a fully optimised stellarator. W7-AS, the presently operated device, is a partly optimised stellarator. The optimisation of stellarators aims at improved neoclassical confinement in the long mean free path regime and improved equilibrium and stability properties. In this report, we address equilibrium, stability, turbulent and collisional energy confinement aspects (role of shear, role of the radial electric field, low and improved confinement regimes), particle transport, edge transport and turbulence, high density operation, ECRH (OXB scheme) and ICRF heating and the development of the island divertor for exhaust. The maximal parameters achieved in W7-AS (at different discharge types) are: $T_e = 5.8$ keV, $T_i = 1.5$ keV, $n_e = 3 \times 10^{20}$ m^{-3}, $\langle\beta\rangle = 2\%$, $\tau_E = 50$ ms.

The W7-X concept:

The stellarator Wendelstein 7-X (W7-X, presently under construction in Greifswald, Mecklenburg-Vorpommern, Germany) is optimised based on the concept of quasi-isodynamicity /1/. A truly isodynamic confinement geometry has poloidal symmetry with the consequence of plasma flows on a flux surface only, without neoclassical radial fluxes. In order to utilise this concept in a toroidally closed system, a specific geometry is necessary. Straight sectors are connected to a polygon - a pentagon in the case of W7-X. The magnetic field is increased at the corners of the pentagon to maintain particles in the straight sectors where their guiding centres rotate poloidally. By this means radial neoclassical fluxes at the low level of that of symmetric systems can be achieved. In order to maintain the optimisation of the vacuum design at high β (resistive ballooning is expected to limit W7-X to 5%), pressure driven parallel currents must also be minimised. The concept of quasi- isodynamicity allows $\langle j_{\parallel}^2\rangle/\langle j_{\perp}^2\rangle$, which is $2/\iota^2$ for a classical stellarator and is reduced to $0.32/\iota^2$ for W7-X, and the bootstrap current to be simultaneously minimised. To reduce $\langle j_{\parallel}^2\rangle$, the plasma cross-sections are strongly eleongated at the corners ($\kappa \approx 6$); bootstrap current can be minimised in W7-X unlike in quasi-helical or quasi-toroidal systems by matching toroidal and helical curvatures. Thus, the properties of the optimised vacuum design are maintained at high β. The rotational transform ι of W7-X is selected around $\iota=1$ ($0.8 \leq \iota \leq 1.2$) with a small variation between core and edge ($0.8 \leq \iota \leq 1$ or $1 \leq \iota \leq 1.25$); low shear promises good confinement as long as low order m and n field perturbations are avoided. In order to also minimise high m/n turbulence, limited shear is provided to the extent that low order rationals are still excluded. An edge separatrix can be formed via a chain of edge islands (5/5 or alternatively 6/5) which are radially extended because of low shear and consequently are expected to effectively divert the fluxes from the plasma and to establish the magnetic part of an island divertor.

The W7-AS device:

W7-AS has the form of a pentagon and its field structure is partly optimised ($\langle j_{\parallel}^2\rangle/\langle j_{\perp}^2\rangle = 0.85/\iota^2$) /2/. The field system is composed of modular coils (ι=0.4): toroidal field coils allow changes of ι, vertical field coils allow to vary the radial plasma position; W7-AS is also equipped with an OH system e.g. to compensate the bootstrap current. In addition, the magnetic field strength in the corners of the pentagon can be varied (variation of mirror ratio). The bootstrap current is tokamak-like and increases ι; generally, operation is such that a superimposed inductive current cancels this increase of the edge rotational transform ι_a to maintain the pre-set value. Shear can be varied with OH current and by ECCD. The vertical field allows changes of the magnetic well and thus modifies stability properties. In addition, it allows changes of the plasma wall interaction with 5×2 graphite tiles mounted symmetrically at the inboard walls.

Equilibrium properties:

The optimisation of W7-AS has been demonstrated by indirect measurement of the parallel currents $\langle j_{\parallel}^2\rangle$ which were found to be reduced as expected /3/ and by the demonstration of reduced Shafranov shift in high β equilibria in comparison to a classical l=2 stellarator /4/. The maximal $\langle\beta\rangle$-value of W7-AS was found close to 2%. The limitation is not via resistive interchange, which are predicted to be unstable, but by a limitation of heating power at given radiation losses. High β operation is carried out at low field of ≈1 T and at high density. Under these conditions, large orbit losses are predicted for energetic particles injected by the counter beam line. The additional increment in β achieved with the counter beams is small in comparison to the rise in β with the co-beams. The high-β programme on W7-AS will be continued with reversing the counter injector into co-direction.

Stability properties:

The high-β plasmas of W7-AS are rather quiescent, reach stationary till the heating has been turned off /5/. No violent MHD processes occur. With a low-order rational in the plasma core, a pressure driven mode may appear which rotates in electron drift direction with a few kHz and which does not reduce the energy content of the plasma. With plasma current - either bootstrap current, or induced current by OH or ECCD /6/ - current driven tearing modes can appear due to resonances. Their impact on the plasma depends on the current level. Although the plasma does not disrupt, the current induced formation of tearing mode islands causes the irreversible loss of a major part of the energy content /7/. A current induced rise in ι_a by $\Delta\iota \approx 0.2$ is sufficient, if ι=0.5 is reached to expel 80% of the energy content. Figure 1 shows the discharge development in such a scenario. Plotted is the central temperature, the variation of ι_a by the plasma current and finally the development of unstable conditions seen in the Mirnov signals.

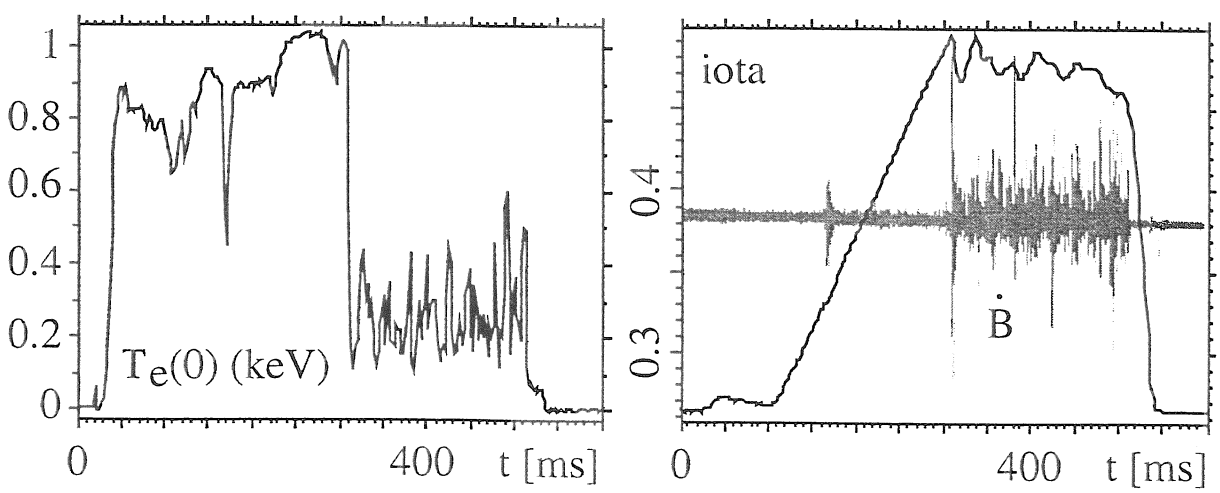

Fig. 1. Development of a discharge with rising OH current. Left: Central electron temperature; right: rise of external rotational transform ι_a and Mirnov signal.

The most conspicuous MHD feature of W7-AS are global Alfvén eigenmodes (GAE) which are driven by that part of the fast particle spectrum which is in resonance /8/. In case of side-band excitation (m±1), particle velocities down to $v_A/10$ can contribute. GAEs appear without the need of a rational ι in the plasma and in the low shear case of W7-AS their frequency resides closely below the corresponding continuum band. The frequency varies with density, isotope mass and field in the expected form. The GAE modes generally saturate at a level up to $\delta B/B \approx 10^{-4}$, there is no evidence, at present, that their presence affects the NBI heating efficiency. With shear (via induced current), the GAE activity changes into TAE modes which are more localised (at the gap) and are characterised by a larger poloidal harmonic content. The mode pattern depends on ι and a large variety is observed - cases up to m=9 and cases with a node in the radial eigenfunction are observed. For both the GAE and the TAE activity, the eigenfunctions are well described by a three-dimensional MHD code (CAS 3D /9/) and by a gyrofluid model /10/.

Confinement and the role of shear:

Low vacuum field shear in the Wendelstein line is a design characteristic. The idea behind low shear is that low-order resonances arising from the mode spectrum of the magnetic field as well as from external field perturbations should be avoided as they reduce confinement - the original thought was by the development of magnetic islands. The most obvious experimental evidence is that, in the accessible ι-range of W7-AS, good confinement is established in the vicinity of ι=1/2 and 1/3 where larger ι-intervals free of resonances occur. (Empirically, it is found that resonances beyond m=20 have no influence.) There is ample experimental evidence which demonstrates the sensitivity of confinement on ι_a (see Fig. 2, left side). At low shear, confinement can be „good" but, without further means, it is at the L-mode level (e.g. in the iota window $0.50 \leq \iota_a \leq 0.53$. Outside this range, the confinement is at a sub-L-mode level. As described below, confinement can be increased to the H-mode level in the favourable ι-windows.

The shear studies of W7-AS are of general interest because of the low central shear obviously required for advanced tokamak scenarios and because different theoretical concepts exist predicting different dependencies of turbulent transport on shear. The studies are carried out for $T_e/T_i >> 1$ (ECRF heating) and only the response of electron transport on shear is investigated. The current necessary to introduce strong shear in W7-AS is too low ($I_p \leq 30$ kA) to affect the power balance /11/.

The impact of ι and shear can be separated at low shear ($I_p < 5$kA, $\Delta \iota_a = 0.007 I_p/\text{kA}$). Good confinement develops if specifically the plasma periphery remains free of resonances. No shear is tolerable in this case. On the contrary, if the edge value, ι_a, is selected such that rational ι-values (m<20) intersperse the plasma outer range, the temperature gradient is flat and confinement is degraded in case of insufficient shear. Good confinement is possible even in the presence of resonances, if sufficient shear is established. With strong shear S ($I_p \approx \pm 25$ kA) - and the sign of S does not matter - the confinement is good and loses its subtle dependencies on iota (see Fig. 2, left side) /11, 12/. The shear where ι loses its impact is about $S \approx 1\ m^{-1}$. A rather sensitive situation is established at low shear. Little shear can degrade good confinement or improve bad confinement depending on the preselected value of ι_a. Under marginal conditions, good confinement can be transformed into degraded confinement (sub-L-mode level) if the plasma current (e.g. self-induced) moves ι_a into the range with resonances. Also the opposite has been observed.

The impact of resonances on transport can be modelled /13/ by a composition of the electron heat diffusivity from three components: the neoclassical χ_{neo}, the anomalous one χ_{an}, which describes the good confinement (L-mode level) and an additional one $\Sigma\chi_{nm}$ which represents the contribution of the resonances. The view is that resonances do not necessarily cause islands, which short-circuit a small radial range, but rather that it gives rise to locally enhanced turbulence. The χ_{nm} term is parameterized by an amplitude a_{nm}, a radial range of effectiveness and a damping factor which itself depends on shear. There are three fit-parameters which are determined from the confinement results in experimental scans which allowed χ_{nm} to be varied. Figure 2 compares the experimentally measured variation of the energy content W with ι_a at different plasma currents (shear values) with the modelling results. The existence of enhanced turbulence at the location of a resonance has not yet been demonstrated. Microwave scattering

shows, however, that the integral density fluctuation level is enhanced under degraded confinement in the radial range of the resonances.

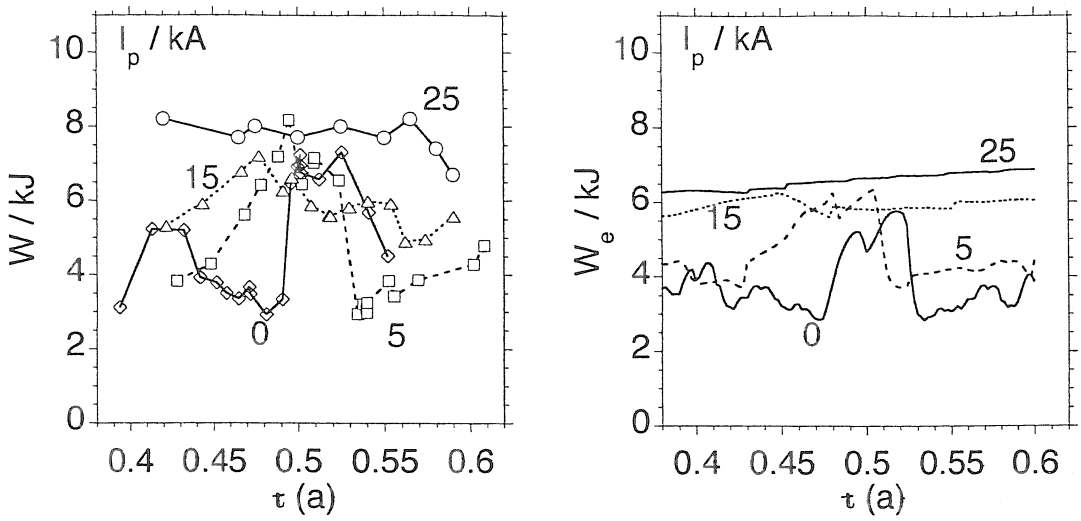

Fig. 2 shows the experimental variation of the energy content W with ι_a; parameter is the plasma current I_p; the right side shows the modelled dependence of the electron energy content W_e.

Neoclassical core transport:

In cases of improved confinement, the core electron temperature rises and because of the strong T_e-dependence of Q_{neo} ($\approx T_e^{9/2}$ (without E_r-field)), the core confinement becomes neoclassical. The better confinement is, the more extended is the neoclassical core /14/.

In those cases where a separate analysis is possible, the ion transport in the plasma core is found to be at the neoclassical level. Under good confinement conditions at high electron temperature, the electron core transport can also be neoclassical. With established electric field, the highest ion- and electron temperatures are measured - in different discharges, however: 1.5 keV and 5.8 keV, respectively. The presence of E_r reduces the heat diffusivities by up to one order of magnitude from the expected neoclassical level without field.

The neoclassical fluxes in stellarators depend explicitly on the radial electric field which itself is determined by the balance of the particle fluxes. The radial electric field represents a thermodynamic force and drives particle flux Γ ($\approx D_{11} E_r/T_e$) whereas the diffusivities (D_{11},D_{12}) depend themselves on E_r. The non-linear relation allows different branches of stable transport equilibria which depend operationally on T_e/T_i/ 15/. The agreement between the measured radial electric field and the one computed on the basis of neoclassical transport even for turbulent plasma conditions points, as in other cases, to the intrinsic ambipolarity of the prevailing electrostatic turbulence. The highest ion temperatures are obtained with NBI when $T_e \approx T_i$. In this case the ion root develops and is characterised by a negative electric field. The highest electron temperature develops with ECRH when $T_e >> T_i$. Here the electron root is establshed in the plasma core whereas the plasma periphery remains at the ion root. Detailed analysis has shown that the electron root cannot develop in W7-AS exclusively on the basis of thermal fluxes rather the loss of non-thermal electrons energised by ECRH contributes to the ambipolarity condition /16/. In the experiment the bifurcation point between the two roots can be selected and the plasma responds at this setting with unstable behaviour (Figure 3 shows the consequence of a dithering behaviour of the neo-classical ambipolarity condition on T_e): T_e of the core plasma oscillates between a state with low electric field (ion root) and one with high field (electron root) with E_r improved neoclassical confinement. The plasma periphery remains passively at the ion root.

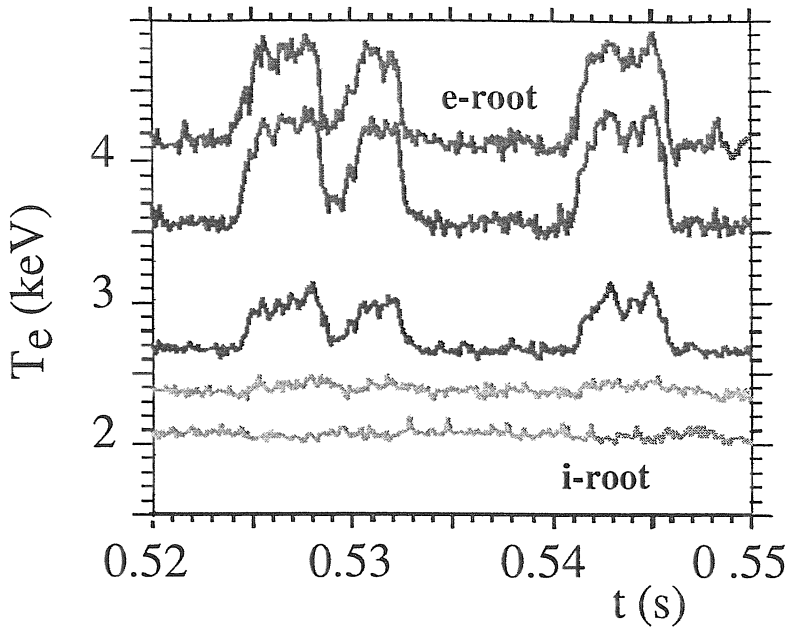

Fig. 3. Plotted is the electron temperature at different radii versus time for a marginal case where the plasma core flips between the electron- (highly positive electric field) and ion root (low positive field). The periphery remains at the ion root.

Global confinement and improved regimes:

The W7-AS energy confinement data are part of the International Stellarator Scaling ISS95 /17/. Data are selected only from the iota ranges around 0.334 and 0.53 where confinement is good at the L-mode level (the turbulent plasma periphery determines τ_E also in cases with neo-classical core). It is interesting that the τ_E values of W7-AS are superior to those of torsatrons typically by 50%. The separate shear studies on W7-AS do not give evidence that the reason is the difference in shear of the two helical concepts. The τ_E scaling of W7-AS alone is: $\tau_E \approx B^{0.73}P^{-0.54}n_e^{0.5}L^{2.72}$. The size scaling (L) is selected to have correct dimensions. It is close to the size scaling of ISS95: $L^{2.86}$. The data base of W7-AS also shows the saturation of confinement time with ECRH heated plasmas at higher densities when analysed by Bayesian probability theory /18/. The W7-AS scaling can be rephrased in dimensionless parameters: $B\,\tau_E \approx \rho^{-2.53}\beta^{-0.03}\nu^{-0.06}$. The scaling is between Bohm and gyro-Bohm.

In the above mentioned ι-ranges the confinement can be improved above the L-mode level. Similar to the tokamak, two obviously different paths are possible: The first is the establishment of the H-mode edge conditions and the steepening of the density profile. Apart from the insight, that the H-mode is rather universal and not restricted to the conditions of tokamaks, the studies on W7-AS have shown that the H-mode develops in specific ι-ranges where poloidal flow damping (from the field structure) is low /19/. The $v_\theta B_\Phi$ term is the dominant contribution to the radial electric field.

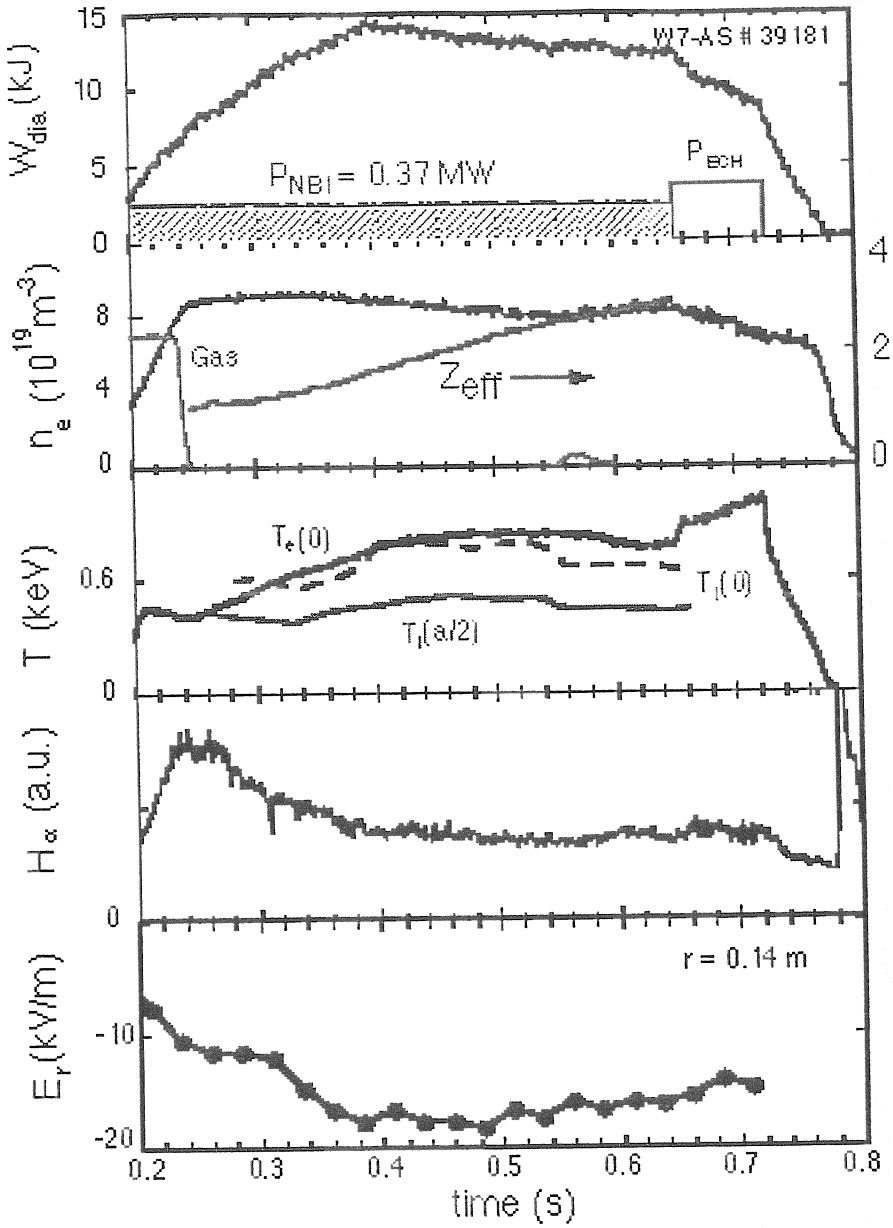

Fig. 4 plots the energy content W_{dia}, the density n_e and Z_{eff}, the temperatures, the H_α radiation and the spectroscopically measured radial electric field E_r versus time for a low power beam heated discharge. At constant density, the confinement improves spontaneously from about 0.25 to 0.4 s.

Figure 4 shows an alternative path to good confinement. The development of the plasma energy content is spontaneous but occurs on a slow time scale ($\delta t \approx \tau_E$). An interesting aspect of this regime is that the energy content rises at constant density via the rise in T_e and T_i. The gradual improvement is accompanied by a gradual reduction of H_α. E_r becomes more and more negative and develops along the neoclassical expectation. The major characteristics of this confinement regime is the narrowing of the density profile and low edge density. The technical prerequisite is a well conditioned device with boronised walls and low recycling properties. There is strong reminiscence to improved tokamak regimes which demonstrate a similar link between bulk confinement quality, edge properties, and recycling control /21/. The source fuelling by NBI or combined NBI+ECRH contributes to the profile peaking. In the phase of confinement improvement, the T_e profile gradually expands. At low power (0.5 MW) and high density (10^{20} m^{-3}), τ_E values above 50 ms have been observed - a factor two above ISS95 and in the ball park of expectations based on ELMy H-mode scaling.

Particle transport:

Stellarator density profiles are flat in the plasma core under heating conditions without central fuelling. The gradients reside at the plasma edge in the range of the recycling source. With core fuelling (NBI), profiles peak as a consequence of the changed source distribution. With strong central ECRH, the density profile becomes hollow. With off-axis ECRH heating and flat central temperature gradients, the core density profile peakens (see Fig. 5) /22/. EIRENE calculations show that core fuelling can be ignored.

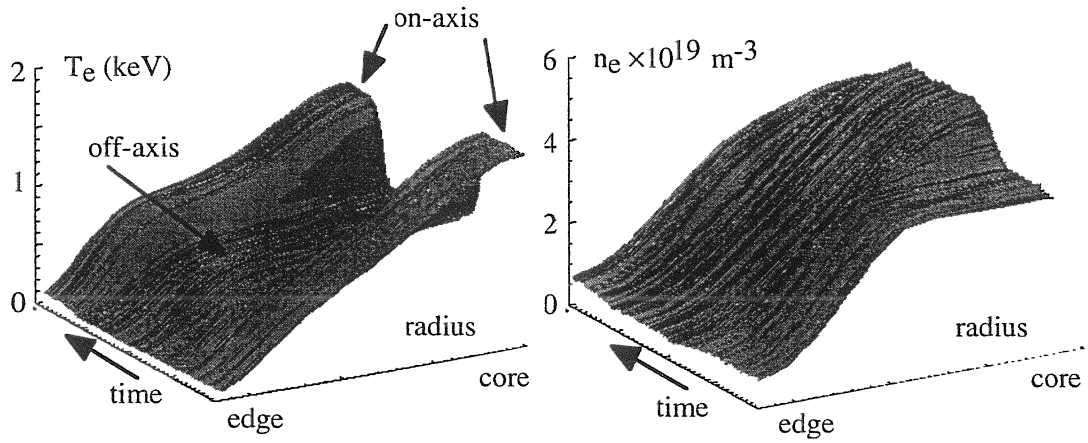

Fig. 5. On the left side, the electron temperature profile (ECE) and on the right side the density profile (10 channel interferometer) is plotted for an experimental scenario, where the ECRH power deposition was varied in steps from the core to the periphery and back again.

These observations elucidate the effects which govern the particle transport. Besides diffusion, thermal diffusion plays a role. The experimental analysis shows, that the thermally driven ($\Gamma \approx T_e'$) neoclassical flux component, which is outward directed in stellarators can explain the hollow profiles of central heating. The consequence of this term in particle transport is detrimental because it leads to unfavourable and even unstable density profiles in large devices /23/. As a consequence, the existence of a concective inward flow (by the E_r/T-term or resulting from the background turbulence) superimposed onto the other two mechanism has also an important practical aspect. This term in the transport equation was therefore carefully studied in perturbation experiments analysing gas oscillation experiments /24/ and by studying the peaking of the core density profile when ECRH was switched from central to off-axis heating (see Fig. 5). The modelling of the temporal phases yields an inward velocity of about 1 m/s for the inner half which rises to the plasma edge to about 4 m/s. Though the particle fluxes in the core are generally close to the neoclassical level and 3D-effects of neoclassical transport causes outward directed thermal diffusion, there remains a favourable inward flow term. Nevertheless, particle transport studies and core fuelling techniques will require specific attention in large helical devices.

Impurity transport has been studied by means of different impurity injection techniques like laser blow-off and gas oscillation. For ECRH plasmas and central electron densities ranging from $(0.4 - 5) \times 10^{19}$ m^{-3} the radiation decay time (Al XII, Al XIII) of laser blow-off injected aluminium follows a dependence $\tau_{Al} \sim P_{ECF}^{-0.8} n_{eo}^{1.2}$ (ECRH power P_{ECF}, central electron density n_{eo}) /25/, indicating increased impurity confinement at higher electron density. This is supported by corresponding measurements of local transport coefficients (using soft-X camera profile evolutions /26/) which reveal a decreased of the diffusion coefficient, D, with increasing density /27/.

In low and medium electron density plasmas ($< 4 \times 10^{19}$ m^{-3}) stationary conditions concerning intrinsic impurity radiation were usually achieved. Towards higher electron densities ($> 5 \times 10^{19}$ m^{-3}) impurity radiation and Z_{eff} often will not reach stationarity within the discharge duration but show a steady increase with the tendency to saturate at times longer than the performed pulse length ($\approx$1s). Assuming constant impurity sources this behaviour is a consequence

of rather low diffusion coefficients as derived from measured data in particular in the outer region of the plasma. Hence, these discharges are also expected to reach a final intrinsic impurity concentration level which is determined by the strength of its source.

A slow increase of Z_{eff} during the pulse duration was also observed in high confinement NBI discharges /28/ (see Fig. 4) at high central electron density (1.2×10^{20} m^{-3}) and a slightly peaked electron density profile. A rather low diffusion coefficient $D(r)=0.07 m^2/s$ and an inward convection velocity of 5r/a m/s were derived from aluminium injection experiments. The consequences of the low diffusion coefficients on high density operation (e.g. for successful exhaust) have to be assessed further.

Edge transport and turbulence:

Detailed edge transport studies were carried out in W7-AS under limiter conditions (to simplify the analysis) /29/. The dominant scaling parameter is the density both for D and χ_e: $\approx 1/n_e$. With increasing heating power the diffusivities increase and thus reflect the scaling of the global confinement times. It is interesting that the edge transport scales similarly to the global confinement and can, on the other hand, be quantitatively investigated by probes.

In the scrape-off layer (SOL) and around the last closed magnetic surface (LCMS), arrays of Langmuir probes are used to investigate the spatio-temporal structure of ion saturation current (I_{sat}) and floating potential (Φ_{fl}) fluctuations and to determine the radial flux. Density fluctuations can be observed from the SOL to several cm inside the LCMS with a fast Li beam diagnostic by applying a deconvolution technique to the radial correlation function of the Li light profiles /30/. For the SOL, the fluctuation characteristics from these measurements are in agreement with those found by Langmuir probes measurements and rule out major perturbations by the probe.

These fluctuations exhibit broad spectra decaying rapidly towards high frequencies. Most of the spectral power is located below a few 10 kHz. A characterisation in terms of correlation functions shows typical lifetimes of 10–30 µs, poloidal correlation lengths of few cm and radial correlation lengths about half the poloidal correlation lengths (i. e. of the order of the radial gradient scale lengths) /31/. Parallel to the magnetic field, a correlation of 90% for 6 m distance between probe tips has been found in the SOL both for I_{sat} and Φ_{fl} /32/. The fluctuations thus have the character of filaments extending between the intersections of a magnetic flux bundle with the limiters. These structures are moving poloidally with several 100 m/s (at 2.5 T) up to 2000–4000 m/s (at 1.25 T) in the ion diamagnetic drift direction in the SOL and in the opposite direction inside the LCMS. Just inside the LCMS, the correlation parallel to the magnetic field is found to be 40–50% for a probe separation of 32 m /33/. Whether this reduction in the parallel correlation is due to the different magnetic field topology on closed magnetic surfaces, due to the higher distance between the probes or due to the fact that the stabilising impact of the high field side enters (in contrast to the SOL measurements), remains to be investigated. I_{sat} and Φ_{fl}. fluctuations are well correlated, with a phase angle of $\pi/4$-$\pi/2$ resulting in an outward directed net particle transport dominated by few short and poloidally located „events" /34/. The spatial and temporal scales of the fluctuations in the SOL, their amplitude and the induced radial transport are well reproduced by a two-dimensional drift-interchange code which allows for a self-consistent development of the radial profiles and retains the sheath boundary conditions at the limiters /35/.

The technique of fast swept Langmuir probes was used to measure simultaneously plasma density, electron temperature and plasma potential fluctuations /36/. For those discharge conditions used, T_e fluctuations have a somewhat smaller relative fluctuation amplitude than density fluctuations ($\tilde{T}_e/T_e \approx 0.5\, \tilde{n}_e/n_e$) and the fluctuations of these two quantities are almost in phase. The conductive part of the radial electron energy transport due to fluctuations of the radial E×B velocity is found to be of the same order of magnitude as the convective part: $n\langle \tilde{T}_e\, \tilde{E}_\theta \rangle/B \approx T_e \langle \tilde{n}_e\, \tilde{E}_\theta \rangle/B$. It is therefore justified to compare the plasma parameter dependencies of the fluctuation-induced radial particle transport calculated from I_{sat} and Φ_{fl}. fluctuations directly with parameter dependencies of the global energy confinement time. In agreement with expectations, the particle transport is reduced and the energy confinement time increases when increasing the plasma density, increasing the field or reducing the heating power in ECRH discharges /37/.

The confinement variations with n_e, B and P are accompanied by changes in the lifetime and poloidal size of the fluctuation structures. The increases in the radial flux when reducing the density or increasing the heating power are caused by increases of the fluctuation amplitude, predominantly of the potential fluctuations. Details will be published elsewhere /38/.

High density operation:

Stellarators can operate at high density. The limitation is by a breakdown of the energy balance at the plasma edge due to excessive radiation and recycling losses /39/. The plasma decay is slow and can be influenced at any phase by reduction of the gas-flow rate or by increasing of the heating power. Of relevance for larger devices is the scaling of the maximal operation density (the value which can be stably sustained). Both edge and line averaged density scale with power and field. The edge density scaling is: $n_e \approx B^{0.8}\ P^{0.5}\ L^{-0.62}$. The L-scaling is selected to yield a dimensional correct relation. With the heating power foreseen for W7-X, the operational density would surpass the one of W7-AS.

Wave heating:

The accessible plasma density for ECRH with electromagnetic waves in ordinary and extraordinary polarisation (O- and X-mode) is limited by the plasma cut-off. For the electrostatic electron Bernstein wave (EBW), the third EC-mode which is able to propagate in a hot plasma, no such limit exists. However, since EBWs cannot be excited from the outside, they have to be generated via mode conversion from the electromagnetic waves. One possible way for this is the so called OXB-process /40/. In a first step (OX-process) a slow ($v_{ph}<c$) X-wave is generated at the O-mode cut-off density from a fast ($v_{ph}>c$) O-wave launched from the outside with an optimal angle oblique to the magnetic field vector. The X-wave then propagates towards the upper hybrid resonance (UHR) layer, where it is converted into an EBW (XB-process). Both processes take place at the density gradient region and are very sensitive to the plasma conditions there (level of turbulence). The influence of the plasma parameters on the conversion efficiencies was investigated at W7-AS for 70 GHz ECRH-frequency. For both processes optimal target plasma conditions could be found, so that the EBWs were generated with an efficiency of more than 80%. After the OXB-process the EBWs propagate towards the dense plasma centre, where they are absorbed near the cyclotron resonance layer. The radial absorption profile was estimated from the soft X-ray emission by switching the power. The radial shift of the absorption zone was investigated by changing the position of the ECR-layer in a magnetic field scan. Due to the very strong damping of the EBWs and due to a non vanishing parallel component of the EBW vector (oblique launch), a large Doppler shift of the EC-absorption towards the lower field is seen. For our experimental plasma parameters (T_e=500 eV, $n_e=1.5 \times 10^{20}\ m^{-3}$) central EBW-heating could be achieved for a central magnetic field of 2.13 T. The target plasma was sustained by 360 kW NBI. Additional OXB-heating with a power of 330 kW increases the plasma energy as well the central plasma temperature by 30% (ΔW=2.5 kJ, ΔT=110 eV) compared with a discharge with NBI only.

Also the inverse process, the EB-wave emission through the O-X-B angular window was detected and EB-wave emission spectra were measured. Beside the local thermal cyclotron emission of EB-waves, which in principle could then be used for temperature measurement, nonlocal broad-band EB-radiation was found /41/.

Therefore the foundation for a new operational regime for EC-heating and an EC-diagnostic of overdense plasmas was layed and the hot plasma wave theory has again found verification.

Operation of ICRH from the high-field-side with a narrow $k_{\parallel}$ spectrum successful ICRF heating became possible /42/. In resonant and non-resonant heating scenarios, the ion and electron temperature of ECRH and NBI target plasmas were increased. Simultaneously the plasma density could be kept constant and there was no rise in impurity concentration. The investigated scenarios were: D(H), ^{4}He(H) minority heating (minority species in brackets), D/H mode conversion heating, second harmonic H heating. Since recycling strongly determines the plasma composition, proper wall conditioning was imperative to obtain sufficiently low hydrogen concentration for minority heating. The efficiency of these scenarios was determined by

comparing the increase in diamagnetic energy with expectations based on power scaling. Thus the efficiency was found to be comparable to that obtained in tokamaks. In particular, D(H) minority heating is similarly more efficient than second harmonic hydrogen heating. Using the same heating scenarios it was also possible to sustain target plasmas solely with ICRF. Several energy confinement times into the ICRF phase, the plasma parameters reached steady-state values of density, temperatures and impurity radiation. The duration of these discharges was determined only by arcs in the RF system or to avoid excessive ohmic heating of the uncooled antenna. The maximum plasma duration was one second.

The island divertor concept:

W7-X will be equipped with an island divertor /43/. W7-AS already allows basic elements of this concept to be evaluated. At $\iota > 0.4$, the edge is bounded by a chain of intrinsic 5/m magnetic islands (with m = 8, 9, 10 in the W7-AS case). The device is presently operated with poloidal inboard limiters which, however, will be replaced in 1999 by ten symmetrically arranged island divertor modules (designed for 5/9 boundary islands) with strong geometrical similarity to the W7-X divertor concept /44/. The divertor concept was prepared by experiments on the plasma flow diversion by islands /45/ and by predictive code simulations of island divertor scenarios. A 3D edge transport code EMC3 (Edge Monte Carlo 3D) has been developed /46/, coupled to the EIRENE neutral transport code /47/, and first applied to pure hydrogen plasmas (inclusion of impurity transport is under way) in the 5/9 island divertor configuration. In parallel, the (geometrically less adequate) B2-EIRENE code /48/ was applied to the same, but helically averaged configuration /49/ for „proof of principle" predictions including more complete physics (impurity transport, strongly radiative and detached scenarios), and for benchmarking the EMC3-EIRENE code. The EMC3-EIRENE code is a candidate also for future W7-X applications.

The results of these preliminary studies show gross agreement with tokamak x-point divertor scenarios, but in detail reflect characteristic geometrical differences. In contrast to tokamak divertors, island divertors in stellarators necessarily have a 3D magnetic structure, toroidally discontinuous targets (localised recycling zones), smaller radial separations between target and main plasma, and, in general, longer field line connection lengths from target to target (small field line pitch inside the islands). These features affect the penetration of recycling neutrals and impurities into the main plasma, as well as the ratio of the cross-field to parallel transport (plasma flow diversion) within the SOL. Both are crucial for divertor performance. Nevertheless, the experiments mentioned give strong indications of a significant radial diversion of the plasma flow by the islands even at these conditions /46/. Slight asymmetries of the plasma flow measured inside the islands at low density, could be well reproduced by the EMC3-EIRENE code by superimposing an E×B plasma drift caused by T_e profiles decreasing towards the 0-point /50/. With increasing density and for typical heating powers and cross field transport coefficients /51/, the code simulations predict divertor regimes passing through the same sequence as in tokamak divertors: from a linear SOL regime over divertor high recycling with strong particle flux enhancement (both, EMC3-EIRENE and B2-EIRENE) to stable (energy) detachment with strong divertor radiation and very low divertor leakage for neutrals (B2-EIRENE, multifluid, with carbon sputtered from the targets). Figure 6 shows the ionisation source $n_e n_0 S_{ion}$ for various densities. At high density (right side), the ionisation front has moved away from the target plate to the separatrix. The stability limit coincides with a breakdown of the particle flux to the targets (complete detachment). In contrast to typical tokamak scenarios, the stronger contributions from cross-field energy, particle and momentum transport lead to significantly flattened downstream deposition profiles over the whole density range and to „layer"-type detachment. Diffusive and viscous radial coupling of particles flowing in opposite direction along the closely neighboured island fans is found to cause momentum losses in addition to charge exchange losses thus easing the transition to detachment. Varying the field line pitch by factors of ±2 (by special control coils in W7-AS) does not substantially change this picture.

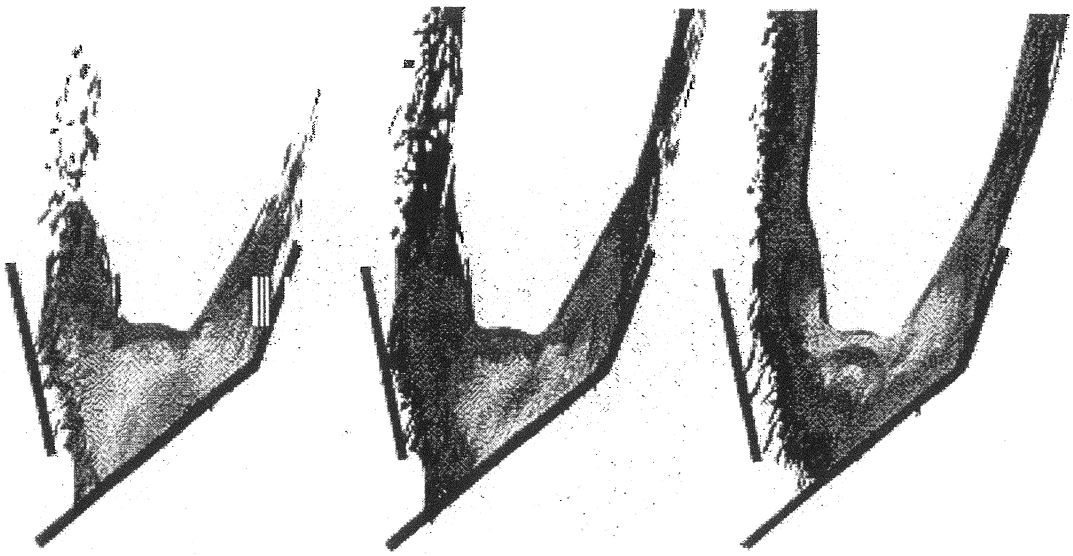

Fig. 6. Shown is a half-cross section of the W7-AS plasma in the elliptical plane; the planned divertor structures (target and baffles) as sketched. Plotted is the ionisation source for three different density values. The high density case is plotted at the right side.

References

/1/ NÜHRENBERG, J., et al., Trans. Fusion Technology, 27 (1995) 71
WOBIG, H., Plasma Physics and Controlled Fusion 33 (1993) 687

/2/ SAPPER, J. et al., Fusion Technol. 17 (1990) 62

/3/ RENNER, H. et al., Controlled Fusion and Plasma Physics, Proc. 19th European Conf. (Innsbruck, 1992) Vol 16C pt I, p 501.

/4/ GRIEGER, G., et al., Phys. Fluids B 4 (1992) 2081.

/5/ KICK, M., et al., in Plasma Physics and Controlled Nuclear Fusion Research 1996 (Proc. 16th Int. Conf. Montreal, 1996) Vol.2, IAEA, Vienna (1997) 27

/6/ ERCKMANN, V., this conference

/7/ WAGNER, F., et al., Proc. 25th Eur. Conf. on Controlled Fusion and Plasma Physics Prague, 1998, to be published

/8/ WELLER, A., this conference

/9/ NÜHRENBERG, C., submitted to Phys. Plasmas

/10/ SPONG, D.A., et al., Nucl. Fusion 35 (1995) 1687

/11/ BRAKEL, R., et al., Plasma Phys. Contr. Fusion, 39B, 273 (1997)

/12/ BRAKEL, R., et al., J. Plasma and Fusion Res. SERIES, 1, 80 (1998)

/13/ BRAKEL, R., Proc. 25th Eur. Conf. on Controlled Fusion and Plasma Physics Prague, 1998, to be published

/14/ KICK, M., 25th Eur. Conf. on Controlled Fusion and Plasma Physics Prague, 1998, to be published in Plasma Phys. Contr. Fusion.

/15/ MAASSBERG, H., et al., submitted for publication in Plasma Phys. Contr. Fusion

/16/ MAASSBERG, H., et al., submitted for publication in Plasma Phys. Contr. Fusion

/17/ STROTH, U., et al., Nucl. Fusion 36(8) (1996)1063

/18/ DOSE, V., et al., accepted for Phys. Rev. Letters

/19/ WAGNER, F., TOKI

/20/ BIGLARI, H., et al., Phys. Fluids B2, 1, 1990

/21/ WAGNER, F., et al., Plasma Phys. Contr. Fusion 35, 1321, 1993

/22/ STROTH, U., et al., submitted to Phys. Rev. Letter.

/23/ SIMMET, E.E., et al., Proc. of the 24th Europ. Conf. on Controlled Fusion and Plasma Physics, Berchtesgaden, 1997, Vol. 4, p. 1673.

/24/ KOPONEN, J.P.T., et al., to be published in Nucl. Fus.

/25/ BURHENN, R., et al., Proc. 1995, 22nd EPS Conf. on Contr. Fusion. and Plasma Physics (Bournemouth) 19C Part III, 145 (1995)
/26/ BURHENN, R., et.al., Rev. Sci. Instrum., Vol.70, No. 1, (1999), (to be published)
/27/ BURHENN, R., et al., Proc. 1997 24nd EPS Conf. on Contr. Fusion. and Plasma Physics (Berchtesgaden) 21A Part IV, 1609 (1997)
/28/ STROTH, U., et al., Plasma Phys. Control. Fusion 40, 1551 (1998)
/29/ GRIGULL, P.,
/30/ ZOLETNIK, S., et al., Plasma Phys. Contr. Fusion 40 (1998) 1399-1416
/31/ BALBÍN, R., et al., 19th EPS Conf. Contr. Fus. Plasma Phys. (Innsbruck), 16C, part II (1992), 783-786
/32/ ENDLER, M., et al., Physica Scripta 51 (1995), 610-616
/33/ BLEUEL, J., et al., 24th EPS Conf. Contr. Fus. Plasma Phys. (Berchtesgaden), vol. 21A, part IV (1997), 1613-1616
/34/ BLEUEL, J., et al., 23rd EPS Conf. Contr. Fus. Plasma Phys. (Kiev), vol. 20C, part II (1996), 727-730
/35/ BLEUEL, J., et al., 25th EPS Conf. Contr. Fus. Plasma Phys. (Prague, 1998)
/36/ GIANNONE, L., et al., Phys. Plasmas 1 (1994), 3614-3621
/37/ PFEIFFER, U., et al., Contrib. Plasma Phys. 38 (1998), 134-144
/38/ BLEUEL, J., Elektrostatische Turbulenz am Plasmarand des Stellarators W7-AS, PhD thesis, Technische Universität München (1998), Max-Planck-Institut für Plasmaphysik Report IPP III/235
/39/ GRIGULL, P., et al., Proc. 11th Int. Stellarator Conf. & 8th Int. TOKI Conf. on Plasma Physics and Controlled Nulear Fusion, Toki, Japan, 1997, J. Plasma Fusion Res. Series, Vol. 1 (1998) 291
/40/ PREINHAELTER, J., and KOPECKY , V., J. Plasma Phys. 10 (1973) 1
LAQUA, H.P., et al., Phys. Ref. Let. Vol. 78, No.18, pp.3467-3470, 1997
/41/ LAQUA, H.P., et al., Phys. Ref. Let. Vol. 81, No.10, pp.2060-2063, 1998
/42/ HARTMANN, D., this conference
/43/ W7-X Divertor ....
/44/ SARDEI, F., et al., J. Nucl. Mater. 241-243 (1997) 135
/45/ GRIGULL, P., et al., J. Nucl. Mater. 241-243 (1997) 935
/46/ FENG, Y., et al., Proc. 13th Intern. Conf. on Plasma-Surface Interactions, San Diego, USA, 1998, to be published in J. Nucl. Fusion
/47/ REITER, D., The EIRENE Code, Report No. 2599, Institut für Plasmaphysik, Association EURATOM-KFA, Jülich, 1992
/48/ BRAAMS, B.J., A Multi Fluid Code for Simulation of the Edge Plasma in Tokamaks, Report No. (NET) EUR-FU/XII-80/87/68, Comm. of the EC, Brussels, 1987
SCHNEIDER, R., et al., J. Nucl. Mater. 196-198 (1992) 810
/49/ HERRE, G. et al., Proc. 13th Intern. Conf. on Plasma-Surface Interactions, San Diego, USA, 1998, to be published in J. Nucl. Fusion
/50/ FENG, Y., et al., 24th EPS Conf. on Controlled Fusion and Plasma Physics, Berchtesgaden, Germany, 1997, Erophys. Conf. Abstracts 21A, IV, p. 1569
/51/ GRIGULL, P., et al., Proc. 10th Intern. Conf. on Stellarators, IAEA Technical Meeting, Madrid, Spain, 1995, Report EUR-CIEMAT 30 (1995), p. 73

INVESTIGATION OF EQUILIBRIUM, GLOBAL MODES AND MICROINSTABILITIES IN THE STELLARATOR W7-AS

A. WELLER, M. ANTON, R. BRAKEL, J. GEIGER, C. GÖRNER, H.J. HARTFUSS, M. HIRSCH, R. JAENICKE, C. NÜHRENBERG, S.D. PINCHES, D.A. SPONG[1], S. ZOLETNIK[2], W7-AS TEAM, NBI- and ECRH GROUP[3]

Max-Planck-Institut für Plasmaphysik
IPP-EURATOM-Association
D-85748 Garching, Germany

Abstract

Equilibrium and stability properties in the WENDELSTEIN 7-AS stellarator are investigated experimentally and compared with theoretical predictions for particular cases. The topology of equilibrium magnetic surfaces and of global MHD modes is inferred from X-ray tomography. The predicted effects of externally driven currents and internal currents on the equilibrium surfaces could be confirmed experimentally. In particular the reduced Shafranov shift due to reduced Pfirsch-Schlüter currents in W7-AS could be verified. Up to the maximum accessible β ($\langle\beta\rangle \approx 2$ %) plasmas can be confined without significant deterioration by pressure driven MHD-activity. However, global modes in the stable MHD spectrum such as global and toroidal Alfvén eigenmodes (GAE, TAE) can be destabilised by energetic ions from neutral beam heating. These instabilities appear as very coherent low frequency modes (≤ 40 kHz) in the lower β regime without significant impact on the global confinement. At medium β very strong particle driven MHD modes with frequencies up to the range of 500 kHz can be observed. These modes can show nonlinear behaviour including periodic bursting and frequency chirping in combination with significant plasma energy losses. With increasing β Alfvén modes are widely stable, because under these conditions the damping relative to the particle drive is increased. Besides the global mode activity small scale turbulent structures have been investigated in the plasma core and at the edge. The measured data of electron temperature, density and magnetic fluctuations do not yet allow to assess turbulence driven transport fluxes. However, correlations with the global confinement have been found, and the measured amplitudes are in the range expected to be relevant for anomalous transport. The observed dependence of the confinement on the edge rotational transform and magnetic shear can be explained in terms of enhanced transport at rational surfaces, however, the underlying mechanism is still unclear.

1. INTRODUCTION

In WENDELSTEIN 7-AS (major radius $R = 2$ m, effective plasma radius $a \leq 0.2$ m) the magnetic configuration has been optimised to some extent with respect to equilibrium, MHD stability and neoclassical transport properties. A key element is the reduction of the internal parallel currents (Pfirsch-Schlüter and bootstrap currents) achieved by a 3-dimensional field geometry, which results in good equilibrium properties (eg. small Shafranov shift) and improved MHD stability simultaneously [1]. The existence of high quality flux surfaces is the basis for good confinement in W7-AS. In the usual net-current-free operation the configuration is characterised by very low magnetic shear, and therefore, small field errors can lead to large stationary islands particularly around low order rational surfaces. Since also MHD instabilities as well as magnetic turbulence are expected to lead to deteriorations of a similar kind, the rotational transform $\iota = 1/q$ is adjusted by means of the toroidal field system to avoid major resonances. Optimum confinement is established when ι stays within nearly resonance-free zones just in the vicinity of 1/3 and 1/2. Detailed measurements of vacuum flux surfaces using a probing electron beam [1,2] have shown both, a good agreement with field line tracing calculations as well as the existence of large islands, if low order resonances are contained in the ι-profile. In the presence of plasma the surfaces are modified by the internal currents. The edge rotational transform can be feedback

[1] Oak Ridge National Laboratory, Oak Ridge, Tennessee, USA.
[2] KFKI Research Institute for Particle and Nuclear Physics, 49 H-1525 Budapest, Hungary
[3] Institut für Plasmaforschung, Universität Stuttgart, Germany

controlled by driving a small Ohmic heating (OH) current, which compensates the bootstrap current (net current-free operation). Current driven MHD such as tearing modes only occurs in the presence of significant net currents driven inductively or by electron cyclotron current drive (ECCD) [3]. In the absence of significant magnetic shear the global MHD stability against pressure driven modes (interchange and ballooning modes) relies on a magnetic well. The predicted ideal MHD stability limits for standard field configurations in W7-AS are in the range $\langle\beta\rangle \approx 2$ %. A main purpose of this paper is the attempt to benchmark the predicted MHD properties with experimental data. Another related aim is to investigate the interrelation of global MHD activity and small scale turbulent fluctuations with anomalous transport, confinement transitions and operational limits. A particular emphasis is on Alfvén Eigenmodes, which are in the stable MHD spectrum, but which can be destabilised by resonant Landau interactions with energetic ions from neutral beam injection (NBI). These modes cannot be easily suppressed by field optimisation, and therefore, their role needs to be further investigated in devices like W7-X.

2. HIGH-BETA EQUILIBRIUM AND MHD MODES

Maximum β values of $\langle\beta\rangle \approx 1.9$ % and $\beta(0) \approx 4.5$ % have been reached in W7-AS at magnetic fields of B = 0.9 - 1.3 T with NBI heating powers up to 3 MW [4]. The almost tangential injection system operates at 50 - 55 kV and allows for balanced injection, in order to avoid too large beam driven currents. Under the conditions of high β the electron density reaches $2-3\times10^{20}$ m^{-3} leading to temperatures of only 200 - 300 eV.

The reconstruction of equilibrium surfaces by magnetic probe measurements in W7-AS is very difficult due to the small field changes. Therefore, a multi-camera soft X-ray detector system was installed for tomographic analyses of equilibrium surfaces and mode structures [5,6]. This device consists of 10 compact cameras with a total number of 320 sight-lines surrounding the plasma inside the vacuum vessel. Various numerical methods for the reconstruction of the emissivity contours and for the separation of mode structures from the equilibrium have been applied.

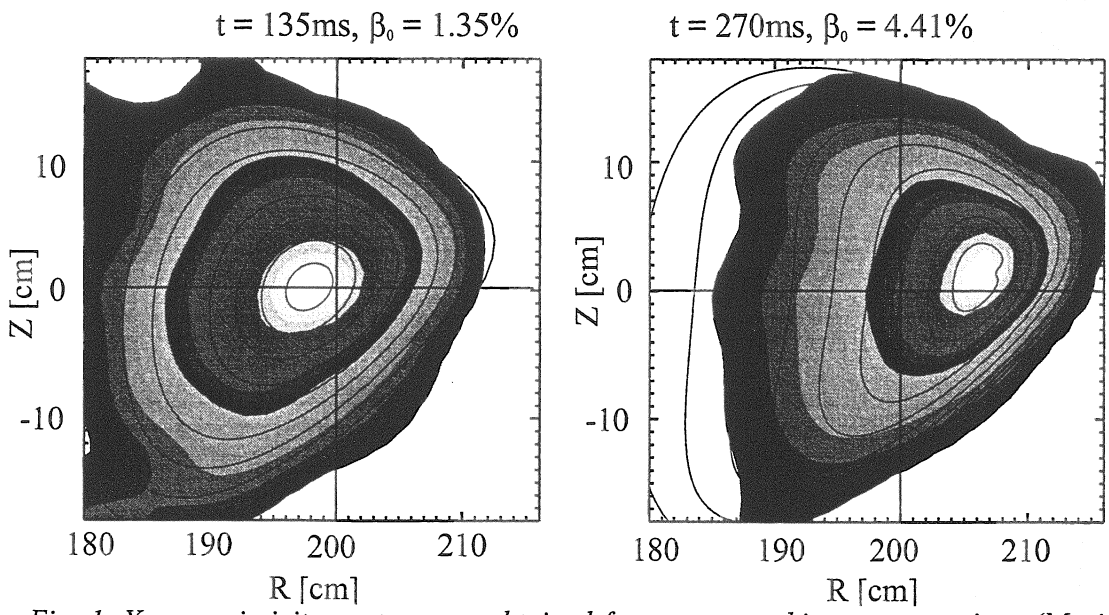

Fig. 1. X-ray emissivity contours as obtained from tomographic reconstructions (Maximum Entropy method) compared with equilibrium flux surfaces (NEMEC code, solid contour lines). The analysis is made for the low-β phase (left, $\beta(0) \approx 1.4$ %) and the high-β phase (right, $\beta(0) \approx 4.4$ %) of #41618. The β induced horizontal axis shift reaches 7 - 8 cm.

A particular aim was to compare the NEMEC free boundary equilibrium code calculations [7] with experimental data. The calculated equilibria are widely used for plasma analysis. Very good agreement is usually obtained between the equilibrium calculations and X-ray tomographic reconstructions, particularly in the gradient region of the X-ray emissivity profiles, where the reconstructions are most reliable. Two major effects predicted by the code calculations could be verified: - firstly, the displacement of the flux surfaces due to Pfirsch-Schlüter currents (Shafranov shift) in agreement with earlier measurements [2], - secondly the different modification of flux

surfaces by parallel and antiparallel inductive currents [7]. The effect of the Shafranov shift is illustrated in fig. 1 where X-ray tomograms at different β during a discharge are compared with NEMEC calculations. In accordance with the calculations the observed horizontal axis shift at high β ($\beta(0) \approx 4.5$ %) reaches values, which correspond to a significant fraction of the plasma radius (0.4 - 0.45 a). Along with the geometric changes of the flux surfaces the ι-profile is modified from $\iota \approx 0.35$ (almost constant in vacuum configuration) to a moderate shear profile at high β that varies between $0.404 \geq \iota \geq 0.27$ between center and edge. Therefore, at high β low order rational surfaces cannot be avoided anymore.

Actually under these conditions often coherent low frequency (≈ 4 kHz) mode activity is observed in the X-ray emission, which indicates a pressure driven global mode at the most important rational surface. In addition weak MHD activity is found around 15 and 35 kHz, which is probably driven by fast particles (see section 3.). For the same discharge, which was used for the equilibrium analysis shown in fig. 1, a stability analysis has been performed for the high-β case (#41618, B = 1.22 T, $\langle\beta\rangle = 1.7$ %, $\beta(0) = 3.6$ %, $n_e = 1.8 \times 10^{20}\ m^{-3}$, $T_e = 0.35$ keV, $P_{NBI} \approx 3$ MW). The local analysis comprised the evaluation of the local stability criteria (Mercier criterion, resistive interchange criterion), and the local ballooning analysis along a closed field line [8]. The Mercier criterion indicates stability across the whole plasma, whereas the resistive interchange criterion is violated for $s \geq 0.75$ (s normalised flux coordinate), which corresponds to an effective plasma radius of $r \approx 15.25$ cm. This is consistent with an earlier study of configurations with reduced magnetic well [9]. The evaluation of the local stability analysis is shown in fig. 2. The field line ballooning indicates also stability in the outer plasma region, for example at the rational surfaces $\iota = 3/10$ at $s = 0.688$ and $\iota = 2/7$ at $s = 0.818$.

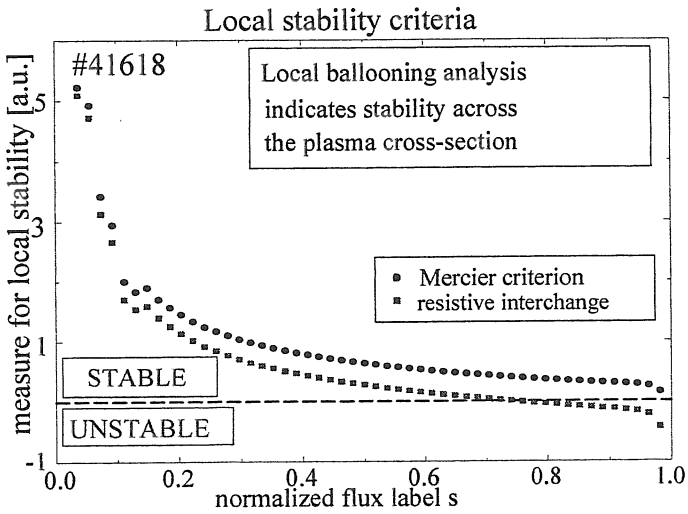

Fig. 2. The local stability analysis of the high-β shot 41618 yields a resistive-interchange unstable region for $s \geq 0.75$ ($r \geq 15.25$ cm). The plasma is ideally stable across the whole plasma.

The global stability properties have been studied with the CAS3D code [10,11]. The latest code version (CAS3D3) [12] also allows to analyse the stable part of the ideal MHD spectrum in full three-dimensional (3-d) geometry, including fluid compression and using a physical kinetic energy term, so that physical growth rates and frequencies can be calculated for comparison with measured frequencies. In the analysis 162 radial intervals and 40 perturbation Fourier harmonics have been used, which were selected according to the ι-profile and the mode family chosen (N = 0,1,2 in the 5-periodic W7-AS) [10]. In the stable MHD spectrum the computational spectra for the N = 1 and N = 2 mode families, which have been studied in more detail, show gap formation, which may occur in the sound spectrum as well as in the Alfvén spectrum. Several gap modes in the CAS3D3 calculations have been detected by comparisons with the analytical sound and Alfvén continua: in the low frequency part several global modes (N = 1) appear in a toroidicity and an ellipticity induced gap of the sound spectrum, respectively ((m,n) = (3,1) + (4,1) at ≈ 1.8 kHz, and (4,1) + (2,1) at ≈ 4.6 kHz), where m,n are the poloidal and toroidal mode numbers). In the higher frequency range the CAS3D3 calculations reveal gap formation in the Alfvén branches of the spectrum and the existence of global, stable modes. In particular, toroidal Alfvén eigenmodes (TAE) with main components (m,n) = (3,1) + (4,1) (N = 1

mode family) at 22 kHz and (m,n) = (6,2) + (7,2) (N = 2 mode family) at 38 kHz are predicted. Typically several global modes are found by CAS3D3, which are composed of similar poloidal mode numbers, but differ in the number of radial nodes and in the sign of the poloidal harmonics (odd and even modes). The global modes may be destabilised by resonant fast particles (see next section) and cause some of the experimentally observed activity. However, more computational and experimental studies are needed to explain this weak MHD-activity in the high-β regime.

3. ENERGETIC PARTICLE DRIVEN MODES

The most striking MHD instabilities in W7-AS have been identified as global Alfvén eigenmodes, which are in the stable MHD spectrum driven unstable by wave particle resonances with energetic ions of the neutral beam slowing down distribution [13]. These modes cannot be suppressed by avoiding rational surfaces since they occur in gaps of the continuous shear Alfvén spectrum given by $\omega_A = k_{\|} \cdot v_A$ with finite parallel wave vector $k_{\|} \equiv (m \cdot \iota - n)/R \neq 0$. Under the usual low shear conditions in W7-AS and close to a low order resonance $\iota = n/m$, where optimum confinement is found [14], the (m,n) continuum does not extend to zero frequency. Underneath the continuous spectrum a gap remains, in which global Alfvén eigenmodes (GAE) with low frequencies are predicted (typically 20 - 40 kHz in W7-AS) [13,15]. Experimentally they appear typically as coherent mode activity with one or a few lines dominating the frequency spectrum. This activity is usually not causing any significant transport. The spatial 2-d structure of GAE and TAE modes has been derived from X-ray tomography analysis.

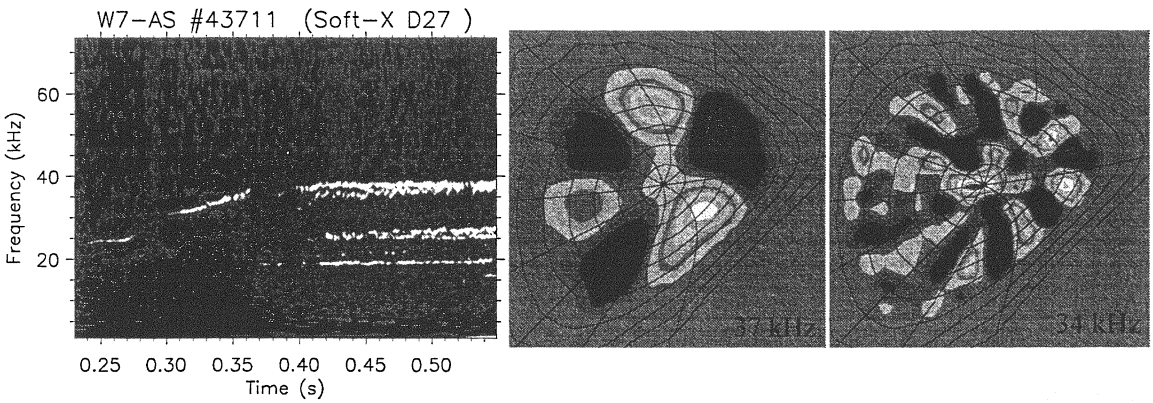

Fig. 3. GAE-activity in a HNBI discharge. In the frequency spectrogram of a soft X-ray signal several lines appear below 40 kHz (left). For the upper 2 lines the X-ray reconstructions show extended mode structures with m = 3 (middle) and with higher (m = 8,9, or 10?, right).

In fig. 3 an example is shown for a more complicated frequency spectrum (left) and for reconstructed mode structures (right) corresponding to the 2 uppermost spectral lines. Whereas in the case of the equilibrium reconstructions the maximum entropy method is used, a first order regularisation method is used for the mode analysis in combination with either Fourier filtering of the raw data or singular value decomposition (SVD) techniques in order to separate different mode structures [5]. The analysis of fig. 3 refers to a high-confinement NBI discharge (HNBI) in W7-AS [16] (#43711, B = 2.5 T, $n_e = 1 \times 10^{20}\ m^{-3}$, $T_e = 0.9$ keV, $P_{NBI} \approx 0.35$ MW). In this case a relatively high bootstrap current develops, which is compensated by an OH-current, resulting in the formation of $\iota = 1/3$ in the plasma, therefore, closing of the (3,1) gap towards the plasma center. In many cases modes with a similar poloidal structure are observed, which are at different frequencies, and also differ by a node in their radial eigenfunctions.
The influence of (moderate) magnetic shear on the Alfvén spectrum has been studied by driving OH-currents of different magnitude and polarity [17]. With increasing shear a transition from GAE to TAE modes has been found. A TAE mode has been identified in discharge #39042 by the poloidal structure, which varies from m = 6 in the outer region to m = 5 towards the inside as deduced from the X-ray tomographic analysis (fig. 4). The mode structure and frequency are in agreement with CAS3D3 code calculations. Additional (axisymmetric) calculations with a TAE/GAE gyrofluid model [15], which includes drive and damping terms to describe the particle effects, give similar results and predict instability for the n = 2 (m =5,6) TAE mode observed.

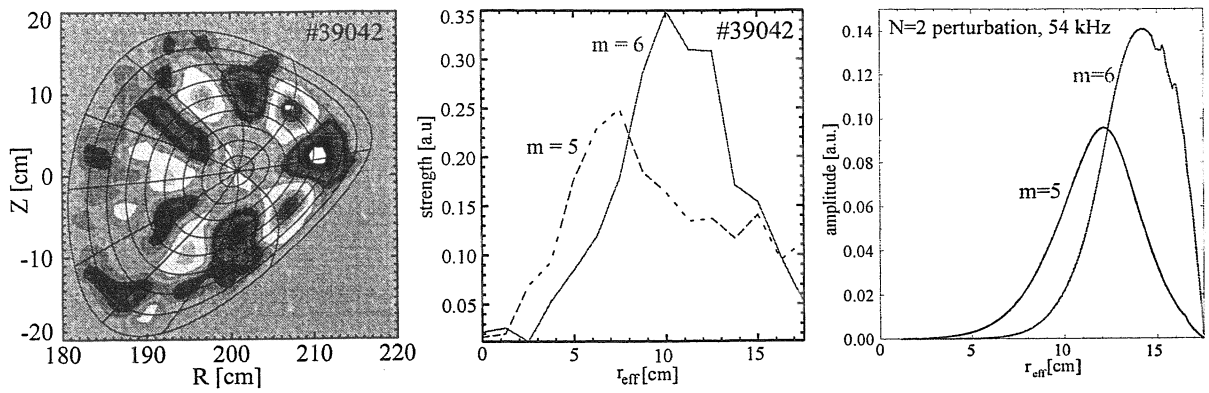

Fig. 4. X-ray tomography of a TAE mode with main poloidal components m = 6 outside and m = 5 inside (left). In the middle radial profiles of the two main poloidal harmonics from Fourier decomposition of the tomogram are shown, which are in qualitative agreement with the Fourier harmonics of the normal displacement as calculated with CAS3D3 (right).

For the case of this (weak) TAE activity the interaction of the mode with the fast particles has been studied with the guiding center particle following code HAGIS [18]. As input toroidal averages of the equilibrium and of the perturbations from CAS3D3 (fig. 4, right), as well as calculated radial and energy distributions of the particles were used. A saturation amplitude of $\tilde{B}/B \approx 2\times10^{-4}$ and a linear growth rate for the particle drive of $\gamma/\omega \approx 1.5\,\%$ has been calculated, which is consistent with typical gyrofluid calculations. The particle interaction with the TAE causes a 15 % shift of the MHD frequency and very small redistributions of the fast particle distributions around the resonances ($\approx 10^{-4}$ relative density perturbation), which, however, do not lead to any significant particle losses.

The low frequency coherent GAE modes occur preferentially in the low-β NBI regime (low shear, $n_e(0) \approx 10^{-20}\ m^{-3}$, low NBI power), where the Alfvén speed typically exceeds the fast ion velocity. Therefore, the modes with poloidal wave number m are excited via the m ± 1 sideband resonances at much lower resonant particle velocities (typically $v_{\|,m+1} \approx 0.1\cdot v_A$) if the ι-profile is close to the rational value n/m (small $k_\|$). This is sketched in fig. 5, where the resonant particle velocities for fundamental and sideband excitation are compared as a function of mode number m.

Under conditions, where a significant fraction of fast particles has velocities $\geq v_A$ and the fast particle beta is sufficiently high, the beam driven mode activity can change significantly. A transition to higher frequencies (up to ≈ 500 kHz) and to bursting behaviour and intermittent

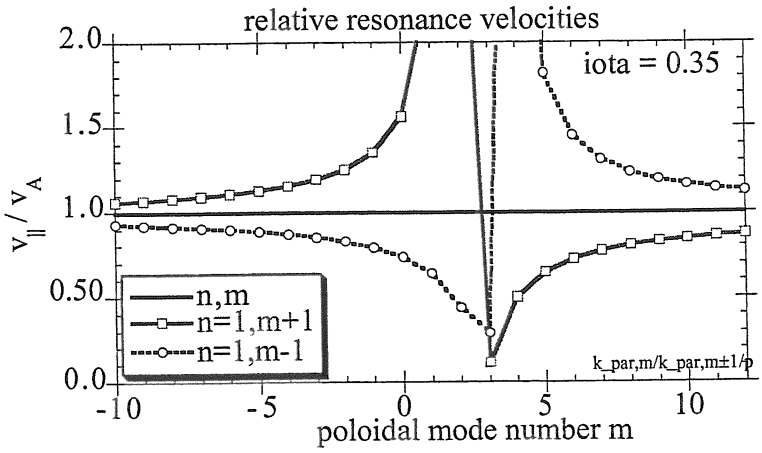

Fig. 5. Resonant parallel particle velocities normalised to the Alfvén speed for fundamental ($v_\| = v_A$) and m ± 1 sideband resonances. The rotational transform used (ι = 0.35) is close to n/m = 1/3. Under this condition the sideband resonance velocities for the (m,n) = (3,1) mode are well below v_A.

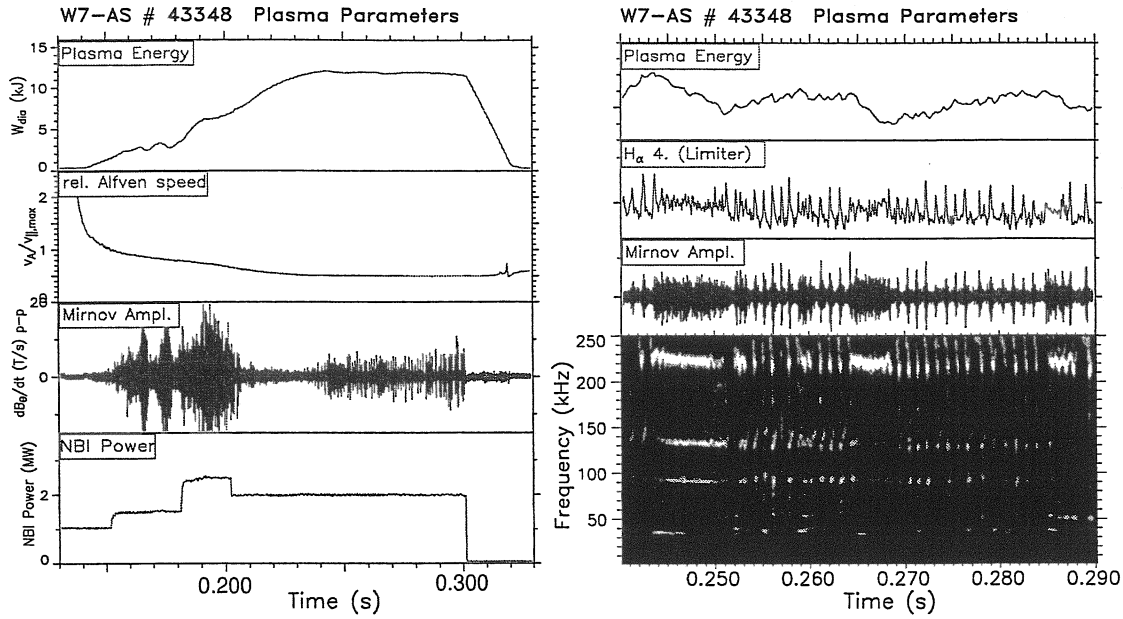

Fig. 6. Bursting MHD-activity in the higher frequency range at higher β. Left: Plasma energy (diamagnetic loop), averaged Alfvén speed normalised to maximum particle velocity, Mirnov signal and NBI power. Right: The mode activity is correlated with small relaxations of the plasma energy and H_α-emission. The Mirnov spectrogram shows several lines up to 250 kHz.

mode activity together with frequency chirping is often observed. This regime is characterised by relatively high β (low field) and intermediate NBI power, for which the plasma density can be kept well below the radiative density limit. This MHD activity can cause significant deterioration of the energy confinement as deduced from correlations with relaxations of the plasma energy and temperature. Inreased particle losses are deduced from the signature of the H_α-emission.

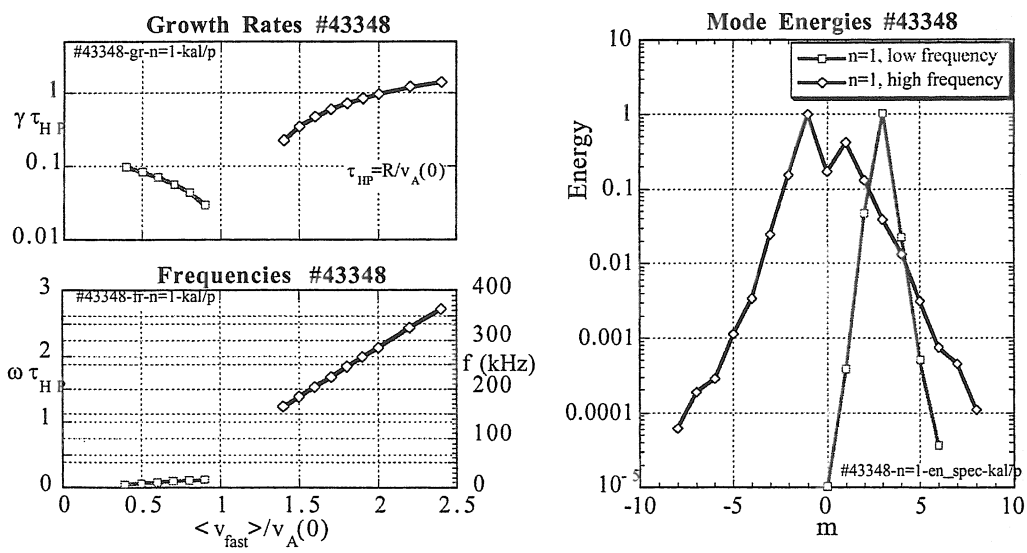

Fig. 7. Dependence of growth rates (upper left), frequencies (lower left) on the mean fast particle velocity normalised to the central Alfvén velocity as calculated with the parameters of #43348 (see fig. 6) by the gyrofluid model for the case n = 1. At higher velocities modes with significantly higher growth rates and frequencies are destabilised with much broader spectra of poloidal harmonics including opposite helicity modes (m < 0).

The bursting and frequency chirping behaviour suggests that at least a part of the lost particles could be fast ions resonating with the modes. In fig. 6 an example is shown for these effects (#43348, B = 1.2 T, $\langle\beta\rangle \approx 1.4$ %, $\beta(0) = 2.4$ %, $\beta_{fast}(0) \approx 0.5$ %, $n_e \approx 1.2\times10^{20}$ m^{-3}, $P_{NBI} \approx 2$ MW). The gyrofluid calculations for this case predict the transition to unstable Alfvén

modes in the frequency range of the observed activity as the mean fast particle velocity normalised to the central Alfvén speed exceeds unity (fig. 7). However, in the experiment $\langle v_{beam}\rangle/v_A(0)$ is marginally below 1. The higher threshold of the fast particle velocity in the calculations might be due to the approximation of the fast ion velocity distribution by a maxwellian. Compared with the low frequency GAE mode the calculated spectrum of poloidal mode harmonics in the case of the high frequency mode is broader and shifted to m numbers which involve higher $k_{\|}$-values.

The onset of the high frequency Alfvén modes is often observed during a density ramp, when v_A falls below the threshold for the fundamental resonance [19]. At higher densities approaching the maximum plasma β the beam driven modes usually become stabilised again, probably due to higher continuum damping (increased shear) and reduced values of $\beta_{fast}/\beta_{thermal}$. At the time of mode stabilisation a transition to better confinement is usually observed. A detailed understanding of the high frequency MHD activity is not possible so far due to lack of experimental data concerning the poloidal and radial structure. There might be also an explanation in terms of kinetic ballooning modes (KBM) or the energetic-particle continuum mode (EPM) [20,21]. The threshold condition to drive the EPM unstable given in ref. 19 is typically exceeded, but the expected frequency should be restricted to the range $\leq$ 80 kHz.

4. TURBULENCE AND FLUCTUATIONS

Under optimum confinement conditions the observed radial energy transport is reduced to neoclassical levels in a large interior region of the plasma [16,22]. In the majority of plasma conditions, however, anomalous transport plays an important role, in particular towards the plasma edge. Although MHD modes can cause enhanced transport, in most cases they cannot account for the anomalous transport, which is considered to be driven by microinstabilities. Small scale fluctuations are investigated by different diagnostics including an electron cyclotron emission (ECE) correlation radiometer, a reflectometer, μ-wave scattering, beam emission spectroscopy (BES) using a Lithium beam and magnetic probes. Due to the lack of measurements of electric field fluctuations inside the plasma no quantitative assessment of turbulent transport fluxes can be made at present. Here we try to describe the essential characteristics of the observed fluctuation and their interrelation with anomalous transport.

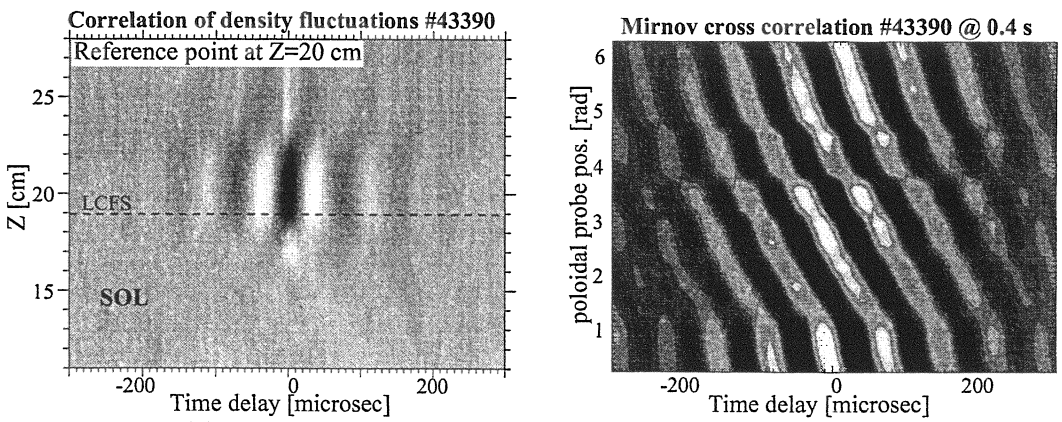

Fig. 8. Burst-like fluctuations inside the LCFS. Left: space-time correlation function of density fluctuations from BES. Right: poloidal correlation function of Mirnov signals.

The dependency of anomalous transport on details of the ι-profile (content of rational values and shear) [14] implies some features of the underlying turbulence: the instabilities are located around rational surfaces, and their effect is reduced by shear. These observations could be consistent with drift Alfvén turbulence [23], which also could provide a drive for Alfvén eigenmodes appearing occasionally during electron cyclotron heating (ECRH) or Ohmic heating [24] in the absence of fast ions. In the confinement region the turbulent electron temperature and density fluctuations in the 40 - 100 kHz range are in phase and well correlated. The temperature fluctuations [25] vanish under $\nabla T_e = 0$ conditions, where density fluctuations are still present. This behaviour could be explained by a convective mixing process which scales with $\tilde{T}_e/\nabla T_e$. The leading parameter dependency of the temperature fluctuations is an inverse scaling with the temperature.

A particular feature of the fluctuations at the edge is the burst-like oscillating instability extending over a few centimeters inside the last closed flux surface (LCFS) [26] well correlated in both density and magnetic signals. Fig. 8 shows the space-time correlation function of the density fluctuations as deduced from the Li-beam BES measurements and the cross correlation function for the poloidal array of 16 Mirnov coils. The Mirnov data imply rotating short-lived structures (50 - 100 μs) with $k_{\|}$-values of ≈ 0 and relatively long poloidal wavelengths in the range 30 - 50 cm. These burst-like fluctuations are considered to be related to transport because of their location, the scaling with density, the sensitive dependence on the ι-profile and their suppression during optimum confinement. Another class of fluctuations causing enhanced transport are ELM-like relaxations with typical duration of 200 - 500 μs, which can occur even outside the H-mode operational window [27]. As in the case of ELMs these relaxations cause a local flattening of the density and temperature profiles around the LCFS (particle and heat expulsion).

5. CONCLUSIONS

The predicted performance of the partially optimised stellarator configuration with respect to equilibrium flux surfaces and stability against pressure driven global modes at high β could be confirmed experimentally. The excitation of global Alfvén eigenmodes by resonant fast particles can lead to a significant deterioration of the confinement under particular operational conditions. Therefore, extensive experimental studies and numerical code calculations have been made in order to improve their understanding, which might help to assess their potential danger in larger machines like W7-X. Further studies, particularly in the higher frequency regime, seem to be necessary. The investigations of small scale fluctuations have shown correlations with anomalous transport. However, the underlying processes are not well known, and quantitative estimates of the turbulent transport are not possible on the basis of the available data.

REFERENCES

[1] GRIEGER, G., et al., Phys. Fluids **B 4** (1992) 2081.
[2] JAENICKE, R., et al., Nuclear Fusion **33** (1993) 687.
[3] ERCKMANN, V., et al., these Proceedings.
[4] WAGNER, F., et al., these Proceedings.
[5] GÖRNER, C., et al., Proc. 24th EPS Conf. Berchtesgaden, **21A** Part IV (1997) 1625.
[6] WELLER, A., et al., Proc. 12th Topical Conf. on High Temperature Plasma Diagn., Princeton 1998, to appear in Rev. of Sci. Instrum.
[7] CALLAGHAN, H., et al., Proc. 24th EPS Conf. Berchtesgaden, **21A** Part IV (1997) 1617.
[8] NÜHRENBERG, J. and ZILLE, R., in Theory of Fusion Plasmas, Varenna 1987, (Editrice Compositori, Bologna, 1988), EUR 11336 EN, p.3.
[9] GEIGER, J., et al., Proc. 23rd EPS Conf. Kiev, **20C** Part II (1996) 491.
[10] SCHWAB, C., Phys. Fluids **B 5** (1993) 3195.
[11] NÜHRENBERG, C., Phys. Plasmas **3** (1996) 2401.
[12] NÜHRENBERG, C., submitted to Phys. Plasmas.
[13] WELLER, A., et al., Phys. Rev. Lett. **72** (1994) 1220.
[14] BRAKEL, R., et al., Proc. 25th EPS Conf. Prague (1998).
[15] SPONG, D.A., et al., Nuclear Fusion **35** (1995) 1687.
[16] STROTH, U., et al., Plasma Phys. Control. Fusion **40** (1998) 1551.
[17] GÖRNER, C., et al., Proc. 25th EPS Conf. Prague (1998).
[18] PINCHES, S.D., et al., Computer Physics Communication **111** (1998) 133.
[19] TEO, C.Y., et al., Nuclear Fusion **38** (1998) 409.
[20] TSAI, S.T. and CHEN, L., et al., Phys. Fluids **B 5** (1993) 3284.
[21] HEIDBRINK, W.W., Plasma Phys. Control. Fusion **37** (1995) 937.
[22] KICK, M., et al., Proc. 25th EPS Conf. Prague (1998).
[23] SCOTT, B., Plasma Phys. Control. Fusion **39** (1997) 1635.
[24] MARASCHEK, M. et al., Phys. Rev. Lett. **79** (1997) 4186.
[25] HARTFUß, H.J., et al., Plasma Phys. Control. Fusion **38** (1996) A221.
[26] ZOLETNIK, S., et al., submitted to Phys. Plasmas.
[27] HIRSCH, M., et al., Proc. 25th EPS Conf. Prague (1998).